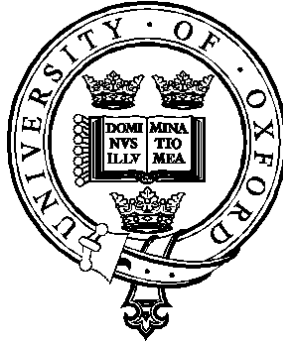


The University of Oxford

Department of Engineering Science



# **Development of a Novel Film Cooling Hole Geometry**

Jane Elizabeth Sargison

Jesus College

Oxford, OX1 3DW

Submitted in partial fulfilment of the requirements  
for the degree of Doctor of Philosophy.

Hilary Term, 2001

# Development of a Novel Film Cooling Hole Geometry

A thesis submitted in partial fulfilment of the requirements for the degree of  
Doctor of Philosophy  
at the University of Oxford  
Hilary Term, 2001

Jane Elizabeth Sargison  
Jesus College  
Oxford, OX1 3DW

## Abstract

This thesis presents the design, development and testing of a new film cooling hole geometry, the converging slot-hole or *console*. Both the thermal and aerodynamic performance were measured, using the adiabatic effectiveness and heat transfer coefficient, and aerodynamic loss respectively, to quantify performance. Comparative measurements were made, by testing conventional film cooling hole shapes in parallel with the *console* experiments. The CFD code, Fluent, was used to predict the performance of the initial design concept before it was manufactured.

Initial performance measurements in incompressible flow were performed in a low speed wind tunnel at an engine representative Reynolds number based on mainstream flow and hole diameter. For these experiments, the coolant to mainstream density ratio was approximately unity, and the cooling performance was measured over a flat plate. The *console* was tested in parallel with cylindrical holes, a slot and fan-shaped holes, all of which had equal throat area per unit width. The heat transfer performance was measured at steady state using thermochromic liquid crystals sprayed onto a flat plate heater. The aerodynamic performance of the holes was measured by traversing the boundary layer 50 cylindrical hole diameters downstream of the injection location with a pitot probe.

Engine representative measurements of the *console* performance were made in a transonic annular cascade that simulates the three-dimensional flow in the gas turbine. The Reynolds and Mach numbers were representative of engine conditions, and the coolant flow was made aerodynamically and thermodynamically similar to engine conditions by matching both the momentum flux and density ratios. This was achieved by using a heavy foreign gas with the composition of 30.2% SF<sub>6</sub> and 69.8% Ar by weight, which simulates the coolant to mainstream density ratio of 1.78, and has a ratio of specific heats of 1.4. The performance of a nozzle guide vane with rows of fan-shaped holes was compared with an NGV with a film cooling configuration designed with rows of *consoles* replacing rows of fan-shaped holes. The heat transfer performance was measured using a modified step change transient liquid crystal technique. The aerodynamic performance was measured using a four hole probe traverse downstream of the NGV.

The heat transfer performance of the *console* was found to be similar to or slightly lower than the performance of fan-shaped holes. The most significant benefit of the *console* was found to be the aerodynamic performance, with a loss due to film cooling of only 20% of the loss due to film cooling of the rows of fan-shaped holes measured at engine representative conditions.

# Acknowledgements

Firstly, I would like to thank my two supervisors Professor Martin Oldfield, and Dr Shengmin Guo for their guidance, advice and encouragement during my time at Oxford. Their combined wisdom kept my determination on track and inspired many solutions.

Dr Gary Lock and Professor Terry Jones both took a keen interest in this work, and provided refreshing new suggestions, and discussion of the work through out the course of the degree.

From the Osney laboratory workshop I must thank Simon Walton, Pat Timms and Trevor Godfrey, who produced most of the equipment used in these experiments. Thanks also to Leo Verling and Geoff Horton who were always ready to prepare extra pieces of test equipment. I am grateful to Andy Soffe from the Engineering laboratories who produced the CAD drawing of the *console* used for all the experimental holes, and NC machined the low-speed *consoles* while under the pressure of my enthusiasm to begin the experimental program.

Acknowledgement must go to the Rhodes Trust, for supporting my D.Phil study at Oxford, and particularly the Warden and staff for making the administration as smooth as possible. Acknowledgements also to the Tasmanian Government for providing extra support.

The CHTT at Oxford University is funded by Rolls-Royce plc, Defence Research Agency, MoD and DTI, whose support is much appreciated.

Finally my deepest thanks must go to Matthew, for technical discussions, support, patience and love.

# Table of Contents

<b>ABSTRACT .....</b>	<b>I</b>
<b>ACKNOWLEDGEMENTS.....</b>	<b>II</b>
<b>TABLE OF CONTENTS .....</b>	<b>III</b>
<b>LIST OF FIGURES.....</b>	<b>VII</b>
<b>NOMENCLATURE .....</b>	<b>XIV</b>
<b>CHAPTER 1 INTRODUCTION.....</b>	<b>1</b>
1.1 MOTIVATION .....	1
1.2 COOLING TECHNOLOGY .....	5
1.3 THESIS AIMS .....	8
1.4 OUTLINE OF THESIS.....	9
<b>CHAPTER 2 REVIEW OF FILM-COOLING AND RELATED WORK.....</b>	<b>11</b>
2.1 FILM COOLING PERFORMANCE PARAMETERS .....	11
2.2 DEVELOPMENT OF FILM COOLING TO OPTIMISE HEAT TRANSFER PERFORMANCE .....	16
2.3 MODELLING FILM COOLING IN THE ENGINE .....	23
2.4 MEASUREMENT OF FILM COOLING PERFORMANCE .....	26
2.5 HEAT TRANSFER MODELS .....	28
2.6 THE AERODYNAMICS OF FILM COOLING JETS .....	32
2.7 AERODYNAMICS OF NGV CASCADE .....	36
2.8 FILM COOLING AERODYNAMIC EFFICIENCY .....	38
2.9 MEASUREMENT OF AERODYNAMIC LOSS .....	41
2.10 AERODYNAMIC LOSS MODELS .....	43
2.11 CONCLUSIONS .....	44
<b>CHAPTER 3 CONSOLE DESIGN.....</b>	<b>45</b>
3.1 CONSOLE CONCEPTUAL DESIGN .....	45
3.2 DESIGN PARAMETERS .....	49
3.3 CFD PREDICTIONS USED IN THE INITIAL DESIGN .....	50
3.4 CONCLUSIONS .....	52

<b>CHAPTER 4</b>	<b>SIMULATION PARAMETERS IN FILM COOLING .....</b>	<b>53</b>
4.1	DIMENSIONAL ANALYSIS AND SIMILITUDE .....	53
4.2	MODELLING DENSITY RATIO USING FOREIGN GAS .....	55
4.3	SIMILARITY FOR LOW-SPEED EXPERIMENTS.....	58
4.4	SIMILARITY FOR HIGH SPEED EXPERIMENTS.....	59
4.5	CONCLUSIONS .....	61
<b>CHAPTER 5</b>	<b>LOW-SPEED HEAT TRANSFER EXPERIMENTS.....</b>	<b>62</b>
5.1	EXPERIMENTAL FACILITY .....	62
5.2	ANALYTICAL TECHNIQUE.....	67
5.2.1	Image processing .....	67
5.2.2	Reduction of experimental data to $h$ and $\dot{h}$ .....	70
5.2.3	Correction for radiation and conduction heat transfer.....	71
5.2.4	<u>Error! Objects cannot be created from editing field codes.</u> Correction for hole discharge coefficients .....	75
5.3	EXPERIMENTAL TECHNIQUE .....	76
5.4	VERIFICATION OF EXPERIMENTAL AND ANALYTICAL TECHNIQUE .....	78
5.4.1	Comparison with published data .....	78
5.4.2	Comparison between large and small cylindrical holes .....	80
5.5	COMPARISON WITH ANALYTICAL SOLUTIONS .....	82
5.5.1	Boundary layer traverse .....	82
5.5.2	Unheated starting length solution .....	83
5.6	EXPERIMENTAL RESULTS.....	84
5.7	DISCHARGE COEFFICIENT .....	99
5.8	UNCERTAINTY ANALYSIS .....	102
5.9	CONCLUSIONS .....	103
<b>CHAPTER 6</b>	<b>HEAT TRANSFER EXPERIMENTS AT ENGINE REPRESENTATIVE CONDITIONS .....</b>	<b>105</b>
6.1	THE FACILITY .....	106
6.2	NOZZLE GUIDE VANES.....	109
6.2.1	Test NGVs .....	109
6.2.2	Dummy NGVs.....	111
6.2.3	Test cassettes.....	112
6.2.4	Heat transfer cassette .....	112

6.3	EXPERIMENTAL MEASUREMENT.....	114
6.3.1	Thermochromic liquid crystals.....	114
6.3.2	Tunnel operating conditions.....	117
6.4	DATA REDUCTION.....	119
6.5	EXPERIMENTAL RESULTS.....	126
6.5.1	Measurement of mass flow rate from hole rows.....	126
6.5.2	Experimental raw data .....	128
6.5.3	Stability of the analytical technique.....	129
6.5.4	Mid span laterally averaged heat transfer coefficient and adiabatic effectiveness results.. .....	131
6.5.5	Full surface result .....	142
6.5.6	Changing the number of rows .....	146
6.6	UNCERTAINTY ANALYSIS.....	149
6.7	CONCLUSIONS .....	150
<b>CHAPTER 7 AERODYNAMIC LOSS DUE TO FILM COOLING .....</b>		<b>152</b>
7.1	MEASUREMENT OF AERODYNAMIC LOSS .....	152
7.2	LOW SPEED EXPERIMENTS .....	154
7.2.1	Experimental facility .....	154
7.2.2	Analytical technique .....	155
7.2.3	Experimental results .....	157
7.2.4	Uncertainty and error analysis.....	160
7.3	CHTT AERODYNAMIC LOSS EXPERIMENTS .....	161
7.3.1	Experimental facility .....	161
7.3.2	Four hole pyramid probe.....	162
7.3.3	Analytical technique .....	164
7.3.4	Experimental results .....	166
7.3.5	Error and uncertainty analysis.....	171
7.4	CONCLUSIONS .....	171
<b>CHAPTER 8 FLOW VISUALISATION OF COOLING JETS.....</b>		<b>173</b>
8.1	EXPERIMENTAL APPARATUS .....	173
8.2	ANALYTICAL TECHNIQUE.....	175
8.3	EXPERIMENTAL RESULTS.....	176

8.3.1	Liquid crystal images.....	176
8.3.2	Contours of gas effectiveness.....	180
8.4	CONCLUSIONS .....	185
<b>CHAPTER 9 FILM COOLING PERFORMANCE PREDICTIONS.....</b>		<b>187</b>
9.1	ANALYTICAL PREDICTION TECHNIQUES .....	187
9.2	COMPARISON OF LOW SPEED RESULTS WITH ANALYTICAL PREDICTIONS .....	189
9.3	COMPARISON OF ENGINE REPRESENTATIVE RESULTS WITH PREDICTIONS .....	193
9.4	COMPARISON OF EXPERIMENTAL RESULTS WITH COMPUTATIONAL MODEL .....	196
9.5	RESULTS OF CFD COMPARED WITH MEASURED DATA.....	198
9.6	CONCLUSIONS .....	206
<b>CHAPTER 10 CONCLUSIONS.....</b>		<b>208</b>
10.1	SUMMARY OF MAJOR THEMES .....	208
10.2	ASSESSMENT OF AIMS .....	210
10.3	FURTHER WORK.....	213
<b>APPENDIX A IMPULSE RESPONSE METHOD.....</b>		<b>215</b>
<b>APPENDIX B ANALYSIS OF TRANSIENT HEAT TRANSFER RESULTS.....</b>		<b>220</b>
<b>BIBLIOGRAPHY .....</b>		<b>237</b>

# List of Figures

Figure 1.1: Rolls-Royce Trent 900	2
Figure 1.2: Diagram of a simple gas turbine system	2
Figure 1.3: Enthalpy – entropy (H-S) diagram of the ideal Joule or Brayton cycle for the simple gas turbine system shown in Figure 1.2	3
Figure 1.4: Theoretical variation of specific fuel consumption and specific thrust for a real engine with compressor pressure ratio and TET (Lakshminarayana, 1996)	4
Figure 1.5: Turbine Cooling Techniques (from Lakshminarayana, 1996)	6
Figure 1.6: Film cooled turbine nozzle guide vanes (Rolls-Royce Publications, 1986)	8
Figure 2.1: Variation of heat flux, $q$ , with effectiveness, $h$ , and sensitivity of $q$ to $h$ (2.8), for typical engine temperatures and $h = 800 \text{ Wm}^{-2}\text{K}^{-1}$	15
Figure 2.2: Variation of heat flux, $q$ , with heat transfer coefficient, $h$ , and sensitivity of $q$ to $h$ (2.9), for typical engine temperatures	15
Figure 2.3: Summary of film cooling hole shapes developed 1943- 2000	18
Figure 2.4: Structure of a single jet in cross flow at (a) low ( $M=0.5$ ) and (b) high ( $M=2.0$ ) velocity ratios (Andreopoulos and Rodi, 1984)	30
Figure 2.5: Kidney and anti kidney shaped vortices and the advantages of shaped holes (from Haven et al, 1997)	35
Figure 2.6: The three dimensional separation of a boundary layer entering a turbine cascade (Langston, 2000)	37
Figure 2.7: Enthalpy entropy diagram for turbine cascade flow	38
Figure 3.1: Basic console configuration	46
Figure 3.2: Cross sectional area and wetted perimeter of console	47
Figure 3.3: Uni Graphics surface definition of two console film cooling holes	48
Figure 3.4: Photograph of Stereolithography NGV with console film cooling hole rows	49
Figure 3.5: Adiabatic wall temperature distribution for console: $T_{0c} = 313 \text{ K}$ , $T_{0m} = T_r = 293 \text{ K}$	51
Figure 3.6: Adiabatic wall temperature distribution for cylindrical holes: $T_{0c} = 313 \text{ K}$ , $T_{0m} = T_r = 293 \text{ K}$	51
Figure 3.7: Adiabatic wall temperature distribution for slot: $T_{0c} = 313 \text{ K}$ , $T_{0m} = T_r = 293 \text{ K}$	51



<i>Figure 4.1: Film cooling effectiveness for air at engine conditions vs. the equivalent value for foreign gas at ambient conditions (Jones, 1999)</i>	58
<i>Figure 5.1 Low-speed wind tunnel</i>	63
<i>Figure 5.2: Film cooling hole configurations</i>	66
<i>Figure 5.3 Experimental apparatus</i>	67
<i>Figure 5.4: Variation in hue and colour signals over the TLC colour play</i>	69
<i>Figure 5.5 Liquid crystal display for console film cooling with extracted temperature contour superimposed onto picture</i>	70
<i>Figure 5.6: Heat flux correction experimental data</i>	74
<i>Figure 5.7: Typical set of data points and fitted straight line used in MATLAB data manipulation</i>	77
<i>Figure 5.8: Slot effectiveness compared with published data</i>	78
<i>Figure 5.9: Slot heat transfer coefficient compared with published data</i>	79
<i>Figure 5.10: Cylindrical hole effectiveness compared with published data</i>	79
<i>Figure 5.11: Cylindrical hole heat transfer coefficient compared with published data</i>	80
<i>Figure 5.12: Large and small cylindrical holes</i>	81
<i>Figure 5.13: Laterally averaged adiabatic effectiveness comparison between large and small cylindrical holes (<math>v_m = 26 \text{ ms}^{-1}</math>, <math>I_{ideal} = 1.1</math>)</i>	81
<i>Figure 5.14: Laterally averaged heat transfer coefficient comparison between large and small cylindrical holes (<math>v_m = 26 \text{ ms}^{-1}</math>, <math>I_{ideal} = 1.1</math>)</i>	81
<i>Figure 5.15: Laterally averaged adiabatic effectiveness comparison between large and small cylindrical holes (<math>v_m = 5 \text{ ms}^{-1}</math>, <math>I_{ideal} = 1.1</math>)</i>	82
<i>Figure 5.16: Laterally averaged heat transfer coefficient comparison between large and small cylindrical holes (<math>v_m = 5 \text{ ms}^{-1}</math>, <math>I_{ideal} = 1.1</math>)</i>	82
<i>Figure 5.17: Boundary layer velocity profile</i>	83
<i>Figure 5.18: Comparison of measured and analytical solution for a flat plate with an unheated starting length</i>	84
<i>Figure 5.19 Adiabatic effectiveness contour for slot, <math>I_{ideal} = 1.5</math>, <math>v_m = 26 \text{ ms}^{-1}</math></i>	86
<i>Figure 5.20: Heat transfer coefficient contour for slot, <math>I_{ideal} = 1.5</math>, <math>v_m = 26 \text{ ms}^{-1}</math></i>	86
<i>Figure 5.21: Adiabatic effectiveness contour for console, <math>I_{ideal} = 1.5</math>, <math>v_m = 26 \text{ ms}^{-1}</math></i>	87
<i>Figure 5.22: Heat transfer coefficient contour for console, <math>I_{ideal} = 1.5</math>, <math>v_m = 26 \text{ ms}^{-1}</math></i>	87

Figure 5.23: Adiabatic effectiveness contour for fan-shaped holes, $I_{ideal} = 1.5$ , $v_m = 26 \text{ ms}^{-1}$	88
Figure 5.24: Heat transfer coefficient contour for fan-shaped holes, $I_{ideal} = 1.5$ , $v_m = 26 \text{ ms}^{-1}$	88
Figure 5.25: Adiabatic effectiveness contour for cylindrical holes, $I_{ideal} = 1.5$ , $v_m = 26 \text{ ms}^{-1}$	89
Figure 5.26: Heat transfer coefficient contour for cylindrical holes, $I_{ideal} = 1.5$ , $v_m = 26 \text{ ms}^{-1}$	89
Figure 5.27 Lateral adiabatic effectiveness results, $I_{ideal} = 1.1$ , $v_m = 26 \text{ ms}^{-1}$	90
Figure 5.28 Laterally averaged adiabatic effectiveness $I_{ideal} = 1.1$ , $v_m = 26 \text{ ms}^{-1}$	92
Figure 5.29 Laterally averaged adiabatic effectiveness $I_{ideal} = 0.5$ , $v_m = 26 \text{ ms}^{-1}$	92
Figure 5.30 Laterally averaged adiabatic effectiveness $I_{ideal} = 1.5$ , $v_m = 26 \text{ ms}^{-1}$	93
Figure 5.31 Lateral heat transfer coefficient results, $I_{ideal} = 1.1$ , $v_m = 26 \text{ ms}^{-1}$	94
Figure 5.32 Laterally averaged heat transfer coefficient $I_{ideal} = 1.1$ , $v_m = 26 \text{ ms}^{-1}$	95
Figure 5.33 Laterally averaged heat transfer coefficient, $I_{ideal} = 0.5$ , $v_m = 26 \text{ ms}^{-1}$	95
Figure 5.34 Laterally averaged heat transfer coefficient $I_{ideal} = 1.5$ , $v_m = 26 \text{ ms}^{-1}$	96
Figure 5.35 Laterally averaged net heat flux reduction $I_{ideal} = 1.1$ , $v_m = 26 \text{ ms}^{-1}$	98
Figure 5.36 Laterally averaged net heat flux reduction $I_{ideal} = 0.5$ , $v_m = 26 \text{ ms}^{-1}$	98
Figure 5.37 Laterally averaged net heat flux reduction $I_{ideal} = 1.5$ , $v_m = 26 \text{ ms}^{-1}$	99
Figure 5.38 Discharge coefficient with crossflow, $v_m = 26 \text{ ms}^{-1}$	100
Figure 5.39 Discharge coefficient with no crossflow	100
Figure 5.40: Comparison of measured discharge coefficients with results from Rowbury (1998): discharge coefficient with crossflow	101
Figure 5.41: Comparison of measured discharge coefficients with results from Rowbury (1998): discharge coefficient with no crossflow	101
Figure 6.1: Photograph of the heat transfer side of the CHTT	106
Figure 6.2: Schematic of the CHTT	107
Figure 6.3: Fanned and console NGVs with cooling hole rows indicated	109
Figure 6.4: Heat transfer cassette	113
Figure 6.5: Schematic of camera location to record TLC colour play	115
Figure 6.6: Surface temperature vs. hue for a single pixel	116
Figure 6.7: Experimental pressure trace	118
Figure 6.8: Experimental temperature trace	118
Figure 6.9: Isentropic Mach Number distribution around vane at design conditions	119

<i>Figure 6.10: Thermocouple temperature trace with ramp and step curve fits</i>	121
<i>Figure 6.11: Experimental heat flux trace obtained from surface thermocouple</i>	122
<i>Figure 6.12: Adiabatic wall temperature distribution</i>	124
<i>Figure 6.13: Comparison of TLC and Thermocouple (TC) data at the location of TC B on the mid pressure surface of the NGV (Thermocouple locations on console NGV shown at right)</i>	125
<i>Figure 6.14: TLC data points with step change and ramp curve fits applied, with an example of an undershoot in temperature in the fitted curve</i>	126
<i>Figure 6.15: Pressure surface camera view</i>	128
<i>Figure 6.16: Leading edge camera view</i>	128
<i>Figure 6.17: Suction surface camera view</i>	129
<i>Figure 6.18: TLC temperature trace from high effectiveness region of surface, near row C14 on the Suction Surface</i>	130
<i>Figure 6.19: Suction surface adiabatic effectiveness (experimental conditions)</i>	134
<i>Figure 6.20: Suction surface heat transfer coefficient (experimental conditions)</i>	134
<i>Figure 6.21: suction Surface predicted total heat flux (experimental conditions)</i>	135
<i>Figure 6.22: Suction surface adiabatic effectiveness (engine conditions)</i>	135
<i>Figure 6.23: Suction surface heat transfer coefficient (engine conditions)</i>	136
<i>Figure 6.24: Suction surface predicted heat flux (engine conditions)</i>	136
<i>Figure 6.25: Pressure surface adiabatic effectiveness (experimental conditions)</i>	138
<i>Figure 6.26: Pressure surface heat transfer coefficient (experimental conditions)</i>	138
<i>Figure 6.27: Pressure surface predicted heat flux (experimental conditions)</i>	139
<i>Figure 6.28: Pressure surface adiabatic effectiveness (engine conditions)</i>	139
<i>Figure 6.29: Pressure surface heat transfer coefficient (engine conditions)</i>	140
<i>Figure 6.30: Pressure surface predicted heat flux (engine conditions)</i>	140
<i>Figure 6.31: Mass flow correction to data downstream of row 14 (Suction surface) (experimental conditions)</i>	141
<i>Figure 6.32: Mass flow correction to data downstream of row C3/4 (Pressure surface) (experimental conditions)</i>	142
<i>Figure 6.33: Adiabatic Effectiveness on the console NGV suction surface (experimental conditions)</i>	143
<i>Figure 6.34: Heat Transfer Coefficient on the console NGV suction surface (experimental conditions)</i>	143

<i>Figure 6.35: Adiabatic Effectiveness on the console NGV pressure surface (Regions without colour indicate that the solution was unstable (see Section 6.5.3) (experimental conditions)</i>	144
<i>Figure 6.36: Heat Transfer Coefficient on the console NGV pressure surface (Regions without colour indicate that the solution was unstable (see Section 6.5.3) (experimental conditions)</i>	144
<i>Figure 6.37: Adiabatic effectiveness on the fanned NGV suction surface (experimental conditions)</i>	145
<i>Figure 6.38: Adiabatic effectiveness on the fanned NGV pressure surface (experimental conditions)</i>	146
<i>Figure 6.39: Adiabatic Effectiveness for consoles on suction surface with row 14 missing (experimental conditions)</i>	148
<i>Figure 6.40: Heat transfer coefficient for consoles on suction surface with row 14 missing (experimental conditions)</i>	148
<i>Figure 7.1: Definition of measurement and calculation planes</i>	155
<i>Figure 7.2: Velocity profiles for all film cooling hole shapes at <math>I_{ideal} = 1.1</math></i>	158
<i>Figure 7.3: Comparison of aerodynamic loss for the four film cooling configurations and no film cooling (mainstream flow only)</i>	158
<i>Figure 7.4: Aerodynamic loss normalised against loss with no film cooling</i>	159
<i>Figure 7.5: Variation of aerodynamic loss with ideal momentum flux ratio, for all cooling hole geometries showing data error bands</i>	159
<i>Figure 7.6: The aerodynamic cassette with the four-hole probe in the measuring position downstream of the NGV</i>	161
<i>Figure 7.7: Definition of the mixed-out plane for CHTT experiment from Main et al (1997)</i>	162
<i>Figure 7.8: The four-hole pyramid probe from Main et al (1996)</i>	163
<i>Figure 7.9: The definition of circumferential (<b>q</b>), swirl (<b>b</b>) and pitch (<b>a</b>) angles in the NGV cascade (Day 1997)</i>	166
<i>Figure 7.10: Normalised total pressure</i>	167
<i>Figure 7.11: Mach number</i>	167
<i>Figure 7.12: Swirl angle</i>	167
<i>Figure 7.13: Pitch angle</i>	168
<i>Figure 7.14: Aerodynamic loss for film cooling configurations</i>	170
<i>Figure 7.15: Aerodynamic loss for film cooling configurations normalised against loss without film cooling (NFC)</i>	170

Figure 8.1: Nylon mesh fabric (actual size) _____	174
Figure 8.2: TLC mesh _____	174
Figure 8.3: Locations of mesh in wind tunnel working section _____	175
Figure 8.4: Low speed wind tunnel working section with TLC mesh at 1d _____	175
Figure 8.5: Photographs of contours at 10 d, with $I = 1.1$ and $v_m = 26 \text{ ms}^{-1}$ _____	178
Figure 8.6: Photographs of contours at 10 d, with $I = 40$ and $v_m = 5 \text{ ms}^{-1}$ _____	178
Figure 8.7: Kidney and anti-kidney vortices in cylindrical and fan-shaped hole jets _____	179
Figure 8.8: Photographs of contours at 3 d, with $I = \text{¥}$ and $v_m = 0 \text{ ms}^{-1}$ _____	179
Figure 8.9: Contours of effectiveness at 1 d, $I=1.1$ , $\text{DP}_c=412 \text{ Pa}$ , $v_m = 26 \text{ ms}^{-1}$ _____	181
Figure 8.10: Contours of effectiveness at 3 d, $I=1.1$ , $\text{DP}_c=412$ , $v_m = 26 \text{ ms}^{-1}$ _____	181
Figure 8.11: Contours of effectiveness at 10 d, $I=1.1$ , $\text{DP}_c=412$ , $v_m = 26 \text{ ms}^{-1}$ _____	182
Figure 8.12: Contours of effectiveness at 25 d, $I=1.1$ , $\text{DP}_c=412$ , $v_m = 26 \text{ ms}^{-1}$ _____	182
Figure 8.13: Contours of effectiveness at 1 d, $I=\text{¥}$ , $\text{DP}_c=412$ , $v_m = 0 \text{ ms}^{-1}$ _____	183
Figure 8.14: Contours of effectiveness at 3 d, $I=\text{¥}$ , $\text{DP}_c=412$ , $v_m = 0 \text{ ms}^{-1}$ _____	184
Figure 8.15: Contours of effectiveness at 10 d, $I=40$ , $\text{DP}_c=412$ , $v_m = 5 \text{ ms}^{-1}$ _____	184
Figure 8.16: Contours of effectiveness at 25 d, $I=40$ , $\text{DP}_c=412$ , $v_m = 5 \text{ ms}^{-1}$ _____	185
Figure 9.1: Comparison of slot and console results (at $I_{\text{ideal}} = 0.5, 1.1, 1.5$ ) with line heat source prediction from Eckert and Drake (1972) (E&D) _____	191
Figure 9.2: Comparison of slot and console experimental results using the Forth and Jones (1986) correlation _____	191
Figure 9.3: Comparison of cylindrical hole results with Eckert and Drake (1972) _____	192
Figure 9.4: Comparison of fan-shaped hole experimental effectiveness with Eckert and Drake (1972) prediction _____	192
Figure 9.5: Correlation of fan-shaped hole experimental effectiveness at varying $I$ using Forth and Jones (1986) correlation parameter _____	193
Figure 9.6: Comparison of measured Nusselt numbers on Suction Surface for console and solid NGVs with analytical results for laminar and for turbulent flow _____	194
Figure 9.7: Comparison of measured Nusselt numbers on Pressure Surface for console and solid NGVs with analytical results for laminar and for turbulent flow _____	194
Figure 9.8: Predicted and experimental effectiveness for console NGV pressure surface _____	195

Figure 9.9: Predicted and experimental effectiveness for console NGV suction surface	195
Figure 9.10: Predicted and experimental effectiveness for fanned NGV pressure surface	196
Figure 9.11: Predicted and experimental effectiveness for fanned NGV suction surface	196
Figure 9.12: CFD model of film cooling hole, plenum chamber and wind tunnel working section, for the console model.	199
Figure 9.13: Console grid definition through and near the hole	199
Figure 9.14: Comparison of predicted and measured surface adiabatic wall temperature for cylindrical holes, $I_{ideal} = 1.1$ , $v_m = 26 \text{ ms}^{-1}$	200
Figure 9.15: Comparison of predicted and measured surface adiabatic wall temperature for console, $I_{ideal} = 1.1$ , $v_m = 26 \text{ ms}^{-1}$	200
Figure 9.16: Comparison of predicted and measured surface adiabatic wall temperature for slot, $I_{ideal} = 1.1$ , $v_m = 26 \text{ ms}^{-1}$	201
Figure 9.17: Comparison of the console, slot and cylindrical hole laterally averaged effectiveness results at $I_{ideal} = 1.1$ with CFD	202
Figure 9.18: Comparison of two-dimensional flat plate and slot heat transfer coefficient CFD results with experimental data	203
Figure 9.19: Comparison of two-dimensional and three dimensional slot effectiveness CFD results and experimental data	203
Figure 9.20: CFD predicted contours of cylindrical hole gas effectiveness	204
Figure 9.21: CFD predicted contours of slot gas effectiveness	204
Figure 9.22: CFD predicted contours of console gas effectiveness	205
Figure 9.23: CFD predicted contours of gas effectiveness at edge of console	205
Figure 9.24: CFD predicted contours of gas effectiveness at centreline of console	205

# Nomenclature

$a$	Local speed of sound ( $\text{ms}^{-1}$ ), $a = \sqrt{gRT}$ for an ideal gas
$A$	Area ( $\text{m}^2$ )
$A_r$	<i>Console</i> outlet aspect ratio. $A_r = w/s$
$B$	Blowing ratio, mass flux ratio, $B = \frac{\mathbf{r}_c v_c}{\mathbf{r}_m v_m}$
$c$	Specific heat ( $\text{Jkg}^{-1}\text{K}^{-1}$ )
$C_D$	Discharge coefficient
$d$	Hole diameter (m)
$D$	Density ratio $D = \frac{\mathbf{r}_c}{\mathbf{r}_m}$
$F$	Thrust (N)
$g$	Acceleration due to gravity ( $\text{ms}^{-2}$ )
$Gr$	Grashof number $Gr_y = \frac{gby^3(T_w - T_m)}{\mathbf{n}^2}$
$h$	Heat transfer coefficient ( $\text{Wm}^{-2}\text{K}^{-1}$ )
$H$	Enthalpy (J)
$I_{\text{ACTUAL}}$	Actual momentum flux ratio, $I_{\text{ACTUAL}} = \frac{\mathbf{r}_c v_c^2}{\mathbf{r}_m v_m^2}$
$I_{\text{IDEAL}}$	Ideal momentum flux ratio, $I_{\text{IDEAL}} = \frac{P_{oc} - P_m}{P_{om} - P_m}$ for incompressible flow
$k$	Thermal conductivity ( $\text{Wm}^{-1}\text{K}^{-1}$ )
$k_c$	<i>Console</i> area contraction ratio, $k_c = pd^2/4sw$
$K$	Acceleration parameter, $K = \frac{\mathbf{n}}{u_m^2} \frac{du_m}{dx}$
$KE$	Rate of kinetic energy flux ( $\text{kgs}^{-3}$ )
$l$	Hole length (m)
$L$	Height of boundary layer calculation (m)
$\dot{m}$	Mass flux ( $\text{kgs}^{-1}\text{m}^{-2}$ )
$m$	Slope

$M$	Mach number, $M = \frac{v}{a}$
$NHFR$	Net heat flux reduction $NHFR = 1 - \frac{q}{q_{nfc}} = 1 - \frac{h}{h_{nfc}}(1 - hq)$
$Nu$	Nusselt number, $Nu = \frac{hx}{k}$
$p$	Hole pitch (m)
$P$	Pressure (Pa)
$Pe$	Peclet number, $Pe_t = \frac{u_m x}{e_M}$
$Pr$	Prandtl number, $Pr = \frac{mc}{k}$
$q$	Heat flux ( $Wm^{-2}$ )
$r$	Radius (m)
$r$	Recovery factor, $r = Pr^{1/3}$ (turbulent flow)
$R$	Gas constant ( $Jkmol^{-1}K^{-1}$ )
$Re$	Reynolds number $Re_x = \frac{rux}{m}$
$s$	Slot height (m)
$S$	Entropy ( $JK^{-1}$ )
$Sc$	Schmidt number $Sc = \frac{m}{g_j}$
$s_m$	Console solidity ratio, $s_m = \frac{1}{2}(1 - d/w)$
$St$	Stanton number $St = \frac{h}{urc}$
$t$	Time (s)
$t$	Plate thickness (m)
$T$	Temperature (K)
$u, v$	Velocity ( $ms^{-1}$ )
$V$	Velocity ratio $V = \frac{v_c}{v_m}$
$w$	Width (m)
$x, y, z$	Cartesian coordinates
$Y$	Stagnation pressure loss coefficient



## ***Greek Letters***

<b><i>a</i></b>	Molecular thermal diffusivity, $\mathbf{a} = \frac{k}{\rho c}$ , (m <sup>2</sup> s <sup>-1</sup> )
<b><i>a</i></b>	Pitch angle (°) (cascade)
<b><i>b</i></b>	Volumetric coefficient of thermal expansion (K <sup>-1</sup> )
<b><i>b</i></b>	Swirl angle (°) (cascade)
<b><i>d</i></b>	Boundary layer thickness (m)
<b><i>e</i></b>	Aerodynamic efficiency
<b><i>e<sub>rad</sub></i></b>	Surface emissivity for radiation (Wm <sup>-2</sup> K <sup>4</sup> )
<b><i>e<sub>M</sub></i></b>	Eddy diffusivity for momentum transfer (m <sup>2</sup> s <sup>-1</sup> )
<b><i>f</i></b>	Inclination angle (°)
<b><i>g</i></b>	Ratio of specific heats, $\mathbf{g} = \frac{c_p}{c_v}$
<b><i>g<sub>j</sub></i></b>	Mass diffusion coefficient for substance <i>j</i> in a mixture (kgm <sup>-1</sup> s <sup>-1</sup> )
<b><i>h</i></b>	Adiabatic effectiveness, $\mathbf{h} = \frac{T_{aw} - T_r}{T_{0c} - T_{0m}}$
<b><i>l</i></b>	Overshoot factor
<b><i>m</i></b>	Dynamic viscosity coefficient, (Nsm <sup>-2</sup> )
<b><i>n</i></b>	Kinematic viscosity, $\frac{\mathbf{m}}{\rho}$ (m <sup>2</sup> s <sup>-1</sup> )
<b><i>q</i></b>	Dimensionless temperature $\mathbf{q} = \frac{T_{0c} - T_r}{T_w - T_{0m}}$
<b><i>q</i></b>	Circumferential angle (°) (cascade)
<b><i>r</i></b>	Density (kgm <sup>-3</sup> )
<b><i>s</i></b>	Stefan-Boltzmann constant (Wm <sup>-2</sup> K <sup>4</sup> )
<b><i>x</i></b>	Unheated starting length (m)
<b><i>y<sub>mass</sub>, y<sub>mole</sub></i></b>	Mass fraction, mole fraction
<b><i>z</i></b>	Loss coefficient

## ***Subscripts***

0	total or stagnation value (pressure, temperature, density)
1	upstream condition
2	downstream condition

a	air flow
A	measurement plane
aw	adiabatic wall
c	coolant
d	diameter
dat	datum
e	engine conditions
ex	experimental conditions
f	fuel flow
hyp	hypothetical
i	initial
m	mainstream
nfc	no film cooling
p	constant pressure
r	recovery
s	ideal or reversible
t	turbulent
v	constant volume
w	wall
x	variation with $x$

### ***Abbreviations***

CFD	Computational Fluid Dynamics
CHTT	Cold Heat Transfer Tunnel
NGV	Nozzle Guide Vane
SFC	Specific Fuel Consumption
ST	Specific Thrust
TBC	Thermal Barrier Coating
TC	Thermocouple
TET	Turbine Entry Temperature
TLC	Thermochromic Liquid Crystal

# Chapter 1

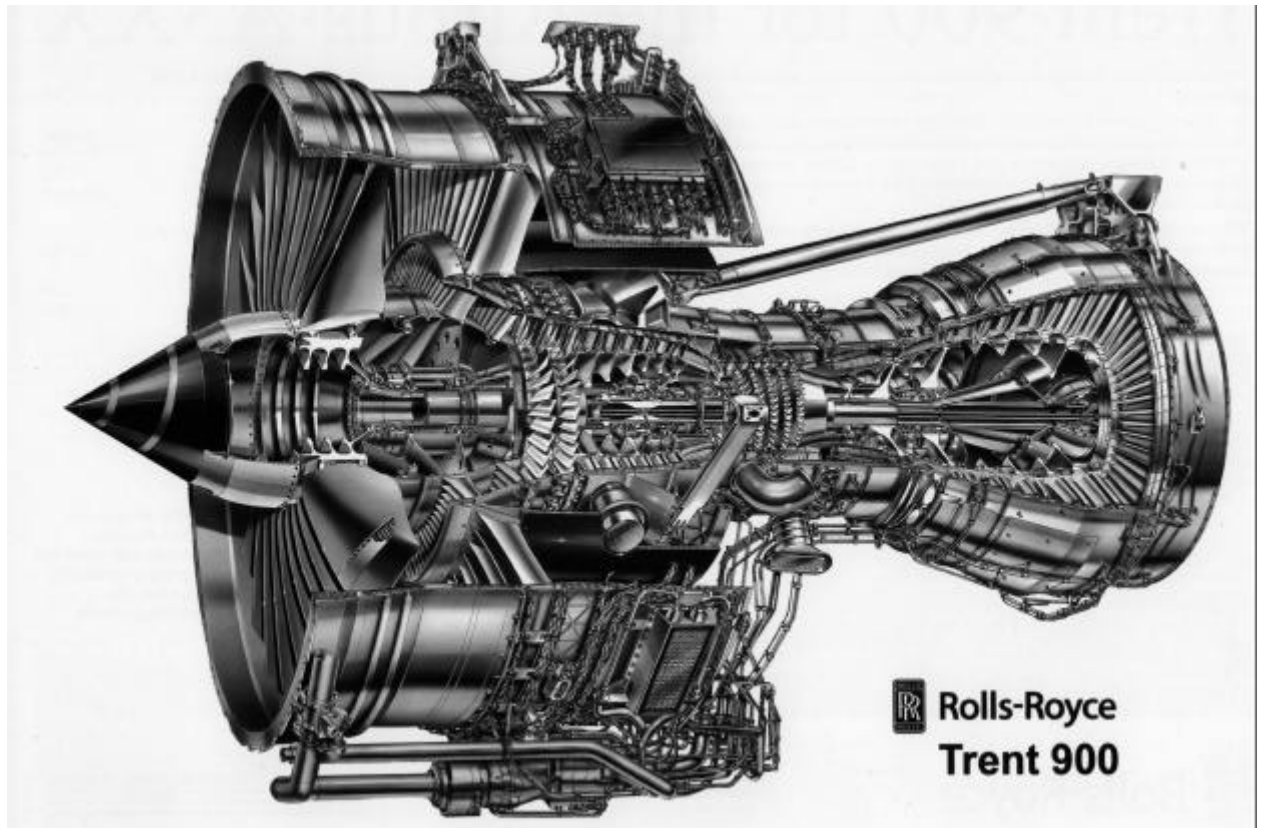
## Introduction

### **1.1 Motivation**

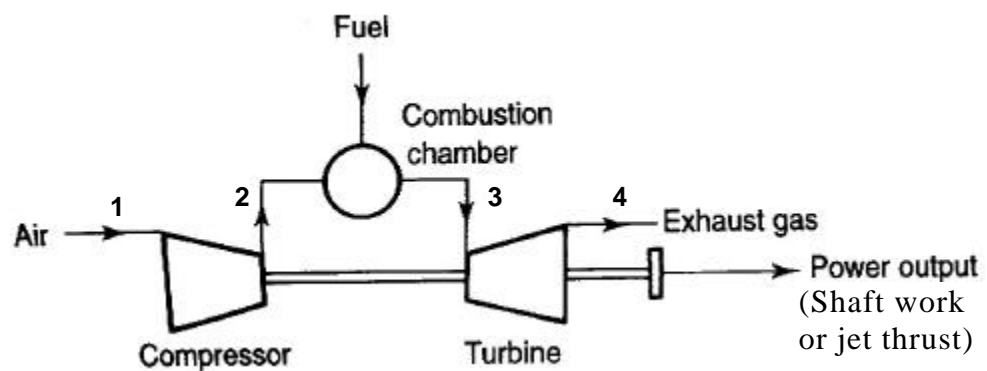
The gas turbine began to be seriously developed for use as a power plant for aircraft propulsion in the 1930s and during the Second World War. Since this time there has been remarkable development, from the early jet engines with 1000 lb (4.5 kN) of thrust in 1942 to the Rolls-Royce Trent 900 (2001), which is rated at 80,000 lb (356 kN) of thrust (Figure 1.1). This progress has been due to a combination of developments in numerical analysis, aerodynamics, gas dynamics, heat transfer, solid mechanics, vibration theory, materials science, acoustics, manufacturing, control systems, and computing power. With pressure arising from both the commercial sector and defence forces, advances have been driven by the need for high efficiency, performance, reliability and low weight in addition to ever increasing environmental constraints covering both chemical and noise pollution.

The main components of the gas turbine engine are the compressor, combustion chamber and turbine and a simple gas turbine cycle consisting of these elements is shown diagrammatically in Figure 1.2. The enthalpy - entropy, or  $H$ - $S$  diagram, shown in Figure 1.3, for this system is the ideal (constant entropy compression and expansion) Joule or Brayton cycle. The gas is compressed from state point 1 to 2 through the compressor, and energy is added to the flow in the form of heat by the burning of fuel in the combustion

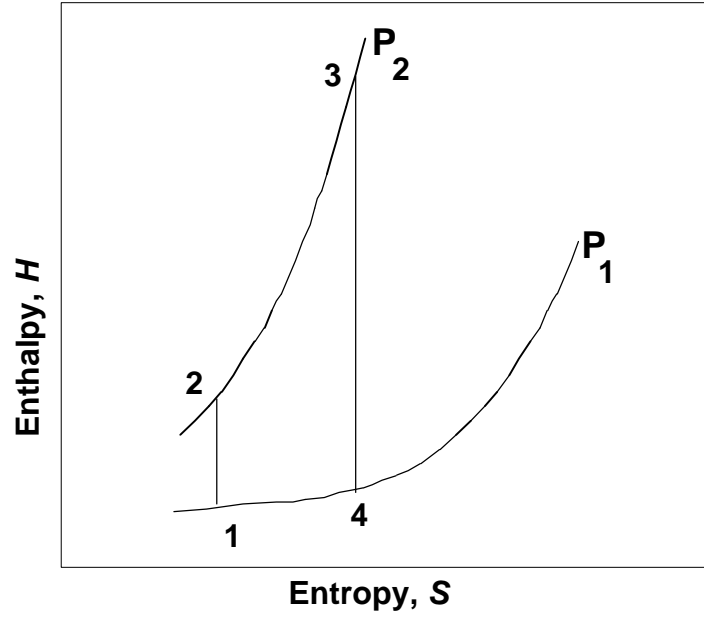
chamber between state points 2 and 3 along an isobaric line. The high pressure and high enthalpy flow is then expanded through the turbine, which produces shaft work that drives the compressor, and extra useful power output that is used to provide propulsion in the aero jet engine by producing thrust due to the jet created in the propelling nozzle or shaft work from extra turbine stages for the industrial gas turbine.



*Figure 1.1: Rolls-Royce Trent 900*



*Figure 1.2: Diagram of a simple gas turbine system*

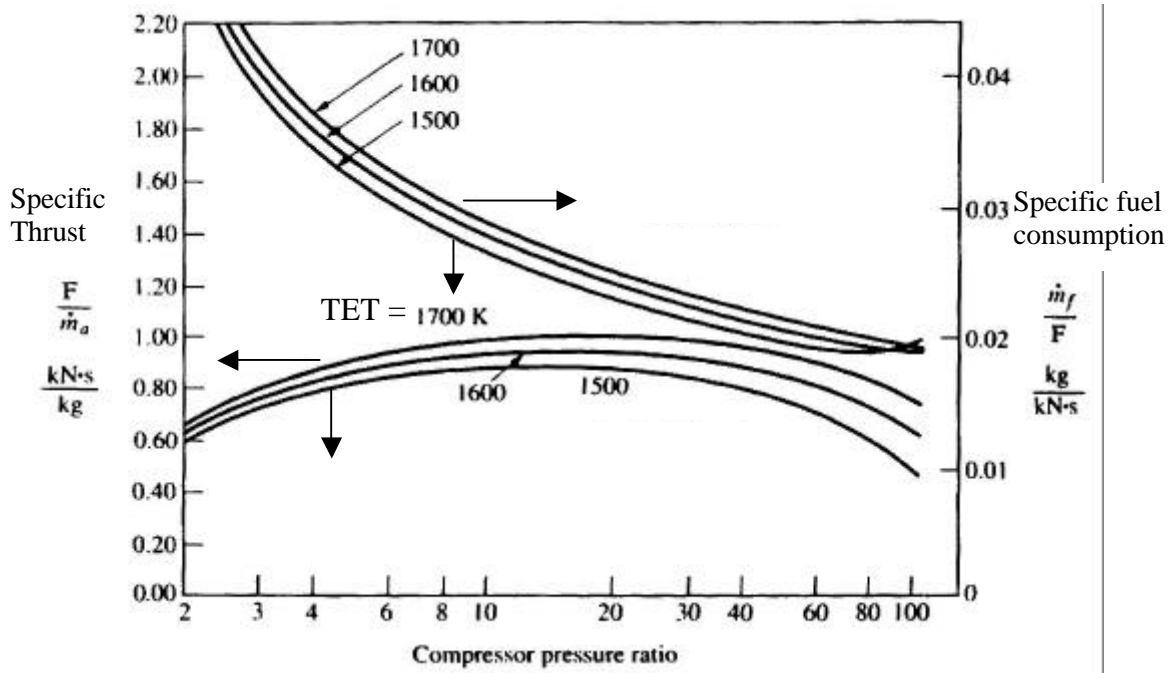


**Figure 1.3: Enthalpy – entropy (H-S) diagram of the ideal Joule or Brayton cycle for the simple gas turbine system shown in Figure 1.2**

The parameters that are used to define the performance of a gas turbine are the Specific Fuel Consumption (*SFC*) and Specific Thrust (*ST*). *SFC* is the fuel consumption per unit net work output or per unit thrust for aircraft engines, i.e.  $SFC = \frac{\dot{m}_f}{F}$ , where  $\dot{m}_f$  is the mass flow rate of fuel, and  $F$  is the engine thrust. The *SFC* is a measure of engine efficiency, where the efficiency of the engine is proportional to  $1/SFC$ . The specific thrust is the thrust produced per unit mass of air, i.e.  $ST = \frac{F}{\dot{m}_a}$ , where  $\dot{m}_a$  is the mass flow rate of air, and *ST* is a measure of the size of the engine.

Figure 1.4 illustrates the variation of *SFC* and *ST* with turbine entry temperature (TET) and compressor pressure ratio, based on the thermodynamics of the gas turbine cycle. From fundamental thermodynamics (e.g. Rogers and Mayhew, 1957), for an ideal cycle, increasing the TET at a constant pressure ratio through a change in fuel/ air ratio causes an increase in the specific work output, or specific thrust, but does not alter the overall

efficiency of the engine. Increasing the compressor pressure ratio, which will have the effect of increasing TET at constant fuel/air ratio, causes an increase in efficiency or reduction in *SFC*. For a real gas turbine cycle, there is an optimum pressure ratio for *SFC* and specific thrust, at a particular TET.



**Figure 1.4: Theoretical variation of specific fuel consumption and specific thrust for a real engine with compressor pressure ratio and TET (Lakshminarayana, 1996)**

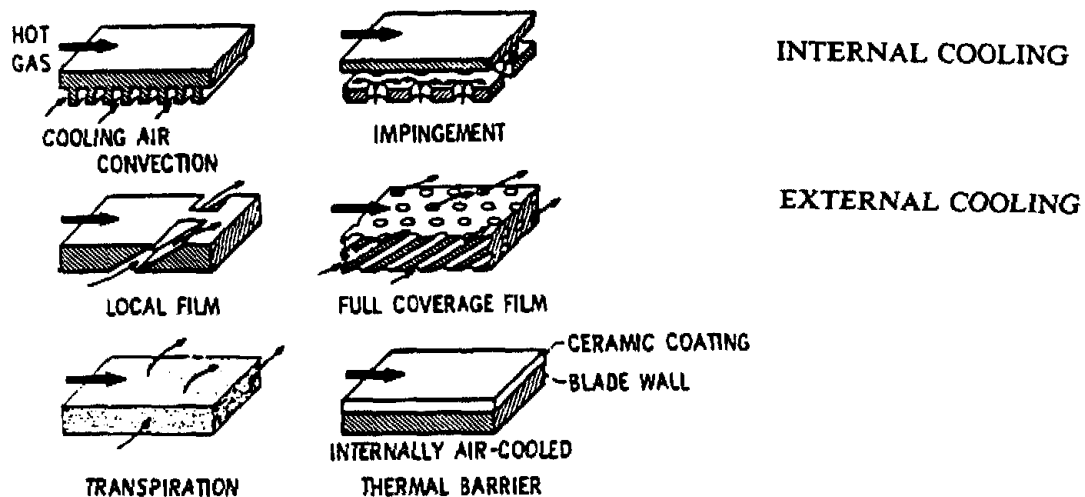
In modern gas turbines, the turbine entry temperature has been increased to as high as 1900 K, well above the turbine blade and vane operating metal temperatures of 1200 K. This advancement has been in part due to improvements in materials used to produce the turbine blades and vanes, but more significantly due to the use of blade and vane cooling technologies that aim to protect the material from the extreme temperatures. A turbine cooling design aims to provide a relatively uniform material temperature within the material operating temperature limit in order to minimise thermal stress and maximise component life.

The increasing TET has placed demands for improvements in engine cooling and the work described in this thesis is the development of a new film cooling geometry to meet this demand.

## **1.2 Cooling technology**

There have been many cooling techniques proposed, but those most commonly used in aerospace applications involve air cooling and are shown in Figure 1.5. The air used for cooling is drawn from the outlet of the compressor, resulting in losses in overall engine efficiency due to the loss of work producing capacity, in addition to thermodynamic and aerodynamic losses due to the ducting of the coolant to the blade surface and mixing of coolant air with hot mainstream flow. Despite this, the benefits in reduced *SFC* and increased specific power output which follow from an increase in permissible TET (combined with an increase in compressor pressure ratio) are still substantial when the additional losses introduced by the cooling system are taken into account (Cohen et al, 1996).

The main turbine cooling techniques shown in Figure 1.5 can be classified into internal and external cooling regimes. For internal cooling regimes the cooling air flows in cast channels below the outer surface that is protected. The cooling air is used as a heat sink to cool by removing heat from the surface. Internal cooling is generally applied to situations where the external stream temperatures are in the range 1300-1600 K. In external cooling regimes, the external surface is protected by a film of cool air or a ceramic Thermal Barrier Coating (TBC). These are generally used in combination with internal cooling in situations where the external stream temperatures are above 1600 K.



*Figure 1.5: Turbine Cooling Techniques (from Lakshminarayana, 1996)*

The turbine cooling techniques shown in Figure 1.5 have the following characteristics:

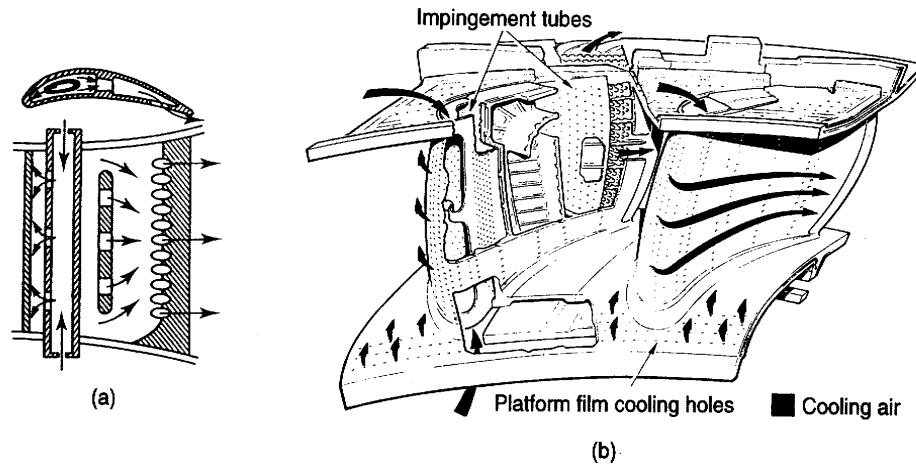
- Convection cooling – air is passed through a series of passages inside the component and ejected, usually at the trailing edge.
- Impingement cooling – the heat transfer coefficient at the blade inner surface is increased by jets of cold air from a row or several rows of small holes in an insert in the blade impacting on the blade wall. This improves the surface cooling by drawing more heat from the metal to the coolant.
- Thermal barrier coatings (TBC) – the surface is protected by insulating it with a low conductivity ceramic coating.
- Film cooling – jets of cool air are ejected through rows of holes in the surface of the blade, providing a thin layer of cool air downstream of the film cooling hole, which insulates the blade from the hot mainstream flow and acts as a heat sink to cool the blade surface.



- Full coverage film cooling – the benefits of film cooling are increased by covering the surface with a large number of closely spaced film cooling holes to provide a more uniform coolant film.
- Transpiration cooling – coolant is introduced through a porous wall so that the wall is uniformly cooled towards the maximum theoretical limit (the coolant temperature) with low velocity coolant. The porous wall is generally produced from woven metal wires or wound wires that have been sintered together. The porosity of the material can be controlled and this will define the transpiration flows. Generally, the finer the structure, the greater the surface area for heat transfer and the material will approach the coolant temperature more closely. However, the disadvantages of the fine porosity are that the increased surface area increases the surface oxidation, and the pores tend to become blocked by particles in the flow. In fact these limit the performance of transpiration cooling at any useful level of porosity. There is, in addition, a high level of aerodynamic loss associated with transpiration cooling, because the coolant loses a large amount of dynamic head through the porous wall. In addition to these problems, the porous materials used to construct the vane for transpiration cooling do not have the structural strength required for turbine blades and vanes. Moskowitz and Lombardo (1971) tested transpiration cooled rotor blades and stator vanes in an engine at 1783K (2750°F), and found that the level of cooling was significantly better than could be obtained using film cooling (more uniform and lower temperature). However, the inherent problems with transpiration cooling have prevented its use in a production engine to date.

As well as the previously mentioned efficiency reductions caused by cooling, the complexity of design and manufacture is significantly increased when cooling is

introduced into a design. This can be observed in Figure 1.6, which shows the complicated internal impingement cooling and external film cooling geometry of a state of the art Rolls-Royce NGV.



**Figure 1.6: Film cooled turbine nozzle guide vanes (Rolls-Royce Publications, 1986)**

### 1.3 Thesis aims

The aim of this thesis is to present the design, development and testing of the latest development in film cooling – the converging slot-hole or *console*. The requirements for the new geometry were to produce a new hole design which produces the same or better film cooling thermal performance compared with the best traditional design (fan-shaped holes), using the same or lower amount of coolant, with a reduction in aerodynamic loss due to film cooling of 40%. In order to achieve this aim, the following practical goals were required:

- To develop a ‘standard’ *console* design based on the design concept
- Measure the thermal performance of the *console* compared with standard holes
- Measure the aerodynamic efficiency of the *console* compared with standard holes
- To use flow visualisation and CFD to obtain some understanding of the *console* flow mechanisms

- Suggest improvements to the original *console* concept
- Develop design methods for implementation of the *console* in the engine

#### **1.4 Outline of thesis**

This thesis summarises the development of the *console*, a new film cooling hole shape. The concepts behind the film cooling hole design are considered, and the performance of the hole is measured and compared with conventional hole shapes in a low-speed, flat-plate facility and at engine representative conditions in an annular cascade of nozzle guide vanes.

The current state of research is outlined in Chapter 2, with particular reference to the development of film cooling and the continuing improvements in thermal protection and aerodynamic efficiency. The measurement techniques and the relevant advantages and disadvantages of many of the proposed hole geometries are discussed, and the performance of the film cooling jets is considered in light of the aerodynamic features of the interaction of the coolant jet with crossflow.

Chapter 3 presents the design of the *console* and describes the predicted performance of the *console* in view of the design features.

In Chapter 4, the issue of similarity of the experiments to engine conditions is addressed and the degree of similarity that is attained for the different experiments is discussed.

In Chapter 5 the low speed, flat plate experiments conducted to measure the thermal performance of the *console* compared with cylindrical holes, fan-shaped holes and a slot are described. The experimental apparatus, experimental and analytical techniques and the results of these experiments are presented and discussed.

In Chapter 6, the experiments conducted to measure the heat transfer performance of the *console* at engine representative conditions using the Cold Heat Transfer Tunnel (CHTT) facility at the University of Oxford Osney Laboratory are presented. The design of a Nozzle Guide Vane (NGV), with rows of *consoles* replacing rows of fan-shaped holes in the traditional NGV is presented. A new method to analyse the results of the transient experiment based on a modification to the step change approach is presented. The results of the analysis are compared with the performance of the NGV with fan-shaped film cooling holes, and an NGV with cylindrical film cooling holes.

In Chapter 7, experiments to measure the aerodynamic performance of the *console* at both low-speed, flat-plate and engine representative conditions are presented. The aerodynamic loss is the parameter of interest, and this is compared with cylindrical and fan-shaped holes and a slot at low speed, and with fan-shaped holes at engine representative conditions.

In Chapter 8 the behaviour of the film cooling jet with and without crossflow is investigated, by using liquid crystals on a nylon mesh, to provide both flow visualisation and temperature information at a number of planes downstream of the film cooling jet injection location. This data helps to explain the behaviour of the jet from each of the film cooling hole shapes.

In Chapter 9, analytical, empirical and Computational Fluid Dynamics (CFD) models are used to model the experiments conducted at low speed, and the results are compared with those measured experimentally. Design tools, which predict *console* heat transfer performance are developed and used to predict the engine representative results.

In Chapter 10 the full body of work is summarised and reviewed, and final conclusions about the *console* performance are drawn, with reference to the aims of the thesis. Recommendations for future work are also discussed.

## Chapter 2

### Review of Film-Cooling and Related Work

In this chapter, the main parameters used to measure film-cooling performance are defined and the published literature reviewed. The predominantly comparative work used to find cooling arrangements which provide the best performance is considered and the analytical models and correlations developed as tools for engine designers to apply experimental results to engine design are discussed. The aerodynamics of the film cooling process is then reviewed, with an emphasis on understanding the performance characteristics that were measured by comparative papers. The measurement of aerodynamic flow features can be extended to the measurement of aerodynamic loss due to film cooling. It is imperative to consider the aerodynamic loss due to a film cooling configuration in conjunction with any thermal performance data.

#### ***2.1 Film cooling performance parameters***

The aim of film cooling in the engine is to thermally protect a surface from the hot mainstream gas. This protection is provided by the reduction in heat flux between the mainstream and the surface and by the coolant absorbing some of the heat from the mainstream gas. For constant property flows, the heat flux to the surface can be written (Goldstein, 1971)

$$q = h(T_w - T_{dat}) \quad (2.1)$$

which introduces a heat transfer coefficient,  $h$ , and datum temperature,  $T_{dat}$ . When the wall is at the adiabatic wall temperature,  $T_{aw}$ , the heat flux is zero, and so (2.1) can be rewritten:

$$q = h(T_w - T_{aw}) \quad (2.2)$$

When there is no film cooling present, this reference or adiabatic wall temperature is the mainstream recovery temperature  $T_r$ , which is defined:

$$T_r = T_{0m} \left( \frac{1 + r \frac{\gamma - 1}{2} M^2}{1 + \frac{\gamma - 1}{2} M^2} \right) \quad (2.3)$$

where  $T_{0m}$  is the upstream total temperature,  $M$  is the local Mach number and  $r$  is the recovery factor. Kays and Crawford (1993) suggest using the Prandtl number raised to the power one third as the recovery factor for turbulent boundary layers, giving the value  $r = 0.89$  for air with  $Pr = 0.7$ .

The heat transfer coefficient,  $h$ , and the adiabatic wall temperature,  $T_{aw}$ , are the two parameters that define the performance of a particular film cooling configuration. While  $h$  is solely a function of the fluid mechanics of the film cooling configuration,  $T_{aw}$  is also dependent on the temperature of the coolant and mainstream flows, and is intermediate between them. In order to remove the temperature dependence, the dimensionless adiabatic wall temperature, called the adiabatic film cooling effectiveness is defined (e.g. Jones, 1991):

$$\eta = \frac{T_{aw} - T_r}{T_{0c} - T_{0m}} \quad (2.4)$$

The film cooling effectiveness and heat transfer coefficient are functions of the cooling geometry, the state of the oncoming boundary layer, the freestream turbulence

intensity, the surface curvature, and the ratios of the coolant-to-mainstream density, mass and momentum fluxes, and specific heats.

To reduce the three temperature variables in the experiment to a single parameter, a dimensionless temperature,  $q$ , is defined:

$$q = \frac{T_{0c} - T_r}{T_w - T_{0m}} \quad (2.5)$$

When a particular film cooling configuration is assessed, it is the overall reduction in heat flux to the surface that is of interest and this relates to the combination of the adiabatic effectiveness and heat transfer coefficient. For example, near the film cooling hole, the heat transfer coefficient may be significantly increased by the introduction of film cooling, but high effectiveness provides sufficient cooling for the surface protection to be increased. Sen et al (1996) introduce the concept of net heat flux reduction ( $NHFR$ ) to quantify this:

$$\begin{aligned} NHFR &= 1 - \frac{q}{q_{nfc}} \\ &= 1 - \frac{h(T_w - T_{aw})}{h_{nfc}(T_w - T_r)} \\ &= 1 - \frac{h}{h_{nfc}}(1 - hq) \quad \text{if } T_r \equiv T_{0m} \end{aligned} \quad (2.6)$$

where the subscript  $nfc$  indicates that the parameter relates to the case with no film cooling.

The introduction of film cooling to a surface flow significantly changes the boundary layer flow, particularly for three-dimensional curved surfaces where the position of transition may be changed. In this case, it may be more accurate to compare the predicted total heat flux at engine conditions rather than the  $NHFR$ :

$$\begin{aligned} q &= h(T_w - T_{aw}) \\ &= h(T_w - T_{0m})(1 - hq) \end{aligned} \quad (2.7)$$

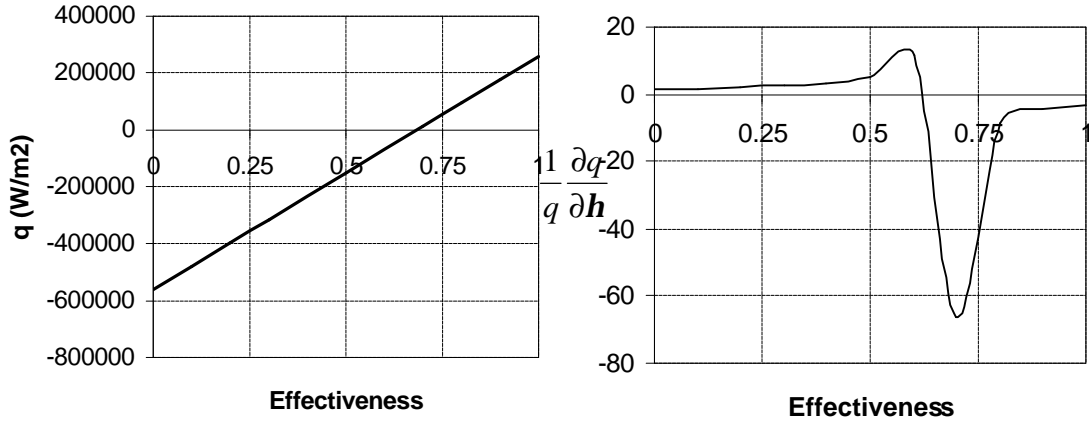
The expression for predicted heat flux above (2.7) can be used to interpret the sensitivity of the heat flux at the surface to the heat transfer performance parameters,  $h$  and  $\mathbf{h}$ . For typical engine conditions  $T_{0c} = 880$  K,  $T_w = 1200$  K, and  $T_{0m} = 1900$  K, the dimensionless temperature  $\mathbf{q} = 1.46$  and the sensitivity of  $q$  to  $\mathbf{h}$  and  $h$  can be written:

$$\frac{1}{q} \frac{\partial q}{\partial \mathbf{h}} = \frac{h(T_w - T_{0m})\mathbf{q}}{q} \quad (2.8)$$

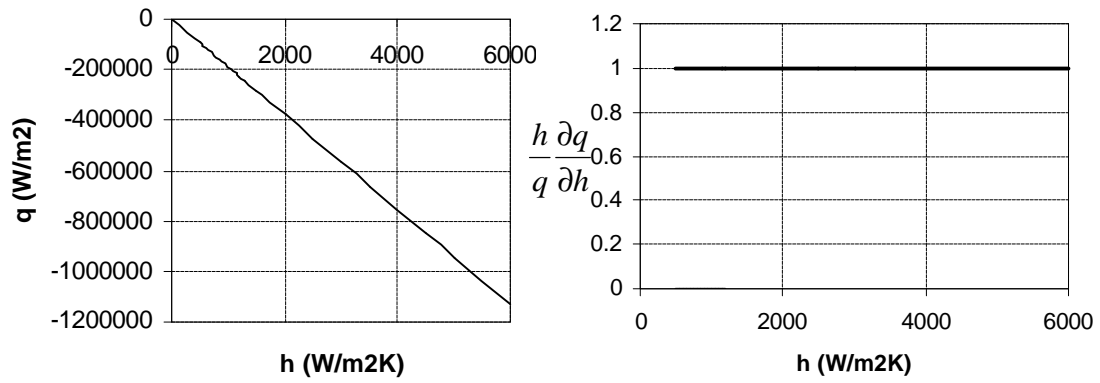
$$\frac{h}{q} \frac{\partial q}{\partial h} = \frac{(T_w - T_{0m})(1 - \mathbf{h}\mathbf{q})h}{q} \quad (2.9)$$

The variation of  $q$  with  $\mathbf{h}$ , and the sensitivity of  $q$  to  $\mathbf{h}$  are shown in Figure 2.1. In this figure, a heat flux less than zero indicates heat transfer to the surface. At an effectiveness of 0.7, the adiabatic wall temperature is equal to the desired wall temperature, and the heat flux is from the surface, that is, the surface is cooled below the required wall temperature. This effectiveness level is only dependent on the engine temperatures, not on  $h$ . The importance of this figure is that above an effectiveness of 0.7, the level of  $h$  is not important, because the wall temperature is below the adiabatic wall temperature. This result is useful, because the heat transfer coefficient is often enhanced near a film cooling hole, but because the effectiveness is typically high near the hole, the thermal protection of the surface is maintained. Near this critical value of  $\mathbf{h}$ ,  $q$  is extremely sensitive to  $\mathbf{h}$  with a peak sensitivity of 6600%, but below  $\mathbf{h} = 0.5$  and above  $\mathbf{h} = 0.8$  the sensitivity is of the order of 100%.





**Figure 2.1: Variation of heat flux,  $q$ , with effectiveness,  $h$ , and sensitivity of  $q$  to  $h$  (2.8), for typical engine temperatures and  $h = 800 \text{ Wm}^{-2}\text{K}^{-1}$**



**Figure 2.2: Variation of heat flux,  $q$ , with heat transfer coefficient,  $h$ , and sensitivity of  $q$  to  $h$  (2.9), for typical engine temperatures**

The variation of  $q$  with  $h$  and the sensitivity of  $q$  to  $h$  are shown in Figure 2.2. These results show that where the effectiveness is lower than 0.7,  $h$  should be kept as low as possible to minimise the heat flux to the surface. The sensitivity of  $q$  to changes in  $h$

$(\frac{h}{q} \frac{\partial q}{\partial h})$  is constant over the range of  $h$  typically measured at 100%.

For a particular hole geometry, the mass flux ratio and the momentum flux ratio of the coolant to the mainstream flows have a significant effect on film cooling performance. Typically, increasing the momentum flux ratio improves the adiabatic effectiveness by increasing the amount of coolant on the surface, up until a point where the cooling jet (particularly for cylindrical holes) will lift off from the surface

and penetrate into the mainstream flow. The mass flux ratio, or blowing ratio is defined:

$$B = \frac{\mathbf{r}_c v_c}{\mathbf{r}_m v_m} \quad (2.10)$$

where  $\mathbf{r}_c$  and  $\mathbf{r}_m$  are the density of the coolant and mainstream flows and  $v_c$  and  $v_m$  are the velocities of the coolant and mainstream flows. The coolant velocity is the average velocity at the exit of the film cooling hole.

The typical definition of momentum flux ratio is the ratio of the dynamic heads of the two flow streams:

$$I = \frac{\mathbf{r}_c v_c^2}{\mathbf{r}_m v_m^2} \quad (2.11)$$

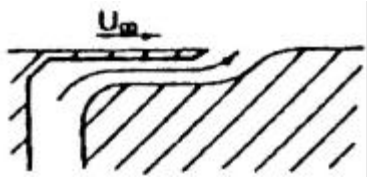
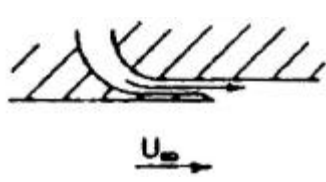

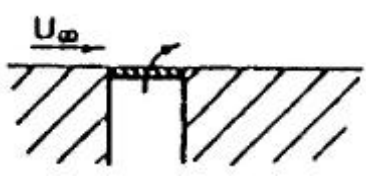
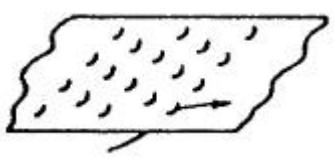
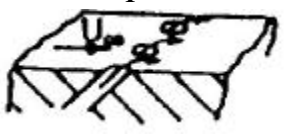
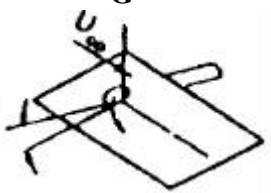
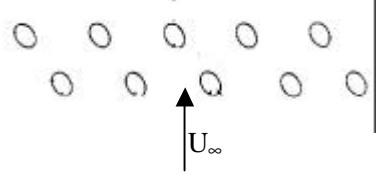
where the symbols have the same meanings as above.

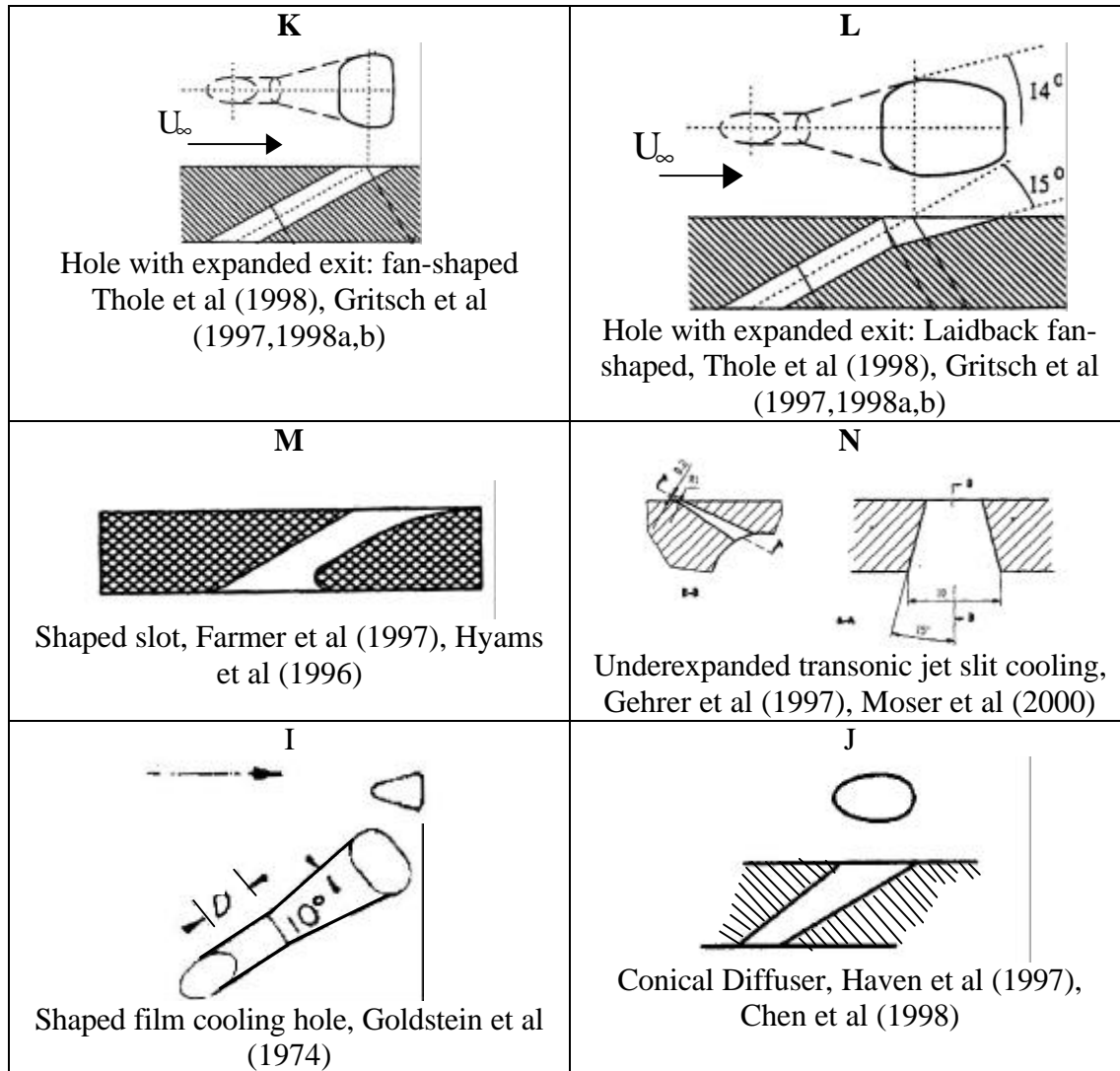
## **2.2 Development of film cooling to optimise heat transfer performance**

The film cooling performance parameters,  $h$  and  $\mathbf{h}$ , are dependent on the film cooling geometry and the coolant and mainstream flow fields. Since the first published work in this field (Wiegardt, 1943) there has been a huge body of work within gas turbine companies, universities and other research institutions, and published in the public domain to develop new ways to present the coolant air to the surface to provide better film cooling performance. A thorough summary of the early development of film cooling is presented by Goldstein (1971).

The first application of a jet of different temperature to the mainstream, to a surface was a film heating application used by Wiegardt (1943) to prevent the formation of ice on aircraft wings. In fact, heated ‘coolant’ is typically used in laboratory heat transfer experiments because of the cost advantage of heating a smaller airflow.

Wieghardt used a tangential slot, shown in Figure 2.3A. The advantage of the slot was that the film was uniform in the spanwise direction, and the slot film benefits from the Coanda effect, which causes it to flow along the surface, rather than lifting off and penetrating into the mainstream flow. As well as the good performance, slots have the advantage that the two-dimensional flow can be modelled analytically. The development of analytical models is reviewed in Section 2.5.

<p style="text-align: center;"><b>A</b></p>  <p style="text-align: center;">Tangential slot, Wieghardt (1943)</p>	<p style="text-align: center;"><b>B</b></p>  <p style="text-align: center;">Tangential step-down slot, Seban (1960)</p>
<p style="text-align: center;"><b>C</b></p>  <p style="text-align: center;"><b>AT ANGLES 90°, 80°, 45°</b> Straight, inclined slot, Metzger et al (1968), Farmer et al (1997)</p>	<p style="text-align: center;"><b>D</b></p>  <p style="text-align: center;">Porous slot, Goldstein et al (1965)</p>
<p style="text-align: center;"><b>E</b></p>  <p style="text-align: center;">Full coverage interrupted slots, Burggraf et al (1961)</p>	<p style="text-align: center;"><b>F</b></p>  <p style="text-align: center;">Discrete, cylindrical holes Goldstein et al (1968)</p>
<p style="text-align: center;"><b>G</b></p>  <p style="text-align: center;">Holes with compound angle injection Goldstein et al (1970)</p>	<p style="text-align: center;"><b>H</b></p>  <p style="text-align: center;">Double row of holes (staggered and with compound angle) Ligrani et al (1994)</p>



**Figure 2.3: Summary of film cooling hole shapes developed 1943- 2000**

A number of researchers (e.g. Seban, 1960, Hartnett et al, 1961, Burns and Stollery, 1969, Ballal and Lefebvre, 1973) presented work on the tangential slot, which was designed to present the flow to the surface as smoothly as possible, by providing a significant streamwise component of momentum to the jet. Hartnett et al used a slot similar to that used by Wieghardt, but the slot used by the other researchers mentioned was a tangential step-down slot such as shown in Figure 2.3B (Seban, 1960). This was designed to further reduce the mixing between the film and the mainstream by injecting the coolant below the mainstream flow. It was generally

found that increasing the slot lip thickness lowered the film cooling effectiveness (Burns and Stollery, 1969).

Metzger et al (1968) used a non-tangential, straight slot, shown in Figure 2.3C. This slot was developed because it is easier to manufacture and more practical for many applications. Goldstein et al (1965) combined film cooling with transpiration cooling, by applying a section of porous material over a slot. In effect, the porous region was cooled by transpiration, and the region downstream was cooled by the film of air issuing from the slot. The effectiveness downstream of the slot was of a similar level to effectiveness downstream of a tangential step-down slot. The advantages of this slot over the open tangential slot are that supplementary mechanical strength is provided to the slot region by the porous material, and the normal slot is simpler to manufacture, and more compact in the surface material. The reduction in momentum of the coolant due to the loss in dynamic head through the porous slot causes the jet to bend towards the surface more easily than for an open, normal slot. However the porous material will have the same disadvantages as for full transpiration cooling with blockage risks and high aerodynamic loss.

The disadvantage of all slot film cooling designs is that they are not suitable for application to turbine blades and vanes except at the trailing edge, because of the lack of mechanical strength. Most of those mentioned were developed for applications such as combustion chambers, afterburner nozzles and rockets. For turbine blade applications it was necessary to use rows of separated openings.

One turbine blade cooling solution was the use of interrupted slots, such as Burggraf et al (1961) shown in Figure 2.3E, but the solution which was more practical from a manufacturing point of view was the use of discrete, circular holes drilled into the

surface. The adiabatic effectiveness of a circular hole normal and at  $35^\circ$  to the surface was first studied by Goldstein et al (1968) shown in Figure 2.3F, and there has been a large amount of research into various configurations using holes since that time. The cylindrical jet is bent by the mainstream flow towards the surface, and the flowfield and position of the jet relative to the wall is strongly dependent on the momentum flux ratio between the mainstream and coolant flows. A disadvantage of cylindrical holes is the jet lifts off the surface, particularly at higher momentum flux ratios ( $\sim 1$  and above) and the effectiveness for a hole is lower than that for a slot film, using the same amount of air, due to the increased penetration and mixing of the jet into the mainstream flow field. In addition to this, the surface is not uniformly cooled by cylindrical jets, and as well as the problem of hot streaks in the material, the temperature gradients between regions downstream of the hole centre line and mid hole regions are large, and introduce significant thermal stresses into the material. From an aerodynamic perspective, the penetration of the jet, and jet mixing, increase the aerodynamic losses due to film cooling compared with slot flow

Goldstein et al (1970), Ligrani et al (1992), Ekkad et al (1997) and Sen et al (1996) amongst others investigated the effect of ejecting the coolant at a compound angle to the flow such as shown in Figure 2.3G. This improves the uniformity of the cooling as the mainstream flow is more completely blocked and tends to flow over the cooling jets, forcing the jets towards the surface. In addition to this, the coolant jets tend to coalesce a short distance downstream from the film cooling holes.

An alternative way to improve the film cooling performance from cylindrical, discrete film cooling holes is to arrange them in double rows, with the holes either inline or staggered (e.g. Ligrani et al, 1994, Martinez-Botas and Yuen, 2000) shown in Figure 2.3H. The presence of the upstream row of holes discourages the downstream row

from lifting off the surface, thus increasing the effectiveness of this row. When the holes are arranged in staggered rather than inline rows, the spanwise uniformity of effectiveness and heat transfer coefficient is improved although the levels of these parameters are not changed compared with inline rows of holes. The spanwise hole spacing, or pitch is also important to the cooling performance. Martinez-Botas and Yuen (2000) show that for a hole pitch of  $6d$ , each film cooling jet acts similarly to a single film cooling jet, but when the pitch is reduced to  $3d$ , the effectiveness is greatly increased. This is because adjacent jets interact to form a closed film from a small distance downstream from ejection, which reduces the entrainment of mainstream air. In addition to this, the spanwise variation in effectiveness is reduced as would be expected.

In order to further improve film cooling performance, the influence of shaping the film cooling hole has been investigated. Goldstein et al (1974) used a cylindrical hole with a conical diffusing section (Figure 2.3I) and measured effectiveness downstream of the hole compared with a straight cylindrical hole. They found from flow visualisation studies, that the jet remained near the surface with mainstream flow applied. The centreline effectiveness was comparable with slot cooling, and the lateral variation in effectiveness was significantly reduced compared with cylindrical holes. Gritsch et al (1997, 1998 a, b) and Thole et al (1998) present heat transfer coefficient, adiabatic effectiveness, discharge coefficient and flow field measurements for flared or fan shaped holes. The exit region of these holes is expanded in either the spanwise or forward direction, or both as shown in Figure 2.3K and L. The purpose of this exit expansion is to reduce the velocity and hence the momentum of the flow so that the penetration of the jet into the mainstream is reduced which, in turn, increases the effectiveness of the jet. Expanding the hole laterally improves the lateral spreading of

the jet, which is a benefit to the film cooling. Haven et al (1997) have found further explanation for the improved film cooling coverage by holes with expanded exits by a investigation into the vortical structure of the jets, which is further discussed in Section 2.6. The disadvantage of these diffusing holes is that the diffusion process is very inefficient, and introduces a significant increase in aerodynamic loss due to film cooling compared with cylindrical holes (Day et al 2000).

Some more recent studies of slot film cooling have used a shaped, non –tangential slot such as shown in Figure 2.3M. Farmer et al (1997) present measurements of effectiveness and heat transfer coefficient for straight and shaped slots, showing that shaping the hole improves the performance by reducing the impact of the jet into the mainstream flow. Hyams et al (1996) present detailed numerical data for a CFD investigation into straight slots and slots with shaped inlets and outlets. The velocity profiles and kinetic energy profiles clearly show that the improvement in heat transfer coefficient and effectiveness when both the inlet and outlet are shaped is due to the suppression of separation at the slot inlet, and a spreading of the region over which the leeward side of the jet must accelerate at the hole exit, reducing the turbulence and shear stress in this region. These designs are not applicable to blade and vane film cooling, because of the previously mentioned lack of structural strength.

A new film cooling technique using an underexpanded transonic jet from a slit has been presented by Gehrler et al (1997) and Moser et al (2000). The jet is choked at the hole exit, and these papers and previous research have shown that as the jet expands in the lower pressure flow in the mainstream, it will adhere strongly to the wall by the Coanda effect (Schlichting, 1979) and provide a highly effective cooling film. It has been proposed for use particularly near the leading edge of the vane, because of the high curvature in this region, and the resultant difficulty in designing an effective film



cooling configuration. The initial results show that the jets do adhere well to the surface, but the cooling is not uniform, because the slits are interrupted and three-dimensional. The other disadvantage of this technique is the high pressure coolant that is required in order to obtain transonic flow, and the pressure difference between mainstream and coolant flows required to obtain the necessary expansion. The coolant driving pressure is effectively the compressor outlet pressure, and the pressure difference between mainstream and coolant flows is due to the pressure drop in the mainstream after passing through the combustor – a pressure drop which is constantly being reduced by improvements in design.

To summarise, the development of film cooling has aimed at producing high effectiveness and low heat transfer coefficient, with uniform protection of the surface, using the minimum amount of coolant air to minimise the penalty of using film cooling. The aerodynamic loss due to film cooling must also be minimised, to prevent the loss penalty in using a film cooling configuration offsetting the benefits of the higher allowable temperature. The best technology in use at the current time is the flared or fan-shaped hole, however this hole produces a significant aerodynamic loss penalty.

### ***2.3 Modelling film cooling in the engine***

The references discussed above have concentrated on finding an optimal cooling configuration by changing one geometrical parameter of the film cooling configuration and comparing the results with other experiments. These experiments have typically been carried out for flow over a flat plate or wall at ambient conditions in a low speed wind tunnel, and there is a large amount of data available for such experiments. Typically, though, the film cooling is applied to blades and vanes, which

often have moderate to large amounts of surface curvature near the cooled region. The effect of surface curvature on film cooling has been investigated by, amongst others, Berhe and Patankar (1998a, b), Chen et al (2000), Arts and Bourguignon (1990), Ito et al (1978), Ko et al (1986), Lin and Shih (1998) and Schwarz and Goldstein (1989). Berhe and Patankar (1998a, b) present numerical and experimental results for film cooling over concave, flat and convex surfaces. The results show that on convex surfaces the shear stresses in the flow are damped, which allows a more stable boundary layer and better film cooling effectiveness at all blowing ratios than the flat plate and concave surfaces. The shear stresses on a concave surface were increased compared with a flat plate, and although the concave surface had better jet spreading than the flat surface, the film cooling effectiveness was lower. Lin and Shih (1998) present numerical computations of film cooling over flat and convex surfaces. The results are similar to those presented by Chen et al (2000) and indicate that at low blowing ratios, the convex surface film cooling is slightly less effective than flat plate effectiveness near the hole, but similar downstream from ejection. For higher blowing ratios, the effectiveness on the convex surface is considerably reduced to provide no film cooling beyond  $x/d = 15$ .

Chen et al (2000) present experimental results for film cooling over concave and convex surfaces with simple, forward expanded and compound angle forward expanded holes. They show that at higher blowing ratios, the coolant on the convex surface has completely lifted off and the heat flux to the surface is higher than the no film cooling case. At a lower blowing ratio the heat flux is diminished near the holes, but the simple hole approaches the no film cooling level far downstream, while the expanded holes show some improvement at all measurement areas. For the concave

surface, the high blowing ratio improves the protection, and for both blowing ratios the cooling from all holes is similar downstream from the coolant ejection.

Ito et al (1978) present an analysis of curvature effects on effectiveness that shows that the relative performance of film cooling on convex and concave wall depends on the momentum flux ratio,  $I$ , of the jet and the inclination,  $\theta$ , of the jet. If  $I \cos^2 \theta < 1$  then the jet would turn more towards the surface on a convex wall than on a flat or concave wall, causing the effectiveness to be higher. The converse is true if  $I \cos^2 \theta > 1$ .

As experiments in film cooling are used to test film-cooling configurations for application to engine designs, other factors that should be considered are the coolant to mainstream density ratio, Mach numbers, Reynolds numbers, turbulence levels and temperature ratios. Teekaram et al (1989) have investigated the use of high density foreign gases to model the density ratio between the cold coolant and hot mainstream flows in the engine. The aim of this is to model both the mass flux and the momentum flux ratios in order to obtain an identical flow field to the engine condition. Ammari et al (1990) also present heat transfer coefficient data at varying density ratios and show that for inclined holes, the density ratio has a significant effect on the heat transfer, a lower density ratio leading to increased heat transfer. Jones (1999) analyses the effect on the heat transfer measurements made using a foreign gas that has different molecular properties to the mainstream gas and suggests a correction that can be made to the heat transfer measurements.

In the gas turbine, the flow through the combustor has a high level of turbulence, which will be transported to the flow at the downstream blades and vanes. Hoffs et al (1996) present heat transfer measurements on a turbine airfoil at various turbulence intensities. The importance of performing measurements at the correct turbulence

level is demonstrated, because increased turbulence not only causes significantly earlier transition on the airfoil suction surface, but also increases the heat transfer coefficient on both suction and pressure surfaces. Hoffs et al (1996) also show a significant increase in heat transfer coefficient with increasing Reynolds number. The level of turbulence from a particular combustor was measured by Moss and Oldfield (1991) to be 13%.

## **2.4 Measurement of film cooling performance**

The large numbers of experiments outlined in the previous section have applied a similarly large number of different techniques to measure the film cooling performance. Reference to equations (2.1) and (2.2) shows that the heat transfer coefficient and adiabatic effectiveness require knowledge of mainstream, coolant, wall and adiabatic wall temperatures and the heat flux to the surface. The heat flux to the plate can be applied by an electrically heated film (Ligrani et al, 1994, Martinez-Botas and Yuen, 2000). The surface temperature of the plate at different downstream and spanwise location can then be measured using thermocouples embedded in the plate (Ligrani et al, 1994), infrared radiation cameras (Moon and Jaiswal, 2000, Boyle et al, 2000) or thermochromic liquid crystals (Sargison et al, 2001a,b). In addition to the different methods used to measure the temperature, the actual heat transfer process can be either steady state (Sargison et al, 2001a, Martinez Botas and Yuen, 2000) where the system is allowed to settle to steady state conditions after each change in plate heat flux or coolant temperature, or it can be transient (Sargison et al, 2001b) where the mainstream temperature is changed in a stepwise fashion and the thermal response of the surface is recorded and compared with the analytical solution. The transient thermal response of the model can also be measured using heat flux gauges (Oldfield et al, 1978, Guo et al, 1998).

The analogy between mass and heat transfer, which is valid at a turbulent Lewis number of unity has also been used to measure adiabatic effectiveness and heat transfer coefficient in a number of applications. The turbulent Lewis number is defined as:

$$Le = \frac{Pr}{Sc} \text{ where } Pr = \frac{\mu}{k} \text{ and } Sc = \frac{\mu}{\rho_j} \quad (2.12)$$

where  $Pr$  is the Prandtl number,  $Sc$  is the Schmidt number, and  $\rho_j$  is the mass diffusion coefficient.

Goldstein et al (1998) used the naphthalene sublimation technique by which the temperature of the plate surface is related to the height of naphthalene that has sublimed during an experiment. The mass transfer coefficient is analogous to the heat transfer coefficient and comparison between experiments using injection of air and injection of naphthalene vapour saturated air yields the adiabatic effectiveness. Ammari et al (1990) used a swollen polymer technique with laser holographic interferometry. The test surface is coated with a silicone rubber polymer swollen to equilibrium in an organic agent. The organic agent is evaporated when it is exposed to the cooling airflow, causing a reduction in the thickness of the polymer layer. The thickness of the layer and hence the heat transfer coefficient,  $h$ , at all points on the surface is measured using laser interferometry. Haslinger and Hennecke (1996) use the ammonia and diazo technique. A mixture of ammonia and air is injected through the film cooling holes over a diazo film located downstream of the holes. The diazo film will turn blue depending on the local concentration of ammonia, and this colouring can be calibrated to read the adiabatic effectiveness directly.

## 2.5 Heat transfer models

In addition to collecting experimental data for the comparison of the performance of various film cooling regimes, one of the aims of film cooling research is to produce and verify analytical tools that can be used by engine designers to predict the performance of a particular film cooling design. Generally, a number of models of film cooling effectiveness have been published, based on a control volume approach, which looks at the mixing of the coolant and mainstream flows. Because the two-dimensional nature of slot film cooling greatly simplifies the flow problem, slot models dominate the analytical solutions for film cooling. Eckert and Drake (1972) present a model of effectiveness for injection from an inclined slot:

$$h = \frac{1.9 Pr^{\frac{2}{3}}}{1 + 0.329(Re_s)^{-0.2} \frac{c_{pm}}{c_{pc}} \left( \frac{\dot{m}_m}{\dot{m}_c} \right)^{0.2} \left( \frac{\mathbf{r}_m u_m x}{\dot{m}_m} \right)^{0.8}} b \quad (2.13)$$

where  $Re_s = \frac{\dot{m}_c}{\dot{m}_t} = \frac{\mathbf{r}_c u_c s}{\dot{m}_t}$  is the slot Reynolds number,  $x$  is the distance downstream

from the slot,  $b = 1 + 1.5 \times 10^{-4} Re_s \frac{\dot{m}_c}{\dot{m}_m} \sin \mathbf{f}$  and  $\mathbf{f}$  is the injection angle.

Various researchers (e.g. Hartnett et al, 1961) have shown that sufficiently downstream from the injection location, the heat transfer coefficient tends to return to the level measured without film cooling and hence the heat transfer rate from the surface can be predicted by using the heat transfer coefficient without injection with the temperature potential equal to the difference between the wall temperature and the adiabatic wall temperature. Hence many people (e.g. Haslinger et al, 1996 and Sinha et al, 1991) have concentrated on producing adiabatic effectiveness data without heat transfer coefficient. While this may be valid far downstream of the cooling holes, the region of interest is often directly downstream of the point of injection, where the

flow pattern is significantly altered by injection and the heat transfer coefficient may be either increased or decreased due to film cooling.

One useful work, which concentrates on heat transfer coefficient, is provided by Metzger et al (1968) who present useful correlations for the heat transfer coefficient downstream of nontangential injection slots that can be used to predict the heat transfer coefficient at a distance from a slot with a particular injection angle,  $f$ . The results can be transferred to engine conditions through the use of the dimensionless temperature parameter,  $q$ . The correlations are:

$$\frac{h}{h_{nfc}} = 1.09 - 7.9qM^{0.6} \left( \frac{s}{l} \right)^{0.5} \text{ for } f = 20^\circ \quad (2.12)$$

$$\frac{h}{h_{nfc}} = 1.18 - 7.5qM^{0.6} \left( \frac{s}{l} \right)^{0.5} \text{ for } f = 40^\circ \quad (2.13)$$

$$\frac{h}{h_{nfc}} = 1.24 - 6.8qM^{0.6} \left( \frac{s}{l} \right)^{0.5} \text{ for } f = 60^\circ \quad (2.14)$$

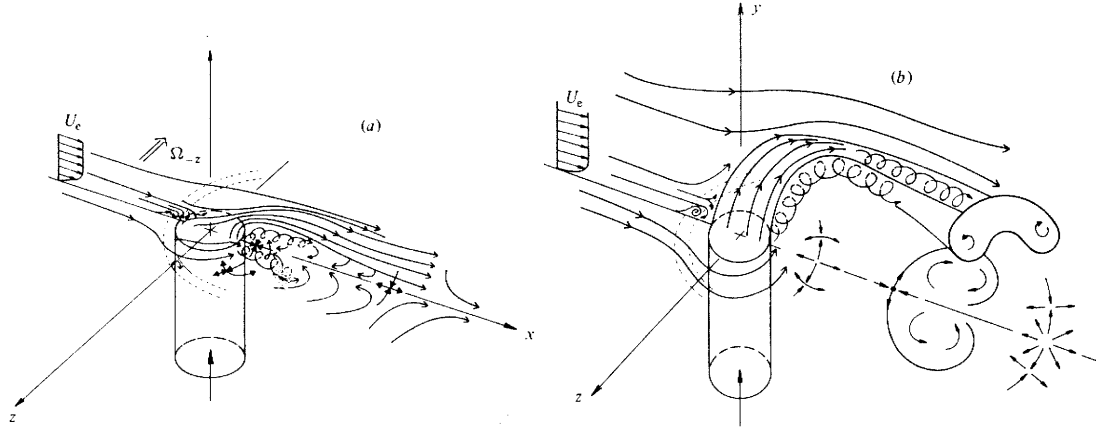
in the range  $0.25 \leq M \leq 1.0$  and  $35 \leq \frac{l}{s} \leq 70$ , where  $l$  is the length of the transient test surface.

Although these relationships are only available for discrete injection angles and particular pitch / diameter ratios, it is clear that the linearity of  $h/h_{nfc}$  with the

parameter  $qM^{0.6} \left( \frac{s}{l} \right)^{0.5}$  holds for the blowing rates studied, and the constants of the

line equations (2.12)-(2.14) change only slightly with injection angle. The range of blowing ratio investigated was not very high, and based on the work of Forth and Jones (1986) and Ammari et al (1990), it is unlikely that this correlation will hold for higher blowing ratios. In addition to this, the blowing ratio has been shown to be not a particularly good parameter to scale results to engine conditions because of the

dependence of film cooling performance on injection to mainstream density ratio (Teekaram et al, 1989).



**Figure 2.4: Structure of a single jet in cross flow at (a) low ( $M=0.5$ ) and (b) high ( $M=2.0$ ) velocity ratios (Andreopoulos and Rodi, 1984)**

Forth and Jones (1986) report an analytical and experimental investigation into the parameters that affect film cooling. They show that there are effectively two regimes of film cooling and the parameters used to correlate the results can be different for each. The two different flowfields are weak blowing, where there is no separation of the jet from the surface and strong blowing where there is significant penetration of the jet into the mainstream. The jet structure for these two cases is shown in Figure 2.4 and discussed in Section 2.6. They show that for weak blowing the momentum flux ratio is a good parameter to correlate data, but for strong blowing it is the velocity ratio. This effect was also measured by Ammari et al (1990) for inclined holes, but normal injection was shown to be insensitive to changes in density ratio.

Forth and Jones (1986) show that the correlation parameter  $\frac{x}{s}(I)^{-\frac{2}{3}}$  can be used for adiabatic effectiveness and heat transfer results for slot, and single and double rows of cylindrical holes for both strong and weak blowing, and at any distance downstream of injection. Ammari et al (1990) show that plotting the normalised spanwise



averaged heat transfer coefficient against  $\left(\frac{x}{d}\right)\left(\frac{u_c}{u_m}\right)^{-\frac{4}{3}}$  collapses data for a range of velocity and density ratios.

The ever increasing availability and power of computing systems has led to a burgeoning growth in the modelling of film-cooling using CFD. The predictive power of CFD models is usually limited to a range within the extents of models that have been carefully calibrated against experimental data. As well as checking the predictive capability against measured heat transfer results, a model is usually required to predict the main aerodynamic features of the flow, and this has led to a requirement for detailed and comprehensive studies to measure and understand the dominant flow structures of film cooling jets in crossflow.

Many numerical studies of film cooling do not model the coolant flow within the film cooling hole and plenum, but instead specified boundary conditions at the hole exit (e.g. Garg and Gaugler, 1997). Garg and Gaugler (1997) showed that the coolant velocity and temperature distributions at the hole exit have a large influence on the heat transfer at the blade surface near the hole, so it is important that these are accurately modelled. An alternative approach is to model not only the jet / mainstream interaction, but to also include the flows within the plenum and cooling holes (e.g. Leylek and Zerkle, 1994, Berhe and Patankar, 1998b, Hyams et al, 1997 and Lin and Shih, 1998). Despite the increased complexity and size of the computation, these models provide extra information and understanding of the flows near and within the holes, and can provide boundary conditions for the models that begin at the hole exit. Once CFD models with generally good reliability have been developed, they can be used to test new film cooling designs and concepts. Giebert et al (1997) developed models of film cooling with cylindrical, fan-shaped and laid-back fan-shaped holes.

This analysis was able to capture many of the dominating flow structures, but was unable to accurately predict the exact jet location for the expanded holes. As previously discussed Hyams et al (1996) also used numerical prediction to compare the performance of straight and shaped slots. The strength of the numerical data is that once the model is verified with experimental results, other data provided by the model, such as shear stress and turbulence can be used to gain an understanding of the likely cause of performance changes.

## **2.6 *The aerodynamics of film cooling jets***

A significant amount of research has been directed towards improving understanding of the mechanisms of film cooling and to capitalise on this knowledge in the design of new film cooling systems. The research has varied from experimental and numerical investigations of a single jet in crossflow (Andreopoulos and Rodi, 1984), to three-dimensional modelling of cooling on a turbine blade leading edge with compound angle injection (Chernobrovkin and Lakshminarayana, 1998).

Figure 2.4 from Andreopoulos and Rodi (1984) illustrates the main flow features of a single jet in cross flow. This figure also demonstrates the difference between the jet structure for high and low momentum flux and blowing ratios. The dominant structure of the flow is the mutual deflection of the jet and the mainstream flow. The jet is turned towards the mainstream direction and the mainstream flow is deflected as if the outer streamlines of the jet formed a solid boundary, except that the jet entrains some of the mainstream fluid. As previously mentioned, the interaction between the flows depends on the momentum flux ratio. For a low momentum flux ratio of 0.25 (Figure 2.4a) the mainstream flow covers the upstream part of the hole, the jet streamlines bend inside the hole and the mainstream flow lifts over the jet, tending to push the jet

towards the surface. For a high momentum ratio of 4.0 (Figure 2.4b) the jet is only weakly affected by the mainstream flow and penetrates into the mainstream before it is bent over. A complicated three-dimensional separation region forms downstream of the jet in both instances and, particularly for the high momentum flux ratio case, conservation of mass can cause a reversed flow region near the wall immediately downstream of the jet which entrains mainstream flow. This effect has been shown by many authors (e.g. Goldstein et al 1968, Martinez-Botas and Yuen, 2000) to cause a maximum in adiabatic effectiveness with increasing momentum flux ratio, due to what is termed “jet lift-off”. Pietrzyk et al (1989) present detailed measurements of the velocity components for a row of jets issuing into mainstream flow, measured using Laser-Doppler anemometry. The results show that while the jet structure is still clearly distinguishable ten diameters downstream there is a major enhancement of turbulence structures downstream of the jet.

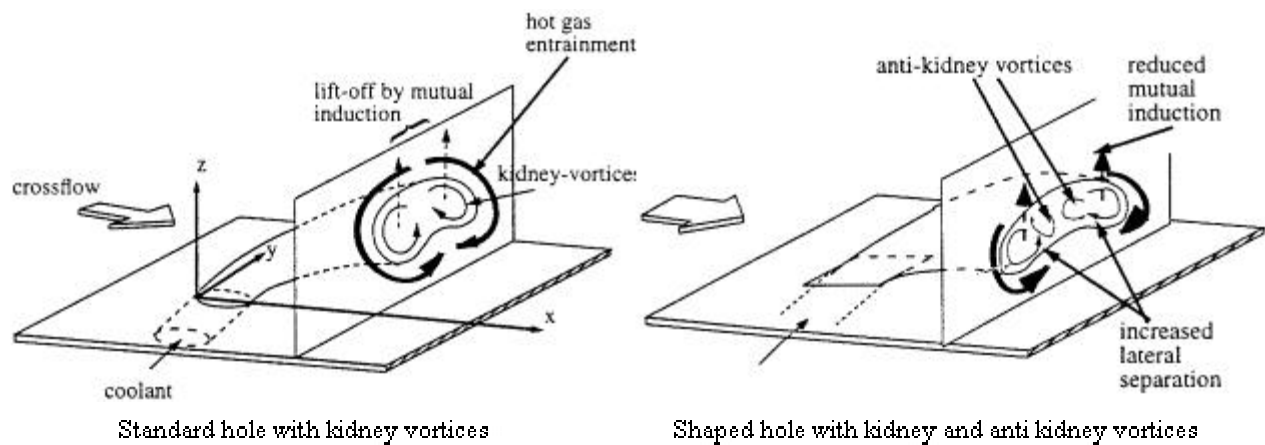
The main vortical features of the flow-field have been identified by a number of authors (e.g. Leboeuf and Sgarzi, 2000, Muldoon and Acharya, 1999) and these have a strong effect on the mixing behaviour of the jet and hence on the thermal and aerodynamic efficiency performance of the cooling jet. The flow upstream of the jet is strongly decelerated near the jet, which causes flow separation and the formation of the horseshoe vortex. This is similar to the structure formed for a cylinder in cross-flow. The vortex tube moves around the jet at a constant radius from the centre of the jet, but downstream it is attracted to the jet by a decrease in static pressure and it mixes with the jet. At the location where the mainstream flow meets the upstream edge of the jet, the lip vortex is formed. This vortex tends to remain attached to the jet and mixes with the jet flow downstream. The main jet flow is a pair of counter rotating or kidney shaped vortices that create the jet cross-sectional shape. The

direction of these vortices promotes the jet lift off from the surface and entrainment of the mainstream flow. The formation of these vortices is linked to the redistribution of the hole boundary layer under the influence of the curvature of the jet trajectory. Downstream of the jet, wake vortices have been identified. These form as the wall boundary layer streamlines are sucked into the wake of the jet.

A row of jets in crossflow has been shown to exhibit similar flow features although the intensity of the effect of each feature is modified. Typically the row of jets produces a more uniform barrier to the mainstream flow, and the effect of vortices other than the counter rotating vortices is reduced.

Following the acceptance of the basic flow structures identified in the preceding discussion, some research has been directed towards controlling the counter rotating vortices (identified above as promoting jet lift off and entrainment of mainstream flow) in order to improve film cooling performance. Vogel (1998) investigated the effect of introducing curvature to the centreline of a cylindrical film cooling hole, in order to generate a vortex structure in the jet which counter rotates against the standard kidney vortex pair in a jet. The effect of this is to transport coolant from the centre of the jet to the cooled surface, thus improving the lateral uniformity of cooling, and increasing the averaged adiabatic effectiveness to levels only obtained using cylindrical holes by compound angle injection. The use of anti-kidney vortices to reduce the detrimental effect of counter rotating vortices has been shown by Haven et al (1997) and Haven and Kurosaka (1996, 1997) to be achieved by shaping the exit of the film cooling hole. The superior performance of fan-shaped film cooling holes over cylindrical holes has conventionally been attributed to the low momentum flow at the hole exit. However, Haven et al (1997) show that lateral expansion of the hole exit produces two major benefits which are summarised in Figure 2.5. The first is that

each counter rotating vortex tends to remain near the edge of the hole, so increasing the width of the hole exit increases the distance between the pair, hence decreasing the interaction and delaying the jet lift off. In addition to this, a correctly shaped hole will generate an anti-kidney vortex pair, with a sense of rotation opposite to the kidney pair. If it is correctly positioned it can cancel the adverse effect of the kidney pair and prevent the jet from lifting off.



**Figure 2.5: Kidney and anti kidney shaped vortices and the advantages of shaped holes (from Haven et al, 1997)**

The improvement in the uniformity and level of film cooling adiabatic effectiveness with cylindrical hole aligned at a compound angle to the flow has already been discussed, and Baier et al (1997) present large scale experimental and numerical data which accounts for this improvement in terms of the vortical nature of the flowfield. The introduction of a compound angle removes the symmetry from the flow field presented in Figure 2.4. The mainstream flow now meets the jet to one side of the jet flow direction, and Baier et al show that this has the effect of reducing the strength of the windward vortex lying closer to the wall, which again inhibits the mutual action of the counter rotating vortices to cause jet lift off and entrainment of mainstream flow.

This discussion of the effect of vortical structures on film cooling jets can be taken one step further by considering slot film cooling. Here the problem of counter rotating

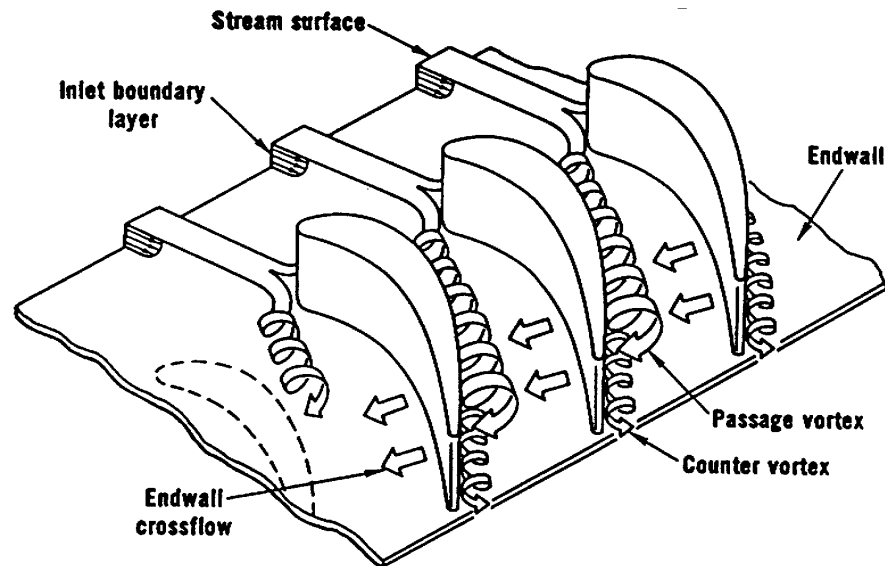
vortices is removed by the lack of solid boundaries inside the slot at which the vortices can form. The horseshoe vortex cannot move around the jet and introduce hot fluid into the jet and into the separation region under the jet because the slot film forms a continuous, closed surface. The slot will be more strongly attached to the wall because the low pressure region at the leeward side of the hole exit can only be filled by jet flow, and the mainstream flow must completely flow over the film, adding to the good attachment of the slot film to the surface. The only location of mixing with the mainstream air is entrainment at the upper boundary of the slot film, and these factors all contribute to the high effectiveness of slot film cooling.

## **2.7 Aerodynamics of NGV cascade**

The complicated flow field generated by the interaction of jets with mainstream flow will be present for flows over flat plates, curved surfaces and airfoils. However, the mainstream flow field over blades and vanes is further complicated by secondary flows generated by the interaction of the solid airfoil with the oncoming flow. The main secondary flow features are shown in Figure 2.6 from Langston (2000) and a thorough description of secondary flow is provided by Harvey (1991).

The transverse vorticity in the sidewall boundary layer in the incoming mainstream flow is separated at a saddle point on the leading edge of the vane and forms a horseshoe vortex. The leg of the horseshoe vortex on the pressure surface side of the leading edge is “fed” by the end-wall flow from the pressure to the suction surfaces and moves from the pressure surface towards the suction surface and becomes the passage vortex. The other leg has the opposite sense of rotation and is drawn into an adjacent passage. This vortex is smaller and is labelled as a counter vortex and many experimenters have found that this vortex wraps around the passage vortex. This

secondary flow has a large impact on the performance of the blade or vane row, reducing the lift and hence the work producing capability of the engine, and reducing the aerodynamic efficiency (secondary or profile loss mentioned in the following section).



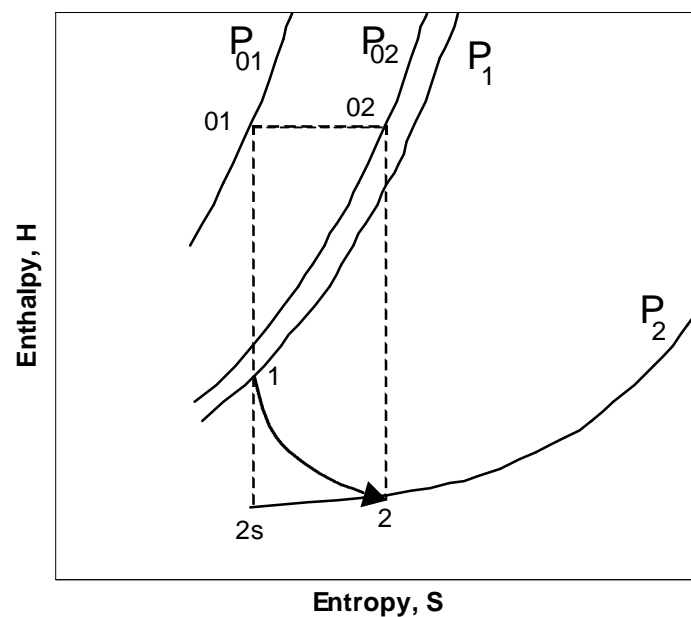
**Figure 2.6: The three dimensional separation of a boundary layer entering a turbine cascade (Langston, 2000)**

Ligrani et al (1989) investigated the effect of the passage vortex on local heat transfer rate in the presence of film cooling. The vortex was generated upstream of film cooling over a flat plate. This allowed control of the vorticity, but the work is not representative of the complexity of the flow in the three dimensional cascade. The work showed that in the presence of a simulated passage vortex and film cooling, the wall heat transfer was significantly altered, with enhancement of Stanton Number by up to 30% near the downwash side of the vortex, and a reduction of Stanton number by up to 10% near the upwash side of the vortex, where the coolant was pushed along the wall by the vortex. There were local changes in heat transfer depending on the position of the vortex relative to the injection location, although the general trends were unchanged. This work clearly shows that the secondary flow behaviour has a

significant effect on the heat transfer and film cooling performance as well as the aerodynamic performance of a blade or vane row.

## 2.8 Film cooling aerodynamic efficiency

The benefits of applying film cooling to provide thermal protection are clear but the penalty associated with applying film cooling jets to a surface is an increase in the aerodynamic loss. Denton (1993) states that with a 1% increase in coolant mass flow rate the turbine entry temperature can be increased by 100°C but there is a loss of aerodynamic efficiency of 1% per 1% coolant flow. This reduction is a viscous effect due to irreversible mixing of the coolant and mainstream flows and losses in the cooling passages. This figure is for a TET near 1500K.



**Figure 2.7: Enthalpy entropy diagram for turbine cascade flow**

The diagram of state for the flow through a single vane stage of a turbine cascade is shown in Figure 2.7. State point 1 indicates the state of the flow immediately upstream of the cascade, and state point 2 is the state of the flow immediately downstream of the cascade, after expansion from state point 1.



State point 2s is the condition that the flow would have had downstream of the cascade, if it had expanded isentropically (i.e. without loss), and this is considered to be the ideal expansion process.

The total aerodynamic loss over a vane or blade is defined a number of different ways in the literature. In engineering terms the efficiency of the flow through a turbine vane or blade passage can be written:

$$e = \frac{\text{Actual Kinetic Energy of the exit flow}}{\text{Ideal Kinetic Energy of the exit flow under the same total pressure ratio}} \quad (2.14)$$

Denton (1993) defines the loss coefficient,  $z$ , as

$$z = \frac{1 - e}{e} \quad (2.15)$$

which can be written:

$$z = \frac{\text{Energy loss}}{\text{Actual Kinetic Energy}} \quad (2.16)$$

An alternative definition of loss coefficient, which is closer to the unambiguous definition of aerodynamic efficiency (Day et al 1998), is

$$z = 1 - e \quad (2.17)$$

which can be written:

$$z = \frac{\text{Energy loss}}{\text{Ideal Kinetic Energy}} \quad (2.18)$$

Referring to the enthalpy entropy diagram for turbine cascade flow (Figure 2.7), the stagnation pressure loss coefficient (Denton 1993) is defined:

$$Y = \frac{P_{01} - P_{02}}{P_{02} - P_2} \quad (2.19)$$

Referring to equations (2.15) and (2.16), the total pressure loss ( $P_{01}-P_{02}$ ) is used instead of the energy loss and the pressure difference ( $P_{02}-P_2$ ) is used instead of the

energy available. The prevalence of this definition is considered to be due to the ease of calculation from measured data rather than its relevance to engine design.

Denton (1993) defines the energy or enthalpy loss coefficient for a single blade row, which is more useful for engine design purposes. The actual specific energy available is  $(h_{02} - h_2)$ . The ideal specific energy available (expansion from  $h_{01} = h_{02}$  to  $h_{2s}$ ) is  $(h_{02} - h_{2s})$  so subtracting these results, the loss in specific energy available is  $(h_2 - h_{2s})$ . The energy or enthalpy loss coefficient is then written (referring to equation (2.16)):

$$z = \frac{h_2 - h_{2s}}{h_{02} - h_2} \quad (2.20)$$

Denton (1993) argues that the entropy loss coefficient is the most correct way to measure loss for the actual machine with rotating blades where the stagnation pressure and relative stagnation enthalpy can change with radius without any implied loss of efficiency. This loss coefficient is defined as

$$z_s = \frac{T_2 \Delta s}{h_{02} - h_2} \quad (2.21)$$

Referring to Figure 2.7, for an ideal gas, the static temperature  $T_2$  is equal to the slope of the constant pressure line (in  $h - s$  space). However, Denton points out that the difference between the energy and entropy coefficients is negligible. This can be observed from Figure 2.7, if the change in static temperature (or static enthalpy) between 2 and 2s is small. At incompressible flow conditions, for Mach numbers less than 0.3, the definitions of loss coefficient are all equivalent.

In the literature, aerodynamic loss is generally divided into three sources, namely profile loss, secondary (or endwall) loss and tip leakage loss. The presence of film cooling contributes loss in the internal cooling passages and cooling holes, loss due to

mixing with the mainstream flow and loss due to heat transfer between the cold coolant and hot mainstream flows.

## **2.9 Measurement of aerodynamic loss**

Day et al (1998,1999,2000) measured the aerodynamic performance of an NGV with film cooling in an annular cascade, with the density ratio matched to engine conditions by using as coolant a foreign gas mixture of argon (30.2% by weight) and sulfur hexafluoride (69.8% by weight). They demonstrate the effect on loss of cooling from different areas of the vane and showed, surprisingly, that coolant ejection on the leading edge and early pressure surface could actually reduce the loss compared to the uncooled case, but injection on the suction surface increases the loss penalty. Day et al (1999) compare the performance of fan-shaped and cylindrical holes in terms of film cooling efficiency and show that loss is significantly increased by using fanned holes because the inefficient diffusion process at the hole exit reduces the available coolant energy.

Osnaghi et al (1997) performed similar measurements in a linear cascade using CO<sub>2</sub> to simulate the density ratio and a five hole probe to traverse downstream of the vane row. They found that the internal losses dominated the loss increase due to coolant injection due to a low hole discharge coefficient and sharp edged holes, and low mixing losses. Urban et al (1998) measured aerodynamic loss on a linear cascade using superheated steam to simulate the engine density ratios. They also investigated the contribution of cooling at different locations on the vane to the loss and found that disturbances on the pressure surface had little effect on loss, disturbances on the suction surface significantly increased loss, and injection from the trailing edge reduced loss of the film cooled blade due to a reenergizing effect in the wake. The

flow outlet or swirl angle was altered by up to 0.6 degrees compared with the case without film cooling. However different distributions of coolant to the film cooling hole rows at the different total mass flow rates made a direct comparison of the effect of increased blowing difficult.

Davies and O'Donnell (1999) show that loss can be measured locally as an entropy generation rate at the surface using heated thin film sensors on the vane surface. This measurement technique depends on the assumption of a relationship between surface shear stress, and surface heat transfer (Reynolds analogy), which is measured directly by the thin film sensors. This is an interesting technique because rather than measuring the effect of coolant injection in a plane downstream of the vane as per the previously mentioned papers, the creation of loss is measured at the point at which it occurs. Data collected using this technique would be of great interest to engine designers for both the design of cooling and the design of the vane surface, because regions that increase the entropy of the flow could be readily highlighted. However, this method does not measure the mixing loss in the flow away from the surface, which is captured using techniques that measure the total loss downstream of the vane or blade.

The measurements presented by Burd et al (1998) provide information about the effect of coolant injected both in a streamwise direction and at lateral angle to the streamwise direction in planes close to the injection point. The local shear stress, boundary layer momentum thickness and the shape factor are presented along with the pressure coefficient to provide more local information about the generation of losses due to film cooling. The results were measured at engine representative turbulence levels, but did not include the effects of compressibility or the three dimensional geometry of the vane. Lateral injection was shown to increase loss measured by

pressure coefficient compared with streamwise injection. At a momentum flux ratio of  $I = 1.0$ , a measured reduction in loss with streamwise injection compared with no film cooling loss is shown to be due to a re-energising of the boundary layer. Particularly near to the hole, the momentum deficit in the boundary layer is significantly reduced at this condition. For lateral injection the momentum thickness of the boundary layer is significantly increased due to mixing with the mainstream flow.

## **2.10 Aerodynamic loss models**

The aerodynamic loss data produced is of most interest to engine designers if it can be used to produce an analytical model to predict the loss under various operating conditions. Hartsel (1972) developed a simple analytical model that assumes that the flow is separated into an unaffected mainstream and a mixing layer, within which the coolant mixes with mainstream fluid at constant pressure. Urban et al (1998) present a simple analytical model based on the Hartsel model, which demonstrates good agreement with experimental data at mass flow ratios less than 1.0. At higher mass flow ratios there is a large increase in loss due to increased penetration of the cooling jets out of the assumed boundary layer of the profile and this is not predicted by the model.

Day et al (1998) present a similar Hartsel model for film cooling from an NGV at compressible conditions, with a correction for the use of foreign gas to simulate the engine density ratio. The model was compared with experimental data collected by selectively blocking rows of film cooling hole to measure the cumulative effect of adding rows of holes to the mid span efficiency. The model predicted loss reasonably well on the suction surface, but the measured effect of a reduction in loss by

uncovering rows in the leading edge and early pressure surface was not accurately modelled.

The use of CFD to predict aerodynamic loss has been widely studied, and a number of papers present data with reasonable prediction of experimental results, although the degree to which the results are postdicted rather than predicted remains rather high. Casciaro et al (1998) present data for a generic turbine profile and applies different modelling techniques available in two commercial codes (TASCflow, MISES) to the prediction of total loss and loss distribution. The predictions are generally good, particularly for the modelling of flow angle, and the authors identify the lack of an accurate transitional model as the main cause of any discrepancies in loss modelling.

## **2.11 Conclusions**

The main parameters that are used to measure film cooling performance have been defined, and a review of the current state of research in film cooling has been presented. There is a considerable amount of knowledge about aerodynamic and thermal physics of film cooling and the advantages and disadvantages of the current film cooling designs has been discussed. The main requirements for a film cooling design are high effectiveness, low heat transfer coefficient and good lateral uniformity of temperature on the surface, while the structural integrity of the material is maintained. The aerodynamic loss introduced by the film cooling should be minimal so that the advantages gained by higher operating temperatures are not lost by increased aerodynamic loss through the blade passage. It is with these requirements in mind that the new film cooling geometry, the *Converging Slot Hole*, or *console*, has been developed.

## Chapter 3

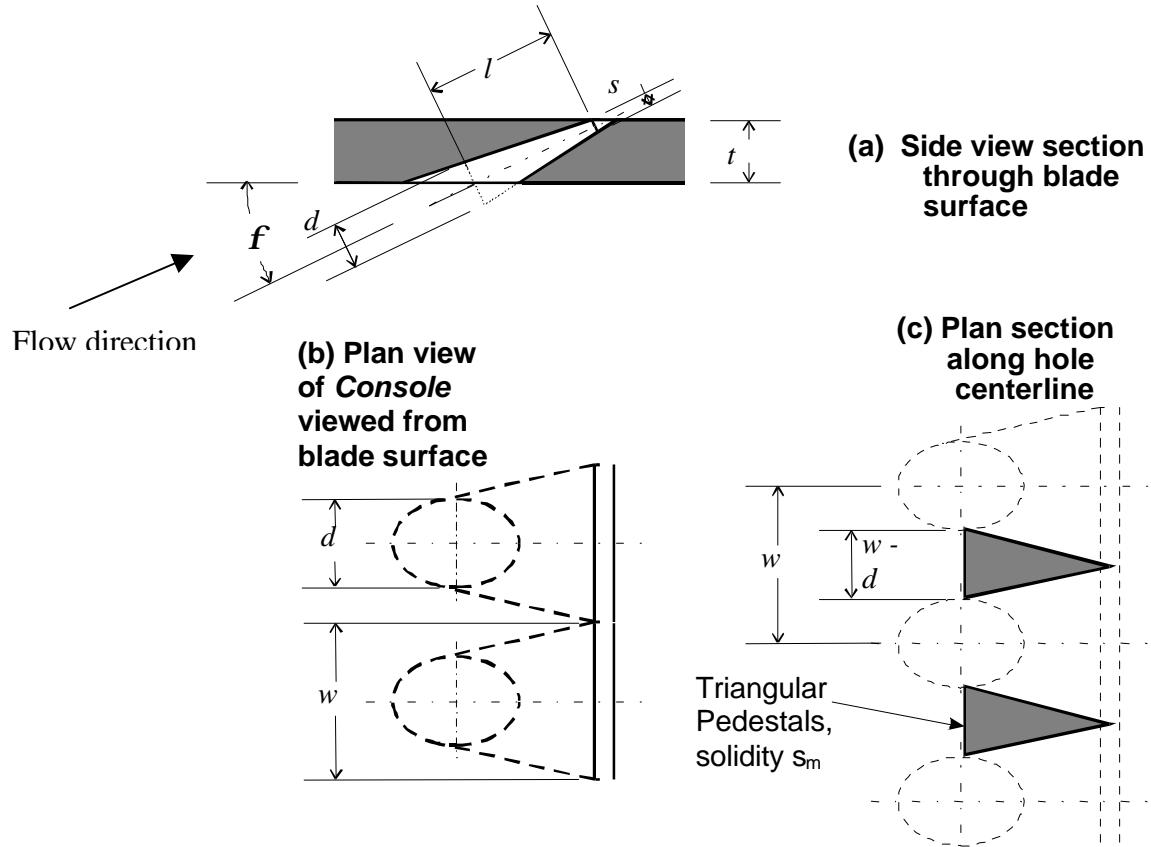
### ***Console* Design**

The concept of the *console* film cooling hole was first proposed by Oldfield and Lock (1998) and is the subject of a patent application. In this chapter the concepts behind the *console* design are outlined. The predicted performance of the *console* is explained with reference to the design features and the surface definition of the *console* generated using the CAD/CAM package Uni Graphics.

#### **3.1 *Console conceptual design***

The Converging Slot Hole or *console* film cooling hole geometry has been developed in response to the identified need for film cooling that provides a high and laterally uniform level of surface thermal protection without significantly augmenting aerodynamic loss over the surface or reducing the structural stability of the component. A slot film cooling geometry traditionally best met these heat transfer and aerodynamic requirements but did not provide the required structural stability. The *console* has been designed to offer the advantages of slot flow, whilst maintaining a structural strength similar to discrete holes.

The main features of the *console* are shown in Figure 3.1. The cross-section of the *console* changes from a near circular shape at inlet to a slot at exit. This change in cross section is produced by a convergence of the walls in side view (Figure 3.1a) and a divergence of the

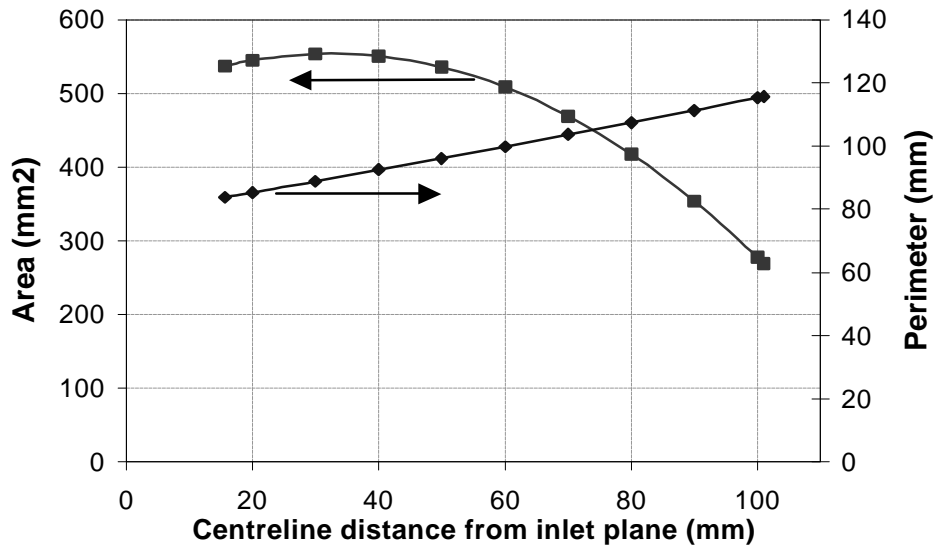


**Figure 3.1: Basic console configuration**

walls in plan view (Figure 3.1b), but the convergence is greater than the divergence so that there is a net decrease in cross-sectional area and the flow accelerates from inlet to outlet. Figure 3.2 shows the reduction in cross-sectional area and increase in wetted perimeter for the console at the scale used for the low speed experiments (5 mm exit slot height) described in Chapter 5. The wetted perimeter is the perimeter in contact with the fluid (Munson et al, 1994). The minimum hole area (throat) and hence maximum flow velocity are at, or just before, the hole exit.

The acceleration of the flow through the length of the hole minimises inlet separations (Schlichting, 1979). The acceleration parameter,  $K$ , was calculated for the experimental flow conditions and as it was greater than  $3 \times 10^{-6}$ , relaminarisation will occur in the hole (Kays and Crawford, 1993). This minimises the aerodynamic loss through the holes and could allow higher coolant mass flows without additional aerodynamic performance

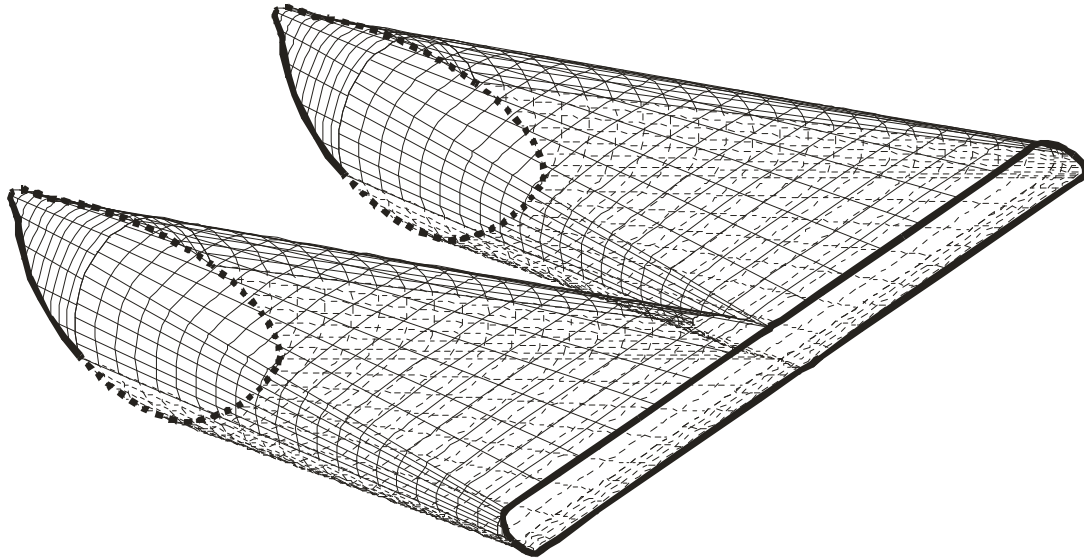




**Figure 3.2: Cross sectional area and wetted perimeter of console**

penalty, although it is generally desirable to minimise the amount of coolant used in the engine. The low levels of aerodynamic loss and accelerating flow are in contrast to conventional fan-shaped or expanded holes where the flow is diffused and slowed down in an attempt to spread the flow of coolant onto the surface with low momentum. The separations in the fan-shaped hole, which reduce the aerodynamic efficiency, should be significantly reduced in the accelerating *console* flow. The low-turbulence exit flow from the *console* should lay a more stable layer of cooling air onto the external blade surface downstream of the exit and should reduce mixing of the coolant and the hot mainstream.

Individual holes in a row of *consoles* are positioned such that adjacent holes meet just below the surface as shown in Figure 3.3, and a continuous slot is formed on the outside blade surface whilst the roughly triangular pedestals between holes maintain the strength of the blade. Although the inlet of the *console* will prevent the coolant film from being completely uniform as it would be for slot flow, by joining the hole exits below the blade surface, there will be a continuous film of coolant in the spanwise direction. This is a significant improvement on discrete holes, for which the jets from adjacent holes only

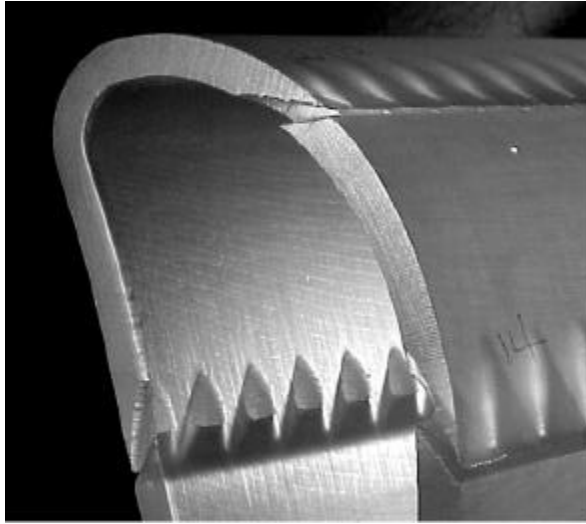


**Figure 3.3: Uni Graphics surface definition of two console film cooling holes**

form a continuous film several hole diameters downstream of the hole exit. The continuous *console* film should therefore benefit from the Coanda effect (Schlichting, 1979) and should not lift off from the blade surface at typical blowing rates. Evidence that the *console* does benefit from the Coanda effect was measured using the technique described in Chapter 8.

The solid area remaining at the plane through the centre of the holes, orientated at the hole inclination is used to compare the structural integrity of each row of film cooling holes. This area, expressed as a percentage of the original (uncut) area is 25% for the *console* compared with 52% for the fan-shaped holes at a pitch of  $3.5 d$ , and 67% for cylindrical holes at a pitch of  $3 d$ . The residual strength of the material with *consoles* should be sufficient, but further studies of the mechanical design of the *console* are required to verify this.

The geometry of the basic *console* design is generated from a family of straight lines as can be seen in Figure 3.3, and hence can be manufactured by available drilling (mechanical or laser) techniques. As precision casting becomes more accurate, it will be possible to modify the basic *console* shape to further improve performance by increasing



**Figure 3.4: Photograph of Stereolithography NGV with console film cooling hole rows**

the thermal protection and reducing aerodynamic loss, by detailed shaping of the hole entry and exit. This has been shown by Farmer et al (1997) experimentally, and Hyams et al (1996) numerically, to improve the adiabatic effectiveness and heat transfer coefficient. The aerodynamic performance should also be improved because of the reduction in shear stress and kinetic energy gradients near the hole exit region demonstrated by Hyams et al (1996). The *console* patent application (Oldfield and Lock, 1998) covers such improvements.

### **3.2 Design Parameters**

If the *console* is used to replace an existing row of conventional film cooling holes, and the same coolant mass flow rate is required with the same coolant to mainstream total pressure ratio, the throat area per unit width of the *console* should be matched to the throat area per unit width of the holes to be replaced, with a correction made for the difference in discharge coefficient between the holes.

The shape parameters that should be considered in the design of a *console* film cooling system are the hole area contraction ratio, aspect ratio and the solidity ratio. These parameters are summarised in Table 3.1 below. The effect of these parameters on console

performance has not been investigated in the current work, but could be considered in future work to optimise the *console* design.

		<b>Low Speed</b>	<b>CHTT</b>
$s$	Exit throat slot height, controls coolant mass flow	5 mm	0.4 mm
$w$	Exit slot width, or console hole pitch	50 mm	4 mm
$d$	Hole inlet diameter	25 mm	2 mm
$A=w/s$	Exit slot aspect ratio	10	10
$k_c = \mathbf{p}d^2/4sw$	Hole area contraction ratio	1.96	1.96
$s_m = \frac{1}{2}(1 - d/w)$	Inlet solidity ratio, the proportion of metal left after hole has been drilled	0.25	0.25

**Table 3.1: Console shape parameters tested (parameters as shown in Figure 3.1)**

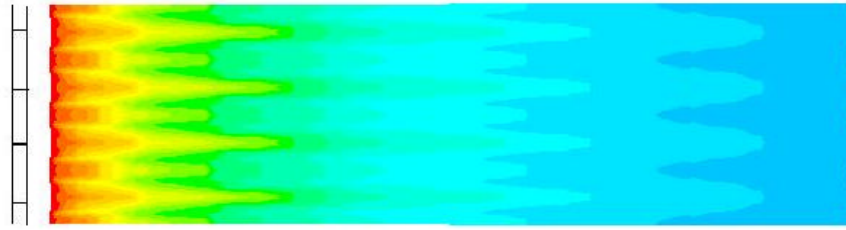
The *console* row for the low speed experiments was designed with equal hole throat area per unit width to the other film cooling hole rows used in the experiments. The effect of the discharge coefficient was compensated for in a correction to the measured results.

For the high speed experiments, conducted under engine conditions in the CHTT, three *console* rows were designed to each replace two rows of fan-shaped film cooling hole rows, and the exit area was equal to the throat area of two fan-shaped rows and located at the mean position of the two rows to be replaced. This was required to ensure that the console row height was large enough to be manufactured. A fourth row was designed to provide twice the flow from a single row of fan-shaped holes for the same reason. A section of the NGV with *console* film cooling hole rows is shown in Figure 3.4. The *console* shape parameters were matched for both experiments and are summarised in Table 3.1. The surface definition shown in Figure 3.3 was scaled and used for both designs.

### **3.3 CFD predictions used in the initial design**

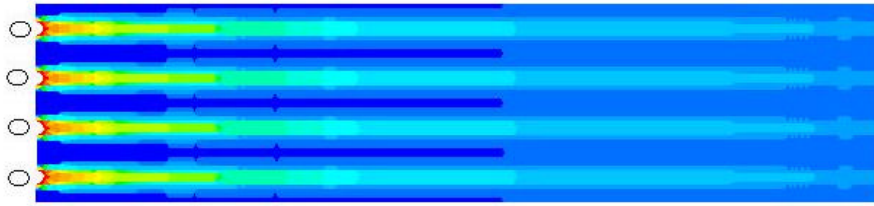
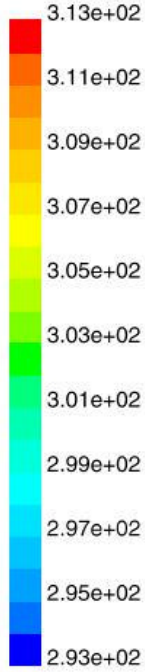
The proficiency of the preliminary *console* design to achieve the design aims was tested using the CFD software package *FLUENT* and compared with an analysis of slot and

cylindrical film cooling holes. The data collected from the analysis provided an initial estimate of the adiabatic effectiveness and an indication of the likely flow patterns. The flow conditions for the analysis matched the conditions in the low speed wind tunnel experiments outlined in Chapter 5. The main flow parameters are summarised in Table 3.2 and contour plots of adiabatic wall temperature for the *console*, cylindrical holes and a slot are shown in Figures 3.5 - 3.7. The film cooling hole geometry is specified in Figure 5.2.



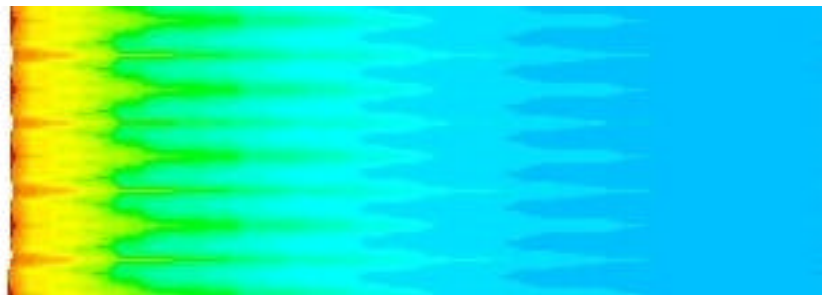
**Figure 3.5: Adiabatic wall temperature distribution for console:**

$$T_{0c} = 313 \text{ K}, T_{0m} = T_r = 293 \text{ K}$$



**Figure 3.6: Adiabatic wall temperature distribution for cylindrical holes:**

$$T_{0c} = 313 \text{ K}, T_{0m} = T_r = 293 \text{ K}$$



**Figure 3.7: Adiabatic wall temperature distribution for slot:**

$$T_{0c} = 313 \text{ K}, T_{0m} = T_r = 293 \text{ K}$$

Referring to the definition of adiabatic effectiveness,  $h = \frac{T_{aw} - T_r}{T_{0c} - T_{0m}}$ , if the other

parameters are equal, the effectiveness is proportional to the adiabatic wall temperature.

The regions of high adiabatic wall temperature in Figures 3.5 – 3.7 represent areas of high

effectiveness. The adiabatic wall temperature downstream of the *console* is considerably more uniform than that shown for the cylindrical holes, although there is some structure to the flow for the *console*. The slot result also shows some three-dimensional streaks, even though the edges of the modelled area were set with a symmetry boundary condition. The shortcomings of the CFD are further discussed in Chapter 9. However, these early results are a good indication that the *console* should provide the high levels of effectiveness expected and that the chosen design is valid and further experimental work is worthwhile.

Coolant temperature (K)	313
Mainstream temperature (K)	293
Plate Heat Flux ( $\text{W/m}^2$ )	0
Mainstream inlet total pressure (PaG) *	0
Mainstream outlet static pressure (PaG)	-309
Coolant inlet pressure (PaG)	60

**Table 3.2: Temperature and pressure definitions for CFD in Figures 3.5 - 3.7**

\* The abbreviation PaG is gauge pressure

### **3.4 Conclusions**

The *console* film cooling hole design concept has been presented and the main features of the holes and the predicted effect that these will have on the film cooling heat transfer and aerodynamic performance have been discussed. The convergence of the hole should minimise the aerodynamic loss through the hole and the merging of the holes into a single slot at exit should improve the thermal protection of the surface and reduce the aerodynamic loss due to mixing.

The Uni Graphics surface definition used to generate the *console* test pieces for the low speed and CHTT experiments was included and the main design parameters were presented. Initial CFD used to test the conceptual *console* design indicated that the adiabatic effectiveness for the *console* was a significant improvement on cylindrical holes and similar to slot film cooling.

## Chapter 4

### Simulation Parameters in Film Cooling

The main variables governing film cooling flows at both compressible and incompressible flow conditions are considered in this chapter. The dimensionless parameters that should be matched to engine conditions in an experiment are discussed and the similarity of the present experimental work to engine conditions is considered.

#### **4.1 *Dimensional analysis and similitude***

Dimensional analysis can be applied to any system to reduce the governing variables to a set of independent, dimensionless parameters. The dimensionless parameters are identified by analysis of the governing equations of the flow or by applying the Buckingham Pi Theorem (Munson et al, 1994) to the set of governing variables. The first requirement for a particular flow system to be correctly modelled is that the geometry of the flow is similar. For a simple, single flow stream, incompressible flow system with heat transfer, the dimensionless parameters governing the flow are Reynolds Number,  $Re$  and Prandtl Number,  $Pr$ . For a similar compressible flow system with heat transfer, the ratio of specific heats,  $\gamma$  and the Mach number,  $M$  are also required to obtain similarity (Munson et al, 1994). In addition to these, the flow

field must have the same turbulence intensity as the modelled flows, in order to model the heat transfer correctly.

When a second flow is added such as a series of film cooling jets, other similarity parameters must be introduced in order to match the complicated flow field. The following dimensionless parameters have been identified (e.g. Forth and Jones, 1986) as being important to the film cooling flowfield:

- Coolant to mainstream density ratio,  $D = \frac{\mathbf{r}_c}{\mathbf{r}_m}$
- Coolant to mainstream velocity ratio,  $V = \frac{v_c}{v_m}$
- Coolant to mainstream blowing ratio,  $B = \frac{\mathbf{r}_c v_c}{\mathbf{r}_m v_m}$
- Coolant to mainstream momentum flux ratio,  $I = \frac{\mathbf{r}_c v_c^2}{\mathbf{r}_m v_m^2}$
- Coolant to mainstream pressure difference ratio (ideal momentum flux ratio

for incompressible flow),  $I_{\text{ideal}} = \frac{P_{0c} - P_m}{P_{0m} - P_m}$

- Coolant to mainstream total pressure ratio,  $\frac{P_{0c}}{P_{0m}}$
- Coolant total to mainstream static pressure ratio,  $\frac{P_{0c}}{P_m}$
- Coolant to mainstream mass flow ratio,  $\frac{\dot{m}_c}{\dot{m}_m}$
- Coolant to mainstream total temperature ratio,  $\frac{T_{0c}}{T_{0m}}$

Other parameters that relate to the flow field generated by the mainstream and coolant flows are

- Ratio of upstream boundary layer thickness to hole diameter  $\frac{d}{d}$
- Non-dimensional pressure gradient  $\frac{d}{P_m} \frac{dP_m}{dx}$
- Ratio of hole diameter to local radius of curvature  $\frac{d}{r}$



These parameters are not independent, which means that if one parameter cannot be modelled in a particular apparatus, other parameters will be affected. One parameter that is typically not modelled in laboratory experiments is the coolant to mainstream temperature ratio. In the engine, typical mainstream and coolant temperatures are of the order of 1750K and 900K respectively, which provides a density ratio of 1.94. In addition to this, the properties of air at these temperatures are significantly different to those at ambient temperature. If the density ratio is not correctly modelled, then it is not possible to simultaneously model the momentum flux ratio, blowing ratio and velocity ratio and hence the flowfield cannot be correctly modelled. Various authors have tended to use either the blowing ratio or the momentum flux ratio, and Forth and Jones (1986) have shown that for strong blowing, results are best correlated with velocity ratio, while for weak blowing, momentum flux ratio is a better correlating parameter, however this is still an approximation to the fully similar flowfield.

#### **4.2 Modelling density ratio using foreign gas**

If the density ratio is not simulated using engine temperature differences between the coolant and mainstream flows, then a foreign gas can be used to simulate the more dense coolant flow, as demonstrated by Teekaram et al (1989). As previously identified, the ratio of specific heats,  $g$ , should be modelled for compressible flows, which adds a requirement that the foreign gas have the property  $g = 1.4$  for the engine case where air is used as coolant. In addition, the density ratio in the range 1.77 – 1.94 for a typical engine case, should be modelled. Teekaram et al (1989) used carbon dioxide (CO<sub>2</sub>) to obtain a density ratio of 1.53. However this gas will not provide the correct similarity for compressible flow experiments because  $g_{CO_2} = 1.3$ . Ammari et al (1990) used argon (Ar) to provide a density ratio of 1.38, and  $g_{Ar} = 1.67$ . In order to

match the ratio of specific heats,  $g = 1.4$ , a mixture of these gases can be used. A mixture of 45.5% by weight Ar and 54.5% CO<sub>2</sub> would have  $g = 1.4$  and D.R. = 1.46. A more realistic density ratio relative to air can be achieved with a mixture of argon (30.2% by weight) and sulfur hexafluoride (SF<sub>6</sub>) (69.8% by weight) which has a density ratio relative to air of 1.77 and ratio of specific heats,  $g = 1.4$ . This foreign gas was used in the current work, and also by Day et al (1998,1999,2000), Rowbury et al (1997) and Lai (1999). The properties of this SF<sub>6</sub> / Ar mixture are given in Oldfield and Guo (1997).

The implication of using foreign gas and cold air for heat transfer experiments is that the molecular properties of the gas are not matched to engine conditions. As outlined in Section 4.1 a further requirement for similarity in heat transfer experiments is that the Prandtl number,  $Pr = \frac{\mu}{k}$ , is correctly modelled. Jones (1999) presents a method to correct the adiabatic effectiveness and Nusselt number to engine conditions, by taking into account the differences in specific heat and conductivity between the cold air and foreign gas used in the experiment and air at engine temperatures. If the flowfield is correctly modelled, viscosity has a secondary effect, because the transport of species, momentum and enthalpy are predominantly dependent on the turbulent flow field. The viscosity is only important in the sublayer, which can be corrected for.

The ratio of Nusselt number for the experimental and engine cases that are at the same Reynolds number, coolant to freestream density and velocity ratios is (Jones 1999):

$$\frac{Nu_e}{Nu_{ex}} = \left( \frac{c_{pm}}{c_{pw}} \right)_{ex} \frac{1 + \left[ Pr_m \frac{c_{pw}}{c_{pm}} \frac{k_m}{k_w} \right]_{ex} f_2}{1 + \left[ Pr_m \frac{k_m}{k_w} \right]_e f_2} \quad (4.1)$$

This equation and the method of deriving the function  $f_2$  is further discussed in Jones (1999), and this equation has been converted to a ratio of heat transfer coefficients for the CHTT conditions by Guo et al (1998):

$$\frac{h_e}{h_{ex}} = \frac{x_{ex}}{x_e} \frac{k_e}{k_{ex}} \left( \frac{c_{pm}}{c_{pw}} \right)_{ex} \frac{1 + 0.924 \left( \frac{c_{pw}}{c_{pm}} \frac{k_m}{k_w} \right)_{ex}}{1 + 0.924 \left( \frac{k_m}{k_w} \right)_e} \quad (4.2)$$

Here,  $h_e$  and  $h_{ex}$  are the heat transfer coefficients,  $k_e$  and  $k_{ex}$  the gas conductivities,  $c_{pe}$  and  $c_{pex}$  the gas specific heats at engine (e) and experimental (ex) conditions respectively. The subscript w refers to the gas properties at the wall, where the gas is a mixture of coolant and mainstream. The conductivity and specific heat are calculated with sufficient accuracy by the relative mole fraction of concentration evaluated at the wall temperature:

$$k = k_m(1 - y_{mole}) + k_c y_{mole} \quad (4.3)$$

where the concentration by mass is defined:

$$y_{mass} = \frac{h c_{pm}}{(1 - h) c_{pc} + c_{pm}} \quad (4.4)$$

and the mole fraction of coolant concentration is defined:

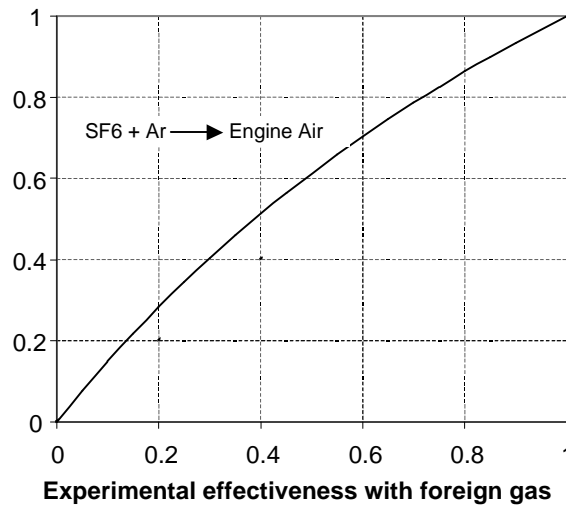
$$y_{mole} = \frac{y_{mass}}{y_{mass} + (1 - y_{mass}) \frac{M_c}{M_m}} \quad (4.5)$$

The correction for adiabatic effectiveness is based on the assumption that the concentration of coolant in the mainstream flow is identical for the experimental and engine conditions. The engine-level effectiveness can be written (Jones, 1999):

$$h_e = \frac{h_{ex}}{h_{ex} + (1 - h_{ex}) \left( \frac{c_{pc}}{c_{pm}} \right)_{ex} \left( \frac{c_{pm}}{c_{pc}} \right)_e} \quad (4.6)$$

where the gas specific heats are evaluated at local recovery temperatures.

This correction to engine level effectiveness for experimental results using cold air for the mainstream and  $\text{SF}_6 + \text{Ar}$  mixture foreign gas for the coolant to air at engine temperatures is plotted in Figure 4.1. This correction is significant, particularly in the range of values typically measured from 0.3-0.7.



*Figure 4.1: Film cooling effectiveness for air at engine conditions vs. the equivalent value for foreign gas at ambient conditions (Jones, 1999)*

### 4.3 Similarity for low-speed experiments

The first series of experiments in the present work is a significant simplification of engine flow conditions. Having presented the requirements for correctly modelling the engine, a more simple experiment can be generated by matching a limited number of the flow parameters that have been identified to be the most significant. However, the results of such an experiment will only be an approximation to the situation that is being modelled, and the results must be reviewed in terms of the limitations of the experiments. The low-speed experiments are an example of this. The purpose of the low-speed experiments was to obtain **comparative results** without the complication of full similarity to engine conditions, and as such the results are useful for comparative purposes, but cannot be directly related to the engine.

The Reynolds number based on the mainstream flow speed and the hole diameter were matched to engine conditions for regions on the suction surface (high  $Re_d$ ) and pressure surface (low  $Re_d$ ) of the engine NGV. The pressure difference ratio or ideal momentum flux ratio was matched to engine values to obtain similarity of film cooling flows. Following the flow definitions provided by Forth and Jones (1986), the film cooling flow field in these regions was in the range of weak blowing, and hence the momentum flux ratio was the best correlating parameter. The pressure difference ratio or ideal momentum flux ratio was used because this is the parameter that is set in the engine design.

Ambient air was used for the mainstream flow and air heated up to 20°C above ambient was used for the coolant flow, so that the density ratio was close to unity and not matched to engine conditions. Hence blowing and velocity ratios differed from engine conditions. The geometry of the system was not three-dimensional as the surface of the engine components would be, so that any curvature or pressure gradient effects were precluded from the analysis and the effects of compressibility were neglected because of the low flow speeds.

#### **4.4 Similarity for high speed experiments**

The performance of the *console* was also comparatively tested at more representative conditions in the CHTT blowdown facility. The facility is more thoroughly described in Chapter 6, but the features relevant to similarity analysis will be discussed here. The working section is an enlarged scale model of the annulus of NGVs in the engine, and the engine mainstream Mach and Reynolds numbers can be set, so that geometric similarity, local static pressures and pressure gradient can be modelled. The facility uses ambient air so that the temperature ratio between mainstream and coolant flows

is not modelled, but a typical engine density ratio caused by the temperature ratio of 1.77 is modelled using the SF<sub>6</sub>/Ar foreign gas mixture. The ratio of coolant to mainstream total pressures is set in order to match the engine design condition for coolant flow rate. The accurate modelling of local pressures in the flow field means that the coolant to mainstream velocity ratio is matched. As the coolant to mainstream density and velocity ratio are matched to engine conditions, the hole blowing ratio and momentum flux ratio are also modelled. The coolant Mach number  $M_c$  is correctly modelled because the coolant total to static pressure ratio  $P_{0c}/P_c$  is correct.

The only parameters that are not correctly modelled in the CHTT are the coolant to mainstream temperature ratio and the Reynolds number for flow through the hole, based on the coolant velocity in the hole and the hole diameter. However the enthalpy

flux ratio  $\frac{H_{0c}}{H_{0m}} = \frac{c_{pc}T_{0c}}{c_{pm}T_{0m}}$  is correctly modelled. These parameters are not independent

and while the mainstream Reynolds number is correct, the hole Reynolds number can not be correctly modelled unless the viscosity ratio is correct, even if the density ratio is correctly modelled.

It has been assumed in the discussions in this chapter that the engine mainstream fluid is air at engine temperatures and pressures, although it is in fact a mixture of combustion products. The main difference between combustion gas and air at the same temperature and pressure is the ratio of specific heats is  $\gamma=1.33$  for combustion gases compared with  $\gamma=1.4$  for air. This will result in an error of up to 2 % in pressure ratio  $P_{0m}/P_{exit}$  for the range of Mach numbers in the experiments, when the Mach number is correctly set. For heat transfer from a flat plate in uniform flow (Kays and Crawford, 1993):

$$Nu_x = \frac{0.0287 Re_x^{0.8} Pr}{0.169 Re_x^{-0.1} (13.2 Pr - 8.66) + 0.85} \quad (4.7)$$

This equation indicates that the effect of the error in pressure ratio on the heat transfer coefficient is secondary if the mainstream Reynolds number is correctly modelled. In addition to this, the purpose of the current experiments is to provide information for validation of CFD codes, which can be run to exactly model experimental conditions.

#### **4.5 Conclusions**

The important parameters governing the film cooling process have been outlined and the selection of similarity parameters for the present experimental work has been discussed.

The low speed experiments will be useful for comparison of the performance of the different film cooling configurations tested, although some of the requirements of similarity to engine conditions are not met. The most important parameters governing the flowfield generated by the interaction of the coolant and mainstream flows were identified to be the momentum flux ratio and the Reynolds number based on mainstream flow and hole diameter, and these were the only flowfield parameters that could be matched. The CHTT experiments simulate the majority of engine condition parameters, and the results can be directly related to the engine, if the corrections for molecular properties of the gases are applied. Only the coolant to mainstream temperature ratio and the hole Reynolds number based on coolant flow and hole diameter are not correctly modelled, but because the coolant to mainstream density and velocity ratios and the mainstream Reynolds, and mainstream and coolant Mach numbers are matched, the flowfield is a good model of engine conditions.

## Chapter 5

### Low-speed Heat Transfer Experiments

This chapter presents the heat transfer experiments conducted in a low-speed wind tunnel over a constant heat flux flat plate. The performance of the *console* compared with fan-shaped and cylindrical holes and a slot was measured. The experimental facility and measurement techniques are described and the new analytical technique used to process the raw data is presented. The full heat transfer results are presented and discussed.

The experiments were designed to be a feasibility study of the *console* before work commenced on producing a full NGV model with *consoles* for experiments at engine representative conditions. The heat transfer coefficient and adiabatic effectiveness were measured for the four hole shapes and compared directly as well as using the net heat flux reduction defined in Chapter 2.

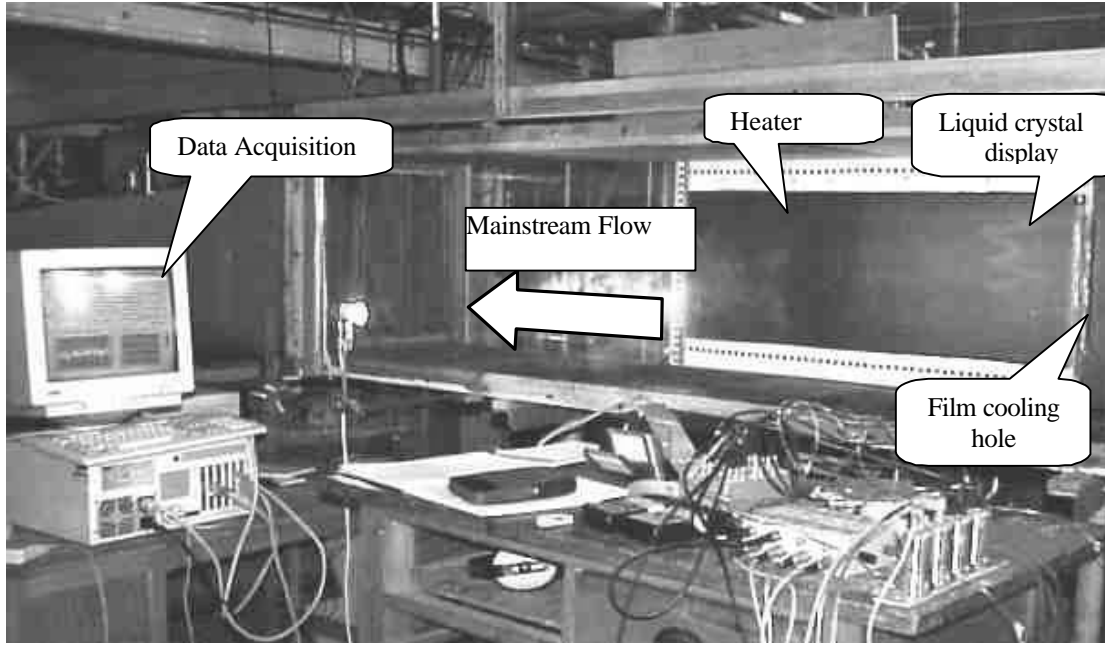
#### **5.1 Experimental facility**

The 500 x 500 mm cross-section low-speed, suck down wind tunnel used for the experiments presented in this chapter is shown in Figure 5.1

The mainstream (primary flow) air speed and temperature were measured upstream of coolant injection using a pitot-static probe and a total temperature probe, which were continuously monitored by the data acquisition system. The air speed could be adjusted, and the experiments were conducted at repeatable mainstream speeds of 5 m/s and 26 m/s



with a low freestream turbulence intensity of the order of 1%. The mainstream flow was taken directly from atmosphere, and there was consequently variation of  $\pm 4$  °C in the mainstream temperature over the course of the work. This variation did not affect the measured parameters, but did affect the size of the radiation correction outlined in section 5.2.3. The mainstream air speed and temperature were independent of the coolant flow.



**Figure 5.1 Low-speed wind tunnel**

The measurements presented were conducted at engine representative Reynolds numbers based on cylindrical cooling hole diameter and mainstream flow velocity,  $Re_d$ , of  $3.6 \times 10^4$  (high speed) and  $6.0 \times 10^3$  (low speed) and a coolant to mainstream density ratio close to 1.0. The Reynolds numbers based on mainstream flow velocity and *console* and slot exit slot height were  $9.0 \times 10^3$  (high speed) and  $1.5 \times 10^3$  (low speed). A pressure difference ratio, or ideal momentum flux ratio (the flow is incompressible) was used to correlate the coolant flows from the different holes. The pressure difference ratio was defined as:

$$I_{ideal} = \frac{P_{0c} - P_m}{P_{0m} - P_m} = \left( \frac{r_c v_c^2}{r_m v_m^2} \right)_{ideal} \quad (5.1)$$

Because the discharge coefficients were different for each hole, the mass flow and hence the blowing ratio and the conventional, or actual, momentum flux ratio,  $I_{\text{actual}}$ , are different

for each hole. The discharge coefficient,  $C_D$ , can be written:  $C_D = \frac{(\mathbf{r}_c v_c)_{\text{actual}}}{(\mathbf{r}_c v_c)_{\text{ideal}}} \approx \frac{v_{c\text{actual}}}{v_{c\text{ideal}}}$

for incompressible flow (Section 5.7) and  $I \propto \mathbf{r}_c v_c^2$  so  $I \propto C_D^2$ . This means that, for

example, if  $C_D = 0.7$ , then  $\frac{I_{\text{ideal}}}{I_{\text{actual}}} \approx C_D^2 = 0.49$

The correction made to the data to correct for the differences in mass flow rate is outlined in Section 5.2.4. Measurements were made at ideal coolant to mainstream momentum flux ratios of 0.5, 1.1 and 1.5. The actual momentum flux and mass flux or blowing ratios for each hole geometry at each ideal momentum flux ratio are shown in Table 5.1. The velocity used for the calculation of the actual momentum flux and blowing ratios was the average velocity at the hole throat, calculated from the mass flow rate and hole area:

$$v = \frac{\text{mass flow rate}}{\mathbf{r}A_{\text{throat}}}$$

	Cylindrical		Fan		Slot		Console	
$I_{\text{ideal}}$	$I_{\text{actual}}$	$B_{\text{actual}}$	$I_{\text{actual}}$	$B_{\text{actual}}$	$I_{\text{actual}}$	$B_{\text{actual}}$	$I_{\text{actual}}$	$B_{\text{actual}}$
0.5	0.17	0.4	0.21	0.46	0.07	0.26	0.14	0.37
1.1	0.48	0.69	0.61	0.78	0.30	0.55	0.36	0.60
1.5	0.67	0.82	0.89	0.94	0.41	0.64	0.75	0.87

**Table 5.1: Comparison of actual momentum flux ratio,  $I_{\text{actual}}$ , and blowing ratio,  $B_{\text{actual}}$ , with ideal momentum flux ratio,  $I_{\text{ideal}}$**

The cooling air was supplied from the laboratory compressed air source and the mass flow rate of the air fed to the plenum chamber was measured through a British Standard BS 1042 orifice plate (17.96 mm diameter). The full *console* test data is outlined in Table 5.2.

	<b>Console coolant flow velocity (m/s)</b>		<b>Console coolant mass flow rate per unit width (kg/ms)</b>	
	$v_m = 26 \text{ ms}^{-1}$	$v_m = 5 \text{ ms}^{-1}$	$v_m = 26 \text{ ms}^{-1}$	$v_m = 5 \text{ ms}^{-1}$
$I=0.5$	8.3	2.0	0.049	0.012
$I=1.1$	16.3	2.9	0.096	0.017
$I=1.5$	22.5	3.6	0.136	0.022

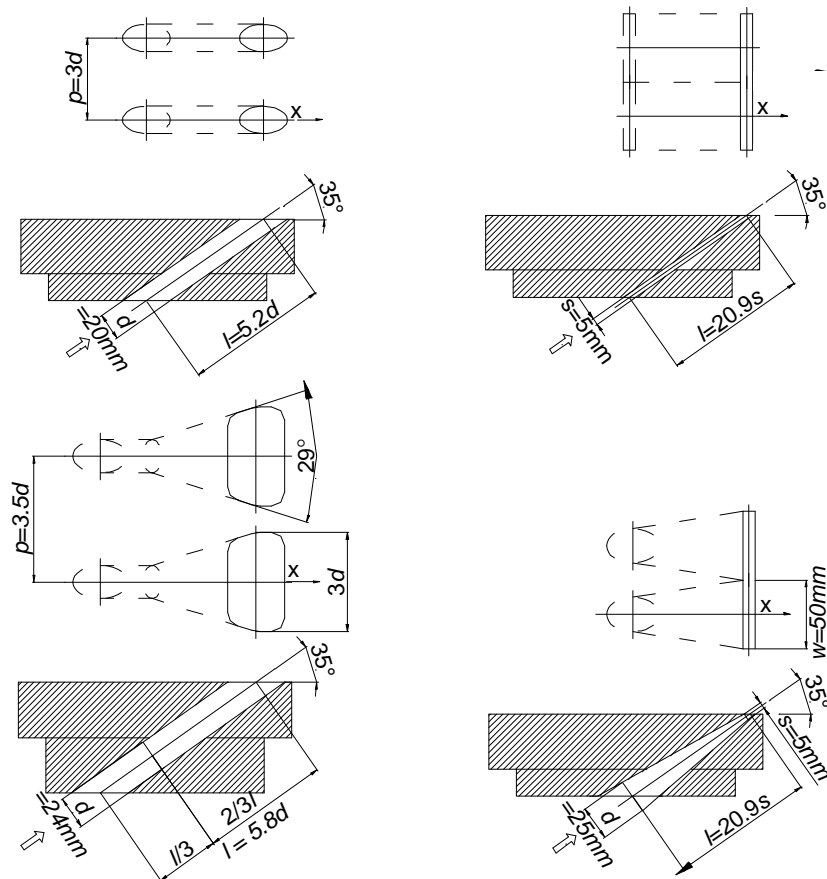
**Table 5.2: Test matrix of coolant flow data. Coolant velocity is mean value at exit**

The coolant air was heated using a variable power inline heater and supplied through a plenum chamber to the film cooling holes. Inside the plenum chamber a baffle plate and a series of screens were used to ensure that the flow was fully mixed before it exited the plenum chamber through film cooling holes mounted in the sidewall of the wind tunnel.

A series of plates with the different film cooling hole geometries investigated were constructed from *Rohacell* Type 51G, a closed pore, structural foam with low thermal conductivity of  $0.028 - 0.030 \text{ Wm}^{-1}\text{K}^{-1}$  at  $20^\circ\text{C}$  compared with the conductivity of air of  $0.025 \text{ Wm}^{-1}\text{K}^{-1}$ . These plates and the main geometrical parameters of the film cooling holes are presented in Figure 5.2. These plates could be easily changed between experiments. The angle of inclination of the holes was  $35^\circ$ . The holes were compared on the basis that the area that controlled the mass flow rate per unit width (throat, exit area or inlet area in the case of the fan) was the same for each different shape tested. This area per unit width was based on a row of 20 mm diameter cylindrical holes at a pitch of  $3 d$ . The fan shaped holes had an expansion angle of  $29^\circ$ , hole diameter of 24 mm, pitch of  $3.5 d$ , and straight section of  $1/3 l$ , where  $l$  is the length of the hole. The slot height was 5 mm for the slot and *console*, the *console* inlet diameter was 25 mm and pitch was 50 mm ( $2 d$ ).

The fan shaped holes were designed to have a larger hole pitch and were longer than the cylindrical holes in order to better match the geometry typically used in the engine. In order to match the mass flow controlling area per unit width (the fan hole inlet diameter), it was necessary to produce holes with a 24 mm inlet diameter. The appropriateness of

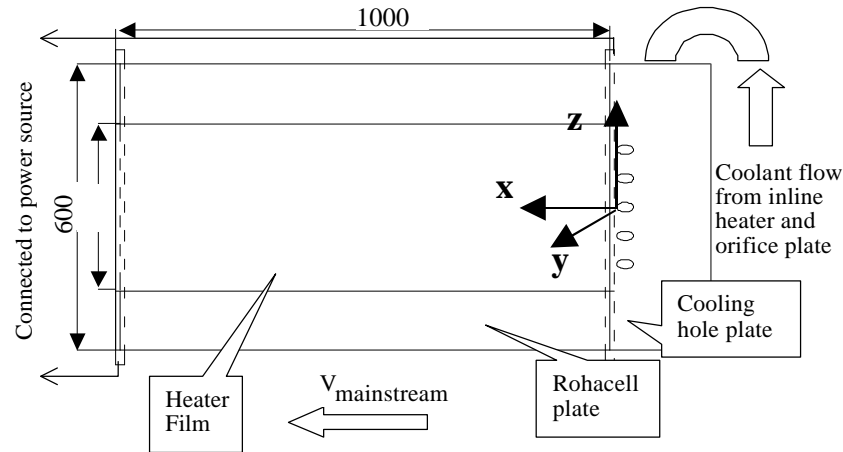
comparing 20 mm diameter cylindrical holes at  $3d$  pitch with 24 mm diameter fan shaped holes at  $3.5d$  pitch was checked by comparing measurements of heat transfer coefficient and adiabatic effectiveness for 20 mm diameter cylindrical holes at  $3d$  pitch and 24 mm cylindrical holes at  $3.5d$  pitch. These results are presented in Section 5.4.2, and show that the assumption is valid when the corrections outlined later in the thesis are applied.



**Figure 5.2: Film cooling hole configurations**

A uniform heat flux flat plate shown in Figure 5.3 was produced from a large sheet of *Rohacell* backed with fibreboard for stiffness and covered with an electrically heated thin film of aluminised Mylar (supplied by Goodfellow plc), which was bonded to the surface with 3M high strength, double sided tape. The resistance of the heating element as specified by the manufacturer was nominally  $2.0 \Omega$  per square, but it varied slightly with temperature, so the voltage and current were measured in order to calculate the power

supplied to the plate. The total resistance of the 350 x 1000 mm plate at 18 °C was 5.4  $\Omega$  and the maximum heater power used was 200 W producing a maximum heat flux of 570  $\text{Wm}^{-2}$ . This plate was situated downstream of the film cooling holes.



**Figure 5.3 Experimental apparatus**

The heating surface was painted with a thin layer of matte black paint with high thermal emissivity, which enhanced the colour of liquid crystals. Narrow band thermochromic liquid crystals type R25C1W, supplied by Hallcrest plc, were used to measure temperature contours on the surface. The colour play of the crystals was between 24.7 and 25.7°C and it was recorded at each steady state point during the experiment using a digital camera mounted outside the wind tunnel.

## **5.2 Analytical technique**

### **5.2.1 Image processing**

Using the mathematical analysis package *MATLAB*, an automatic system was developed to calculate the heat transfer coefficient and adiabatic effectiveness at each point on the plate.

The first part of the analysis was to extract the temperature contour indicated by the liquid crystal colour in the digital images. The information in a digital image can be presented in a number of ways, as a matrix of RGB (red, green, blue), YUV (luminance and 2

chrominance) or HSV (hue, saturation, value) data. RGB data is a common form for the presentation of coloured images and YUV is the representation used for television, because the data can be displayed using both colour and black and white receivers. The luminance (Y) signal provides the intensity information required for a monochrome receiver and the two chrominance signals (U, V) provide the colour information. These signals are defined as follows (Gonzalez and Woods, 1993):

$$Y = 0.3R + 0.59G + 0.11B \quad (5.2)$$

$$U = 0.493(B - Y) \quad (5.3)$$

$$V = 0.877(R - Y) \quad (5.4)$$

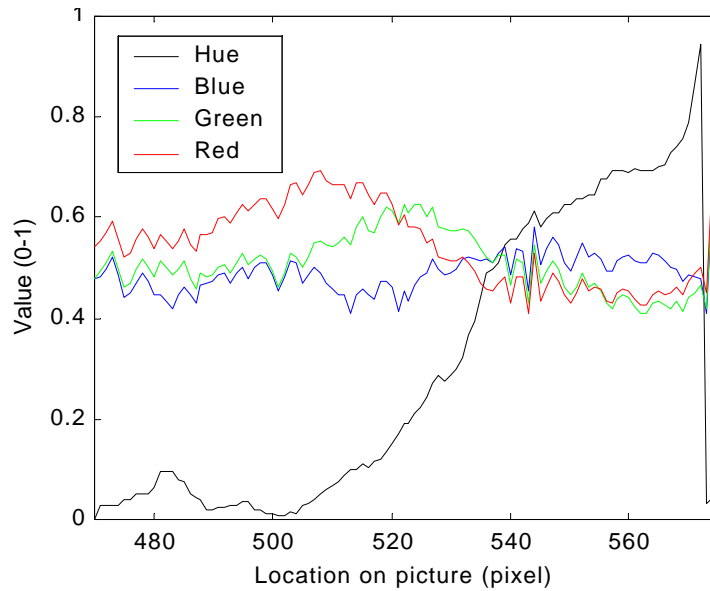
The colour information stored in the chrominance signals  $U$  and  $V$  can be represented diagrammatically as a phasor with mutually perpendicular components  $U$  and  $V$ . In such a representation, the amplitude and phase of the resultant phasor are the saturation and hue respectively.

$$Hue = \tan^{-1}\left(\frac{b}{a}\right) \quad (5.5)$$

where  $a$  and  $b$  are the magnitudes of the chrominance components,  $U$  and  $V$  respectively.

Any of the summarised representations of digital images could be used to extract the temperature contour from the image, but the most accurate representation was found to be the hue signal, because this gave the best signal over the TLC colour play region as demonstrated in Figure 5.4. The variation in hue over the colour play (from pixel 480 – 570) is 0 - 0.9, while the colour signals only vary between 0.4 and 0.6. The calibration of temperature against hue is therefore a far more accurate method to extract the temperature contours.

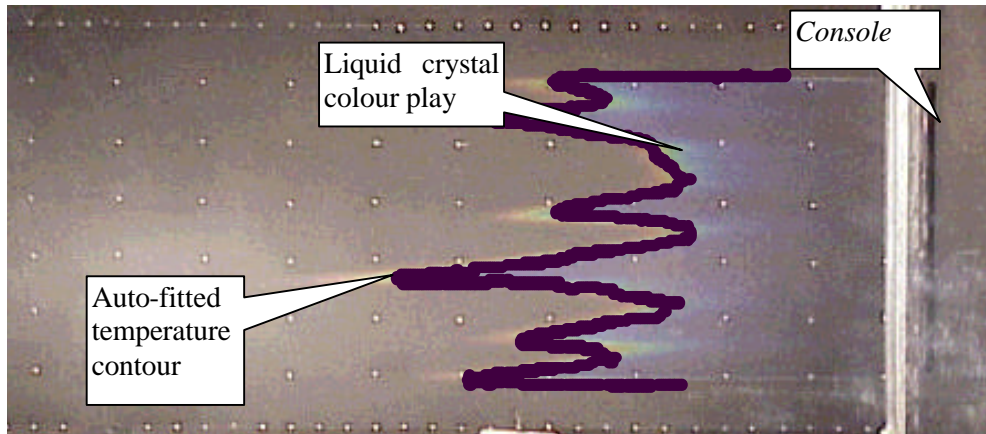
The digital image was converted to hue using the *MATLAB* function *rgb2hsv*. The image was enhanced so that the hue contour in a region of maximum slope with temperature was clearly defined and the *MATLAB* function *edge* was used to extract a binary image matrix of the hue contour.



**Figure 5.4: Variation in hue and colour signals over the TLC colour play**

The hue contour was calibrated against temperature using two thin film surface thermocouples located on the surface of the plate and, for each series of experiments, the calibration was checked by recording the surface thermocouple temperature measurement as the extracted hue contour crossed the thermocouple locations.

An example of a TLC image and the temperature contour extracted using this method is shown in Figure 5.5. The temperature contours from each series of experiments were collated and the analytical method outlined below was applied to sets of data to calculate the film cooling parameters.



*Figure 5.5 Liquid crystal display for console film cooling with extracted temperature contour superimposed onto picture*

### 5.2.2 Reduction of experimental data to $h$ and $h$

Substituting the definition of heat transfer coefficient into the expression for effectiveness, the following linear expression in dimensionless temperature,  $q$  (defined in Chapter 2), is obtained:

$$h_{mw} = \frac{q_c}{T_w - T_r} = h - hq \quad (5.6)$$

where  $h_{mw}$  is the heat transfer coefficient based on the difference between the wall and mainstream recovery temperatures,  $T_w$  and  $T_r$  respectively. In the low-speed work presented in this chapter, the recovery temperature is equal to the mainstream temperature, but this definition is important when the Mach number is greater than 0.3, such as in the following chapter. The recovery temperature is defined in Chapter 2, using a recovery factor,  $r = 0.89$ . The slope of the line defined by equation (5.6) is the heat transfer coefficient,  $h$ , and the  $q$  axis intercept is  $1/h$ .

Downstream of a row of cooling holes, the effectiveness  $h$  varies periodically in a spanwise direction and previous workers (e.g. Ligriani et al 1992) have simply arithmetically averaged  $h$ . Since  $h$  also varies, this procedure is not technically correct and



the correct method to calculate the lateral average is obtained by taking the average of both sides of (5.6):

$$\overline{\left[ \frac{q_c}{T_w - T_m} \right]} = \bar{h} - \overline{h\mathbf{h}} \quad (5.7)$$

The two properties of the film cooling heat transfer that are required for the prediction of the laterally averaged heat flux are  $\bar{h}$  and  $\overline{h\mathbf{h}}$ . The correct way to calculate the laterally averaged effectiveness from the contour map of  $h$  and  $\mathbf{h}$ , if it is to be used to determine laterally averaged heat flux is:

$$\bar{h} = \frac{\overline{h\mathbf{h}}}{\bar{h}} \quad (5.8)$$

In practice, for moderate, uniform levels of heat transfer coefficient the difference between this definition and spatially averaged  $\mathbf{h}$  is less than 5%.

### 5.2.3 Correction for radiation and conduction heat transfer

The heat flux supplied to the flat plate is not all transferred from the surface as convective heat flux. The heat flux supplied to the surface is transferred by a combination of radiation from the black surface, a small amount of conduction through the surface to the outside of the wind tunnel and convection from the surface. Hence the actual convective heat flux  $q_c$  could be found from the following expression:

$$q_{heater} = q_x + q_c \quad (5.9)$$

where  $q_{heater}$  is the electrical heat flux applied to the plate and  $q_x$  is the combined heat loss due to radiation and conduction. In order to correctly calculate the convective heat flux from the surface, which is the parameter of interest, a correction of the value of  $q_x$  must be made to the electrical heat flux supplied to the plate.

The calculation of this correction will be approached in two ways based on analytical models of heat transfer in order to check the validity of the argument in each case.

Kays and Crawford (1993) propose the following theoretical expression for the heat transfer due to convection from a heated flat plate with uniform gas flow:

$$\begin{aligned} St_x Pr^{0.4} &= 0.03 Re_x^{-0.2} \\ \text{or } Nu_x &= 0.03 Re_x^{0.8} Pr^{0.6} \end{aligned} \quad (5.10)$$

Considering the heat transfer coefficient at a constant point on the plate, where all parameters are identical except for the mainstream flow speed we can write for convection from a heated flat plate

$$h = Cv^{0.8} \quad \text{where } C \text{ is a constant.} \quad (5.11)$$

Hence at a fixed position on the plate (namely the position of a surface thermocouple) the heat flux equation above can be written:

$$\frac{q_{heater}}{\Delta T} = \frac{q_x}{\Delta T} + Cv^{0.8} \quad \text{where } DT = (T_w - T_r). \quad (5.12)$$

From the flat plate experiments at high and low mainstream speed (26m/s and 5m/s respectively), this equation can be solved simultaneously for  $\frac{q_x}{\Delta T}$  and  $C$  with the numerical result:

$$\frac{q_x}{\Delta T} = 4.8 \quad (5.13)$$

An alternative method was devised and used to check the validity of this result. If the plate is heated with no mainstream flow, then it will reach a steady temperature and the heat flux will balance natural convection, radiation and conduction from the surface. As the heat flux is increased, there will be a resultant increase in the steady state plate temperature.

The conduction and radiation components at a particular temperature difference between the mainstream and plate temperatures will be independent of the flow in the tunnel; hence the correction term  $\frac{q_x}{\Delta T}$  can be found from this experiment if the natural convection term is removed.

For laminar flow over a constant-temperature, vertical and semi-infinite flat plate caused by natural convection Kays and Crawford (1993) provide the result:

$$Nu_x \propto Gr_y^{0.25} \quad (5.14)$$

This can be expanded to give:

$$\frac{hx}{k} \propto \left( \frac{gby^3(T_w - T_r)}{v^2} \right)^{0.25} \quad (5.15)$$

Therefore at constant position,  $(x,y)$ , and gas properties  $v$ ,  $b$  and  $k$ , the relationship between the heat transfer coefficient for natural convection and the driving temperature difference between the wall,  $T_w$  and mainstream  $T_r$  can be written:

$$h \propto \frac{gby^3k}{v^2x} (T_w - T_r)^{0.25} \quad \text{i.e.: } h = D\Delta T^{0.25} \quad (5.16)$$

where  $D$  is a constant,  $D = \frac{gby^3k}{v^2x}$ , and  $\Delta T = (T_w - T_r)$

From the definition of heat transfer coefficient, it is then possible to write:

$$\frac{q_{natural}}{\Delta T} = D\Delta T^{0.25} \quad \text{or } q_{natural} = D\Delta T^{1.25} \quad (5.17)$$

When there is no mainstream flow in the wind tunnel, the heat flux equation for the heated flat plate can be written:

$$q_{heater} = q_{natural} + q_x \quad (5.18)$$

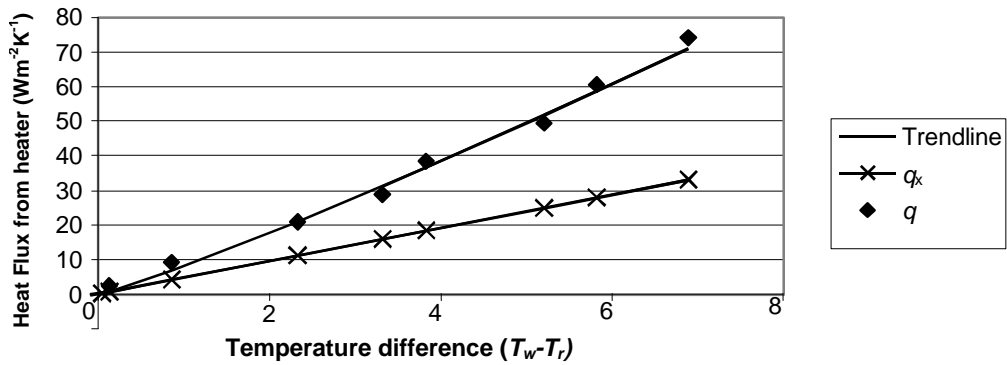
Substituting equations (5.13) and (5.17) into this expression gives

$$q_{heater} = D(\Delta T)^{1.25} + C(\Delta T) \quad (5.19)$$

A curve of this form was fitted to the data points ( $\Delta T$ ,  $q_{heater}$ ) and the fitted constants  $C$  and  $D$  were used to determine the components of natural convection and the correction for radiation and conduction that is of interest. Figure 5.6 shows the data points with the fitted curve:

$$q_{heater} = 3.4(\Delta T)^{1.25} + 4.8(\Delta T) \quad (5.20)$$

The value of  $C$  was between 4.6 and 4.8 for the curves fitted. Thus the two methods applied gave the same radiation and conduction correction of  $4.8(T_w - T_r)$ , which was applied to the results for every experiment. The size of the correction was typically of the order of 20-30  $\text{Wm}^{-2}$ , for heat flux measurements between zero and 570  $\text{Wm}^{-2}$ .



**Figure 5.6: Heat flux correction experimental data**

It should be noted that the theoretical radiation correction should have some dependence on the mainstream recovery temperature as radiation from a surface at  $T_w$  to the other tunnel walls at  $T_r$  is theoretically:

$$\begin{aligned} \dot{q}_{rad} &= \epsilon_{rad} \mathbf{s} (T_w^4 - T_r^4) \\ &\approx 4\epsilon_{rad} \mathbf{s} T_r^3 (T_w - T_r) \end{aligned} \quad (5.21)$$

where  $\epsilon_{rad}$  is the emissivity of the surface and  $\mathbf{s}$  is the Stefan-Boltzmann constant. This temperature dependence is removed by the correction, which was calculated at a typical ambient temperature. Based on an estimation of the conduction term based on the

properties of the *Rohacell* backing, the error in the correction, based on an ambient temperature of  $21^{\circ}\text{C} \pm 2^{\circ}\text{C}$  is typically 4%, but because it is small compared with the total heat flux supplied to the plate, the error in the total measured heat flux is 2%. Refer to Section 5.8 for a more complete estimate of error.

#### 5.2.4 Correction for hole discharge coefficients

The defining parameter for the amount of coolant discharged through the film cooling holes was the ideal momentum flux ratio, which, for incompressible flow, was effectively a pressure difference ratio between the coolant and mainstream flows. Because of the difference in the shapes of the holes, the discharge coefficients were different, so that the coolant mass flow was not identical for each film cooling hole. This difference was corrected for in the final heat transfer coefficient and adiabatic effectiveness data as outlined below.

##### Adiabatic effectiveness

The adiabatic effectiveness is a dimensionless parameter and the effectiveness downstream of holes of the same geometry and same  $Re_d$  and  $I$ , but different scale would be identical if plotted against dimensionless downstream distance,  $(x/d)$ . To compare the effectiveness of holes of different discharge coefficient, it is necessary to define a hypothetical diameter or slot height,  $d_{hyp}$  such that the actual mass flows per unit width would be identical. The  $x$  parameter for each set of results is then scaled by the ratio of the hypothetical to the actual hole diameter or slot height:

$$x_{cor} = x \left( \frac{d_{hyp}}{d} \right) \quad (5.22)$$

## Heat transfer coefficient

The  $x$  parameter for the heat transfer is scaled in the same way as for adiabatic effectiveness. However, assuming turbulent flow,  $h$  is dependent on distance from the cooling hole, by the following relationship (Kays and Crawford, 1993), and must also be corrected:

$$St_x Pr^{-0.4} \propto Re_x^{-0.2} \quad (5.23)$$

which can be written as

$$\frac{hx}{k} \propto Re_x^{0.8}, \text{ since the Prandtl number, } Pr \text{ is constant. This expression can be}$$

expanded to:

$$\frac{hx}{k} \propto \left( \frac{rux}{m} \right)^{0.8} \quad (5.25)$$

hence, since  $k, r, u, m$  are constant in this case:

$$h \propto x^{-0.2} \quad (5.26)$$

where  $x$  will be corrected for hole diameter or slot height as described for the adiabatic effectiveness:

$$h \propto d^{-0.2} \quad (5.27)$$

Hence the correction in  $h$  is:

$$h_{corrected} = h \left( \frac{d_{hyp}}{d} \right)^{-0.2} \quad (5.28)$$

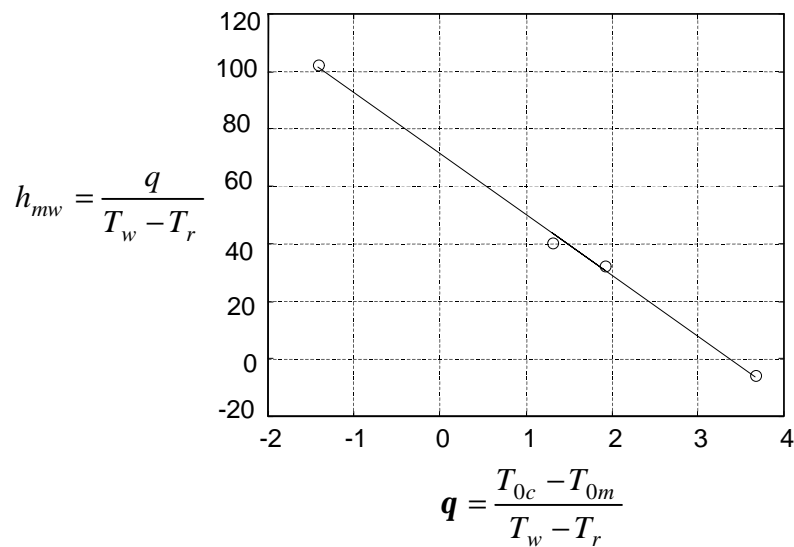
## 5.3 Experimental technique

The purpose of each set of experiments was to obtain a contour map in a parameter of interest, by changing either the heat flux or the coolant temperature and recording the position of the liquid crystal contour in a series of steps. Each recorded point was a steady

state point, so after a change was made the system was allowed to equilibrate before the photograph was taken. This usually took 5-10 minutes. The wind tunnel ran constantly during a series of experiments to collect one full contour map of the surface.

In order to calculate  $h$  and  $\mathbf{h}$  using the technique outlined in section 5.2, it is necessary to obtain a line in  $h_{mw}$  and  $\mathbf{q}$  at each point on the surface. By varying the heat flux supplied to the plate, the map of liquid crystal contours recorded represents  $h_{mw}$  and the dimensionless temperature  $\mathbf{q}$  is constant over the surface. By holding the heat flux constant and varying the dimensionless temperature, an independent set of data can be collected. In this case the contour map represents  $\mathbf{q}$  and the heat flux is constant over the surface. Note that at a measured contour, the value of  $T_w$  is constant at the TLC colour, and it is either the  $h_{mw}$  or  $\mathbf{q}$  which varies at each contour, depending upon whether the change in contour position was caused by a change in heat flux or coolant temperature respectively.

The linearity of  $h_{mw}$  with  $\mathbf{q}$  was tested as part of the *MATLAB* analysis sequence, by plotting  $h_{mw}$  against  $\mathbf{q}$ , for a number of positions on the plate. An example of this output is presented in Figure 5.7.



**Figure 5.7: Typical set of data points and fitted straight line used in *MATLAB* data manipulation**

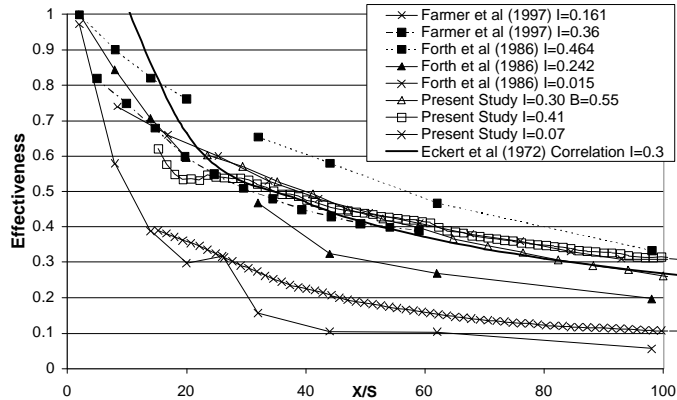
## 5.4 Verification of experimental and analytical technique

### 5.4.1 Comparison with published data

Figures 5.8-5.11 compare the laterally averaged adiabatic effectiveness and heat transfer coefficient measured in the present study with published results. The comparison is made between results at the same actual momentum flux ratio, where the exit momentum flux is defined:

$$\text{Exit Momentum Flux} = \frac{\dot{m}^2}{r} \quad (5.29)$$

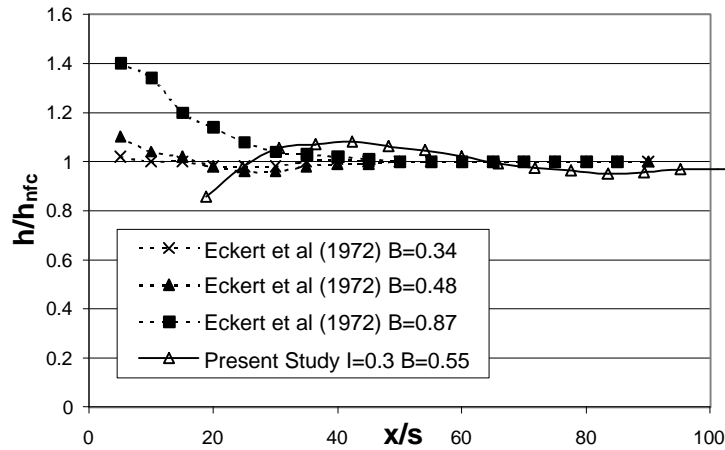
At different momentum flux ratios, the slot film cooling effectiveness in Figure 5.8 compared well with other results. A model of slot cooling presented by Eckert and Drake (1972) and discussed in Chapter 2 also predicts the current results well.



**Figure 5.8: Slot effectiveness compared with published data**

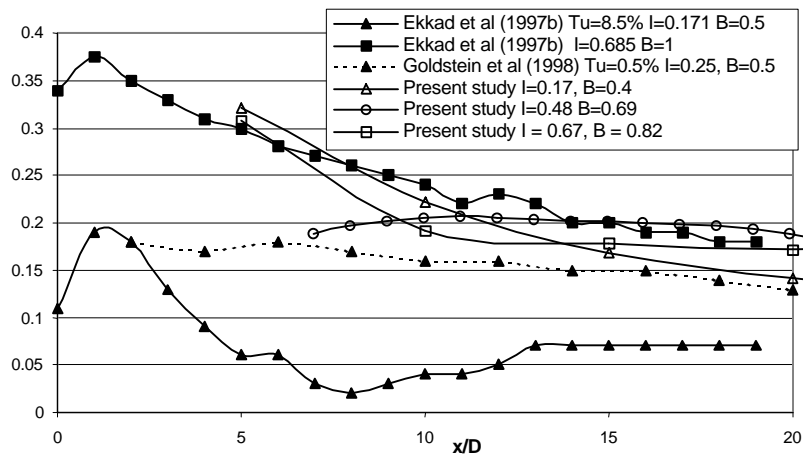
The slot heat transfer coefficient shown in Figure 5.9 demonstrates good agreement downstream of the slot, for the  $I = 0.3$  case, but some difference in the near hole region. This is most likely due to small differences in the hole geometry and experimental conditions. In particular, there is a step change in wall temperature where the heated plate starts, a distance of 15 mm downstream from the hole exit.





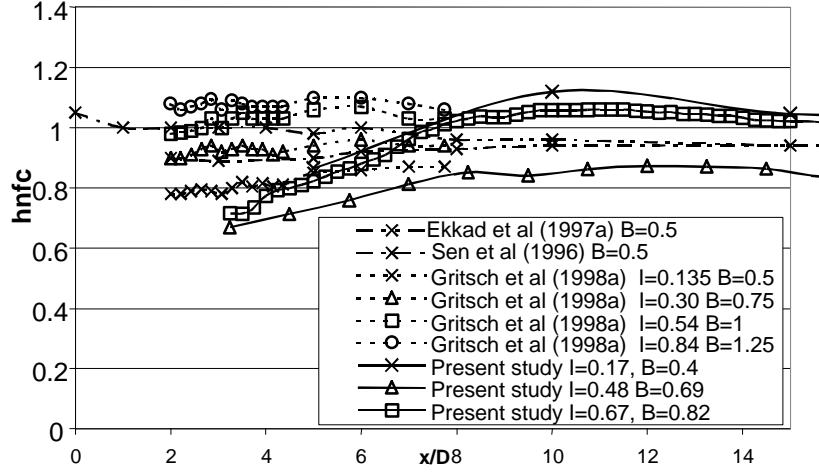
**Figure 5.9: Slot heat transfer coefficient compared with published data**

The comparison of cylindrical hole laterally averaged film cooling effectiveness with published data is shown in Figure 5.10. At higher momentum flux ratios, there is good agreement between the results and those of Ekkad et al (1997b). The very low value of effectiveness measured by Ekkad et al (1997b) at the low blowing rate of  $B = 0.5$ , is due to the high turbulence, the agreement between the present work and that of Goldstein et al (1998) with a similar turbulence level and density ratio is far better.



**Figure 5.10: Cylindrical hole effectiveness compared with published data**

The cylindrical hole heat transfer coefficient shown in Figure 5.11 demonstrates good agreement with published results, particularly towards the downstream region. Differences near the film cooling holes are most likely due to the differences in the experimental apparatus, upstream boundary layer thickness and turbulence intensity.



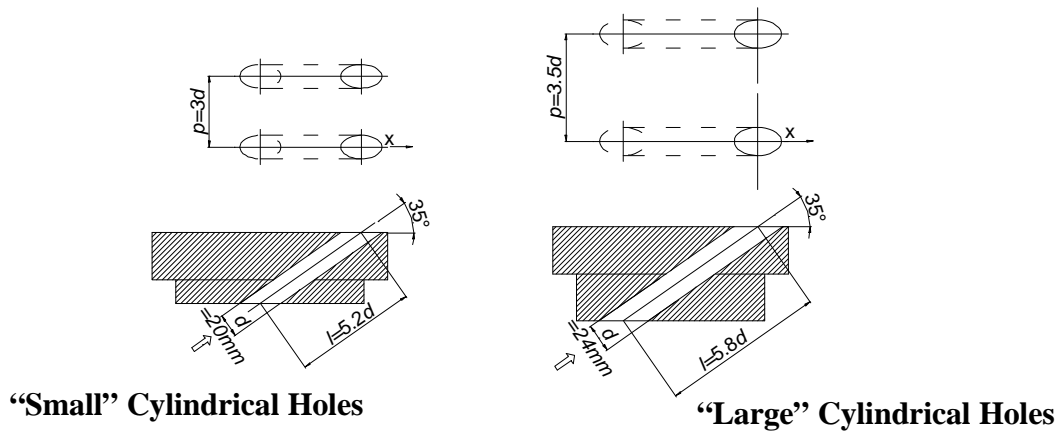
*Figure 5.11: Cylindrical hole heat transfer coefficient compared with published data*

#### 5.4.2 Comparison between large and small cylindrical holes

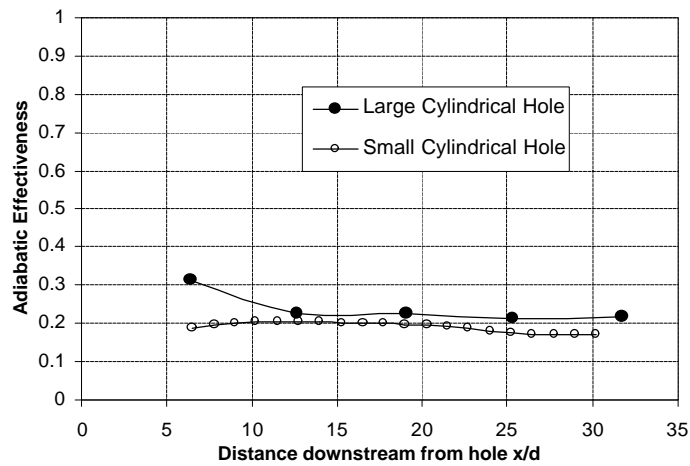
As discussed in Section 5.1, the inlet diameter and pitch of the fan and cylindrical holes are different, although the inlet area per unit width is matched in order to match the theoretical mass flow per unit width. To check that matching the inlet area per unit width was a sufficient condition by which to compare different hole geometries, the following experiment was devised. A hole plate was machined with straight cylindrical holes at the same pitch, diameter and length as the fan shaped holes. These holes are referred to as large cylindrical holes in the following results and are shown Figure 5.12. The laterally averaged adiabatic effectiveness and heat transfer coefficient for this set of holes was measured and compared with the typical (smaller) cylindrical holes used in the comparative results.

Figures 5.13-5.16 indicate that there is little difference between the laterally averaged results for the two arrangements of cylindrical holes, and this result validates the comparison of the defined fan shaped and cylindrical holes used in the present study. The higher adiabatic effectiveness for the large hole, near the hole exit, may be due to the fact that the mainstream speed, and not Reynolds number based on hole diameter was constant.

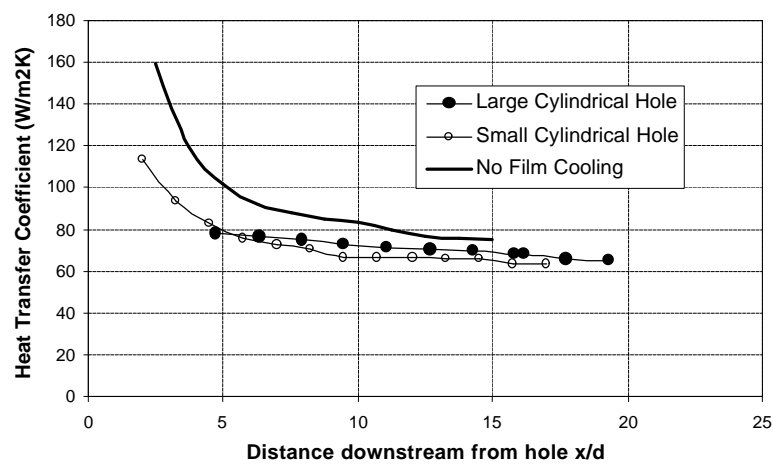
Also, the ratio of boundary layer thickness to hole diameter at injection was only 0.83 for the larger hole compared with 1 for the small hole.



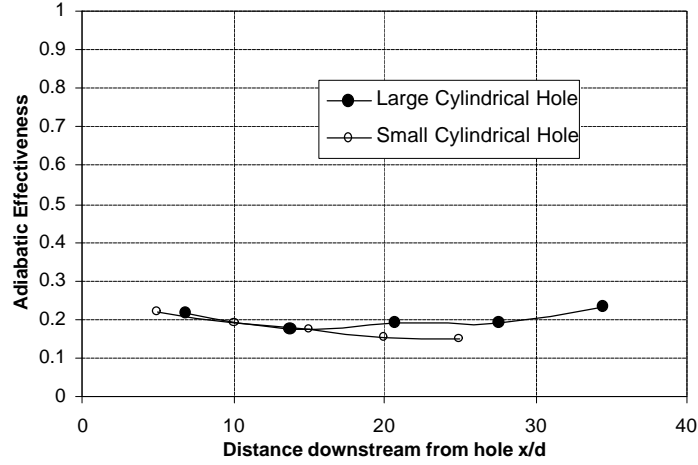
**Figure 5.12: Large and small cylindrical holes**



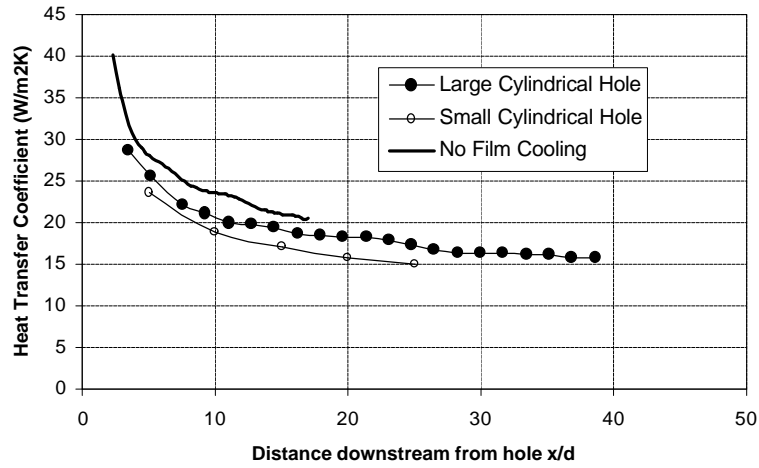
**Figure 5.13: Laterally averaged adiabatic effectiveness comparison between large and small cylindrical holes ( $v_m = 26 \text{ ms}^{-1}$ ,  $I_{ideal} = 1.1$ )**



**Figure 5.14: Laterally averaged heat transfer coefficient comparison between large and small cylindrical holes ( $v_m = 26 \text{ ms}^{-1}$ ,  $I_{ideal} = 1.1$ )**



**Figure 5.15:** Laterally averaged adiabatic effectiveness comparison between large and small cylindrical holes ( $v_m = 5 \text{ ms}^{-1}$ ,  $I_{ideal} = 1.1$ )



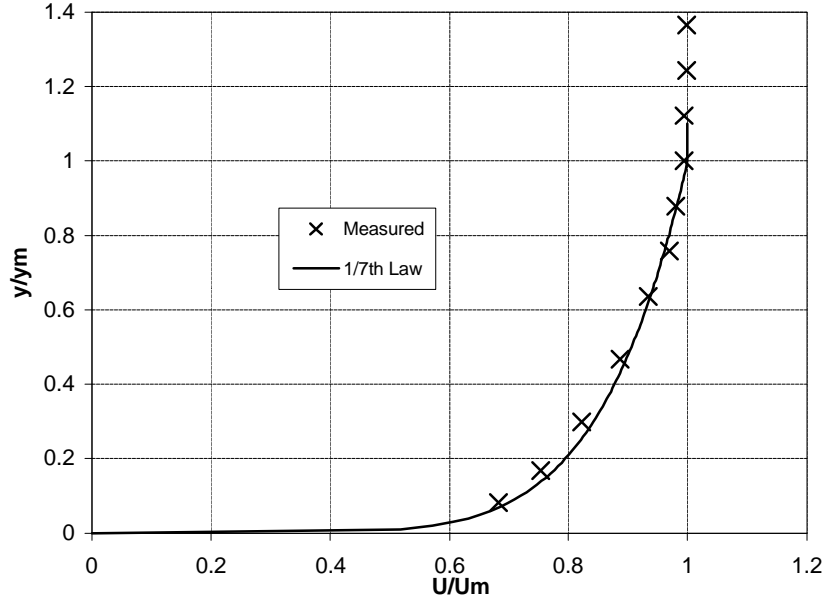
**Figure 5.16:** Laterally averaged heat transfer coefficient comparison between large and small cylindrical holes ( $v_m = 5 \text{ ms}^{-1}$ ,  $I_{ideal} = 1.1$ )

## 5.5 Comparison with analytical solutions

### 5.5.1 Boundary layer traverse

The boundary layer velocity profile was measured a small distance upstream of the film cooling holes to ensure that the boundary layer was fully turbulent and that the thickness of the boundary layer was approximately equal to one cylindrical hole diameter. The measured velocity profile, shown in dimensionless form in Figure 5.17, demonstrates that the boundary layer was indeed fully turbulent at the injection location. The 99% boundary

layer thickness at the measurement location was 17 mm, which corresponds to a thickness of 19.5 mm at the injection location, which is sufficiently close to the required thickness of one cylindrical hole diameter or 20 mm.



**Figure 5.17: Boundary layer velocity profile**

### 5.5.2 Unheated starting length solution

The analytical method and the experimental apparatus were first tested by measuring the heat transfer coefficient for a flat plate with no film cooling and comparing this result with the analytical solution for a flat surface with an unheated starting length in turbulent flow (Kays and Crawford, 1993):

$$St Pr^{0.4} = 0.0287 Re_x^{-0.2} \left[ 1 - \left( \frac{\mathbf{x}}{x} \right)^{9/10} \right]^{-1/9} \quad (5.30)$$

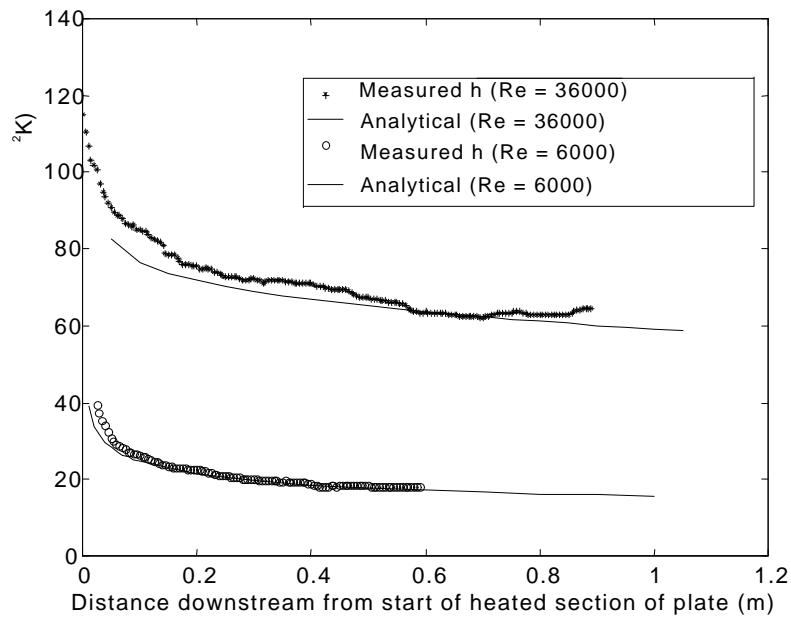
Here,  $\mathbf{x}$  is the unheated distance,  $x$  is the distance from the start of the surface.

In the current work, the upstream, unheated starting length was not a flat plate as assumed by this expression, but the convergent inlet of the wind tunnel, and the first part of the wind tunnel test section. Hence the ‘equivalent’ unheated starting length,  $\mathbf{x}$ , was not the measured distance from the start of the tunnel. The value of  $\mathbf{x}$ , used in this comparison was

the equivalent length of flat plate required to produce the boundary layer thickness of 19.5 mm at the injection location for high velocity flow. The same physical length was then used for the low  $Re$  flow. This was calculated from the expression for the boundary layer thickness (Kays and Crawford, 1993):

$$\frac{d}{x} = 0.37 Re_x^{-0.2} \quad (5.31)$$

The results of the comparison between the measured and predicted heat transfer coefficient distributions are shown in Figure 5.18. This comparison verifies the measurement technique because of the good agreement between the experimental and analytical results within the experimental uncertainty.



**Figure 5.18: Comparison of measured and analytical solution for a flat plate with an unheated starting length**

## 5.6 Experimental results

The use of liquid crystals to measure the wall temperature contours provides a large amount of useful information. Primarily, data is available for the full surface in the camera view. This data provides information about the location of the coolant fluid, the structure

of the jets and the mixing with the mainstream at the surface. In the following figures, contours of heat transfer coefficient and adiabatic effectiveness over the full surface, local spanwise effectiveness at locations downstream from the holes, and laterally averaged heat transfer coefficient, adiabatic effectiveness and net heat flux reduction are presented.

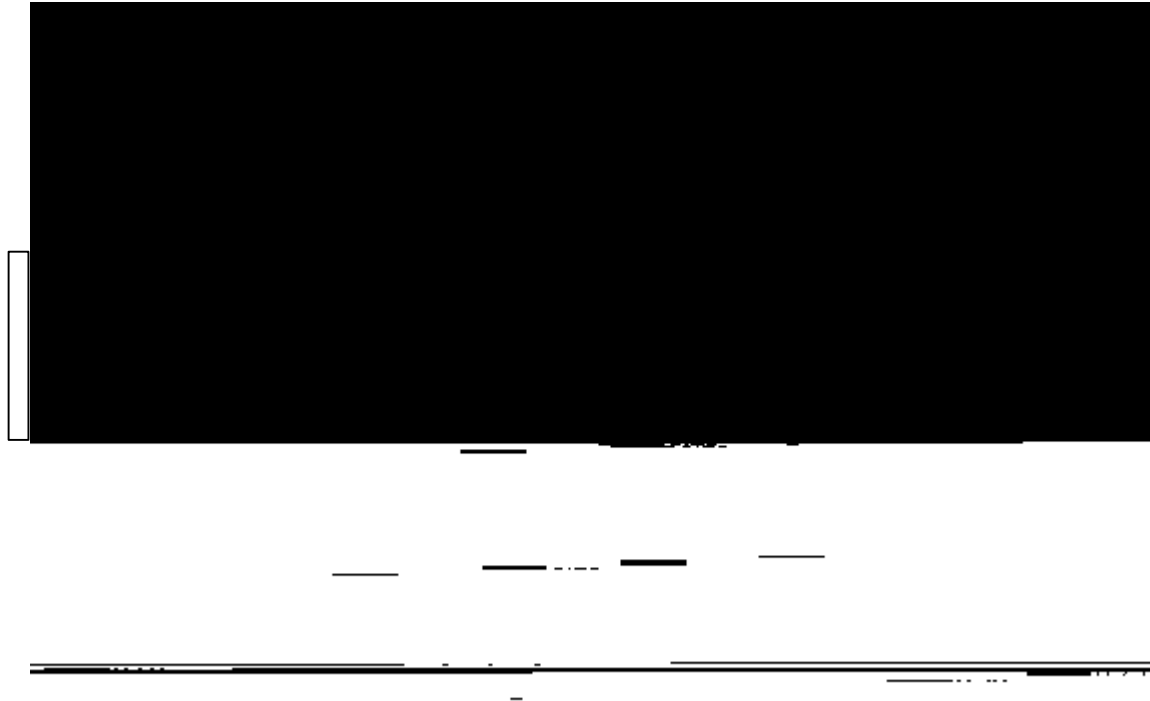
Figures 5.19 – 5.26 present the full surface heat transfer coefficient and adiabatic effectiveness for each hole shape at  $v_m = 26 \text{ ms}^{-1}$  and  $I_{ideal} = 1.5$ . The values of these parameters are compared at later line plots, but there are a number of interesting points to note about these charts.

The slot adiabatic effectiveness contour plot shown in Figure 5.19 demonstrates that there is some edge effect, which is most visible in the slot results, and effects the measurements near the ends of the slot, or the external holes in the case of the cylindrical hole and the *consoles*. For this reason, results presented in later charts are taken from the centre two holes, or central region of the slot. Apart from this, the heat transfer coefficient and adiabatic effectiveness for the slot are relatively uniform across the exit, compared with the *consoles* and discrete holes.

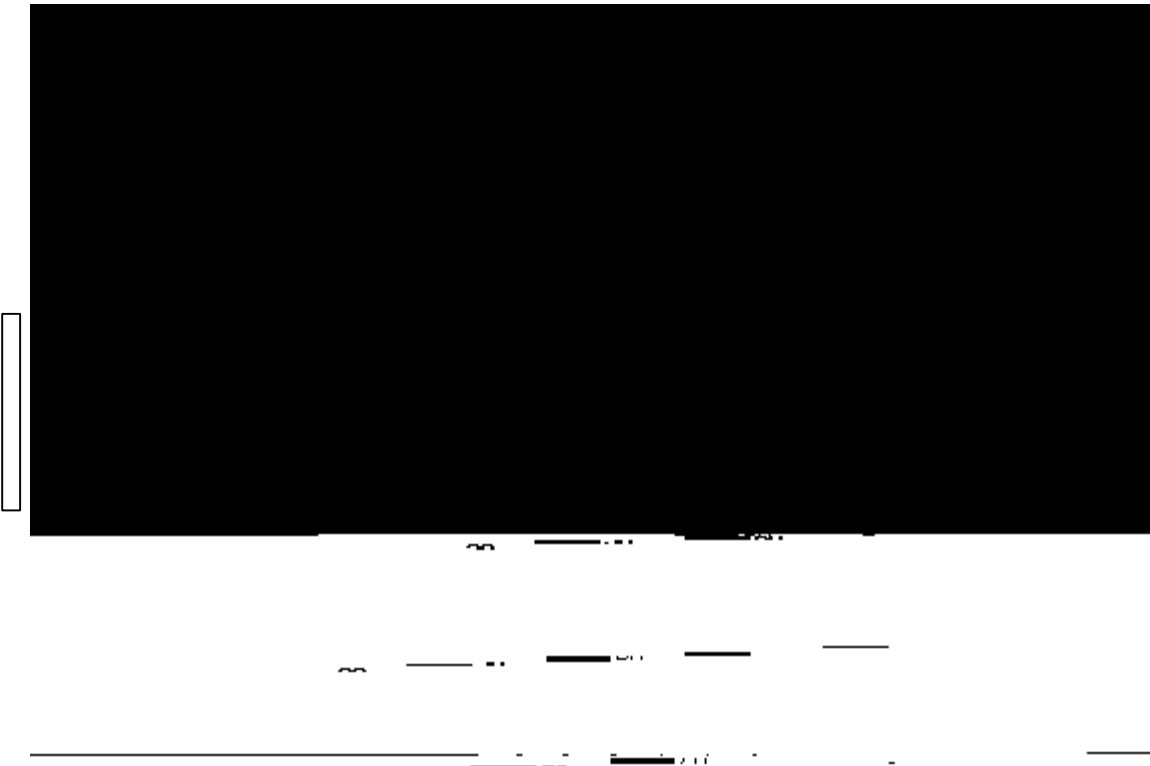
The *console* adiabatic effectiveness in Figure 5.21 and heat transfer coefficient in Figure 5.22 show that the *console* flow is more uniform than discrete holes, but there are distinct peaks in both  $h$  and  $\eta$  downstream of the intersection of two adjacent holes. These peaks in effectiveness and heat transfer coefficient are possibly due to the interaction of vortices between the two *consoles*. This interaction was also present in the results of CFD analysis, discussed in Chapter 9.

The fan shaped hole results in Figures 5.23 and 5.24 demonstrate that the diffusion in the exit does create a good lateral spread of coolant onto the surface, with only small regions near the holes without cooling.

The cylindrical hole results in Figures 5.25 and 5.26 show the contours typical of discrete film cooling holes, with significant regions between the film cooling holes without effective cooling.

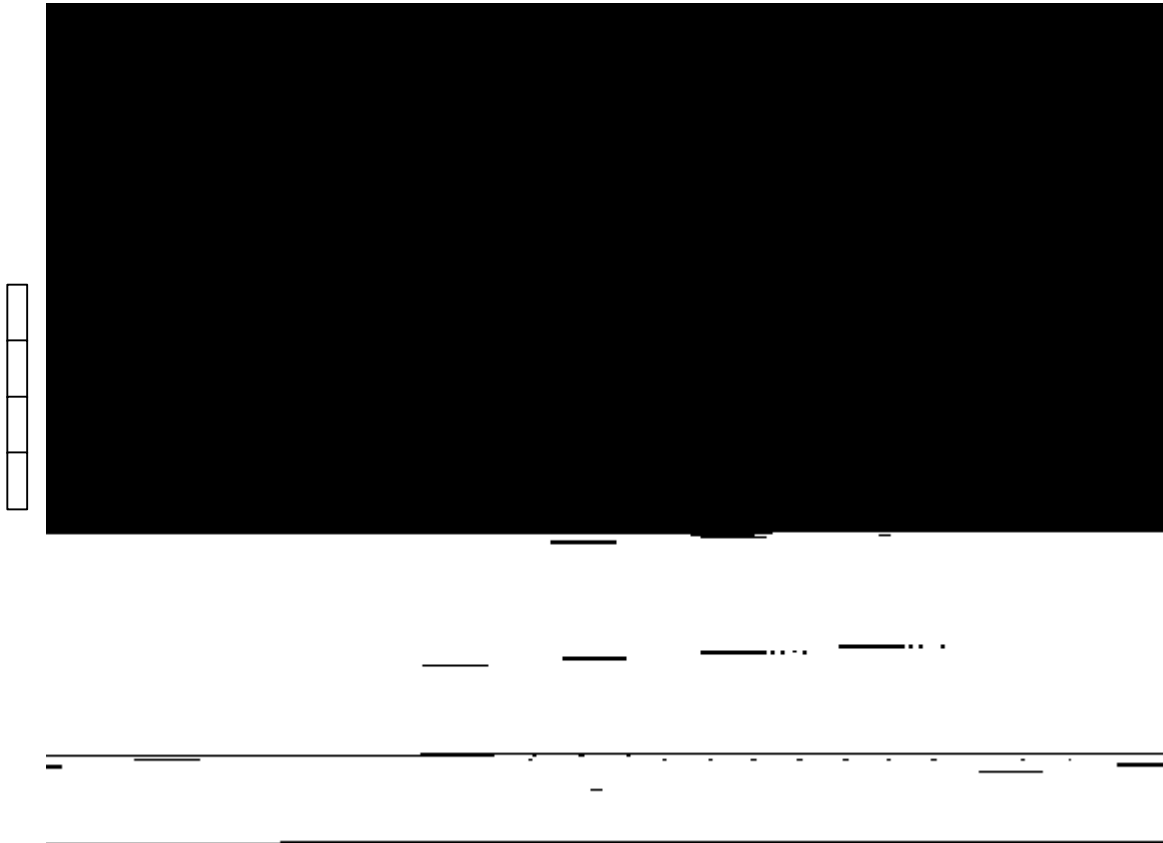


*Figure 5.19 Adiabatic effectiveness contour for slot,  $I_{ideal} = 1.5$ ,  $v_m = 26 \text{ ms}^{-1}$*

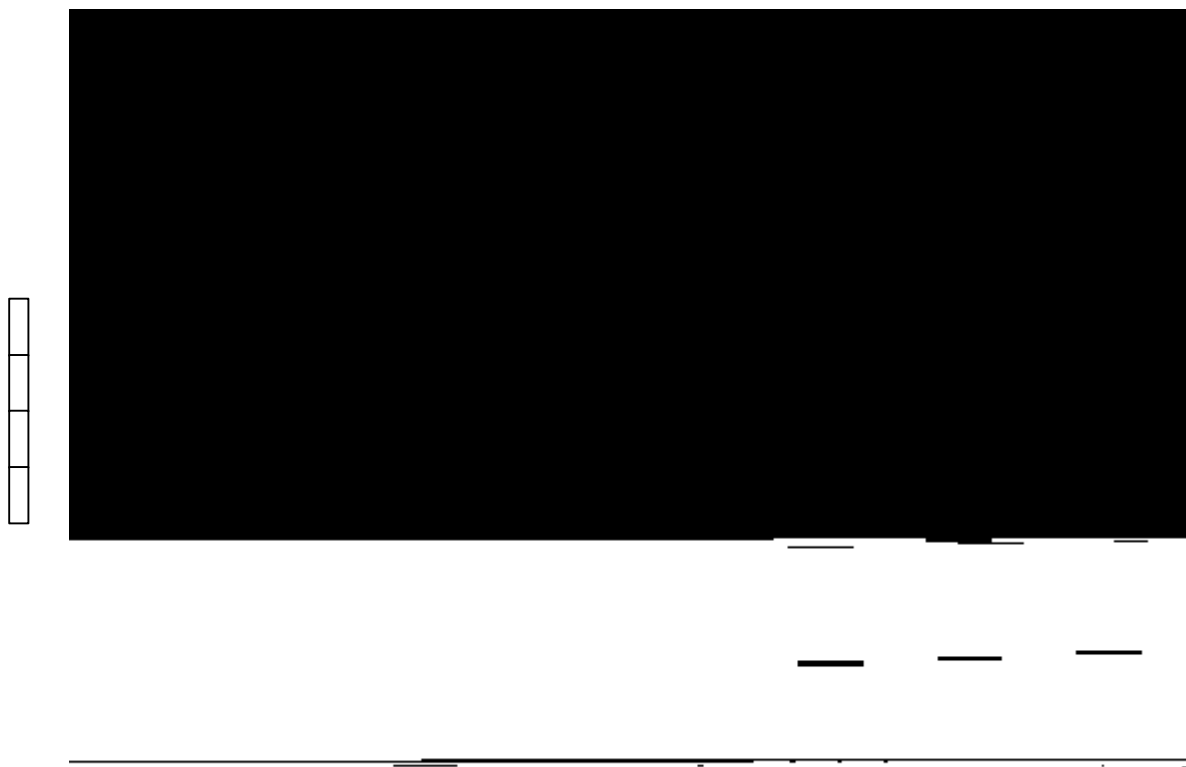


*Figure 5.20: Heat transfer coefficient contour for slot,  $I_{ideal} = 1.5$ ,  $v_m = 26 \text{ ms}^{-1}$*

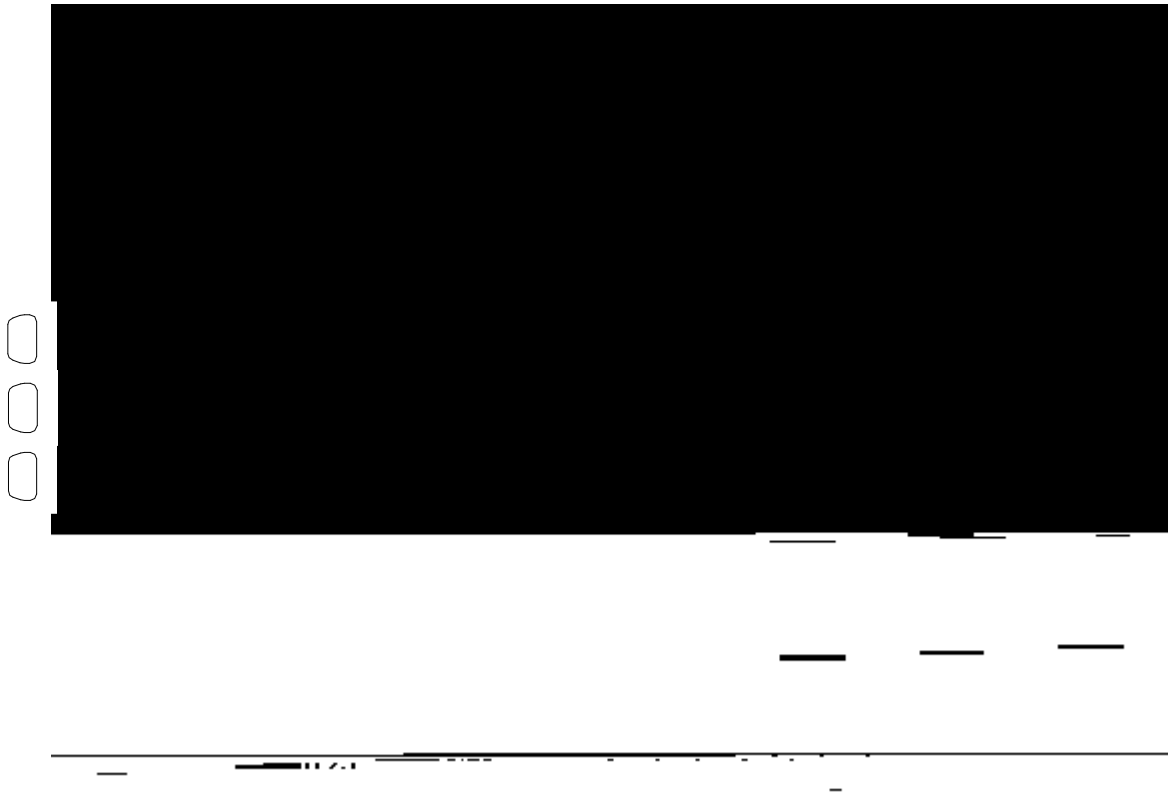




*Figure 5.21: Adiabatic effectiveness contour for console,  $I_{ideal} = 1.5$ ,  $v_m = 26 \text{ ms}^{-1}$*



*Figure 5.22: Heat transfer coefficient contour for console,  $I_{ideal} = 1.5$ ,  $v_m = 26 \text{ ms}^{-1}$*



*Figure 5.23: Adiabatic effectiveness contour for fan-shaped holes,  $I_{ideal} = 1.5$ ,  $v_m = 26$   
 $ms^{-1}$*



*Figure 5.24: Heat transfer coefficient contour for fan-shaped holes,  $I_{ideal} = 1.5$ ,  $v_m = 26$   
 $ms^{-1}$*

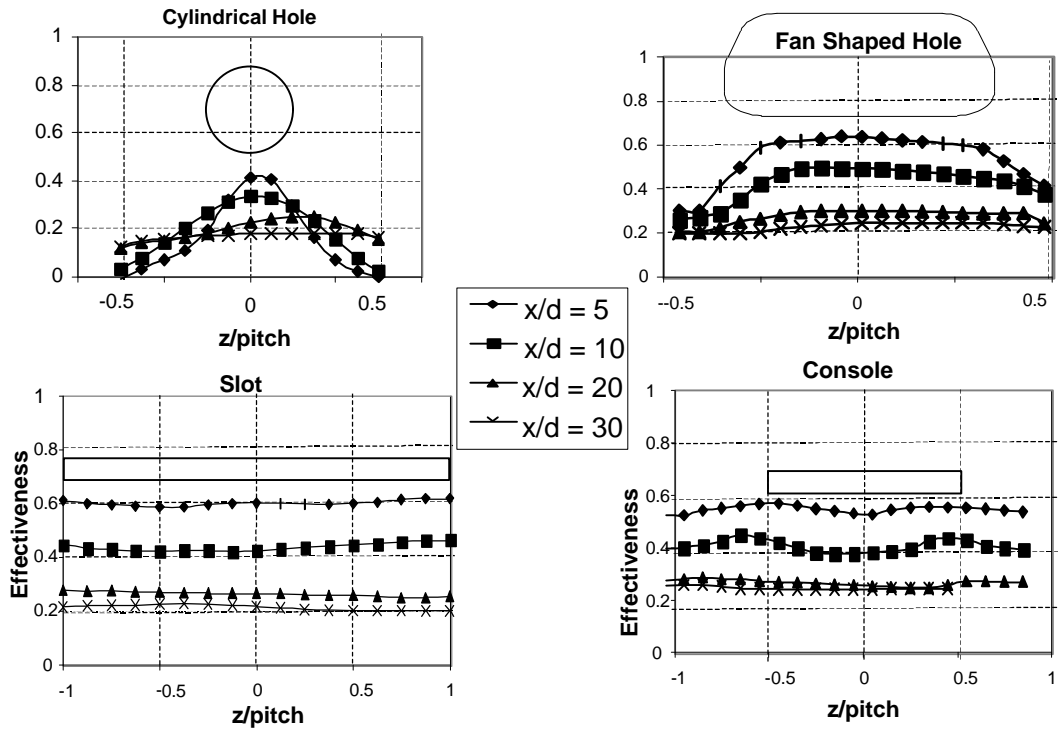


*Figure 5.25: Adiabatic effectiveness contour for cylindrical holes,  $I_{ideal} = 1.5$ ,  $v_m = 26$   $ms^{-1}$*



*Figure 5.26: Heat transfer coefficient contour for cylindrical holes,  $I_{ideal} = 1.5$ ,  $v_m = 26$   $ms^{-1}$*

In Figure 5.27 the adiabatic effectiveness in a lateral direction (across the film cooling holes) is presented at various downstream distances. The results are for  $I_{ideal} = 1.1$  and  $v_m = 26 \text{ ms}^{-1}$  and the size and location of the hole exit are indicated on each graph. The presented results have been averaged over the centre two film cooling holes. For these and the following charts, the parameter of interest is plotted against a dimensionless distance,  $x/d$ . For every hole shape, the parameter  $d$  is the cylindrical hole diameter, to provide consistency of the results, and to present similar charts to previous experimenters. For the *console* and the slot,  $x/s = 4 x/d$ . In the charts of lateral variation in effectiveness and heat transfer coefficient, the lateral dimension  $z$  is scaled by the hole pitch, and the slot result is scaled by the *console* pitch.



**Figure 5.27 Lateral adiabatic effectiveness results ,  $I_{ideal} = 1.1$ ,  $v_m = 26 \text{ ms}^{-1}$**

The cylindrical results show a pronounced peak in effectiveness,  $h$ , downstream of the hole centre. The peak in  $h$  downstream of the fan shaped hole is far broader, and the peak value is similar to the slot and *console*  $h$  and significantly higher than the cylindrical hole peak  $h$ . Downstream of the *console*,  $h$  is relatively uniform, except for small increases

downstream of the location where two *consoles* join previously discussed for the contour plots of *console* parameters.

The laterally averaged  $h$  results at each momentum flux ratio at the high  $Re_d$  presented in Figures 5.28 - 5.30 have been averaged using the technique outlined in Section 5.2.2. For all blowing rates,  $h$  reaches the same value far downstream within the range of the experimental uncertainty. At the design condition of  $I = 1.1$ , the slot demonstrates the best performance. The *console* and the fan demonstrate very similar effectiveness, with the *console* slightly higher. The cylindrical holes show a very low value of effectiveness with little variation in averaged effectiveness over the entire measurement region. For the lower momentum ratio  $I = 0.5$ , the fan effectiveness is only slightly lower than the  $I = 1.1$  case, while the other holes show a significantly lower effectiveness. The *console* effectiveness is higher than the slot and the slot is similar to the cylindrical hole case. The cylindrical hole effectiveness is higher near the holes for this momentum flux ratio, compared with the design value. This is most likely due to the reduced penetration of the jets into the mainstream flow, which reduces the amount of mixing in this region. Further downstream  $h$  is lower, similarly to the other hole shapes, because the concentration of coolant is lower than for the design case. For a momentum flux ratio,  $I_{ideal} = 1.5$ , the fan-shaped holes, *console* and slot all demonstrate very similar levels of  $h$ . This may be because with the higher amount of coolant ejected from the holes, in each case a similar, closed film is produced and the concentration of coolant over the surface is similar for each case from a short distance downstream of the holes. This is shown in the contour plots Figures 5.19, 5.21 and 5.23. The level of  $h$  for these holes is also higher than in the previous levels. The cylindrical holes show a lower  $h$  although the other hole shapes appear to reduce to the cylindrical value of  $h$  far downstream of the holes.

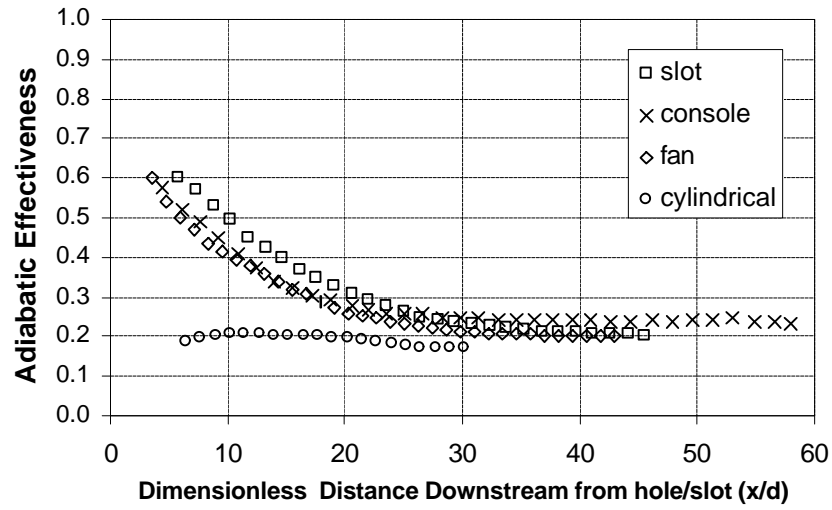


Figure 5.28 Laterally averaged adiabatic effectiveness  $I_{ideal} = 1.1$ ,  $v_m = 26 \text{ ms}^{-1}$

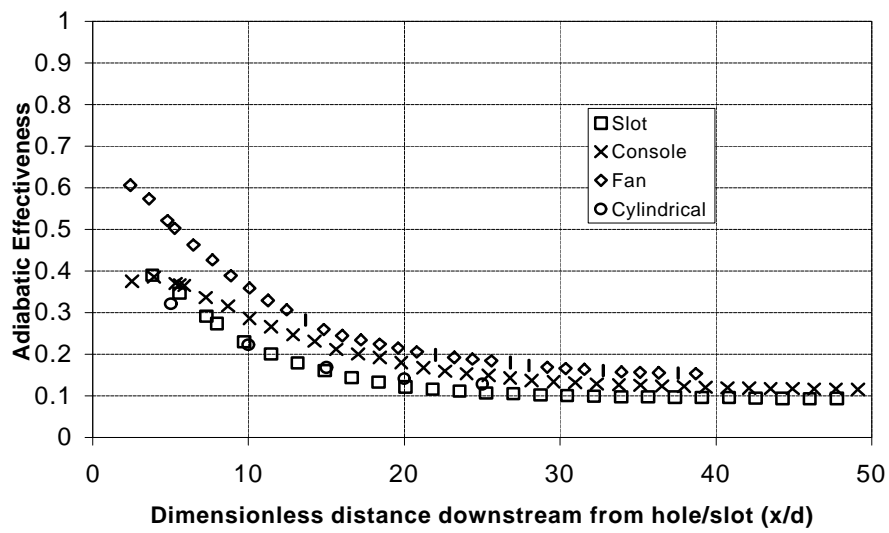
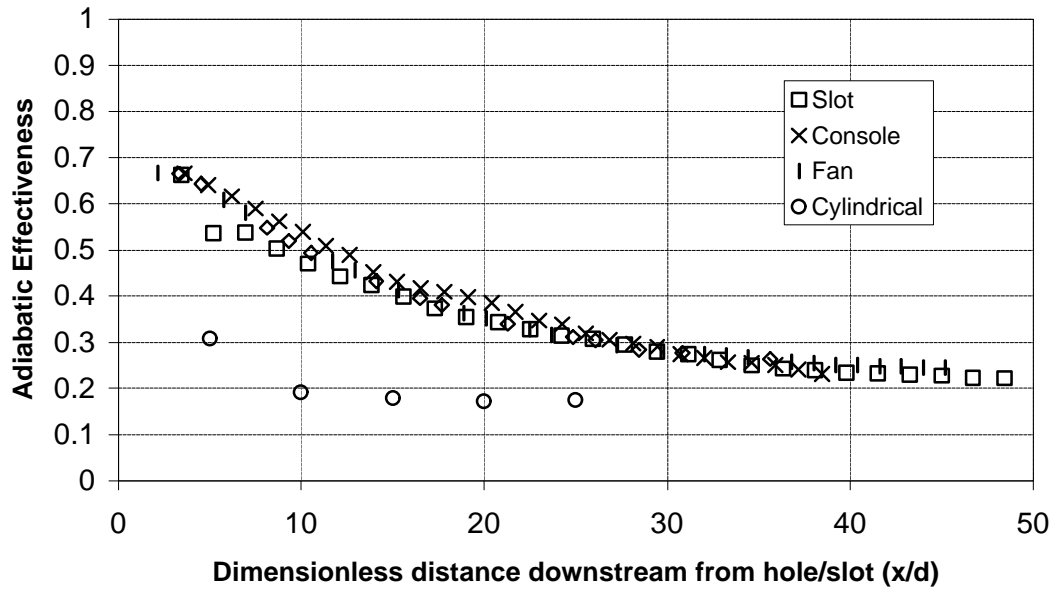


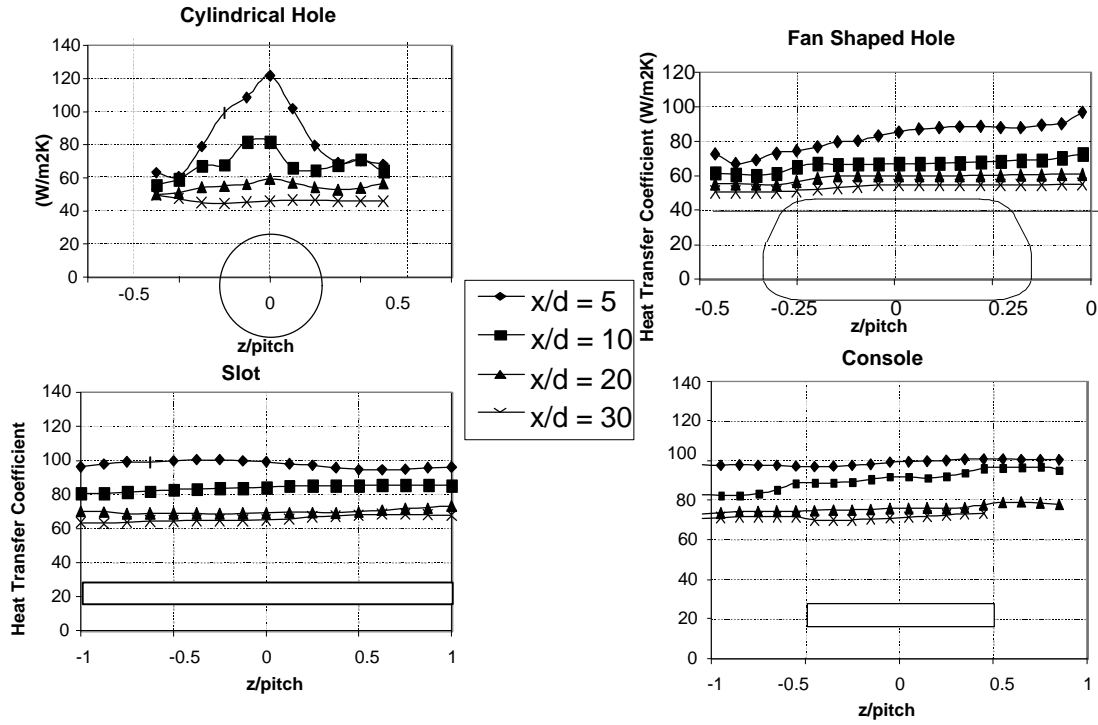
Figure 5.29 Laterally averaged adiabatic effectiveness  $I_{ideal} = 0.5$ ,  $v_m = 26 \text{ ms}^{-1}$



**Figure 5.30 Laterally averaged adiabatic effectiveness  $I_{ideal} = 1.5$ ,  $v_m = 26 \text{ ms}^{-1}$**

Figure 5.31 presents the lateral heat transfer coefficient,  $h$ , at the same locations as the lateral adiabatic effectiveness results that have been discussed. The  $h$  distributions are similar for the slot and *console* and uniform across the holes, although the *console* level of  $h$  is slightly higher at increasing distance from the film cooling hole. The level of  $h$  for the fan shaped hole is also relatively uniform across the hole exit, and the level is consistently lower than the slot or *console* level. This result indicates that the low momentum coolant distributed onto the surface by the fan shaped hole is producing a considerable thickening of the boundary layer, which reduces the gradient of the thermal boundary layer and hence reduces  $h$ . The slot and *console* flows with coolant of similar momentum to the mainstream, do not significantly change the thermal boundary layer compared with a flat plate with no film cooling and the laterally averaged  $h$  is not changed compared with the no film cooling value as indicated by the laterally averaged results in Figure 5.32. The heat transfer coefficient data in Figure 5.31 for the cylindrical hole shows a strong peak in  $h$  downstream of the hole centre which is 20% higher than the slot level, however  $h$  is

significantly reduced between the cylindrical holes, and the laterally averaged  $h$  shown in Figure 5.32 is comparable with the fan level, and lower than the slot and *console* levels.



**Figure 5.31** Lateral heat transfer coefficient results,  $I_{ideal} = 1.1$ ,  $v_m = 26 \text{ ms}^{-1}$

The variation in  $h$  with  $I_{ideal}$  in Figures 5.32 – 5.34 highlights some interesting features of the flow from the different hole shapes. At  $I_{ideal} = 1.1$  and 1.5, the slot and *console* show similar levels of  $h$  which is higher than the level without film cooling. At the higher  $I$  the slot has higher  $h$ . At the lower value of  $I_{ideal} = 0.5$ , the *console* is still slightly higher than the flat plate results, but the slot is significantly lower. The fan shaped hole is consistently lower than the result with no film cooling. This is most likely due to the fact that the fan hole provides low momentum flow to the surface, which thickens the boundary layer and hence reduces the thermal gradient and  $h$ . The fan heat transfer coefficient increases with momentum flux ratio, indicating that high momentum fluid causes an increase in  $h$ . At design  $I_{ideal} = 1.1$  and high  $I_{ideal} = 1.5$ , the cylindrical holes also show a lower  $h$  than the slot and *console*, but at low  $I_{ideal} = 0.5$ , the value is just above the value without film cooling. At this low momentum flux ratio, the effectiveness of the cylindrical holes is also



higher than other cases (Figure 5.29) and it was suggested that this might be due to reduced penetration of the jets into the mainstream flow. The effect of this on  $h$  may be that the boundary layer is not thickened as it is for the higher momentum flux cases, and  $h$  is hence increased.

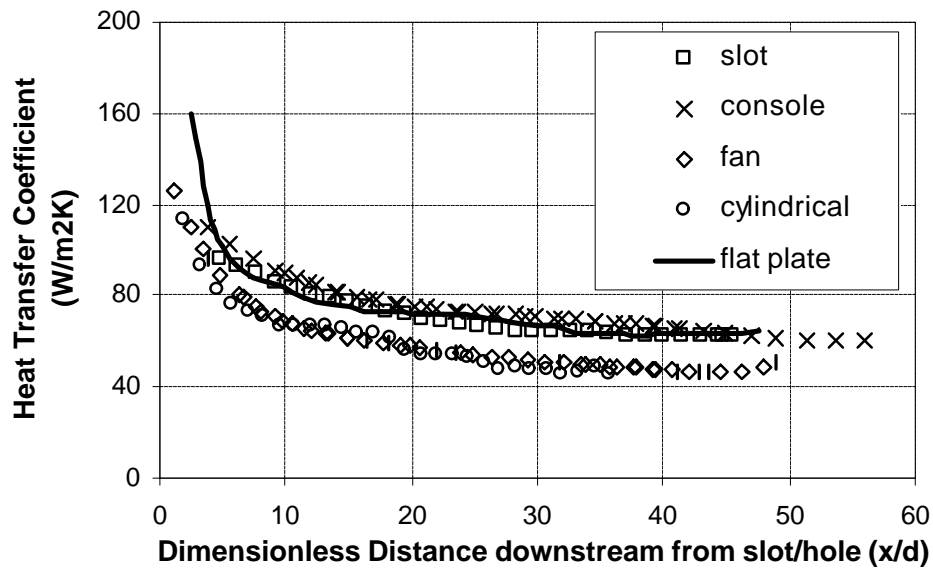


Figure 5.32 Laterally averaged heat transfer coefficient  $I_{ideal} = 1.1$ ,  $v_m = 26 \text{ ms}^{-1}$

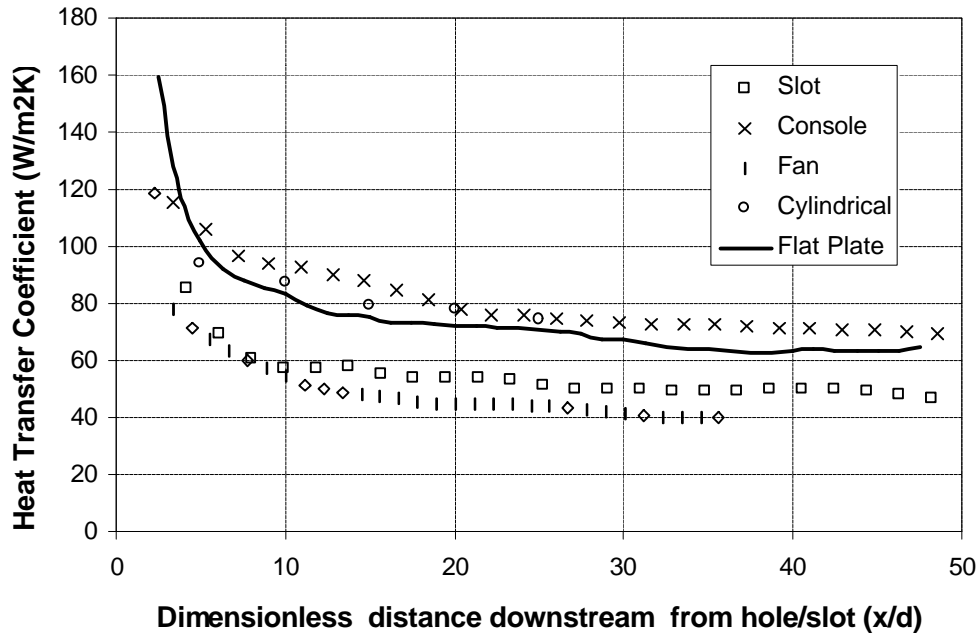
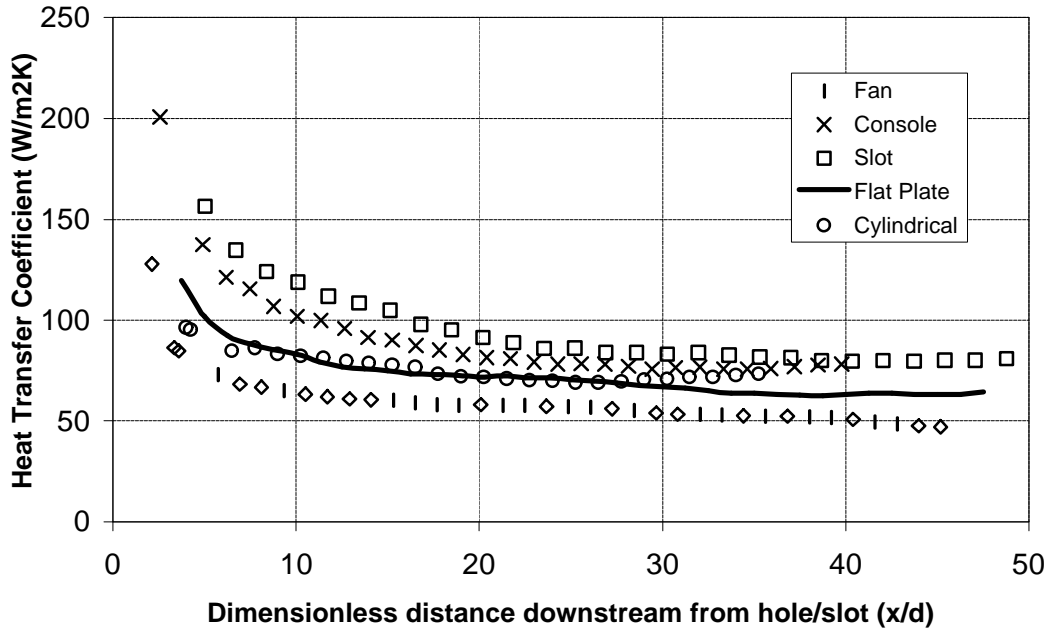


Figure 5.33 Laterally averaged heat transfer coefficient,  $I_{ideal} = 0.5$ ,  $v_m = 26 \text{ ms}^{-1}$



**Figure 5.34 Laterally averaged heat transfer coefficient  $I_{ideal} = 1.5$ ,  $v_m = 26 \text{ ms}^{-1}$**

These measurements were repeated at the low  $v_m = 5 \text{ ms}^{-1}$ , but there was a large error in the pressure measurements and it was not possible to correctly set the pressure difference ratio. This caused repeatability problems in the experiments and the data collected was not considered to be reliable.

The net heat flux reduction (*NHFR*) is shown in Figure 5.35 to Figure 5.37 for  $v_m = 26 \text{ ms}^{-1}$  and  $I = 1.1, 0.5$  and  $1.5$ . The *NHFR* is a measure of the reduction in heat flux compared with the case with no film cooling, and is a useful parameter for the comparison of different film cooling holes by taking into account both  $h$  and  $\dot{h}$ . It should be noted that a positive value of *NHFR* indicates lower heat flux from the surface than without film cooling, and a larger value of *NHFR* indicates a greater reduction in heat flux to the surface. The definition of *NHFR* is (from equation 2.6):

$$NHFR = 1 - \frac{h}{h_{nfc}}(1 - hq)$$

The value of dimensionless temperature used to calculate the *NHFR* is  $q = 1.46$ , corresponding to typical engine representative conditions of  $T_{oc} = 880\text{K}$ ,  $T_w = 1200\text{K}$ , and

$T_{om} = 1900\text{K}$ . To make the *NHFR* correctly engine representative, the heat transfer coefficient and adiabatic effectiveness values measured using cold air should be corrected using the method outlined by Jones (1999) and discussed in Chapter 4, from the molecular properties of cold air compared with the properties of air at engine temperatures. However, when this correction was applied to the data, there was less than 0.5% difference in the level of *NHFR*, so the effect of this correction was considered to be negligible.

At the design condition of  $I_{ideal} = 1.1$  shown in Figure 5.35, and near the film cooling hole, the slot shows the best performance, and the fan and *console* are lower but have a similar value. The cylindrical holes have considerably lower *NHFR*. Further downstream, the cylindrical and fan shaped holes exhibit a higher value of *NHFR*, and the slot and *console* are at the same value. The main reason for this difference is the lower value of  $h$  for the fan and cylindrical holes at the downstream region of the flat plate shown in Figure 5.32.

At the lower ideal momentum flux ratio of  $I_{ideal} = 0.5$  (Figure 5.36), the fan shaped holes exhibit the best performance, followed by the slot, *console* and finally the cylindrical holes. The poor performance of the *console* at this condition is due to the high heat transfer coefficient measured, and the similarity of adiabatic effectiveness to the cylindrical hole level.

At the higher ideal momentum flux ratio of  $I_{ideal} = 1.5$  (Figure 5.37), the *console* exhibits a similar level of *NHFR* to the fan shaped holes near the film cooling holes, but the *console* level reduces more rapidly with downstream distance. The slot shows a lower level of *NHFR* than the *console*, but approaches the *console* level in the downstream region, and the cylindrical holes again demonstrate the lowest level of *NHFR*. Here the high value of  $h$  again penalises the *console* performance.

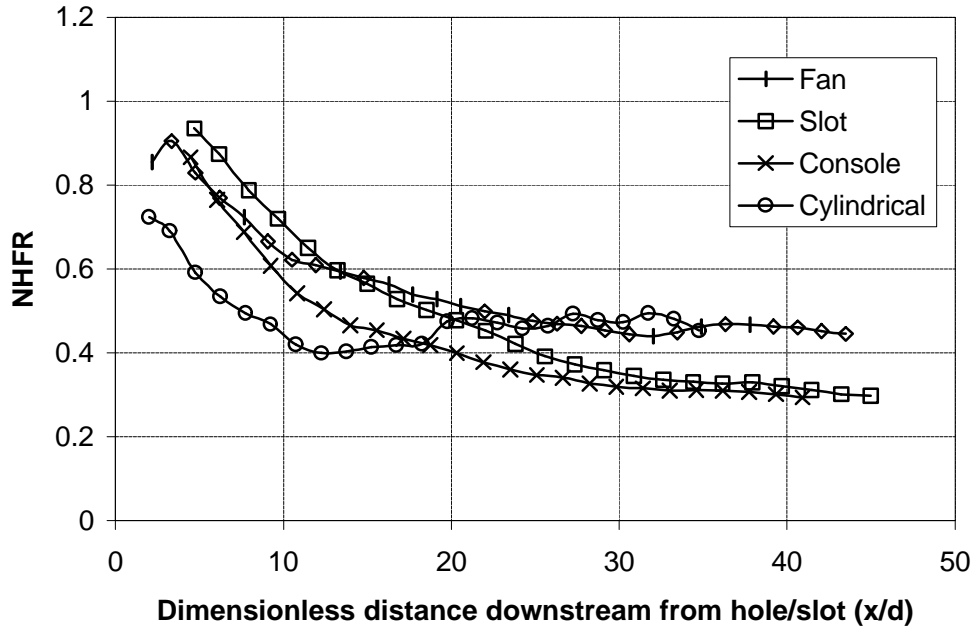


Figure 5.35 Laterally averaged net heat flux reduction  $I_{\text{ideal}} = 1.1$ ,  $v_m = 26 \text{ ms}^{-1}$

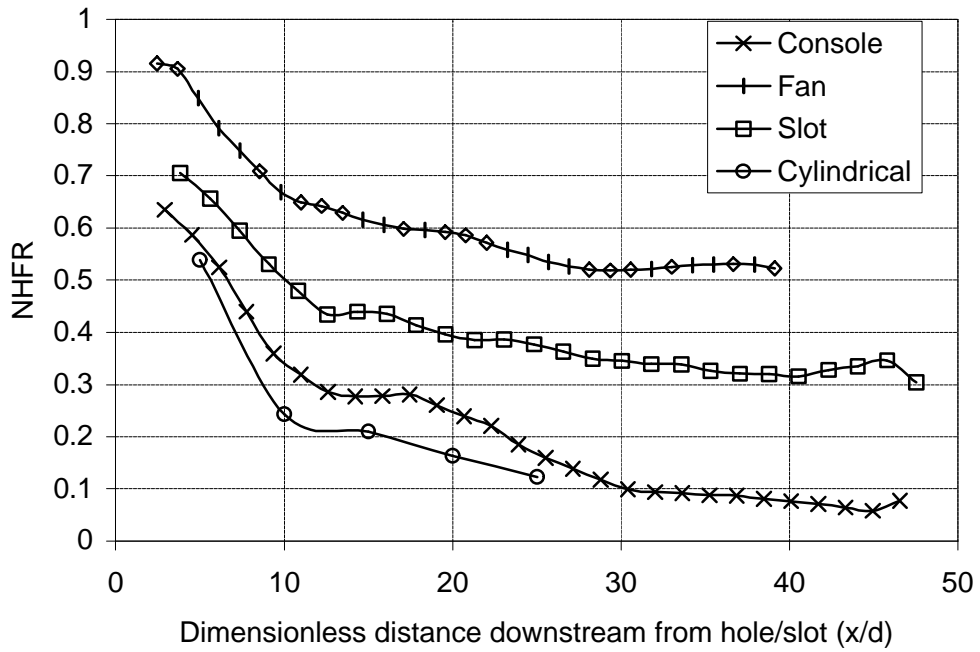
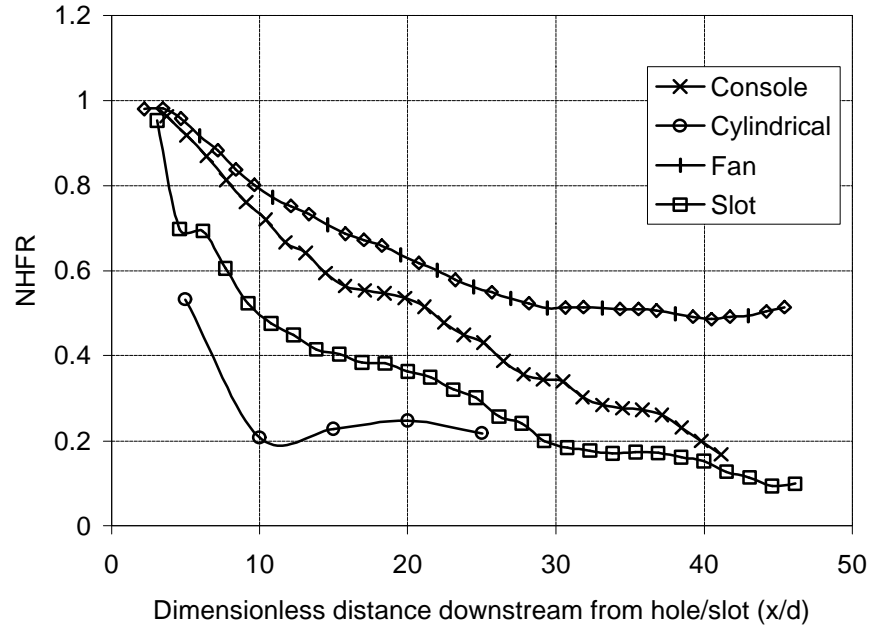


Figure 5.36 Laterally averaged net heat flux reduction  $I_{\text{ideal}} = 0.5$ ,  $v_m = 26 \text{ ms}^{-1}$



**Figure 5.37 Laterally averaged net heat flux reduction  $I_{ideal} = 1.5$ ,  $v_m = 26 \text{ ms}^{-1}$**

### 5.7 Discharge coefficient

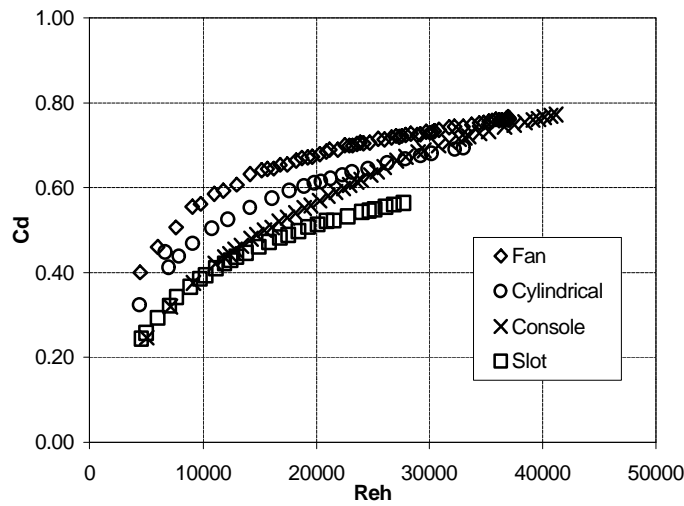
For flow through film cooling holes, Rowbury (1998), defined the discharge coefficient for incompressible flow to be:

$$C_D = \frac{\dot{m}_{actual}}{\dot{m}_{ideal}} = \frac{\dot{m}_{actual}}{A \sqrt{2 \Delta P_c} r_c} \quad (5.32)$$

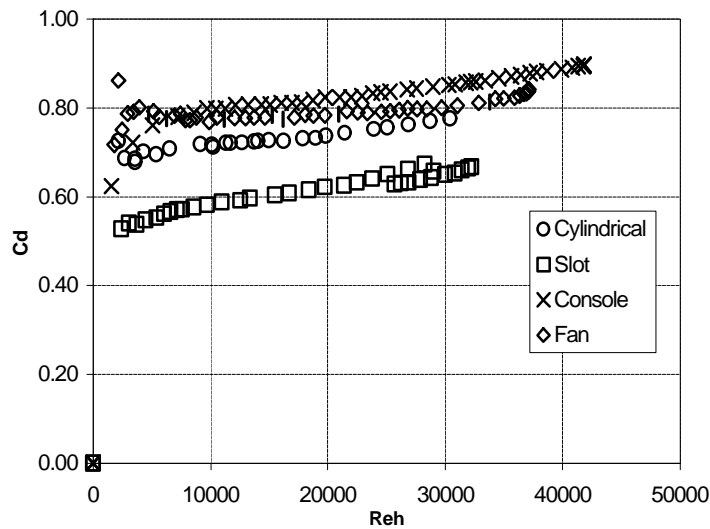
where the pressure difference  $\Delta P_c = P_{0c} - P_m$  is the difference between total and static pressure across the holes.

Figure 5.38 shows the discharge coefficient measured with mainstream crossflow with a velocity of  $26 \text{ ms}^{-1}$ , which, for the cylindrical holes, corresponds to the Reynolds number at row 12 of the engine NGV. Figure 5.39 shows discharge coefficient with no crossflow, and these results are compared with the fan and cylindrical hole discharge coefficients measured by Rowbury (1998) in Figures 5.40 and 5.41. The results for no crossflow agree with those measured by Rowbury, however the results with crossflow are 10% lower than the Rowbury results. The Rowbury results are for holes inclined at  $40^\circ$ , whilst the holes in

the present work are inclined at  $35^\circ$ . The relationship between the  $d$  coefficients developed by Rowbury et al (2000) as a predictive technique to correct the hole discharge coefficients for changes in hole inclination angle  $f$  depend on  $\sin f$ . The reduction in the correction  $d$  due to the change in hole inclination from  $35^\circ$  to  $40^\circ$  is 24%, and the effect of this on  $C_D$  is a reduction of 5%. This, at least in part, explains that there can be expected to be a significant change in  $C_D$  with crossflow, with change in hole inclination. In Figures 5.38 - 5.41,  $Re_h$  is the Reynolds number based on the velocity and flow properties at the hole throat or exit, and the cylindrical hole diameter.

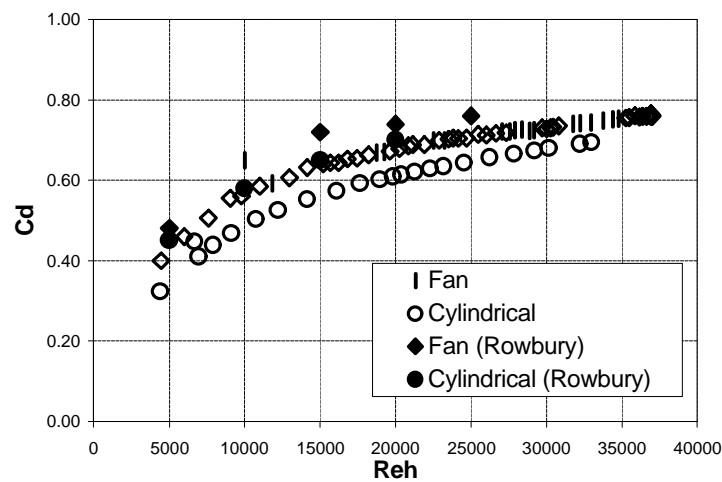


**Figure 5.38 Discharge coefficient with crossflow,  $v_m = 26 \text{ ms}^{-1}$**

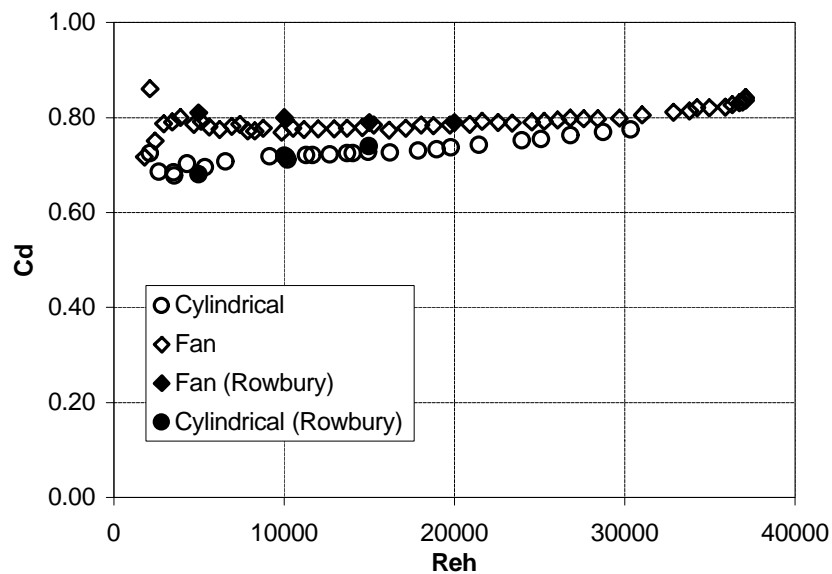


**Figure 5.39 Discharge coefficient with no crossflow**

In Figure 5.38, the most interesting result is the variation of discharge coefficient of the *console*. It would appear that at low flow rates, the discharge coefficient is at a similarly low level to the slot, but as the flow rate increases the discharge coefficient becomes more typical of discrete fan-shaped or cylindrical holes. The discharge coefficient of the *console* without crossflow (Figure 5.39) shows that the *console* has the highest discharge coefficient. This suggests that the losses incurred by the flow inside the hole are indeed lower than the other hole shapes, due to the acceleration of the flow through the hole.



**Figure 5.40:** Comparison of measured discharge coefficients with results from Rowbury (1998): discharge coefficient with crossflow



**Figure 5.41:** Comparison of measured discharge coefficients with results from Rowbury (1998): discharge coefficient with no crossflow

## 5.8 Uncertainty analysis

The uncertainty in the measurements of heat transfer coefficient and adiabatic effectiveness were estimated by first analysing the sources of error and the contribution these made to the heat transfer coefficient based on wall and recovery temperatures,  $h_{mw}$  and the dimensionless temperature,  $q$ . The error based on 99% confidence level is 6% and 5% for these parameters respectively. This error was due to  $\pm 0.2$  K error on thermocouples and  $\pm 3 \text{ Wm}^{-2}$  error on heat flux measurement corresponding to 1% and 2% measurement error on typical values for both of these measurements. The error contribution from the different sources was added using the square root of the sum of the squares. The calculated error was used to vary the inputs to the line fitting routine, to measure the extent of these two errors on the intercepts used to measure  $h$  and  $h$ . The error in these parameters was then 8% and 7% respectively. This data is summarised in Table 5.3. It should be emphasised that the repeatability of the experiments was high, and both  $h$  and  $h$  were repeated months later to within 2% of the original measurement.

The source of error that was less easy to quantify was the error due to differences in pressure ratios and mass flow for the heat transfer measurements. At high mainstream speed, the error in mass flow and pressure ratio was 0.8% and 0.9 % respectively, and this was considered negligible compared with the error contribution from thermocouples and heat flux measurement. At low mainstream speed, however, the error in mass flow rate and pressure ratios were 14% and 30% respectively, based on 95% confidence level. This produced a 22% error in discharge coefficient, compared with 0.9% at high mainstream speed. For this reason, the discharge coefficient measurement was not considered to be sufficiently accurate and the heat transfer measurements at low mainstream speed are not considered to be reliable.



Source of error	Magnitude	Percentage error
Temperature	$\pm 0.2$ K	1%
Heat flux	$\pm 3$ Wm <sup>-2</sup>	2%
$h_{mw}$		6%
$q$		5%
$h$ (from curve fit)		8%
$h$ (from curve fit)		7%

**Table 5.3: Summary of uncertainty analysis**

## 5.9 Conclusions

A set of comparative heat transfer experiments has been performed at low-speed, incompressible flow conditions over a constant heat flux flat plate. The purpose of the experiments was to compare the performance of the *console* with conventional film cooling hole shapes for which there is data widely available in the literature. The hole shapes compared were fan-shaped holes, cylindrical holes and a slot. The holes were compared on the basis of equal coolant massflow per unit width.

An analytical technique has been developed to process the full surface data collected using liquid crystals at steady state conditions in order to obtain values of heat transfer coefficient and adiabatic effectiveness at all points on the surface of the plate.

The *console* has been shown to provide relatively uniform cooling compared to discrete holes. The only variation in effectiveness in a spanwise direction is enhanced cooling between *consoles* due to interaction between vortices downstream of the location where adjacent *consoles* join.

The *console* level of  $h$  at design conditions of  $v_m = 26$  ms<sup>-1</sup> and  $I = 1.1$ , is slightly lower than the slot  $h$  and equal to the fan shaped hole  $h$ . The *console*  $h$  at design conditions and higher and lower momentum flux ratios is significantly higher than the level for fan shaped holes, and equal to or higher than  $h$  with no film cooling. This has been explained by the difference in momentum of the coolant film spread onto the surface for these film

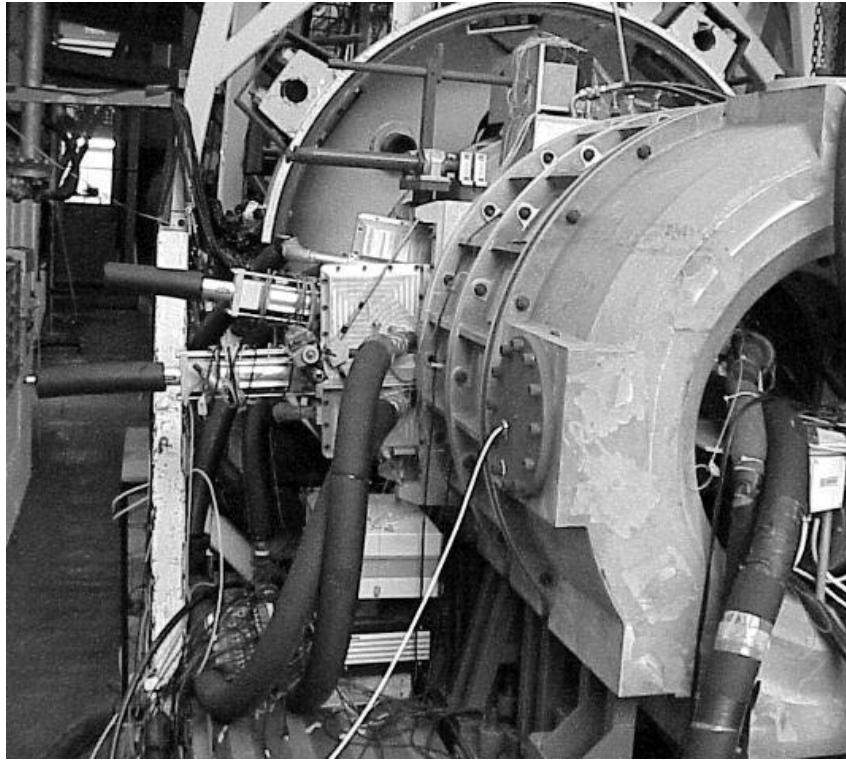
cooling holes. The fan has low momentum, decelerating coolant flow, which tends to thicken the boundary layer, reducing the thermal gradient from the wall to the mainstream and hence reducing  $h$ . In contrast, the *console* coolant flow is accelerating and has higher momentum, which produces a thin boundary layer, similar to the boundary layer that would have been present in the absence of film cooling. Hence, although the *console* effectiveness is high, the net heat flux reduction, which combines the heat transfer and adiabatic effectiveness measurements, is lower for the *console* than the fan shaped hole at all levels of ideal momentum flux ratio. The *console* performance remains higher than the cylindrical holes for all conditions and typically exhibits similar behaviour to the slot.

In summary, the low-speed heat transfer experiments have demonstrated that the *console* provides uniform cooling compared with discrete holes, and the heat flux from a surface is reduced when cooled by *consoles* compared with no film cooling. The *console* exhibits better performance than discrete cylindrical holes and similar performance to a slot, but the net heat flux reduction is higher for fan shaped holes. These promising results confirmed that the *console* demonstrated many of the benefits expected from the design, and justified both further experiments at engine representative conditions on a nozzle guide vane and experiments to measure *console* aerodynamic efficiency.

## Chapter 6

# Heat Transfer Experiments at Engine Representative Conditions

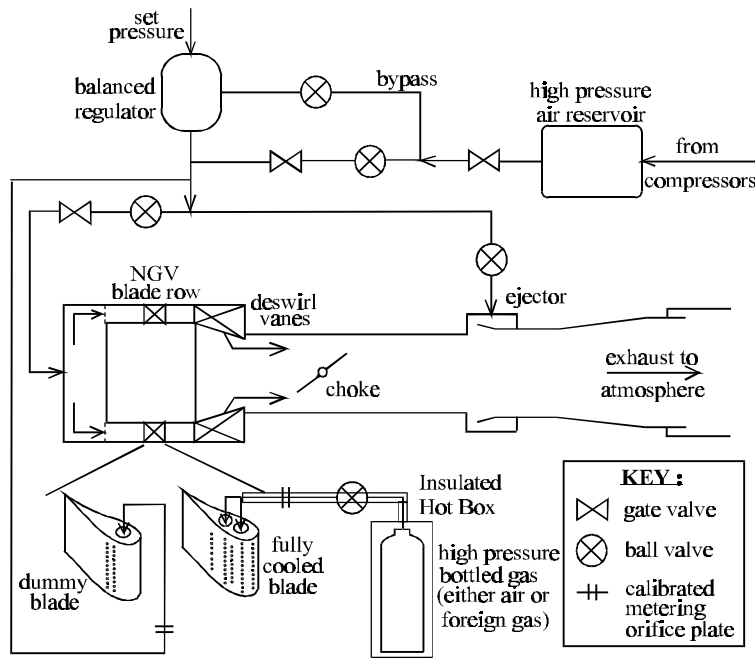
In this chapter the experiments conducted to measure the film cooling thermal performance of the *console* at engine representative conditions are presented. The Oxford University Cold Heat Transfer Tunnel (CHTT) facility is described with particular reference to these experiments. The purpose of the experiments was to measure the heat transfer coefficient and adiabatic effectiveness downstream of rows of *consoles* manufactured in a scale nozzle guide vane (NGV) based on the Rolls-Royce RB211 engine. The heat transfer performance of the NGV without film cooling and with cylindrical and fan-shaped cooling holes configurations have been studied thoroughly in the CHTT (Martinez-Botas et al, 1994, Lai, 1999) A new method of analysis of the results of the transient experiment, based on a modified step change solution, is presented. The experimental results are presented and compared with previously measured results. Proposals for further improvements in heat transfer performance for the *console* rows on an NGV are discussed.



*Figure 6.1: Photograph of the heat transfer side of the CHTT*

### **6.1 The facility**

The Cold Heat Transfer Tunnel (CHTT) is a short duration, transonic blow down tunnel, described in detail by Martinez-Botas et al (1993). The working section is an annular cascade of 36 NGVs at a scale of 1.4 times the size of the high pressure turbine first stage NGV row from the Rolls Royce RB211 524G. A photograph of the tunnel is shown in Figure 6.1 and a schematic of the tunnel is shown in Figure 6.2. The three dimensional engine flow characteristics in the NGV passage, including secondary flow, are accurately modelled by the annular NGV geometry. The increased scale of the cascade provides a reduced rate of heat transfer at the vane surface, so that the temperature change measured by liquid crystals on the NGV surface is at a rate that can be accurately recorded. The increase in scale is balanced by a reduction in density such that the Reynolds number based on mainstream flow and blade chord is matched to the engine. This means that the Nusselt number, which is a function of Reynolds number is also constant i.e.:



**Figure 6.2: Schematic of the CHTT**

$$Nu = \frac{hx}{k} = fn(Re) = const \quad (6.1)$$

Hence  $h \propto x^{-1}$  and the increase in scale of 1.4 times causes the heat transfer coefficient, and hence the heat flux to be reduced by  $(1.4)^{-1}$  times, that is a reduction to 70% of the value. In addition to this reduction in heat transfer, the larger scale improves the resolution on the surface of the NGV.

The tunnel is fed from a 31m<sup>3</sup> ambient temperature reservoir of air which discharges over the run duration of 5-7 seconds, during which time the reservoir pressure falls from 2.7 MPa to approximately 2.0 MPa. A regulator maintains the total pressure of the flow at 2.0 MPa during the experiment, while the supply pressure is higher than this level, but cannot operate once the supply pressure drops below 2.0 MPa. The capacity of this reservoir limits the run time of the tunnel to a maximum of 10 seconds. The use of ambient ('cold') mainstream air has two implications. The first is that the heat transfer experiments are carried out with heated NGV row section and cold mainstream, the opposite to the engine case. This was proposed by Jones (1978), as a simpler and more economical method to run heat transfer experiments than correctly modelling the engine temperature ratios, but the

parameters that affect heat transfer are correctly maintained. The second implication is that the density ratio between the coolant and mainstream flows, produced in the engine by the temperature ratio, must be modelled in an alternative way. In the CHTT experiments described, this is achieved by using a foreign gas as coolant as discussed in Chapter 4.

The tunnel inlet pressure is maintained at a constant level by a balanced by-pass regulator system and an ejector can be used to reduce the downstream pressure level if required. The inlet flow is fed into a plenum chamber, which is separated from the test section by a perforated plate with 9% open area. This plate is incorporated both to maintain the uniformity of the flow and produce a high level of turbulence (~13% and length scale 21mm) in order to simulate the engine conditions downstream of the combustor (Moss and Oldfield, 1991) at the test NGV inlet plane. The importance of correctly modelling the turbulence intensity was highlighted by Hoffs et al (1996) to ensure that both the location of transition from laminar to turbulent flow on the blade surface and the level of heat transfer coefficient are correctly modelled. Moss and Oldfield (1991) also showed that turbulent heat transfer is effected by freestream turbulence.

The mainstream flow is accelerated through the NGV row, and leaves the NGV row with an average swirl angle of  $74.6^\circ$ . Downstream of the NGV row, the flow passes through deswirl vanes before being exhausted to atmosphere. The deswirl vanes remove the angular momentum of the exit flow, so that it can pass through a smaller diameter pipe. For the design condition used in the current experiments, the downstream conditions are atmospheric, but the tunnel downstream pressure can be varied independently of the upstream pressure, so that a range of Reynolds and Mach numbers can be set. The tunnel operation is controlled by pneumatically operated valves, initiated by solenoids, which are programmed to act at the required point during a run of the tunnel.

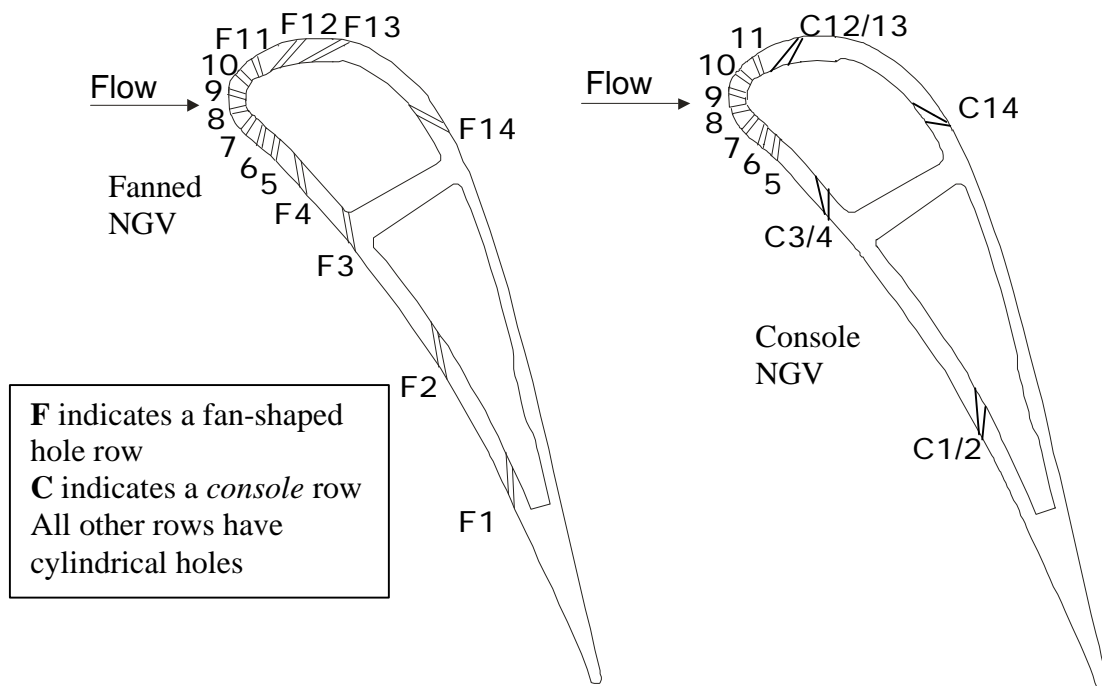
Parameter	Engine	Tunnel
Inlet Total Pressure (MPa)	3.2	0.2
Coolant/Main Stream Pressure Ratio	1.02	1.02
Coolant/ Main Stream Density Ratio	1.78	1.78
Turbine Inlet Temperature (K)	1750-1800	290 K
Exit Reynolds Number (Based on Axial Chord)	$2.02 \times 10^6$	$2.02 \times 10^6$
Exit Mach Number	0.96	0.96
Mass Flow Rate (kg/s)	120	38

**Table 6.1 Engine/Tunnel comparison**

## 6.2 Nozzle Guide Vanes

The row of NGVs that forms the working section of the tunnel is divided into twenty-one NGVs that are fixed to the test section, to maintain periodicity of the flow, and fifteen NGVs that are located in three test cassettes, which can be easily removed from the tunnel and modified for specific experiments. The NGVs held in the test cassettes are typically either test NGVs with an engine cooling configuration, or simplified, ‘dummy’, NGVs to maintain the periodicity of the flow within the cassette.

### 6.2.1 Test NGVs



**Figure 6.3: Fanned and console NGVs with cooling hole rows indicated**

A number of different test NGVs have been used in the CHTT to measure heat transfer performance. The first heat transfer experiments in this facility were made with a solid NGV (machined from acrylic) with no film cooling (Martinez-Botas et al, 1994). These experiments were conducted using the transient liquid crystal technique and provide baseline data for the NGV without film cooling. The design details of the NGV are given in Table 6.2.

The heat transfer performance of an NGV with an array of 340 discrete cylindrical film cooling holes was measured by Lai (1999) using the transient liquid crystal technique with a machined acrylic NGV. The heat transfer coefficient of the cylindrical hole NGV was also measured by Lai (1999) using direct heat flux gauges on an NGV machined from aluminium. The film cooling hole rows for the cylindrical hole NGV are located at positions 1-14 as shown for the fanned NGV in Figure 6.3.

The ‘fanned’ NGV with eight rows of fan-shaped holes on the pressure and suction surfaces and six rows of cylindrical holes around the leading edge is a scaled version of the film cooled NGV used in the engine. The location of the fan shaped and cylindrical holes is shown in Figure 6.3, and the fan shaped holes are holes with a lateral expansion, as modelled in the low speed experiments. Lai (1999) measured the heat transfer performance of a fanned NGV machined from acrylic using the transient liquid crystal technique, and also measured the heat transfer coefficient of a fanned NGV machined from aluminium using direct heat flux gauges.

As part of the work described in this thesis, a ‘console’ NGV was designed (Chapter 3) to provide at least the same reduction in heat flux due to film cooling as the fanned NGV. The amount of coolant used to achieve this was designed to be as close as possible to the amount of coolant used by the fanned NGV, given that before the vane was made, no



measurements of hole discharge coefficient at CHTT conditions could be made. The location of the hole rows for the *console* NGV are shown in Figure 6.3. The *console* NGV was manufactured from epoxy resin using stereolithography (Springer, 1998) and a picture of a section of a stereolithography NGV with *consoles* manufactured using this technique was shown in Figure 3.4.

Each of the film cooled NGVs contain two internal cavities from which the coolant is fed (Figure 6.3). The front cavity feeds the leading edge and early pressure and suction surface rows, and the rear cavity feeds only the two fan-shaped or cylindrical hole rows (rows 1 and 2) or the *console* row (C1/2) on the pressure surface nearest the trailing edge. The two coolant cavities inside the test NGV are supplied with coolant from a bottled supply through a feed system, which includes calibrated, choked orifice plates to measure and control the mass flow. The pressure and temperature inside each cavity is measured, and the orifice plates and feed system are designed to ensure that the pressure is equal in both cavities.

Mean axial chord (mm)	66.73
Mean pitch at exit (mm)	97.18
Span at exit (mm)	80.76
Cascade throat area (m <sup>2</sup> )	0.0805
Mean blade diameter (m)	1.113

*Table 6.2: Nozzle guide vane details*

### 6.2.2 Dummy NGVs

The simplified ('dummy') film cooling configuration used for the 21 dummy NGVs that are fixed to the test section, consists of only four rows of film cooling holes rather than the complicated test vane cooling geometry. Day et al (1999) have shown that in order to correctly model a cooling system, the effective ratio of areas occupied by the coolant and mainstream flows, or blockage, should be matched. Day et al have also shown that

matching the blockage is equivalent to matching the momentum flux ratio. The dummy vanes have been designed to correctly match the blockage due to the coolant in order to provide the correct periodicity of the flow. This reduces the expense and the complexity of the facility, whilst maintaining the advantages of the full annular cascade. The dummy NGVs are supplied with cold air coolant from the mainstream air supply.

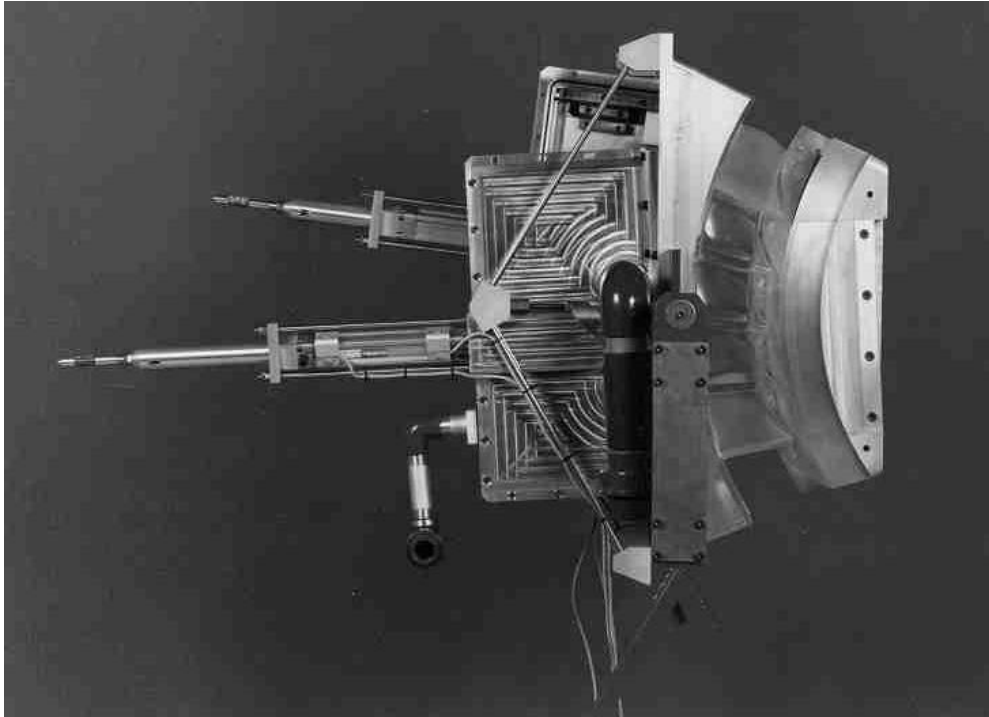
### **6.2.3 Test cassettes**

The remaining fifteen NGVs are arranged in three test cassettes of five NGVs. The cassettes are each dedicated to a particular type of experiment, namely heat transfer (Guo, 1997, Lai, 1999), aerodynamics (Main, 1994, Main et al, 1995,1996, Day, 1997, Day et al, 1998, 1999, 2000) and discharge coefficient (Rowbury, 1998, Rowbury et al, 1997). The cassettes can be removed from the tunnel, and the NGVs in the cassette can be interchanged. There are typically at least three NGVs with the correct film cooling hole arrays in each cassette, which provide two passages with the correct film cooling flow with the test vane located between the two correctly modelled passages. The other NGVs in the cassette may be dummy vanes or have a different cooling geometry to the test vane. The heat transfer cassette was used for the experiments presented in this chapter and the aerodynamic cassette will be described in the following chapter.

### **6.2.4 Heat transfer cassette**

The heat transfer cassette contains five NGVs constructed from acrylic (fan and cylindrical geometries) or stereolithography resin (*console*). For the transient measurement technique used in the present work, it is necessary to use low conductivity materials so that the conduction into the blade is approximately one-dimensional and the substrate can be considered to be semi-infinite. Previously, Lai (1999) developed the combined TLC and direct heat flux gauge technique to measure full coverage heat transfer coefficients

using a metal NGV. The central NGV in the cassette is the test vane, which in the present experiments is instrumented with thermochromic liquid crystals and surface thermocouples. The techniques that have been used for heat transfer measurement in the CHTT are summarised by Sargison et al (2001c).



*Figure 6.4: Heat transfer cassette*

The cassette can be isolated from the tunnel using shutters upstream and downstream from the cassette. The transient method for measuring heat transfer coefficient and  $T_{aw}$ , presented by Jones et al (1993), requires a sudden step change in mainstream fluid temperature, which is achieved in practice by preheating the blades when isolated from the tunnel by blowing warm air around the cassette. The tunnel can be started with the cassette isolated such that the blade maintains a uniform, high, initial temperature while the mainstream flow is initiated. When the tunnel steady operating condition is reached, the shutters are rapidly opened over 0.1 s and the blade is subjected to a sudden change in fluid temperature.

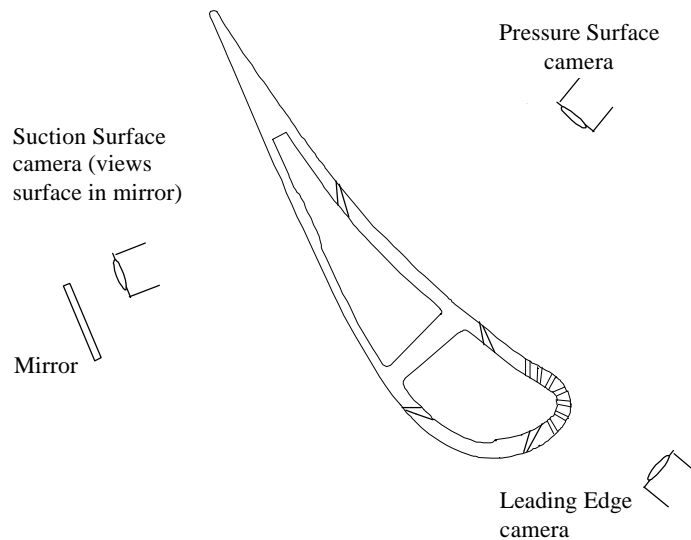
## **6.3 Experimental measurement**

### **6.3.1 Thermochromic liquid crystals**

In order to measure the surface temperature at any point on the surface of the NGV, thermochromic liquid crystals (TLC) are sprayed onto the surface over a layer of matt black paint, which improves the contrast of the crystal colour. The application of TLCs to heat transfer measurement has been previously documented by Ireland et al (1993) and the response time of the TLC has been measured by Ireland and Jones (1987) to be of the order of 3 ms. The TLCs used in the current work are wide band liquid crystals, so called because a colour change is present over a temperature range of 20 °C. For the particular TLC used in the current work, the colour play temperature range was from 26°C to 46°C with a colour change from clear to red through green to blue to clear with increasing temperature. It is always necessary to calibrate TLC colour against temperature when a new layer of TLC is applied to a test piece, and as the crystal ages, because the colour can vary with the particular mixture of crystal and binder, the application and the age of the crystal. In addition to this, the liquid crystal colour is dependent on the viewing angle and lighting so a calibration curve is produced, before and after each run, for each point on the blade at which a surface temperature trace is required.

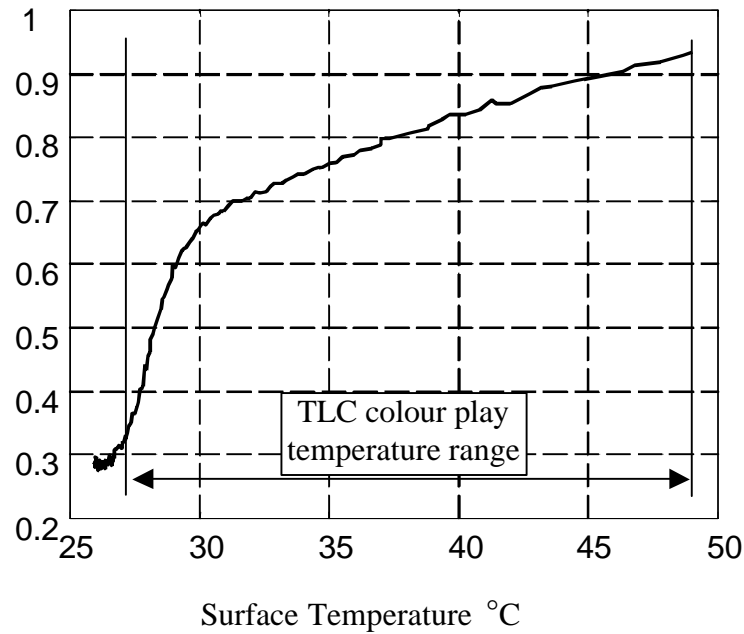
Three CCD cameras installed in the wind tunnel monitored the response of the liquid crystal colour to temperature. They were carefully positioned in the wind tunnel to maximise the area of the NGV in view and to minimise the aerodynamic disturbance in the wind tunnel. One camera positioned downstream of the NGV views the suction surface using a mirror installed in the wind tunnel and two cameras positioned upstream of the NGV row view the pressure surface and the leading edge as shown in Figure 6.5. Images were recorded at 25 frames per second directly to the PC using a frame acquisition card.

The system recorded the images using the YUV (luminance and 2 chrominance) model outlined in Section 5.2.1 and the colour history at any pixel location was converted to hue using the definition in Section 5.2.1. For each view of the NGV, a set of measurement points on the vane surface was produced and at each measurement point, the measured hue was an average of the hue over a region of three by three pixels around the measurement point. The sensitivity of the analysis to the number of pixels averaged to obtain one data point was tested by performing an analysis with a two by two pixel region and a four by four pixel region, and it was found that the difference in the final results was negligible compared with the accuracy of the experiment.



***Figure 6.5: Schematic of camera location to record TLC colour play***

To obtain the calibration data for each view of the blade, the blade was heated to above the upper crystal temperature and allowed to cool slowly and uniformly in ambient conditions. The colour response (converted to a hue signal) was then matched to the temperature measured by surface thermocouples attached to the surface of the blade in order to produce a calibration curve for each measurement point on the surface. A typical calibration curve is shown in Figure 6.6.



**Figure 6.6: Surface temperature vs. hue for a single pixel**

Prior to each run, the coolant supply and the blade surface were heated to the same initial temperature, above the TLC colour play range. The coolant was kept at the same temperature as the vane initial temperature in order to prevent internal heat transfer between the coolant and the vane during the run. One difficulty with the use of liquid crystals in this facility to measure the transient heat transfer is that during the first 0.25 s of the experiment the colour response could not be measured. This is because the shutters obscure the view for the first frames whilst opening, then the camera iris takes a short time to adjust to the resultant change in lighting, and hence part of the surface temperature history is not recorded. In addition to this, the level of heat flux during this period is extremely high. The level of heat flux in the steady part of the experiment is of the order of  $2 \times 10^4 \text{ Wm}^{-2}$  and during the start up transient the heat flux is up to 5 times this level. The upper level of heat flux that can be measured by TLC, as suggested by Ireland and Jones (2000), is  $2 \times 10^4 \text{ Wm}^{-2}$ . The starting transient is well outside this range, but during the steady part of the experiment, the TLC are operating just within the level of heat flux that they are usually used to measure.

The analysis of the experimental results depends on a regression curve fit of an analytical solution to the data, and without the initial temperature data important information is lost. A typical surface temperature history measured using TLC is presented in Figure 6.14.

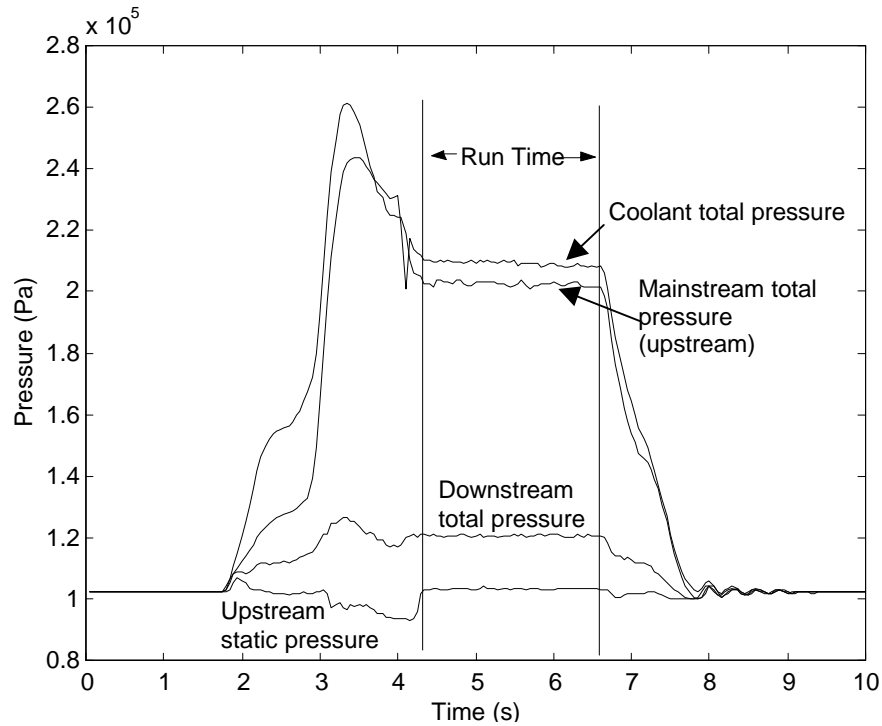
### **6.3.2 Tunnel operating conditions**

During a tunnel run, the upstream total and static, downstream total and static and coolant cavity total pressure in both cavities of the test NGV are monitored. Typical pressure traces of the mainstream and coolant pressures are shown in Figure 6.7. The mainstream pressure is monitored at several locations around the perimeter of the tunnel.

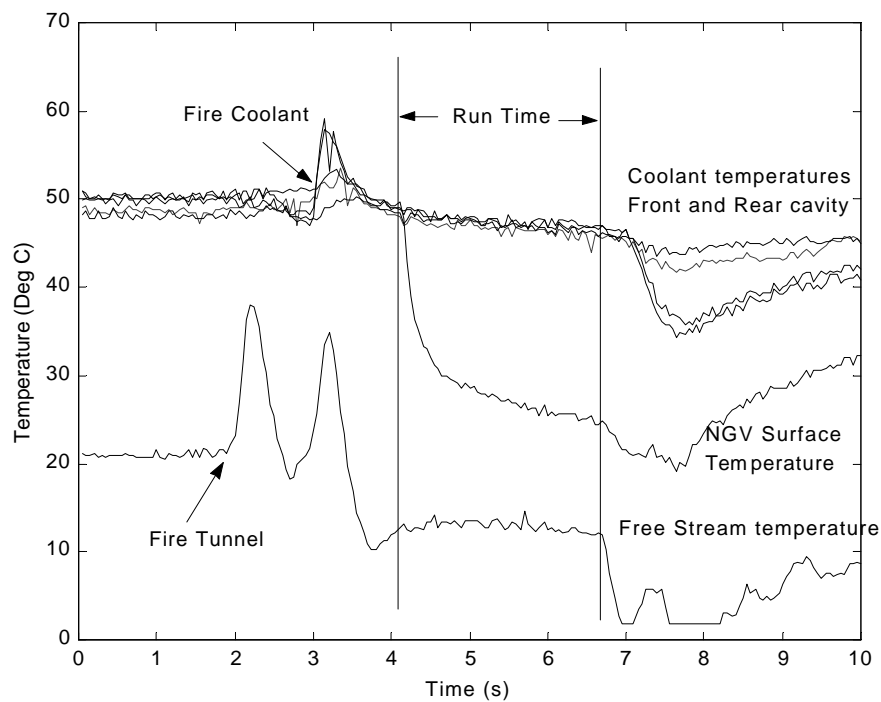
Figure 6.8 shows surface temperature history measurements around the central NGV within the cassette, coolant temperatures within the forward and rear cavities of the NGV and the total temperature of the mainstream. These have been recorded using thin-foil surface thermocouples on the vane surface and standard bead thermocouples located inside the vane cavity and in total temperature probes in the tunnel mainstream flow.

Referring to Figures 6.7 (pressure) and 6.8 (temperature), the tunnel begins operation at  $t = 2$  s, the coolant is introduced at  $t = 3$  s, and the shutters open at  $t = 4$  s. The temperature on the NGV surface, up to the point where the shutters are opened, is seen to remain constant at its initial value near 55 °C and is not influenced by the hot ‘coolant’ in the test vane and two adjacent vanes or the cold mainstream air passing through the 32 passages outside the cassette. The total temperature of the mainstream has two initial peaks associated with compression heating of the gas upstream of the test section. The peak pressure of the mainstream and coolant flows that causes this temperature rise is shown in Figure 6.7. The shutters are opened once this mainstream temperature and pressure have stabilised, and over the three second course of the experiment the total temperature decreases by less than 1 °C and the mainstream and coolant total pressures remain

constant at 0.2 MPa and 0.204 MPa respectively. The NGV surface temperature (here measured by a surface thermocouple) falls rapidly once the shutters have opened to initiate the sudden change in fluid temperature from the blade initial temperature of 55°C to the mainstream temperature of 12°C.



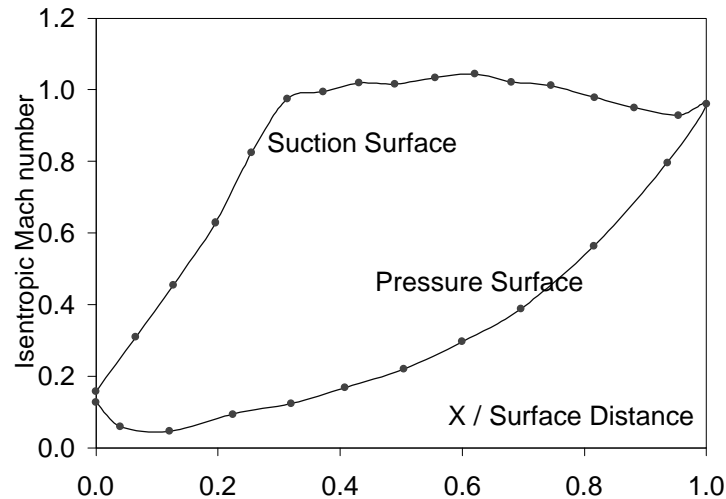
**Figure 6.7: Experimental pressure trace**



**Figure 6.8: Experimental temperature trace**



Using a NGV with static pressure tapings located on the vane surface, the Mach number distribution around the NGV at design conditions shown in Figure 6.9 has been published previously by Guo et al (1998).



**Figure 6.9: Isentropic Mach Number distribution around vane at design conditions**

#### **6.4 Data reduction**

The preceding sections have described the experimental facility and techniques used to perform a transient heat transfer experiment by generating a rapid change in fluid temperature and measuring the transient surface temperature history on the surface of the NGV. The purpose of these experiments is to measure the heat transfer coefficient and adiabatic effectiveness of the NGV with film cooling. In general,  $h$  and  $\eta$  for a transient process can be obtained from the surface temperature history by comparing an analytical solution of the heat transfer process to the measured transient response of the system. As previously discussed, the experimental apparatus was designed so that the rapidly opening shutters provided a near step change in fluid temperature and in previous work (Lai 1999), the solution for a step change in fluid temperature was matched to the experimental results in order to extract the heat transfer coefficient and adiabatic effectiveness.

For the purposes of the transient experiments conducted, the NGV surface can be considered to be a semi-infinite substrate, because the thermal pulse will not travel through the 3 mm thick NGV wall during the 2-3 second duration of the experiment (Appendix B and Schultz and Jones, 1973). The governing equation for the process is:

$$\frac{\partial^2 T}{\partial x^2} = \frac{1}{a} \frac{\partial T}{\partial t} \quad (6.2)$$

and the boundary conditions are:

$$-k \left( \frac{\partial T}{\partial x} \right)_{x=0} = h(T_{\infty} - T(0, t)) \quad (6.3)$$

$$-k \left( \frac{\partial T}{\partial x} \right)_{x=\infty} = 0 \quad (6.4)$$

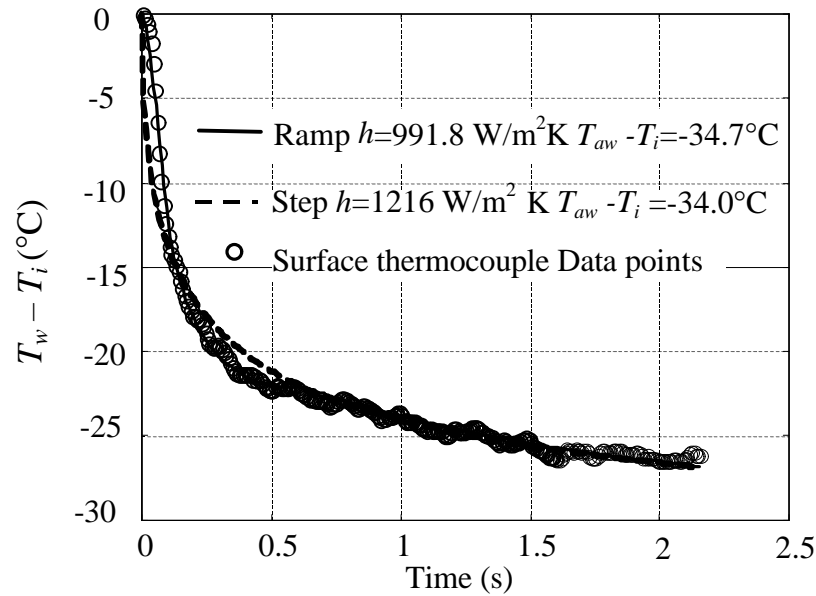
where  $x = 0$  is the surface of the substrate,  $x$  increases from the surface through the substrate,  $T$  is the temperature of the substrate at position  $x$  and  $T_{\infty}$  is the reference gas temperature. The reference gas temperature to be used for the definition of heat transfer coefficient,  $T_{\infty}$ , is the adiabatic wall temperature,  $T_{aw}$ , when film cooling is present, and the gas recovery temperature at the wall,  $T_r$ , when there is no film cooling.  $T(0, t)$  is the wall temperature,  $T_w$ .

When the surface temperature variation is caused by a step change in fluid temperature, and  $h$  is constant, the step change solution to equation (6.2) presented by Schultz and Jones (1973) is:

$$\frac{T_w - T_i}{T_{aw} - T_i} = 1 - e^{b^2} \operatorname{erfc}(b) \quad \text{where } b = \frac{h\sqrt{t}}{\sqrt{rck}} \quad (6.5)$$

Here  $\sqrt{rck}$  is the thermal product of substrate density, specific heat and thermal conductivity,  $\operatorname{erfc}$  is the complementary error function, and  $t$  is the time.

Using the calibration, the wide band TLC data can be converted to a wall surface temperature history,  $T_w(t)$ , with known initial surface temperature  $T_i$ . Regression analysis can be used to solve for the two unknowns  $h$  and  $T_{aw}$  in equation (6.5).

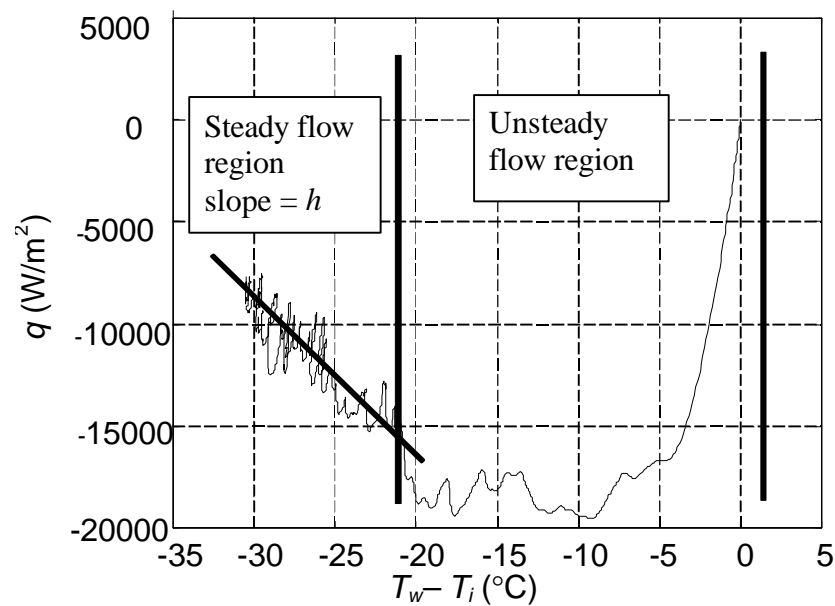


**Figure 6.10: Thermocouple temperature trace with ramp and step curve fits**

When this technique was applied to the data collected in the present experiments, it was found that the step change was not an accurate model of the run history as it yielded  $h$  results that were significantly higher than those measured using thin film gauges (Guo et al 1998). The proposed reason for this error was that the shutters did not provide the perfect step change that was required for the run history to match the analytical solution. This problem had not previously been highlighted and the hypothesis was difficult to test using the TLC results because the most critical data to the curve fit, at the beginning of the temperature trace was not available from the TLC as previously discussed. In order to test the accuracy of the step change assumption during the starting process, the full wall temperature history from the surface thermocouples was compared with a curve fit corresponding to the step change solution. This result is shown in Figure 6.10, which demonstrates that during the

critical first 0.5 seconds, the step change curve fit does not accurately fit the surface temperature history.

Clearly a modification of the analytical solution for the experimental process was necessary, and the surface thermocouple temperature traces were analysed to determine the nature of the modification required. The impulse-response method (Oldfield, 2000 and summarised in Appendix A) was applied to the temperature trace to transform the data to surface heat flux using the governing equations (Doorly and Oldfield, 1987, Ainsworth et al, 1989). For the typical heat flux trace obtained from a measured temperature response shown in Figure 6.11,  $h$  is the slope of the steady region and  $T_{aw}$  is the intercept at zero heat flux. This figure indicates that the NGV surface does not experience a true step-change in fluid temperature due to the starting thermal transient and the solution must be altered to include this starting transient.



**Figure 6.11: Experimental heat flux trace obtained from surface thermocouple**

Solutions of the governing equations for heat transfer, such as (6.5), are linear in  $T_{aw}$  but not in  $h$ . Hence the most logical first attempt at an improved solution should be obtained by assuming that  $h$  is constant and that  $T_{aw}$  varies so that the principle of

linear superposition can be applied to build a modified analytical solution. Assuming that  $h$  is constant at the value obtained from the slope indicated in Figure 6.11, the adiabatic wall temperature history in the non-steady segment of the experiment was calculated from equation (2.1), where the heat flux and surface temperature are known and  $h$  is assumed constant. This assumption is reasonable since  $h$  is primarily determined by the fluid mechanics of a system rather than the thermal boundary conditions.

The adiabatic wall temperature (subtracted from the initial temperature) obtained using this method is shown in Figure 6.12. The experimental data could be well modelled by two initial ramps with time parameters  $t_1$  and  $t_2$ , an initial overshoot of magnitude  $I(T_{aw}-T_i)$  and a horizontal section corresponding to the steady state part of the experiment. Ireland and Jones (2000) have solved the one dimensional conduction equation with a semi-infinite boundary condition for a ramp change in adiabatic wall temperature:

$$T_w(t) = ma \left[ \frac{t}{a} + \frac{1}{a^3} - \frac{2\sqrt{t}}{a^2\sqrt{p}} - \frac{e^{a^2t} \operatorname{erfc}(a\sqrt{t})}{a^3} \right] \quad (6.6)$$

where  $a = \frac{h}{\sqrt{rck}}$  and  $m$  is the slope of the ramp,  $T_{aw}$  vs. time.

The adiabatic wall distribution in Figure 6.12 can be expressed mathematically as:

$$T_{aw} - T_i = m_1 t + m_2 (t - t_1) u(t - t_1) + m_3 (t - t_2) u(t - t_2) \quad (6.7)$$

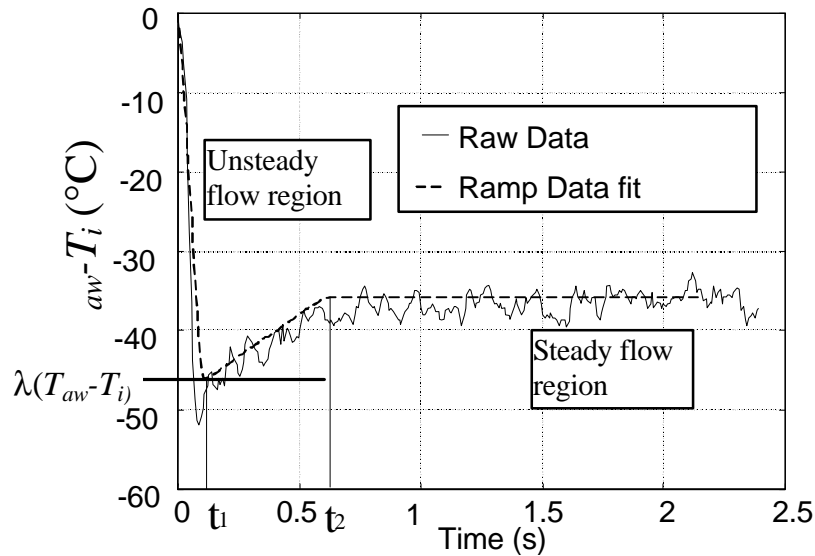
where  $u(t)$  is the unit step function,  $t_1$  and  $t_2$  are the ramp time parameters (Figure 6.12) and  $m_1$ ,  $m_2$  and  $m_3$  are the slope of the three sections of the temperature distribution.

For the present case, the third section is horizontal, so the slope of the final section must be defined as  $m_3 = -(m_1 + m_2)$ . From this definition of the variation in  $T_{aw}$ , the

theoretical wall temperature response to the change in  $T_{aw}$  was produced by applying the principle of linear superposition and summing the wall temperature response to each ramp, displaced by the time parameter of the ramp,  $t_1$  or  $t_2$ :

$$T_w(t) = \sum_{n=1}^3 T_{wn}(t - t_n) u(t - t_n) \quad (6.8)$$

Hence if the system time parameters are known from the surface thermocouple data, regression can be applied to the surface temperature history obtained from the TLC coating or the surface thermocouples to solve for the three unknowns  $T_{aw}$ ,  $h$  and the initial overshoot,  $I$ . The fit to the surface thermocouple data is shown in Figure 6.10, which is a significant improvement on the step change curve fit particularly at the start of the temperature trace.

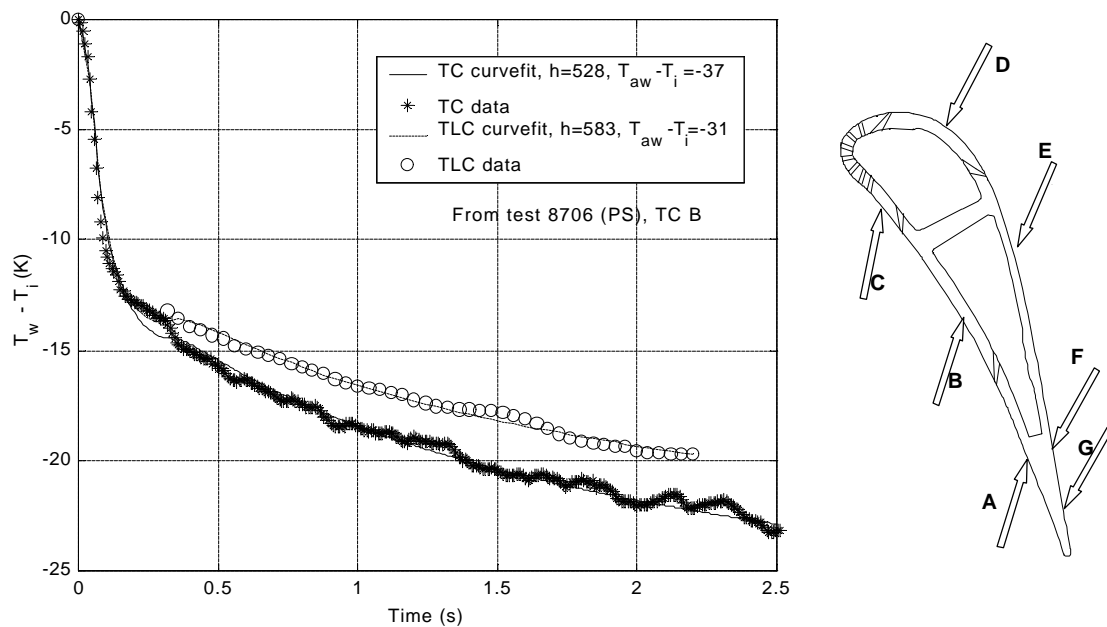


**Figure 6.12: Adiabatic wall temperature distribution**

In Figure 6.13 the temperature trace measured during a pressure surface test (8706) from the thermocouple at the mid pressure surface (location B) is compared with the temperature trace from TLC at the point closest to the thermocouple junction. This figure shows that the temperature measured at the thermocouple is lower than the TLC for reasons discussed in Appendix B. Both curves have a similar shape, and demonstrate good agreement with curves generated using the ramp change solution.

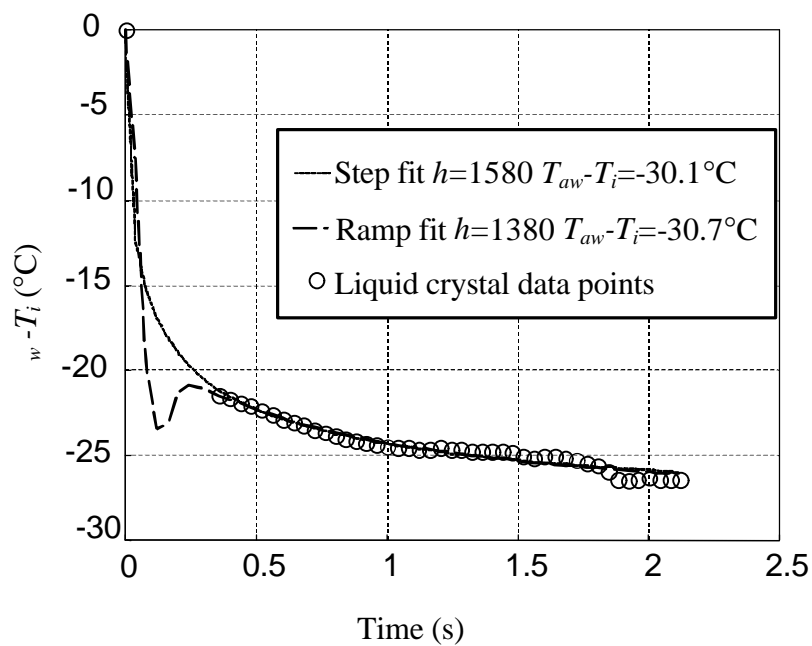
In some regions of the NGV the fitted ramp change curve displayed an early undershoot in temperature such as is shown in Figure 6.14. Although the thermocouple response was not good enough to measure this undershoot in the experiments, a similar undershoot was measured for similar heat transfer experiments in the same facility by Guo (1997) using thin film gauges.

For all regions of the NGV, the ramp change solution provides a lower value of  $h$  and a better fit to the data points than the step change solution, particularly in the early region of the experiment. The value of  $h$  measured using the ramp change technique was closer to the level measured by Guo et al (1998) using thin film gauges and there is little difference in  $T_{aw}$  between the two analysis techniques. The accuracy and robustness of this curve fitting method was thoroughly tested and the methods and results of this testing are outlined in Appendix B.



**Figure 6.13: Comparison of TLC and Thermocouple (TC) data at the location of TC B on the mid pressure surface of the NGV**  
(Thermocouple locations on console NGV shown at right)

The response of the surface thermocouples to the heat flux and temperature change was carefully analysed numerically, to ensure that the shape of the temperature trace measured by the thermocouple was representative of the wall temperature trace, and not a result of delay in the thermocouple temperature measurement. This analysis is included in Appendix B, and the results of the analysis show that the thermocouple signal does not show any indication of a ramp change type response when the heat flux pulse is the result of a step change in fluid temperature.



*Figure 6.14: TLC data points with step change and ramp curve fits applied, with an example of an undershoot in temperature in the fitted curve*

## 6.5 Experimental results

### 6.5.1 Measurement of mass flow rate from hole rows

As previously discussed in Section 6.2.1, the NGV with *console* film cooling hole rows was manufactured, using stereolithography, from epoxy resin and using a different technique to the NGVs with fan-shaped and cylindrical film cooling hole rows, which were NC machined from acrylic. Although the *console* NGV was designed such that the rows had equal throat area to the fan-shaped rows, the manufacturing technique produced



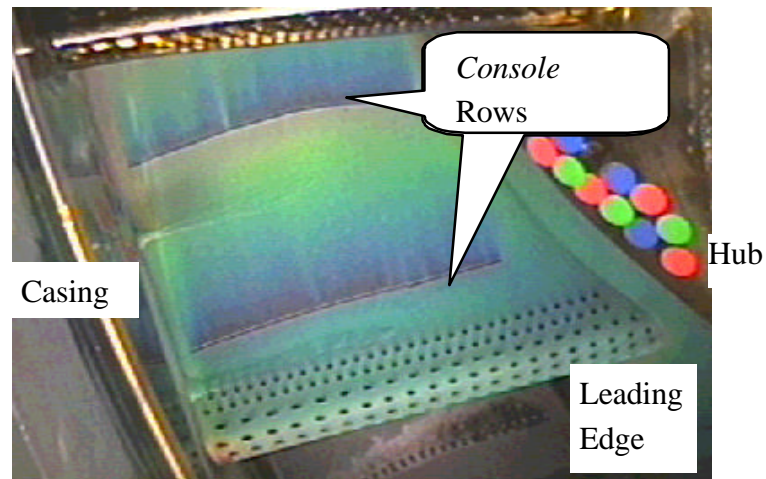
holes with slightly smaller throat area, which could not be accurately cleared post-manufacture. In addition to this, the discharge coefficient of the *console* was measured in the large-scale apparatus to be lower than that for the fan-shaped hole. In order to compare the effects of these differences, the mass flow rate from each row of *consoles* was measured and compared with the mass flow from the equivalent fan-shaped rows. This experiment was conducted at static conditions in a bench test (not in the CHTT), with the ratio of coolant total pressure to mainstream static pressure at the hole exit matched to the equivalent value for each row in the CHTT experiment. The coolant total pressure in the blade was increased, where the exit static pressure was atmospheric, to generate the pressure ratio across the hole that would be present in the CHTT. The results of this experiment are presented in Table 6.3. It should be noted that this experiment is approximate only, because differences in the discharge coefficient with crossflow and positions of the film cooling holes will alter the distribution of coolant in the CHTT experiment. The total coolant flow rate for the fanned NGV was  $0.029 \text{ kgs}^{-1}$  and the total coolant flow rate for the *console* NGV was  $0.027 \text{ kgs}^{-1}$  in this experiment. In the CHTT experiments, the total mass flow rate for the fanned NGV was 6.0 % of the mainstream flow and for the *console* NGV, the flow rate was 6.1% of the mainstream flow. These were considered to be equal within the uncertainty of this measurement.

<b>Hole Row (Figure 6.3)</b>	<b>Percentage of total coolant flow</b>	
	<i>Console</i>	<b>Fanned</b>
1/2	10.8	14
3/4	7.1	7.6
5-11	53.9	47.5
12/13	13.4	20.6
14	14.8	10.2
Total Suction Surface	28.2	30.8
Total Pressure Surface	17.9	21.6
Total Leading Edge	53.9	47.5

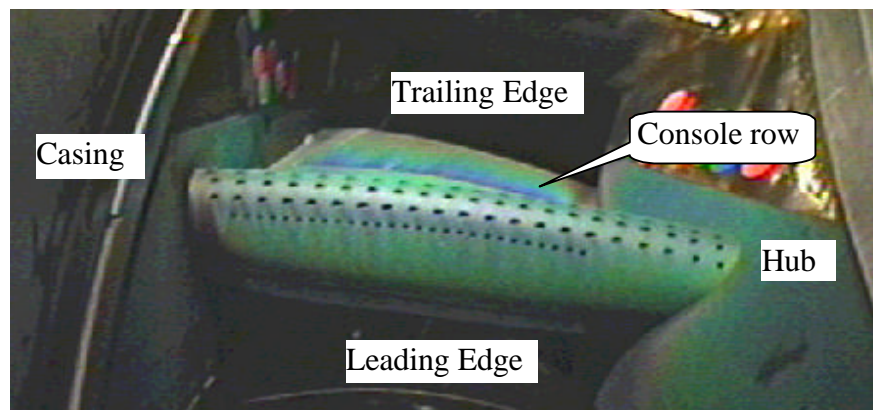
**Table 6.3: Coolant distribution by row**

### 6.5.2 Experimental raw data

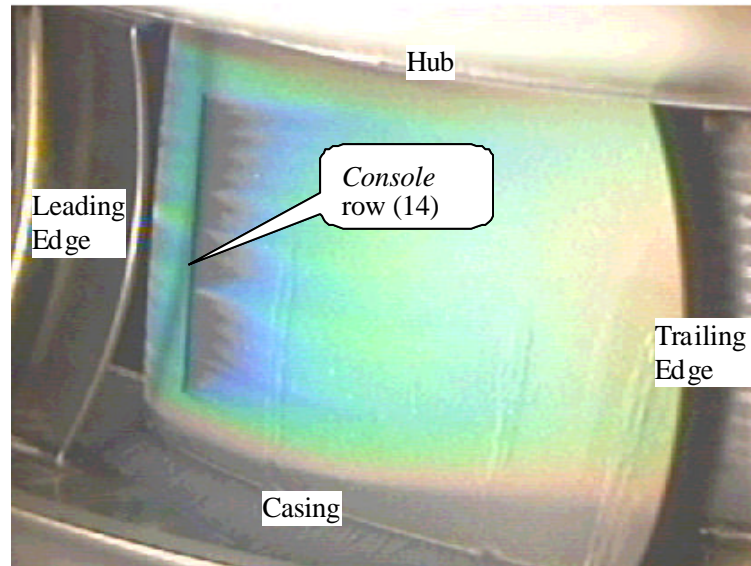
Figures 6.15-6.17 are typical raw digital images recorded during the experiments. The cooling film from the *console* rows on the pressure surface (Figure 6.15) has good uniformity and the dark TLC colour near the slot exit represents high adiabatic effectiveness. This can also be seen near the trailing edge of the vane in the leading edge view (Figure 6.16). The coolant film on the suction surface, from row C14 (Figure 6.17) is not as uniform as the pressure surface, and the peaks of temperature which equate to high effectiveness are located downstream of the point where adjacent *consoles* join. This result was also observed for the low speed experiments (Chapter 5) and CFD (Chapter 9).



*Figure 6.15: Pressure surface camera view*



*Figure 6.16: Leading edge camera view*



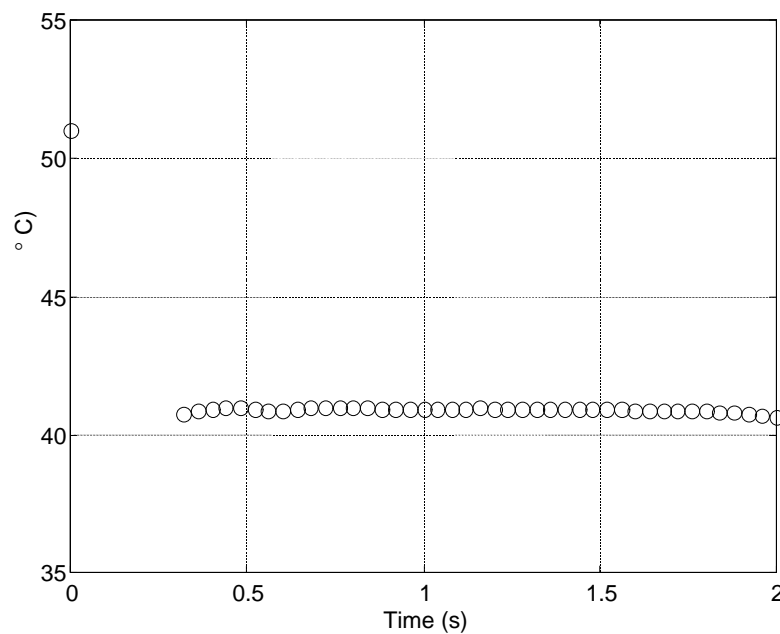
*Figure 6.17: Suction surface camera view*

### 6.5.3 Stability of the analytical technique

The ramp method of analysis outlined in Section 6.4 was used to analyse the temperature traces obtained from the series of raw data images produced during an experiment. Despite the improvements in the results obtained using the ramp method, it was found that the solution technique could still be unstable, particularly in regions near the film cooling holes. An example of such a temperature trace from a point near the *console* C14 on the suction surface is shown in Figure 6.18. Compared with the temperature traces such as the one shown in Figure 6.14, which show some of the initial variation in temperature, the temperature is almost constant. The difficulty in trying to apply the curve fit to this data is that the location of the initial temperature reduction is impossible to accurately determine from the measured information.

The difference between this chart, and one such as shown in Figure 6.14, is that the time ordinate has shifted to lower values. Considering the solution of the governing equation for a step change in fluid temperature (equation 6.4), all other variables being equal, the result of this change is an increase in the heat transfer coefficient. Thus these regions

represent area with high heat transfer coefficient, but the actual level cannot be accurately determined. It may also be the case that in these regions the change in adiabatic wall temperature during the starting process is more extreme than for regions with a slower temperature response, resulting in high overshoot ratio,  $I$ . The change in temperature profile with increasing overshoot ratio is included in Appendix B. The resulting temperature curve shows an initial undershoot in temperature level, but again the exact location and size of this undershoot can only be determined by the curve fit, and without more initial data the result is not reliable.



**Figure 6.18: TLC temperature trace from high effectiveness region of surface, near row C14 on the Suction Surface**

Further limitations of the method were discovered when the method was applied to the analysis of experiments using the fanned NGV, which was manufactured from acrylic. The value of  $\sqrt{rck}$  for acrylic is lower than that for stereolithography resin. From inspection of the analytical solution for either step change (equation 6.5) or ramp change (equation 6.6) in fluid temperature, a lower  $\sqrt{rck}$  will result in a more rapid initial decrease in temperature, exacerbating the problem identified for regions near film cooling

holes. This result is shown graphically in Figure B.10 (Appendix B), where increasing  $h$  is equivalent to reducing  $\sqrt{rck}$  (refer to equation 6.5). The large instability in the fan and cylindrical acrylic NGV results using the ramp solution meant that it was necessary to compare the liquid crystal results from the stereolithography resin *console* NGV with results previously measured by Lai (1999) using direct heat flux gauges to measure  $h$  for the acrylic fan-shaped and cylindrical hole NGVs. This method was not available for the *console* NGV, because it required a NGV manufactured from a material with a high value of  $\sqrt{rck}$ , such as aluminium, to be used measure  $h$ . Facilities for the manufacture of a *console* NGV by conventional drilling techniques at the scale of the NGV were not available at the commencement of this work and hence the direct heat flux gauge technique could not be used. Ideally, in order to compare exactly equivalent experiments, a fanned NGV could have been produced from epoxy resin using stereolithography and the ramp method applied to this data, but this option was unfortunately not available at the time that the experiments were conducted.

#### **6.5.4 Mid span laterally averaged heat transfer coefficient and adiabatic effectiveness results**

The measurement points used for the calculation of the mid span laterally averaged results were a set of ten points spaced across three hole pitches. The heat transfer coefficient was arithmetically averaged, and the laterally averaged effectiveness was calculated using the expression  $\bar{h} = \frac{h\bar{h}}{\bar{h}}$ , defined in Chapter 5. After the average values of  $h$  and  $\bar{h}$  were calculated, the results were corrected for the difference between the molecular properties of the foreign gas and cold air used in the experiment and the engine temperature coolant and mainstream air flows as outlined in Chapter 4.

For the CHTT experiments, film cooling at the leading edge of the vane causes transition earlier than occurs on a vane with no film cooling and the *NHFR* comparison used for the low-speed results is not accurate due to the difference in the boundary layer state between the film cooled and non film cooled states. Consequently, for the results presented below, the different film cooling geometries are compared by use of the predicted total heat flux under engine conditions for each case:

$$q = h(T_w - T_{aw}) = h(T_w - T_r)(1 - hq) \quad (6.9)$$

where the non-dimensional temperature  $q = \frac{(T_{0c} - T_{0m})}{(T_w - T_r)}$ .

For typical engine conditions of  $T_{0c}=880\text{K}$ ,  $T_w=1200\text{K}$ , and  $T_{0m} = 1900\text{K}$ , the value of the dimensionless temperature,  $q$ , used was  $q = 1.46$  in low Mach number regions and higher in high Mach number regions where  $T_r < T_{0m}$ .

The first set of results presented for the suction and pressure surfaces in the following sections are the results for the experimental conditions in the CHTT. The second set of results has been corrected for the difference in gas properties between the experimental conditions and actual engine conditions according to the theory and the method presented in Section 4.2. These results (with higher  $h$ ,  $h$  and predicted  $q$ ) are the results at engine conditions and engine gas properties.

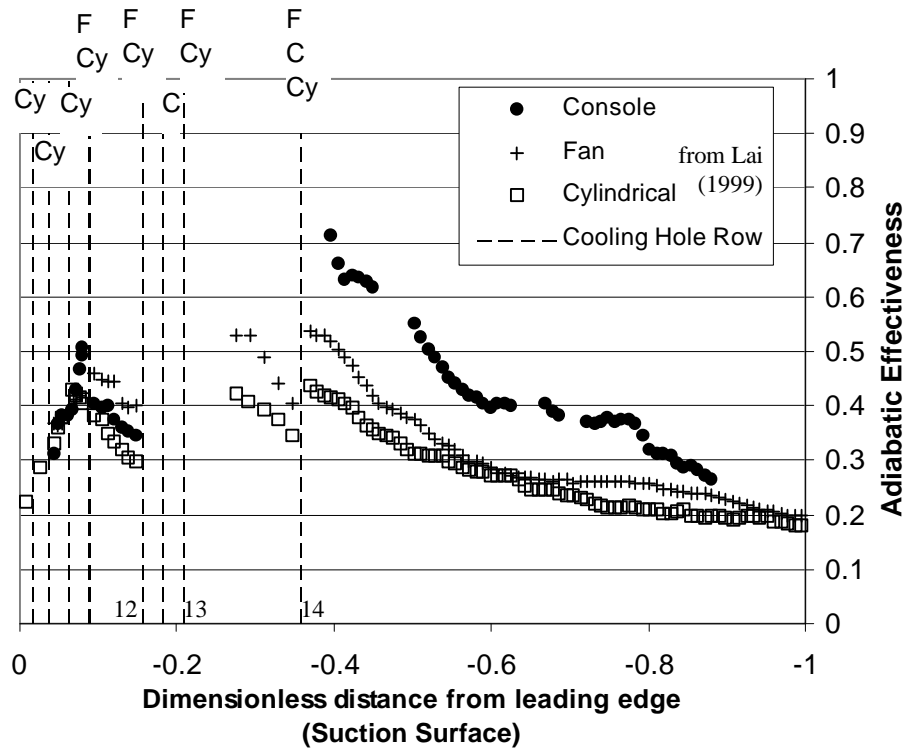
## Suction Surface

The adiabatic effectiveness results for the suction surface in Figure 6.19 show that the *console* exhibits higher effectiveness particularly near to the film cooling hole row. When corrected to engine conditions (Figure 6.22), the level of effectiveness is increased for all configurations, but the comparison between cases remains the same. Note that the region from the first suction surface fan-shaped hole row (12) to upstream of the final suction

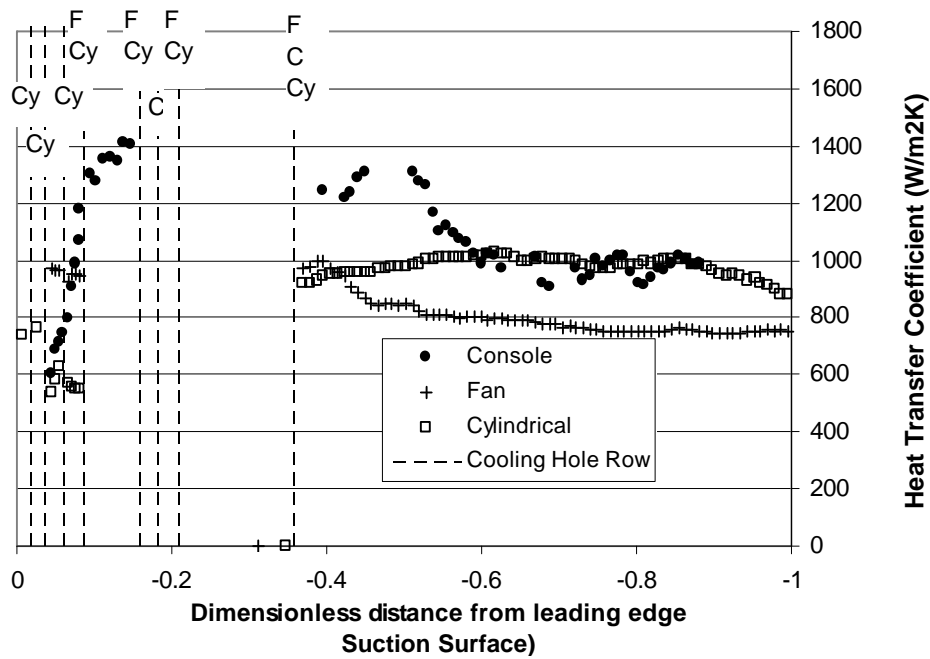
surface row (14, C14) can not be viewed by any of the cameras in the tunnel, so no data can be obtained in this region. A shadow from the trailing edge of an adjacent NGV also falls on the surface in this region, which makes it difficult to analyse the results in this area. The vertical dashed lines in these figures and those following mark the position of the cylindrical, fan-shaped and *console* film cooling rows (Cy, F and C respectively). The fanned film cooling effectiveness is higher than that for cylindrical holes only near the film cooling hole row. The heat transfer results in Figure 6.20 show that at experimental conditions, the *console* level of  $h$  is initially higher than, and further downstream becomes equal to the cylindrical results. When corrected to engine conditions (Figure 6.23), the *console* varies from a level similar to the cylindrical result to mid way between the fanned and cylindrical results. The heat transfer coefficient for the fanned NGV is lower than both the *console* and cylindrical results for the entire region shown.

The combined effect of adiabatic effectiveness and heat transfer coefficient on the suction surface is shown in Figure 6.21 as predicted total heat flux from the surface under engine conditions. The cylindrical holes show a significantly higher level of predicted heat flux than both the *console* and fanned holes for the entire region. The *console* data show a significant improvement in predicted heat flux in the region from the film cooling hole to a dimensionless surface distance of 0.8, where the predicted heat flux increases above the fanned level to the trailing edge of the vane. Hence on the suction surface the *console* performs better than both the fanned and cylindrical rows for the majority of the surface, except for a region near the trailing edge. Note that a total of 28.2% and 30.8% of the coolant mass flow was supplied to the suction surface through rows C12/13/14 and F12/13/14 for the *console* and fan-shaped geometries respectively (see Table 6.3). When the predicted heat flux results are corrected to engine conditions (Figure 6.24), the *console* data shows even lower predicted heat flux, compared with the fan and cylindrical results,

up to the dimensionless surface distance of 0.8. Beyond this point, the *console* predicted heat flux is higher than the fan result.

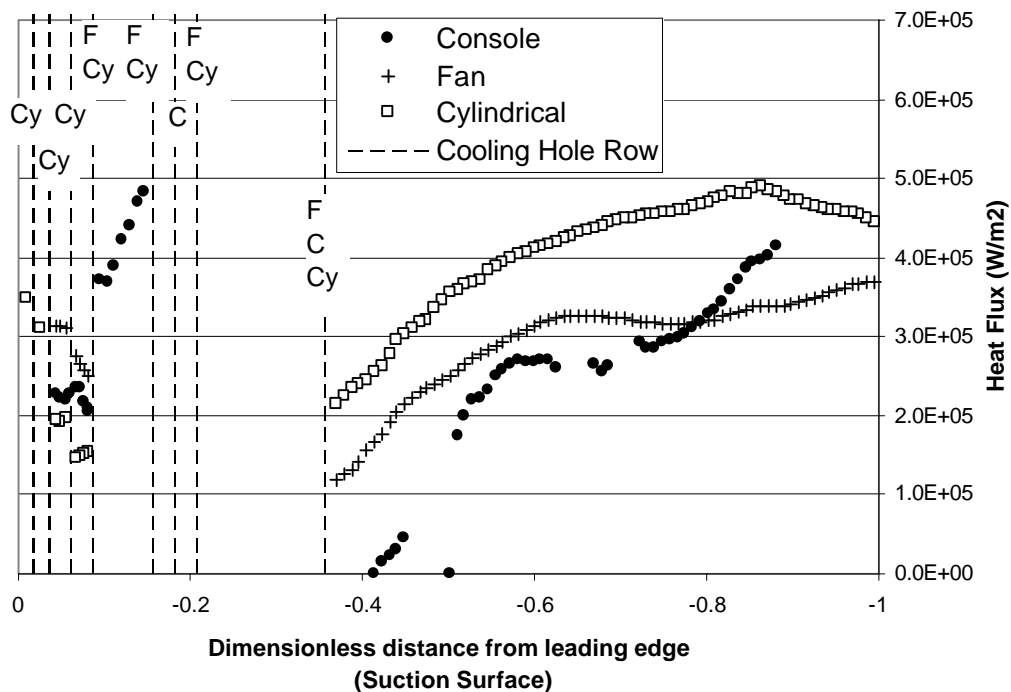


**Figure 6.19: Suction surface adiabatic effectiveness**  
(experimental conditions)

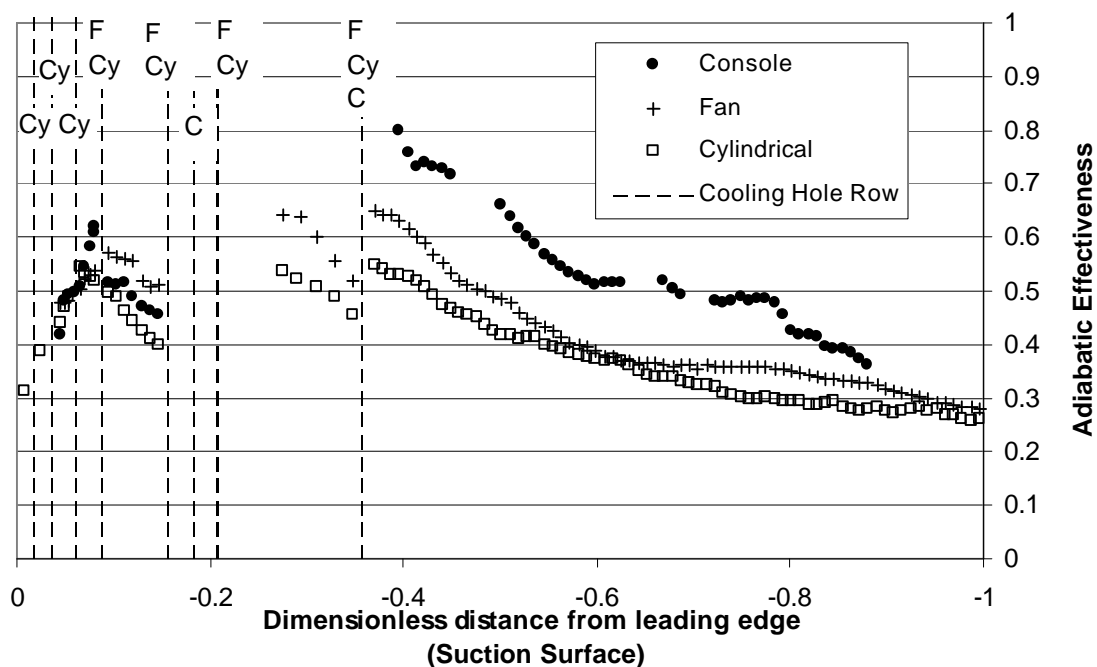


**Figure 6.20: Suction surface heat transfer coefficient**  
(experimental conditions)

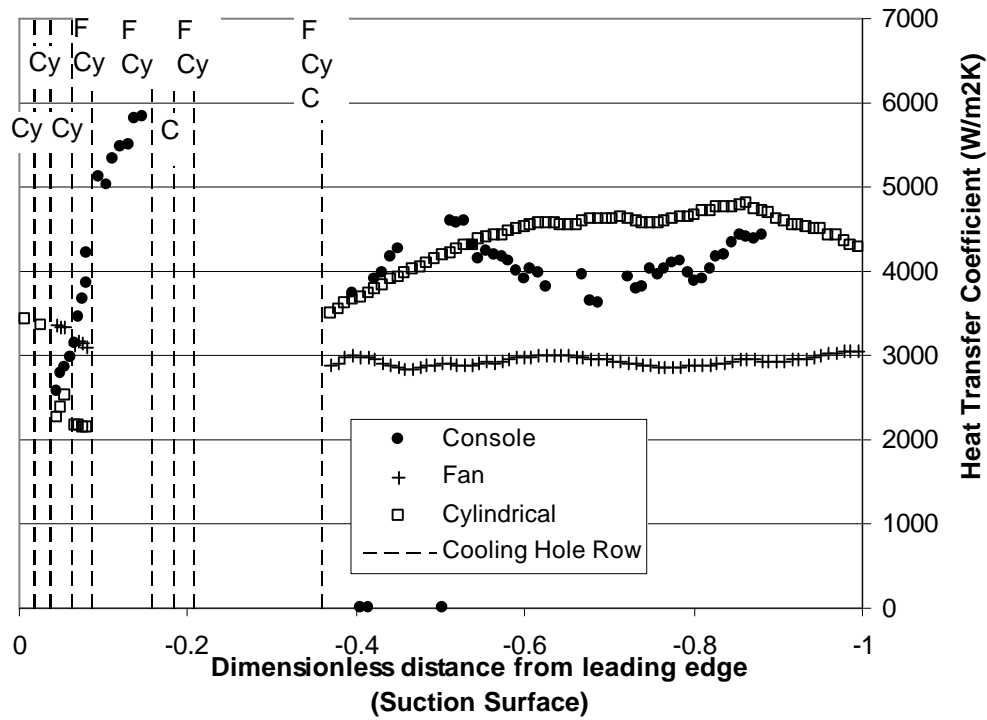




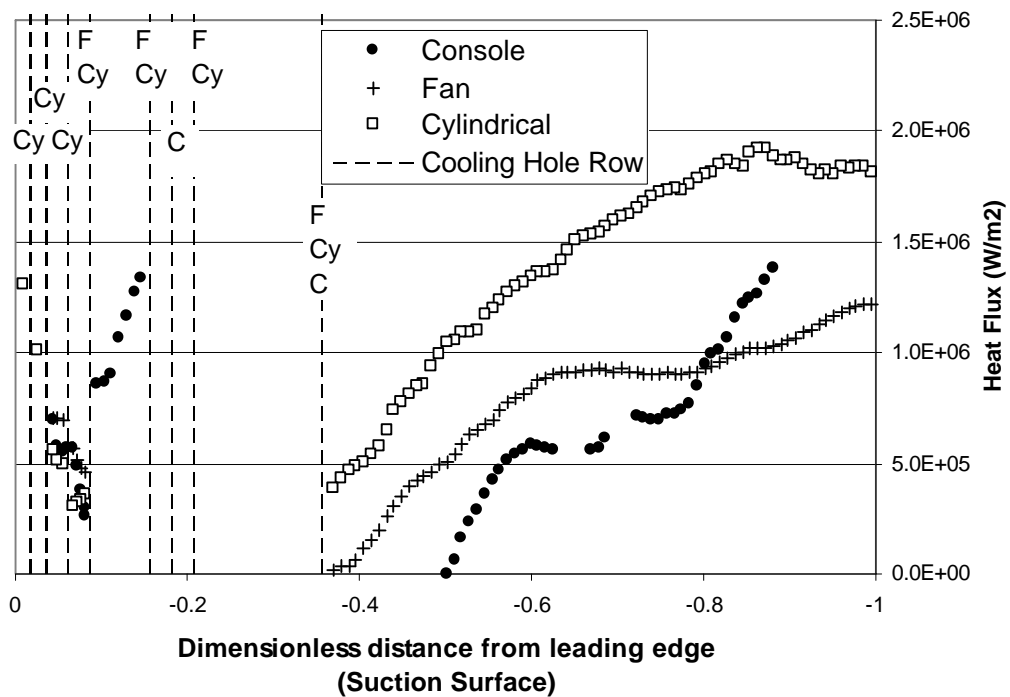
**Figure 6.21: suction Surface predicted total heat flux  
(experimental conditions)**



**Figure 6.22: Suction surface adiabatic effectiveness (engine conditions)**



**Figure 6.23: Suction surface heat transfer coefficient (engine conditions)**



**Figure 6.24: Suction surface predicted heat flux (engine conditions)**

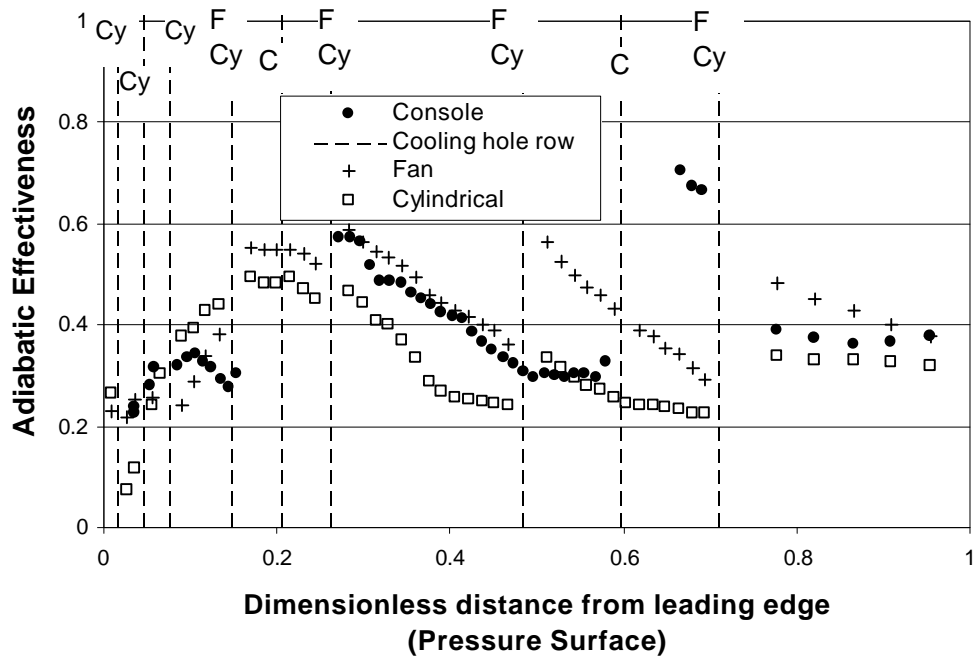
## Pressure Surface

Figure 6.25 shows the pressure surface adiabatic effectiveness and illustrates that the film cooling effectiveness downstream of a *console* row is almost equal to the level from the fanned row. Regions where the *console* data falls below the fanned NGV effectiveness are downstream of a new fanned row where there has not been a new *console* row due to the design decision to replace two rows of fans with a single *console*. The amount of coolant supplied at each *console* is 60% and 70% of the amount of coolant supplied from each set of 2 fanned rows replaced by *consoles*, so the total amount of coolant supplied to the surface is reduced for the *console* NGV. The effectiveness results indicate that with an appropriate design, the film cooling effectiveness distribution on the surface could be made equivalent to the fanned NGV result. The correction of these results to engine conditions (Figure 6.28) increases the level of effectiveness for each cooling configuration, but the comparison between cooling configurations is not altered.

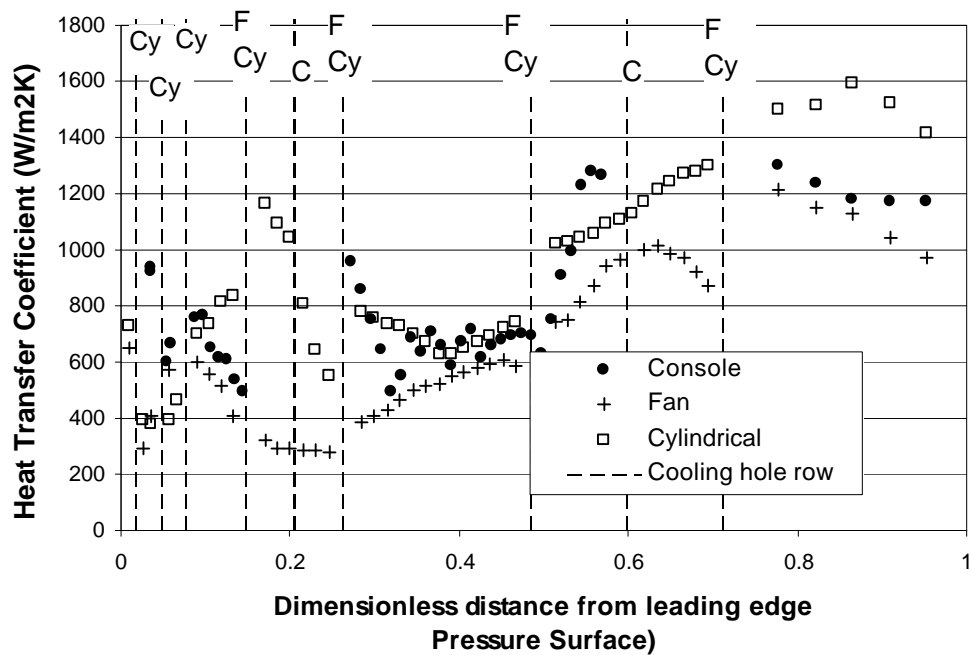
The heat transfer coefficient results in Figure 6.26 mirror the flat-plate experimental results (Chapter 5) in showing that the *console* has higher heat transfer coefficient than the fanned NGV, but the *console* results were similar to the cylindrical hole results. When corrected to engine conditions (Figure 6.29),  $h$  is lower for the *console* NGV than for the cylindrical results.

The total predicted heat flux result in Figure 6.27 shows a similar level to the fanned NGV downstream of the first *console*, which becomes significantly higher than the fanned result after the next fanned row. When corrected to engine conditions (Figure 6.30), the predicted heat flux is reduced compared with the cylindrical results, and is closer to the fan results near the hole, but higher further downstream. These results should be considered in light of the reduction in coolant flow rate in this area, and the different

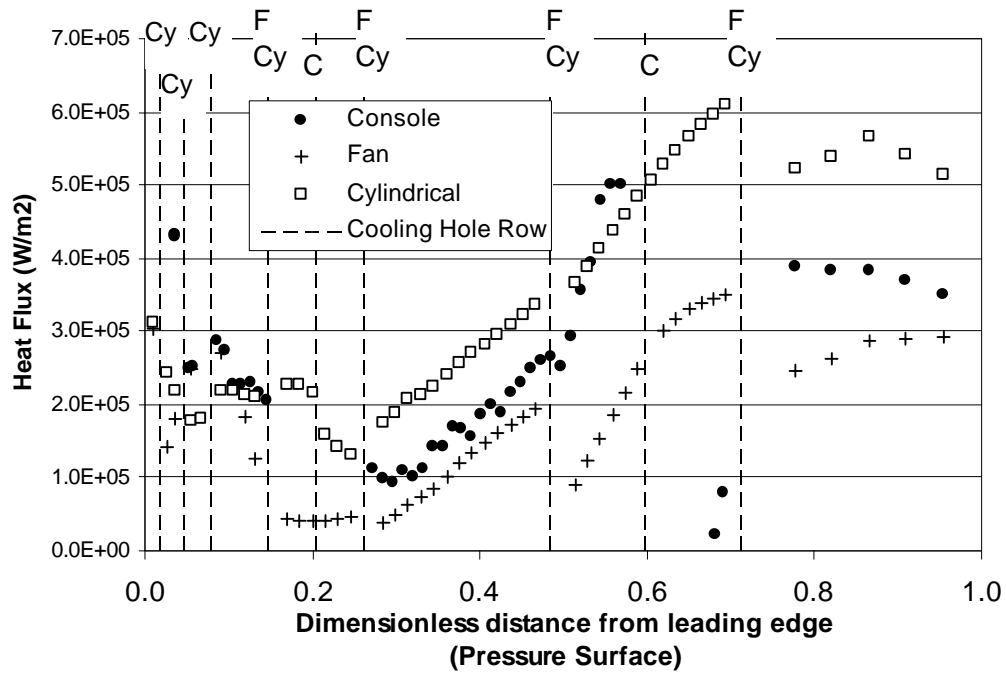
locations of *console* rows. The results for the pressure surface indicate that if correctly positioned, the *console* should achieve the same performance as fanned rows with equal or lower coolant flow rates.



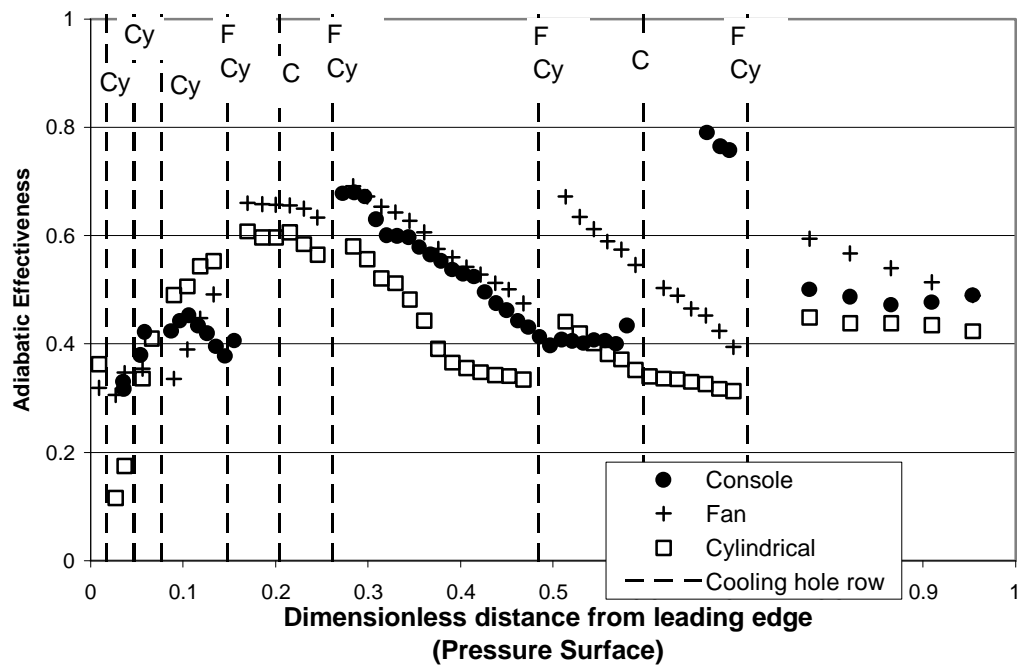
**Figure 6.25: Pressure surface adiabatic effectiveness**  
(experimental conditions)



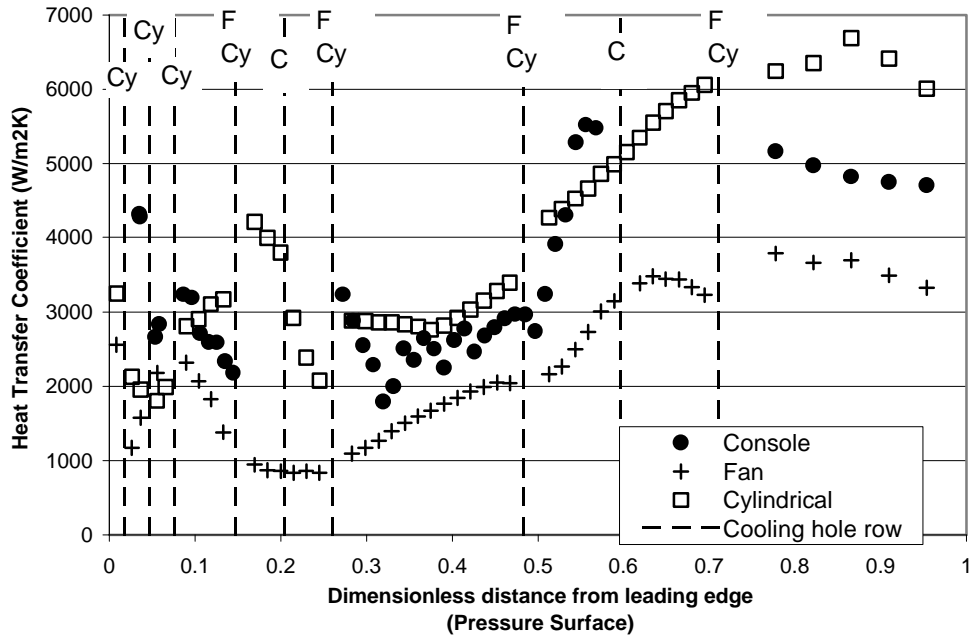
**Figure 6.26: Pressure surface heat transfer coefficient**  
(experimental conditions)



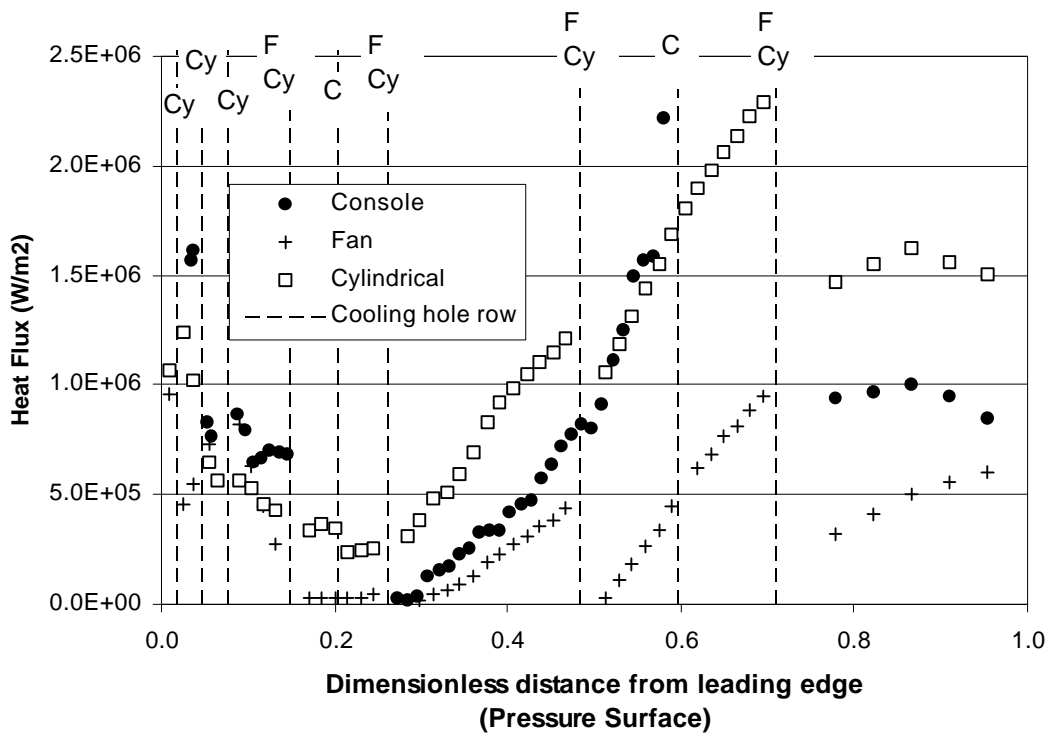
**Figure 6.27: Pressure surface predicted heat flux  
(experimental conditions)**



**Figure 6.28: Pressure surface adiabatic effectiveness  
(engine conditions)**



**Figure 6.29: Pressure surface heat transfer coefficient**  
(engine conditions)

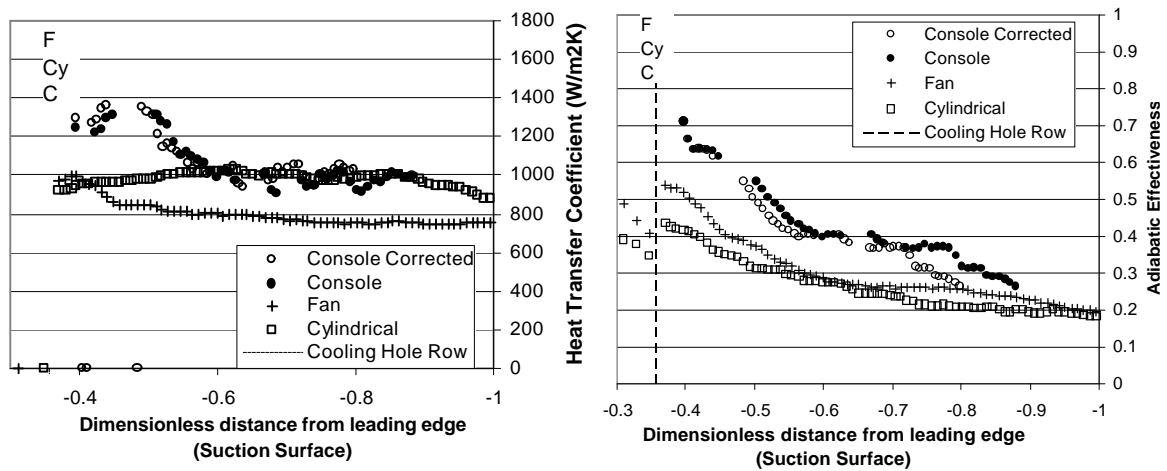


**Figure 6.30: Pressure surface predicted heat flux**  
(engine conditions)

## Mass flow correction to data

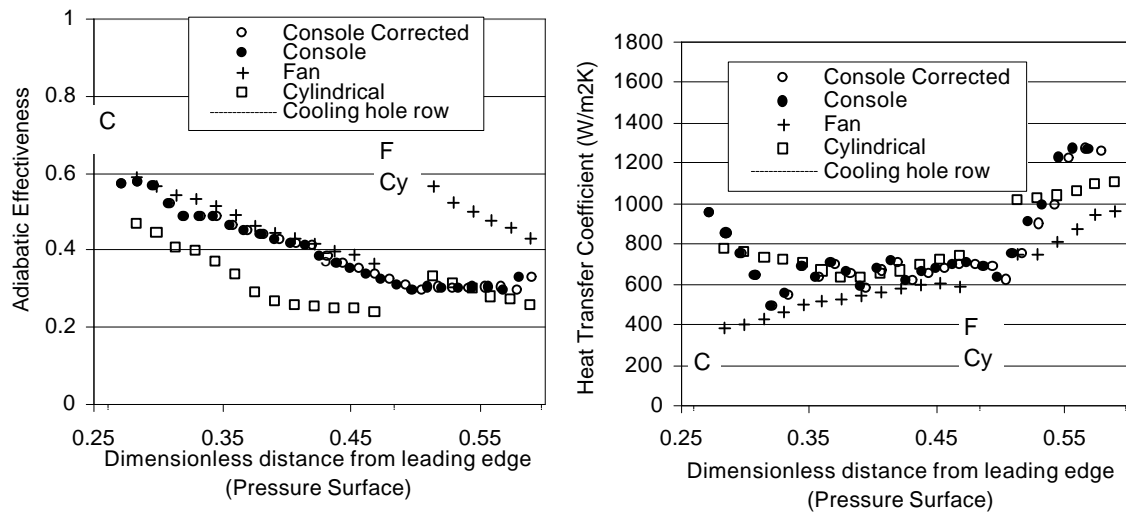
Based on the measured mass flow rates of coolant from each film cooling hole row for the fanned and *console* NGVs, a correction can be applied to the  $h$  and  $\mathbf{h}$  data for the suction and pressure surface cooling hole rows. The correction applied is identical to the correction for hole discharge coefficient described in Chapter 5, and is based on the similarity of effectiveness with dimensionless distance  $x/d$  and the dependence of  $h$  on  $Re_x$  for a flat plate. This correction is a considerable simplification when applied to NGV data, because it is only applicable to flat plate data. However the correction is useful to verify the discussion of performance based on a consideration of the mass flow rates from the rows, when it is not possible to repeat these experiments with the correct mass flows.

The correction was applied to data for the *console* NGV downstream of row 14 (suction surface), which had higher mass flow rate than the fan NGV, and to the data downstream of row C3/4 (pressure surface), which had a lower mass flow rate than the fan NGV. The suction surface data shown in Figure 6.31 demonstrates a small reduction in  $\mathbf{h}$  and a slight increase in  $h$ . The corrected effectiveness drops to the fan level at a distance of  $-0.8$  instead of  $-0.9$ , but remains significantly higher than the fan level upstream of this point.



**Figure 6.31: Mass flow correction to data downstream of row 14 (Suction surface)**  
(experimental conditions)

The correction applied to the pressure surface shown in Figure 6.32 indicates that there would be a small increase in effectiveness, to bring it slightly closer to fanned NGV levels. The level of  $h$  is slightly reduced, particularly where there is a high rate of increase of  $h$  between distances of 0.5 and 0.55.



**Figure 6.32: Mass flow correction to data downstream of row C3/4 (Pressure surface)**  
(experimental conditions)

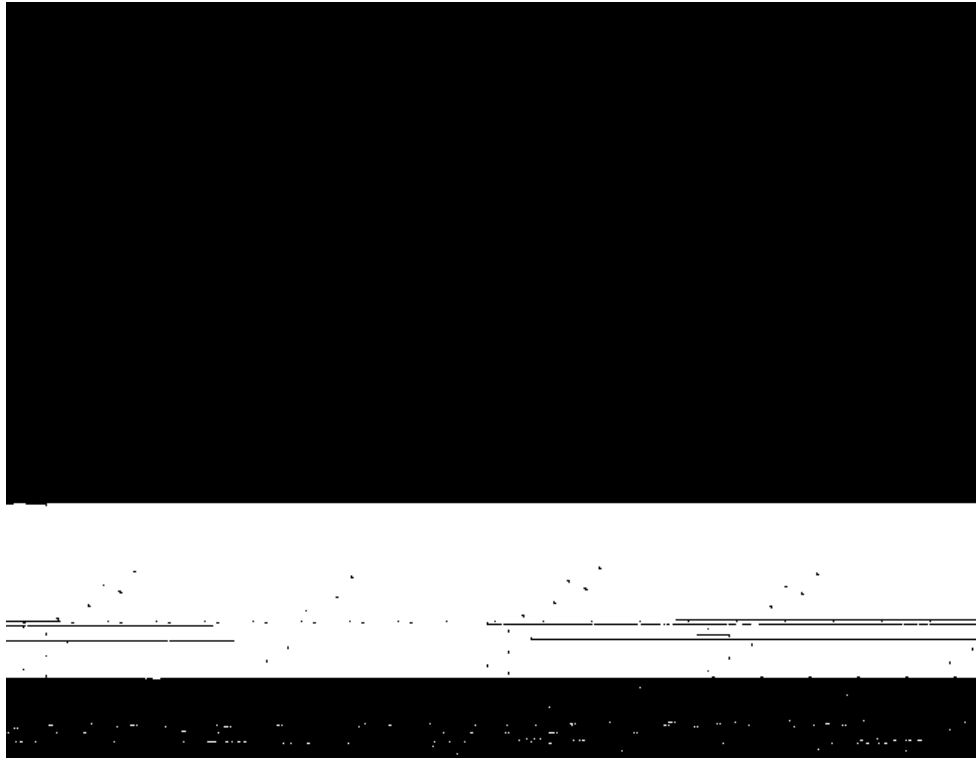
### 6.5.5 Full surface result

The disadvantage of using liquid crystals to measure heat transfer coefficient in the CHTT facility because of the initial loss of data has been discussed previously, but although the alternative method of measurement using thin film gauges overcomes this problem, one of the most significant benefits of liquid crystals is that temperature data is available for the full surface in view of the camera.

The results in Figures 6.33 – 6.36 at experimental conditions show that the *console* provides a film with good continuity, although there is some variation in both  $h$  and  $h$  in the span wise direction, particularly near the hole exits. This is an enhancement of effectiveness downstream of the intersection of two holes, similar to that observed for the low speed results presented in Chapter 5. Similar plots of adiabatic effectiveness for the



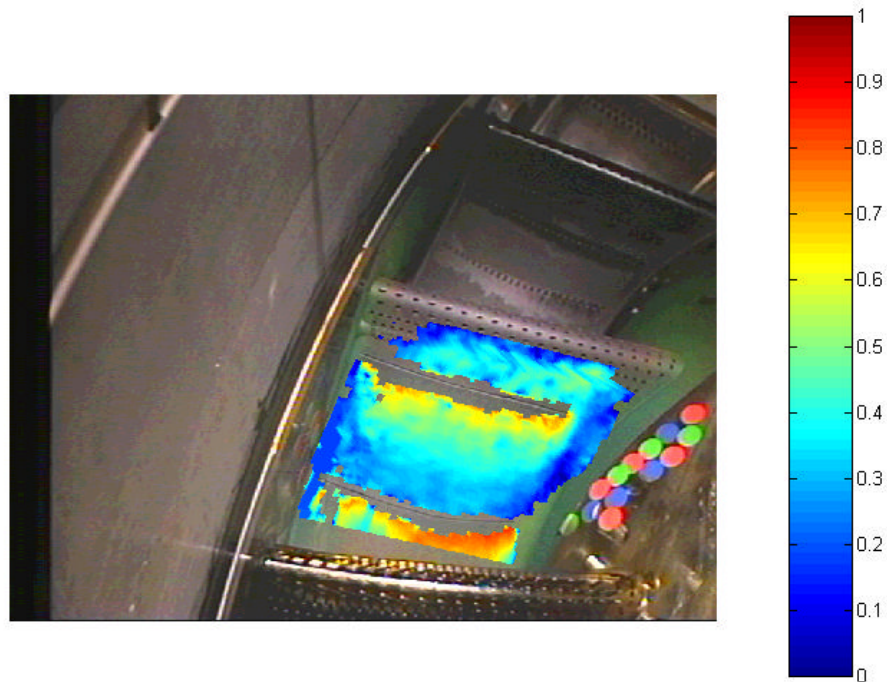
fanned NGV suction and pressure surfaces are shown in Figures 6.37 and 6.38. It was not possible to obtain an  $h$  result however, because of the difficulty in measuring  $h$  using TLC on an acrylic NGV, as previously discussed.



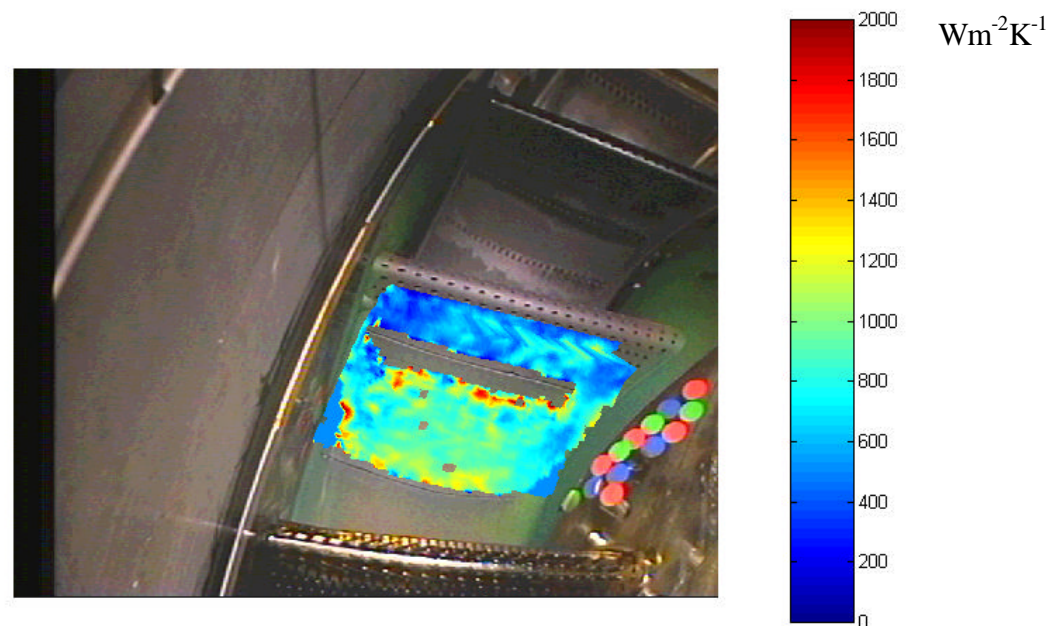
***Figure 6.33: Adiabatic Effectiveness on the console NGV suction surface  
(experimental conditions)***



***Figure 6.34: Heat Transfer Coefficient on the console NGV suction surface  
(experimental conditions)***

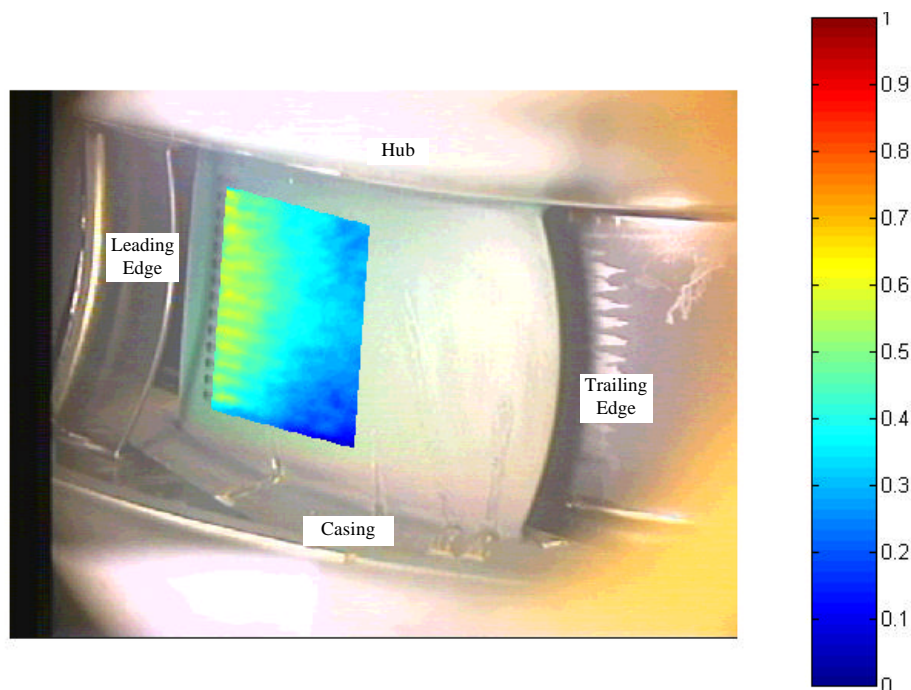


**Figure 6.35: Adiabatic Effectiveness on the console NGV pressure surface (Regions without colour indicate that the solution was unstable (see Section 6.5.3) (experimental conditions))**

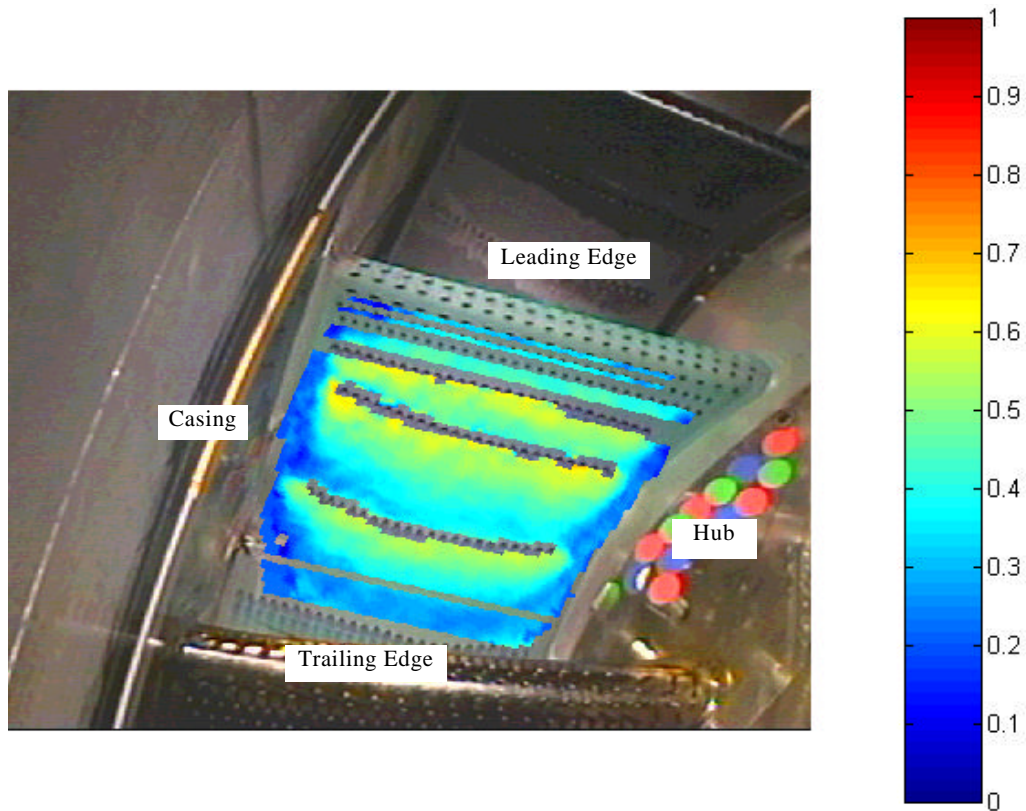


**Figure 6.36: Heat Transfer Coefficient on the console NGV pressure surface (Regions without colour indicate that the solution was unstable (see Section 6.5.3) (experimental conditions))**

On the suction surface, the effectiveness downstream of the F14 row of fan-shaped holes (Figure 6.37) shows that the surface is not uniformly cooled with a variation in  $h$  from 0.6 downstream of the hole to 0.5 between the jets. The *console* effectiveness on the suction surface (Figure 6.33) near the film cooling holes is higher than the fan-shaped holes in the region analysed, and appears to have better uniformity at the scale of the holes, although there are some peaks in  $h$  at a larger scale than the hole width, possibly due to the interaction of multiple jets. Comparing  $h$  on the NGV pressure surface for the *console* NGV (Figure 6.35) and the fanned NGV (Figure 6.38) demonstrates some of the results observed in the mid span averaged results. The peak levels of  $h$  downstream of *console* rows for the *console* NGV are near 0.8 which is significantly higher than the fanned NGV levels of 0.6 – 0.7 behind the holes. However, downstream of the holes, the fanned NGV has on average a slightly higher level of effectiveness, because the film is replenished by intermediate rows of fan-shaped holes.



**Figure 6.37: Adiabatic effectiveness on the fanned NGV suction surface (experimental conditions)**



**Figure 6.38: Adiabatic effectiveness on the fanned NGV pressure surface (experimental conditions)**

### 6.5.6 Changing the number of rows

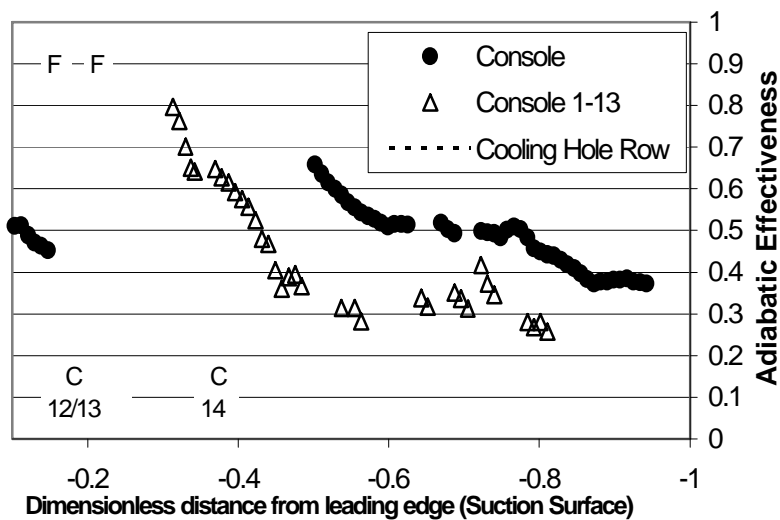
A further experiment was devised to test the performance of the C12/13 row of *console*s by removing row C14. This is of interest to improve aerodynamic efficiency, because in this high Mach number region of the vane, the addition of coolant rows suffers a worse aerodynamic loss due to mixing than in other regions of the vane.

To remove row C14, the suction surface of the *console* NGV was covered with a thin (50 micron) layer of kapton film attached with 3M high strength glue. The layer was attached from three slot heights downstream of row C12/13 to the trailing edge of the vane, and should not have caused any significant change in the shape of the vane. The kapton / glue layer was measured to have a different value of  $\sqrt{rck}$  to stereolithgraphy resin ( $490 \text{ kgs}^{-2}\text{K}^{-1}$  compared with  $720 \text{ kgs}^{-2}\text{K}^{-1}$ ). In order to analyse the liquid crystal images obtained

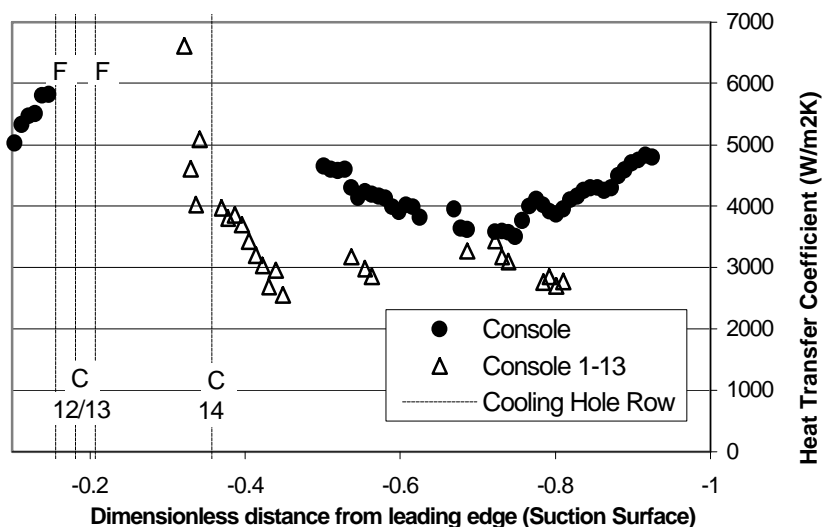
from this experiment, it was necessary to apply a filter analysis technique similar to that used to analyse the results from layered gauges, except that unlike thin film gauge data, there was a lack of data in the first part of the experiment. This was overcome by producing a curve fit routine in *MATLAB*, which generated the full temperature trace for a hypothetical set of fitted parameters ( $h$ ,  $T_{aw}$ ,  $I$ ) and worked on a minimisation routine to fit the hypothetical data curve to the region of the curve for which there was experimental data. This analysis was tested by analysing data for the runs without the kapton layer, assuming that the surface was covered by a film with an identical  $\sqrt{rck}$  value to stereolithography resin. The results obtained by this analysis agreed with the analysis using the previously discussed regression technique. The analysis was also made more difficult because without the coolant film from row C14, the vane surface temperature did not remain within the liquid crystal colour play range for the full run time, so the amount of temperature data available was reduced, particularly near the trailing edge.

The results of this analysis are shown in Figures 6.39 and 6.40. The adiabatic effectiveness measured without row 14 (*console* 1-13) is lower than that with row C14 included, which would be expected since the coolant mass flow rate is reduced, but the level is not significantly lower than the effectiveness measured for the fan-shaped holes shown in Figure 6.19. The heat transfer coefficient is also reduced. In the low speed results (Chapter 5), the presence of console film cooling, particularly at the higher momentum flux ratio, increased the heat transfer coefficient compared with a surface with no film cooling. From this evidence, it is logical to expect that removing a *console* row, and more particularly one with a relatively high momentum flux ratio, would remove the source of an increase in heat transfer coefficient, and hence reduce the heat transfer coefficient over this region. Also, the kapton layer was flexible and during a tunnel run, the tape over the row of *consoles* could have moved outward slightly to create a small protrusion into the flow due

to the pressure ratio across it. This disturbance in the flow would have had the effect of creating a thicker boundary layer, which would also be expected to reduce the heat transfer coefficient. Because this effect could not be removed or accurately measured in the experiments, these heat transfer coefficient results should be considered with caution. The adiabatic effectiveness is not as dependent on the near wall boundary layer as heat transfer coefficient, being a large scale mixing concentration parameter, and this was reliably measured using this technique.



**Figure 6.39: Adiabatic Effectiveness for consoles on suction surface with row 14 missing (experimental conditions)**



**Figure 6.40: Heat transfer coefficient for consoles on suction surface with row 14 missing (experimental conditions)**

## 6.6 Uncertainty Analysis

The two main sources of error in the experimental results can be divided into errors in raw data (e.g. thermocouples, substrate properties), and errors introduced by the data reduction method (curve fitting errors). The first set of errors can be reasonably well estimated, and are summarised in table below. The error due to the curve fitting routines is more difficult to quantify. Numerical experiments to test the sensitivity of the curve fit to a hypothetical set of data are documented in Appendix B. The effect of removing the first section of the curve, adding noise, and an error in the time parameters is tested, by applying the error to the hypothetical data, generating a curve fit, and comparing the values of  $h$  and  $T_{aw}$  from the curve fit to the values used to generate the curve. The total error was calculated as the root mean square values of the sum of the errors due to each source, resulting in an error in  $h$  of 13% and error in  $T_{aw}$  of 5%. These errors combine to give an error in predicted heat flux of 14%. The error in  $h$  measured using thin film gauges by Lai (1999) was 5%.

The effect of this error on the results compared in the previous section is not particularly great, except in regions where the results are very similar. The trends observed in the previous discussions hold. The error estimates made are also total error. Because the same apparatus was used by Lai (1999) to produce the compared results, the random errors generated by the experimental apparatus, such as the shutter opening times, thermocouple error and surface initial temperature, will be consistent, meaning that these errors could be neglected in the comparison of the results.

Error Source	Magnitude	Error in $h$ (%)	Error in $T_{aw}$ (%)
Substrate properties	$720 \pm 10 \text{ Wm}^{-2}\text{K}^{-1}\text{s}^{0.5}$	4	0.6
Surface temperature from TLC calibration	$36 \pm 0.2 \text{ K}$	1	0.5
Surface initial temperature	$50 \pm 1 \text{ K}$	3	3
Time from shutter opening	$2.5 \pm 0.04 \text{ s}$	3	0.6

Removal of initial points from calibration		3	0.4
Experimental noise	Mean ( $T_{\text{noise}}$ ) = 0, - $1 < T_{\text{noise}} < 1$	10	4
Time parameters, $t_1$	$0.10 \pm 0.04$ s	6	1
Time parameter $t_2$	$0.60 \pm 0.04$ s	3	0.6
<b>Total Error</b>		<b>13 %</b>	<b>5 %</b>

**Table 6.4: Data used for uncertainty analysis**

## 6.7 Conclusions

The CHTT facility has been described, with particular reference to heat transfer measurements made at engine representative conditions. The traditional step change method for analysing the transient experimental results has been updated for the current facility to more accurately represent the transient ramp change in adiabatic wall temperature at the start of the experiment. This method was used to process the surface temperature data collected to produce heat transfer coefficient and adiabatic wall temperature data at any location on the NGV surface in view of the camera.

These techniques were used to measure the performance of *console* film cooling at engine representative conditions and this was compared with previously measured results for a NGV with fan-shaped and cylindrical film cooling holes. Measurements of the mass flow rate from the film cooling hole rows demonstrated that the results need to be considered in light of the coolant mass flow available, because there were some significant differences in mass flow due to the different techniques used to manufacture the vanes. In addition to this, a single *console* row generally replaced two fan-shaped rows and was located at the mean position between the two replaced rows. On the suction surface, the *console* effectiveness was significantly higher than the level from fan-shaped and cylindrical holes and the heat transfer coefficient was typically higher than the fanned level and lower than or equal to the cylindrical level. The predicted heat flux showed that the *console* row was lower than the fan-shaped, except towards the trailing edge. On the pressure surface the



coolant flow was less than 70% of the flow-rate from fan-shaped and cylindrical rows. The predicted heat flux was equal to the fanned level downstream of a row, but performance was worse in the region between the next fan-shaped rows and the next *console* row. The predicted heat flux was better than the cylindrical hole in most regions, except for the region mentioned above where the predicted heat flux was equal to the cylindrical region. It would have been preferable to replace a fan-shaped hole row exactly with a *console* row, and to have produced the fanned and *console* NGVs using identical techniques, such that the comparison could have been more exact. The size of the *console* (0.4 mm to replace two rows of fan-shaped holes) was the limiting factor in the exact replacement of fan-shaped hole rows with *consoles* and at the time of the experiments, the opportunity to manufacture a fanned NGV using stereolithography was not available.

The errors in heat transfer coefficient and adiabatic wall temperature using the liquid crystal technique are 13% and 5% respectively. This error is due to both errors in the collection of raw data, and sensitivity of the curve fitting technique to the data provided. The errors in measurement of heat transfer coefficient is halved by using thin film gauges, and in addition to this, the heat transfer data can be acquired at regions where the curve fitting technique was unstable due to the limited data available. The ramp method was developed to reduce the effect of this problem, but it would have been preferable to have produced NGVs with the *console* film cooling configuration from a high conductivity material as well as the low conductivity resin, so that direct heat flux gauges could have been used in combination with liquid crystals, to measure the heat transfer coefficient. This would also have allowed a more direct comparison with the results measured for the fanned and cylindrical hole NGVs, for which heat transfer coefficient was measured in this way. Unfortunately, at the time of the experiments, facilities to manufacture the *console* NGV from a high conductivity material were not available.

## Chapter 7

### Aerodynamic Loss due to Film Cooling

In this chapter the aerodynamic loss due to film cooling using *console* film cooling holes is measured at low speed and at engine representative conditions, using the two facilities already described for the measurement of heat transfer performance. It was found that the *console* caused considerably lower loss than the fan-shaped and cylindrical hole cooling geometries in both facilities. This aerodynamic performance improvement was obtained by a combination of reduced loss in the film cooling hole and reduced mixing loss downstream from the hole exit.

#### 7.1 Measurement of aerodynamic loss

The method used to measure aerodynamic loss and the data analysis techniques follow the work presented by Main et al (1996), Day (1997) and Day et al (1998, 1999, 2000), which will be only briefly summarised here. The general definition of aerodynamic efficiency has already been provided in Chapter 2:

$$e = \frac{\{\text{Actual Kinetic Energy}\}_{\text{mixingplane}}}{\{\text{Theoretical Kinetic Energy}\}_{\text{available}}} \quad \text{at the same exit pressure} \quad (7.1)$$

This definition raises two issues to be answered. The first is, at which plane the actual kinetic energy of the flow should be measured, and the second is the question of what is the ideal situation that defines the theoretical kinetic energy available for the flow.

At the exit plane of the NGV row, the flow is not completely mixed, which means that the measured kinetic energy will vary and be a function of the measurement location. To overcome this, it is usual to relate the non-uniform flow measured at the measurement plane to a uniform, mixed out plane using the equations of continuity of mass, momentum and energy. For linear flow (without a radial pressure gradient) such as the low speed results reported in this chapter, the flow temperature, pressure and velocity will be related to single values of each of these parameters at the mixed out plane. However, for the three dimensional annular cascade, there should be a radial pressure gradient at the mixing plane. This problem is discussed by Day (1997) and a fully three dimensional solution based on mixing the exit plane flow to a free vortex has been described by Main et al (1997). The current work follows the technique used by Day, namely the method of Dzung (1971), which uses a swirl averaging technique to evaluate a set of averaged parameters at a mean radius. Although this method is mathematically equivalent to the radial field, it is not physically correct. Main et al (1997) have shown that this method agrees closely with their own three dimensional results for an uncooled blade.

When the method of Dzung is used to define the exit flow at the mixed out plane, the ideal kinetic energy available is defined by expanding the two streams separately from the initial conditions to the common mixed out plane. In this case the total ideal kinetic energy available is defined as the sum of the kinetic energy of the mainstream and the coolant flows obtained from an isentropic expansion from the upstream conditions to the mixing plane. While the upstream conditions of the mainstream flow are clearly defined by the total pressure upstream of the coolant injection, or the NGV row, the correct coolant condition is not obvious. The coolant is usually delivered from the high pressure compressor outlet and total pressure is lost between there and the outlet of the film cooling holes, at which point it becomes useful. These losses could be included in various places

in the engine analysis, and some may be included in the aerodynamic loss due to film cooling. Day et al (1998) used three different definitions of coolant total pressure and found that these caused significant differences in the calculated loss. These were:

- Coolant total pressure measured in the vane cavity, which is the typical design definition
- Mainstream total pressure which is the pressure that the coolant would have had, had it not been bled off at the compressor outlet
- Coolant total pressure calculated at the exit of the hole, which removes the effect of loss through the film cooling hole

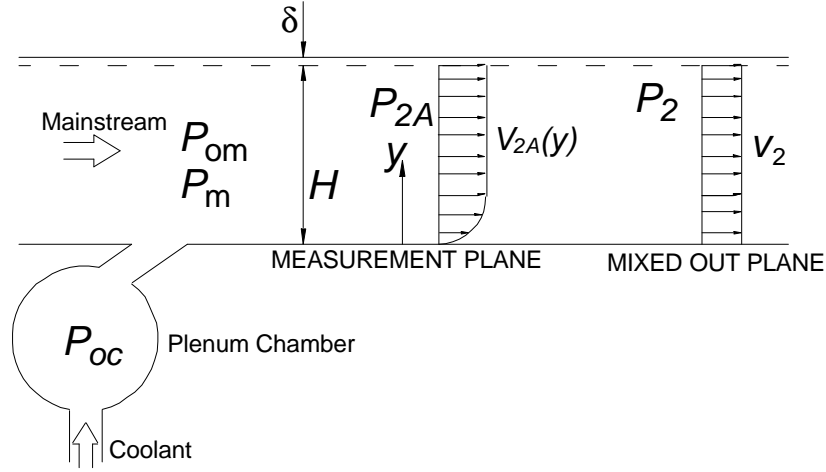
These definitions will be considered in the calculation of loss from the experimental results.

## **7.2 Low speed experiments**

### **7.2.1 Experimental facility**

The low speed facility described in Chapter 5 was used for the measurement of aerodynamic loss at low speed conditions, over a flat plate located in the vertical side wall of the wind tunnel. The only difference was that for the loss measurements, it was not necessary to generate temperature differences, so that the coolant and mainstream were held at the same temperature, and no heat flux was applied to the heater film. The boundary layer pressure and velocity profiles were measured with a horizontally traversing pitot probe at the downstream edge of the plate, at positions directly downstream of the centre of a hole and mid way between two holes. A schematic diagram of the main parameters measured and the location of the measurement and mixing planes is shown in Figure 7.1. The same set of cooling holes and ideal momentum flux ratios

were used as in the previous low speed heat transfer experiments (Chapter 5), namely, cylindrical and fan-shaped holes, *consoles*, a slot and no film cooling. The ideal momentum flux ratios of 0.5, 1.1 and 1.5 were tested at the high Reynolds number based on cooling hole diameter and freestream conditions of 36000.



**Figure 7.1: Definition of measurement and calculation planes**

### 7.2.2 Analytical technique

The boundary layer traverse at the measurement plane is extended to the width of the wind tunnel, less the boundary layer thickness on the far side as shown in Figure 7.1. Although the results of this measurement are dependent on the dimensions of this particular wind tunnel, the purpose of the current experiments is to produce comparative data. In the engine, the height of a downstream traverse required to measure aerodynamic efficiency is one blade pitch, with boundary layers on both suction and pressure surfaces.

For two-dimensional, incompressible flow, the equations of conservation of mass and momentum are used to relate the static pressure and velocity measured at the measurement plane to the hypothetical values at the mixed out plane. Note that an energy conservation equation is not required because the system is at constant temperature:

$$\int_0^H v_{2A} dy = H v_2 \quad (\text{Mass}) \quad (7.2)$$

$$P_{2A} + \mathbf{r} \int_0^H v_{2A}^2 dy = P_2 + \mathbf{r} H v_2^2 \quad (\text{Momentum}) \quad (7.3)$$

From these two relationships, the actual kinetic energy flux of the flow at the mixed out plane can be calculated:

$$KE_{actual} = \frac{1}{2} \dot{m} v_2^2 = \frac{1}{2} \mathbf{r}_2 v_2^3 \quad (7.4)$$

For incompressible flow, the ideal kinetic energy flux available is calculated by isentropically expanding both the coolant and mainstream flows from the upstream total pressures to the static pressure at the mixed out plane:

$$KE_{theoretical} = \frac{\dot{m}_m}{\mathbf{r}_m} (P_{om} - P_2) + \frac{\dot{m}_c}{\mathbf{r}_c} (P_{oc} - P_2) \quad (7.5)$$

From the definitions of aerodynamic loss (2.15) and efficiency (7.1), the final expression for aerodynamic loss for two dimensional, incompressible flow can be written in terms of the measured and calculated parameters as:

$$Loss = 1 - \frac{\frac{1}{2} \mathbf{r} v_2^3}{\frac{\dot{m}_m}{\mathbf{r}_m} (P_{om} - P_2) + \frac{\dot{m}_c}{\mathbf{r}_c} (P_{oc} - P_2)} \quad (7.6)$$

As discussed in Section 7.1, there are three possible definitions of coolant total pressure,  $P_{0c}$ . The first is coolant plenum pressure, which is the value measured in the plenum chamber in the experiments. The mainstream total pressure definition assumes that the coolant has lost the same amount of pressure as the mainstream flow, and the measured total pressure of the mainstream flow is used in the calculation. The third definition of  $P_{0c}$  is the calculated total pressure at the hole exit. This pressure is calculated by assuming that the coolant expands to the mainstream static pressure at the hole exit. The mean flow speed at the hole exit is calculated from the measured mass flow rate of coolant through the hole and the hole exit area, and the calculated coolant exit total pressure is the sum of the static pressure and the dynamic head due to the mean speed, i.e.:

$$P_c = P_m \quad v_c = \frac{\dot{m}_c}{r_c} \text{ where } \dot{m}_c = \frac{\text{mass flow rate}}{A_{throat}} \quad (7.7)$$

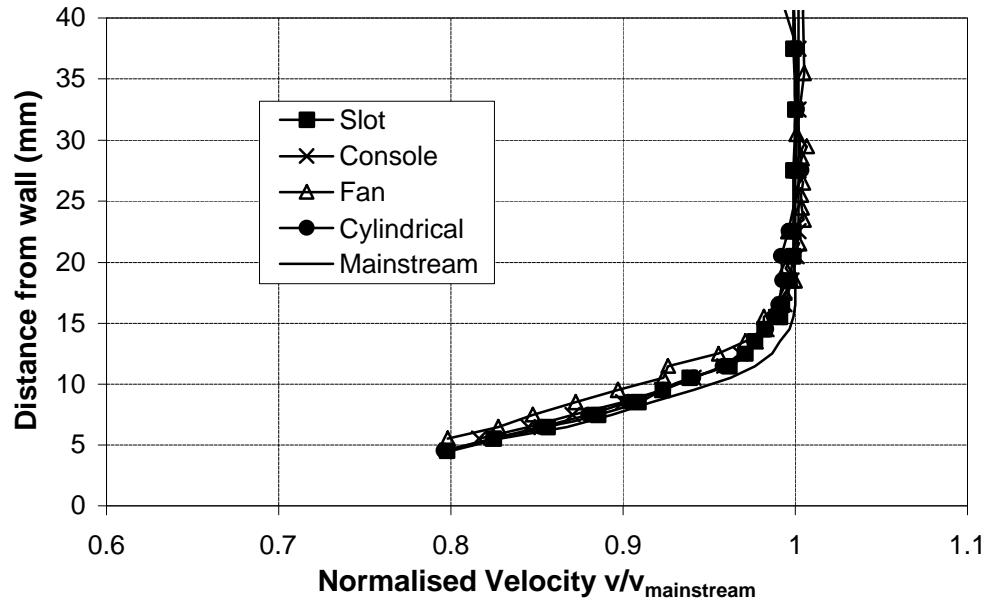
$$P_{0c_{calculated}} = P_c + \frac{1}{2} r_c v_c^2 = P_m + \frac{1}{2} \frac{\dot{m}_c^2}{r_c}$$

### 7.2.3 Experimental results

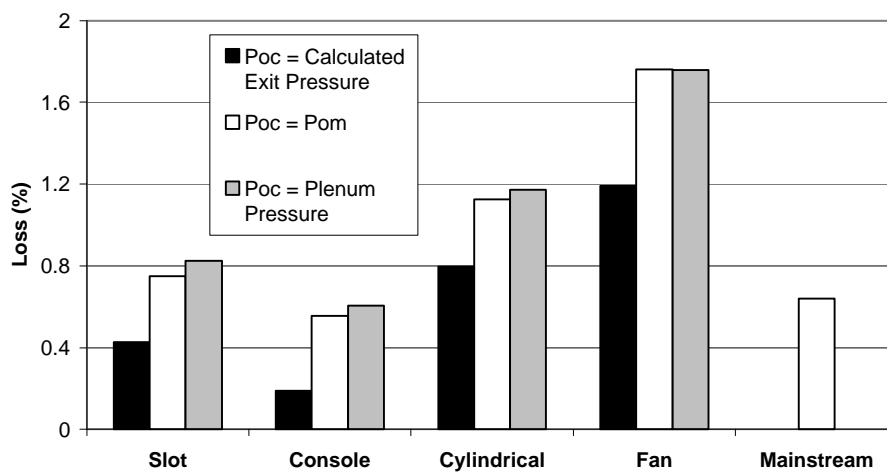
The measured boundary layer velocity profiles for the four film cooling hole geometries and no film cooling are shown in Figure 7.2. The measurement plane is a distance of 1 m or 50  $d$  (based on the cylindrical hole diameter) downstream from the point of injection. All profiles with film cooling show a reduction in velocity and hence actual kinetic energy compared with the profile with no film cooling. The profiles for the cylindrical, slot and *console* flows are similar and the cylindrical holes have the lowest velocity near to the wall. The fan-shaped holes cause an even greater reduction in kinetic energy near the wall than the other holes.

These results can be related to the chart of aerodynamic loss with film cooling hole shape shown in Figure 7.3. The level of aerodynamic loss for the *console* is significantly less than the other film cooling holes, and particularly the difference between the *console* and fan-shaped hole results shows that although the *console* performance was typically similar to, or slightly lower than, the fan-shaped hole performance in the heat transfer experiments, the aerodynamic loss due to film cooling is significantly reduced. In fact, the loss is comparable to the level measured with no film cooling (mainstream), indicating that the *console* flow effectively caused no reduction in aerodynamic efficiency. When the results calculated with different definitions of coolant total pressure are considered, the *console* improves the aerodynamic efficiency compared with no film cooling. The large difference between the fan level with the plenum pressure and exit pressure definitions indicates that a large amount of loss that is generated through the hole due to the

inefficient diffusion process at the hole exit. The loss through the hole is comparable for the other hole shapes.



**Figure 7.2: Velocity profiles for all film cooling hole shapes at  $I_{ideal} = 1.1$**

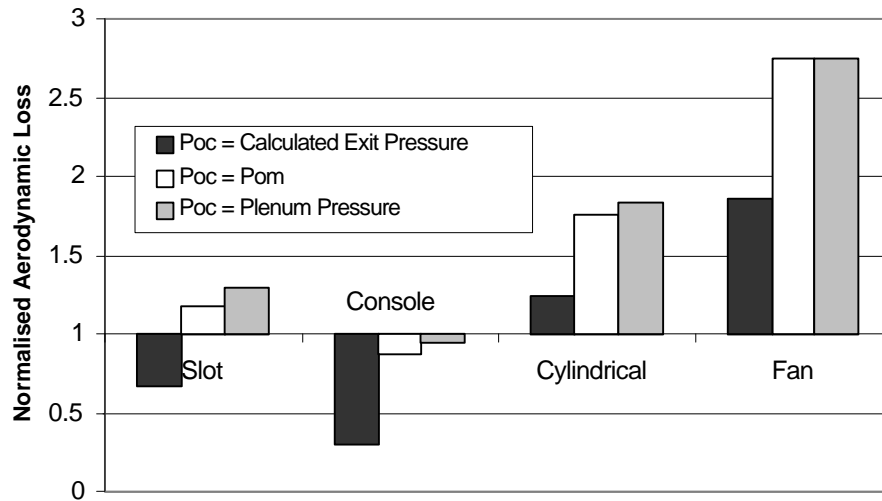


**Figure 7.3: Comparison of aerodynamic loss for the four film cooling configurations and no film cooling (mainstream flow only)**

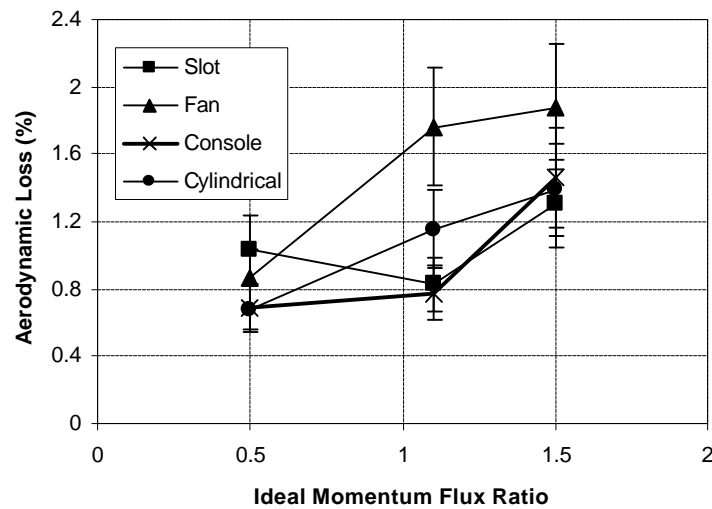
Figure 7.4 shows the same results as Figure 7.3, normalised against the loss with no film cooling by simply dividing by the no film cooling loss value of 0.64% shown in Figure



7.3. This alternative presentation of the data more clearly shows the advantage of the *console* in reducing loss due to film cooling.



**Figure 7.4: Aerodynamic loss normalised against loss with no film cooling**



**Figure 7.5: Variation of aerodynamic loss with ideal momentum flux ratio, for all cooling hole geometries showing data error bands**

In Figure 7.5 the variation in loss with ideal momentum flux ratio is shown. The loss in this figure is calculated using the plenum pressure definition for coolant total pressure. As may be expected, loss typically increases with momentum flux ratio, due to the increased velocities through the hole, increased penetration of the jets into the mainstream and increased mixing losses.

#### 7.2.4 Uncertainty and error analysis

The results above must be interpreted with some understanding of the uncertainty present in the experiments. The sources of error are the measured parameters that are input to the analysis. For this work, a sensitivity analysis was carried out by changing each of the input parameters by the amount of the error and recalculating the loss based on the perturbed data set. The input parameters and the error in each are outlined in Table 7.1. The error due to each source was typically random error, and the 95% confidence level was used. The squares of errors were added and the square root of this sum was the total error.

The final error in loss at the design condition is very sensitive on the upstream total pressure,  $P_{0m}$  and the total and static pressures measured at the measurement plane,  $P_{02A}$  and  $P_{2A}$ . The final relative error in loss is  $\pm 20\%$  of the quoted value. The results shown in Figure 7.3 should be interpreted with this relatively high uncertainty in mind, but the conclusions made above remain valid. The *console* and no film cooling loss are equivalent within the experimental error, and the slot result is on the limit of the error, The cylindrical and fan results, are both higher than the *console* result, and the fan is higher than the cylindrical results beyond the band of uncertainty.

Source	Estimated Error (%)	Error in Loss Calculation (%)	Sensitivity (%)
$m_c$	0.8	0.0	0
$P_{0m}$	0.3	6	2000
$P_m$	1.0	1	100
$P_{2A}$	0.3	15	5000
$P_{0c}$	1.0	1.0	100
$P_{02A}$	0.3	9	3000
$x$	0.3	9	3000
	Total	20 %	

**Table 7.1: Error analysis for low speed aerodynamic loss measurement**

### 7.3 CHTT Aerodynamic Loss Experiments



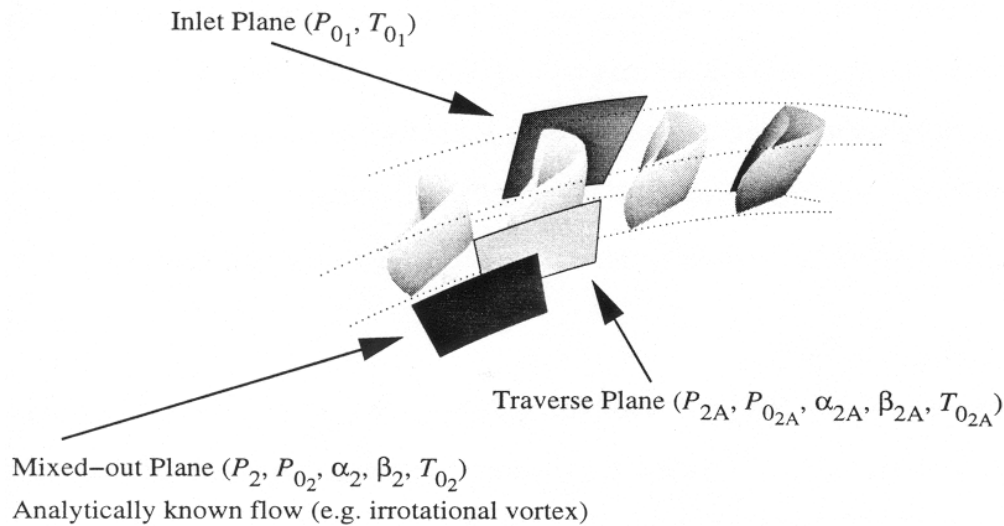
*Figure 7.6: The aerodynamic cassette with the four-hole probe in the measuring position downstream of the NGV*

#### 7.3.1 Experimental facility

Engine representative measurements of aerodynamic loss using an NGV containing rows of *consoles* and an NGV containing rows of fan-shaped holes were made using the aerodynamic cassette in the CHTT. The stereolithography *console* NGV used in the experiment was described in Chapter 6, and the fanned NGV is identical in design to that described in Chapter 6, except that it was manufactured from aluminium. The measurements were all conducted at ambient temperature (with no preheating or heated coolant), using foreign gas as coolant to simulate the engine density ratio.

The aerodynamic cassette contains five NGVs, the first of which is the test vane (stereolithography resin *console* NGV or aluminium fanned NGV), beside an aluminium NGV with a full fanned cooling configuration. The remaining aluminium NGVs have simplified cooling geometry (dummy blades). The aerodynamic cassette is fitted with a

traverse mechanism, with which the experimental probe can be rapidly traversed across two vane passages six times during a single run of the tunnel (3 seconds). The measurement plane is located nominally 117% of the axial chord downstream of the leading edge of the vane.



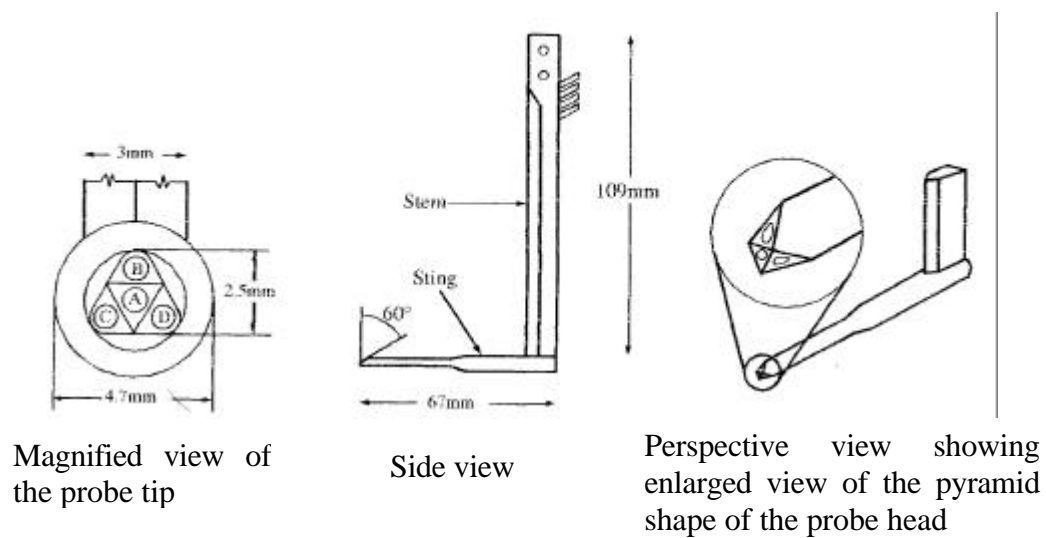
**Figure 7.7: Definition of the mixed-out plane for CHTT experiment from Main et al (1997)**

### 7.3.2 Four hole pyramid probe

The four-hole pyramid probe used to measure the flow at the traverse plane was previously described and calibrated by Main et al (1996) and also used by Day et al (1998, 1999, 2000) and is shown in Figure 7.8. The four hole design was preferred to the traditional five hole probes such as used by Dominy and Hodson (1992) because only the four independent variables that are required to calculate the loss are measured by the probe with no redundant data. This means that the size of the probe can be reduced, as well as reducing the amount of data measured and calibration required.

The tip size of the probe is 2.5 mm and the spacing between the holes is 1 mm. The probe is designed with pyramid faces, rather than the typical rounded or elliptical shape in order to define flow separations at the edges and hence reduce the sensitivity to Reynolds

number, particularly as it was not possible to match the experimental Reynolds number for the calibration. The pressures at the four holes were measured differentially against the upstream static pressure using Kulite XT-190 semi-conductor pressure transducers. The measurement system had a frequency response of 300Hz. The pressure transducers were calibrated each day before a set of measurements was made. The probe velocity was approximately 1 m/s, which had an appreciable effect on the measured results, and the correction developed and described by Main et al (1996) was applied to the data.



**Figure 7.8: The four-hole pyramid probe from Main et al (1996)**

The four pressures at each measured point were transformed to a set of four calibration coefficients, and these were transformed to total pressure, Mach number and pitch and swirl angles using the calibration matrix and the technique described by Main et al (1996). This data was then used to calculate loss using the method of Dzung (1971). The temperature, which is shown as a parameter of the flow in Figure 7.7, is not required in the current work, because all flow streams were held at the same, constant total temperature.

### 7.3.3 Analytical technique

For the mid span traverse in the three dimensional, compressible flow, the equations of continuity, radial and angular momentum and energy were used to relate the measured exit plane to the mixed out plane using the Dzung mixed out plane definitions (Day et al 2000):

$$I_{mass} = \int_{q_1}^{q_2} \mathbf{r}_{2A} v_{2A} \cos \mathbf{b}_{2A} \cos \mathbf{a}_{2A} r_{Dzung} d\mathbf{q} \quad (7.8)$$

$$= L_{tr} \mathbf{r}_2 v_2 \cos \mathbf{b}_2 \cos \mathbf{a}_2$$

$$I_{axial} = \int_{q_1}^{q_2} [\mathbf{r}_{2A} v_{2A}^2 \cos^2 \mathbf{b}_{2A} \cos^2 \mathbf{a}_{2A} + P_{2A}] r_{Dzung} d\mathbf{q} \quad (7.9)$$

$$= L_{tr} [\mathbf{r}_2 v_2^2 \cos^2 \mathbf{b}_2 \cos^2 \mathbf{a}_2 + P_2]$$

$$I_{angular} = \int_{q_1}^{q_2} [\mathbf{r}_{2A} v_{2A}^2 \sin \mathbf{b}_{2A} \cos \mathbf{b}_{2A} \cos^2 \mathbf{a}_{2A}] r_{Dzung} d\mathbf{q} \quad (7.10)$$

$$= L_{tr} \mathbf{r}_2 v_2^2 \sin \mathbf{b}_2 \cos \mathbf{b}_2 \cos^2 \mathbf{a}_2$$

$$I_{energy} = \int_{q_1}^{q_2} [c_{p2A} T_{02A} \mathbf{r}_{2A} v_{2A} \cos \mathbf{b}_{2A} \cos \mathbf{a}_{2A}] r_{Dzung} d\mathbf{q} \quad (7.11)$$

$$= L_{tr} c_{p2} T_{02} \mathbf{r}_2 v_2 \cos \mathbf{b}_2 \cos \mathbf{a}_2$$

Where  $r_{Dzung}$  is the mean radius that is assumed to represent the flow at the mixed-out plane,  $L_{tr} = (q_2 - q_1) r_{Dzung}$  is the length of the traverse,  $\mathbf{q}$  is the circumferential angle and the flow angles  $\mathbf{a}$  and  $\mathbf{b}$  are defined in Figure 7.9. Note that although the total temperature was constant and the same for all flows the energy equation was required, because  $c_p$  was different for air and foreign gas.

Hence in the same manner as for the low speed analysis, the aerodynamic loss can be written:

$$\begin{aligned}
Loss &= 1 - \frac{\text{Actual Exit Kinetic Energy}}{\text{Isentropic KE of mainstream} + \text{Isentropic KE of coolant}} \quad (7.12) \\
&= 1 - \frac{\left( 1 + \frac{\dot{m}_c c_{pc} T_{oc}}{\dot{m}_m c_{pm} T_{om}} \right) \left( 1 - \left( \frac{P_2}{P_{o2}} \right)^{\frac{g-1}{g}} \right)}{\left( 1 - \left( \frac{P_2}{P_{om}} \right)^{\frac{g-1}{g}} \right) + \frac{\dot{m}_c c_{pc} T_{oc}}{\dot{m}_m c_{pm} T_{om}} \left( 1 - \left( \frac{P_2}{P_{oc}} \right)^{\frac{g-1}{g}} \right)}
\end{aligned}$$

This definition takes into account energy introduced to the flow field by the injection of the cooling flow, and establishes the actual decay in the whole blade system, including the feeding loss in the cooling holes, the mixing loss due to injection and the profile loss.

The size of the apparatus means that it is not feasible to measure the mainstream mass flux  $\dot{m}_m$  directly using orifice plates or other flow measurement devices. Day et al (1999) present a method to calculate  $\dot{m}_m$  using the traverse data. This method accounts for the unknown variation in the gas constant  $R_{2A}$  over the traverse region caused by the presence of foreign gas coolant. An approximation to the mass flow may be obtained from the formula:

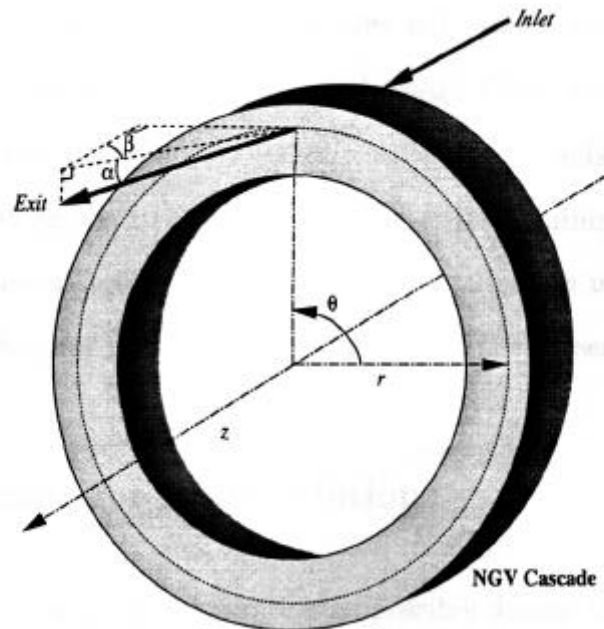
$$\dot{m}_{total} = \dot{m}_{m-air} + \frac{1}{2} \left( 1 - \frac{R_c}{R_m} \right) \dot{m}_c \quad (7.13)$$

where  $\dot{m}_{m-air}$  is the mass flow calculated from the downstream traverse assuming that the coolant is air (ignoring the variation in  $R_{2A}$ ). The coolant mass flow  $\dot{m}_c$  is measured using calibrated orifice plates. This approximation to the mass flow rate typically introduces an error in mass flow of  $< 0.1\%$ , which is considerably lower than the error inherent in aerodynamic probe measurements.

### 7.3.4 Experimental results

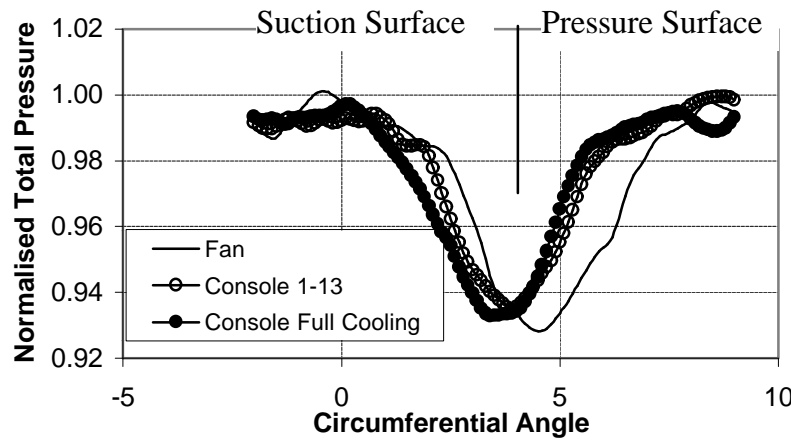
The variation of total pressure, Mach number, swirl and pitch angles across the vane passage (with circumferential angle) downstream of the vane (at the measurement plane) are shown in Figures 7.10 – 7.12 and the definitions of the angles shown in these figures are given in Figure 7.9. These figures show that console film cooling on an NGV creates significant differences compared with fan-shaped hole film cooling on an NGV.

The total pressure downstream of the NGV normalised against the total pressure upstream of the cascade is shown in Figure 7.10. The *console* NGV wake is shifted to the left by 1.5 degrees and has a higher minimum pressure compared with the fanned NGV. Previously, Day et al (1998) performed an experiment in which rows of film cooling holes were progressively uncovered to investigate the effect of changing the amount of film cooling. The minimum pressure changed, but the position of the wake did not.

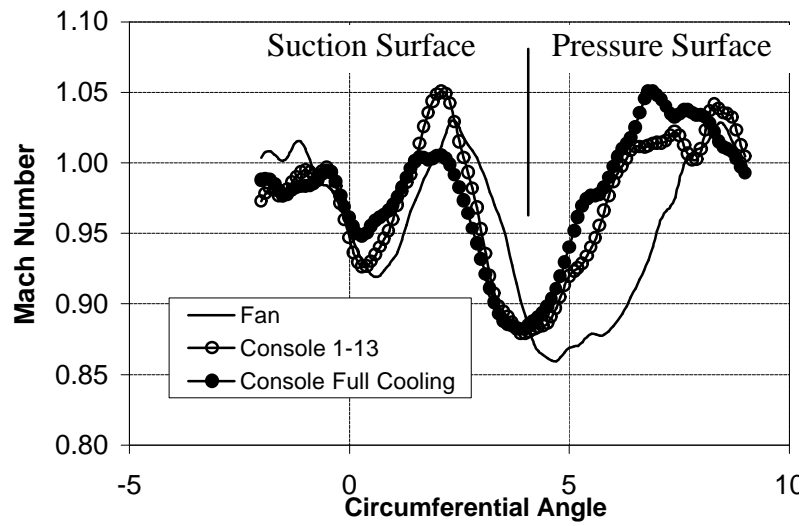


**Figure 7.9: The definition of circumferential ( $\alpha$ ), swirl ( $\beta$ ) and pitch ( $\gamma$ ) angles in the NGV cascade (Day 1997)**

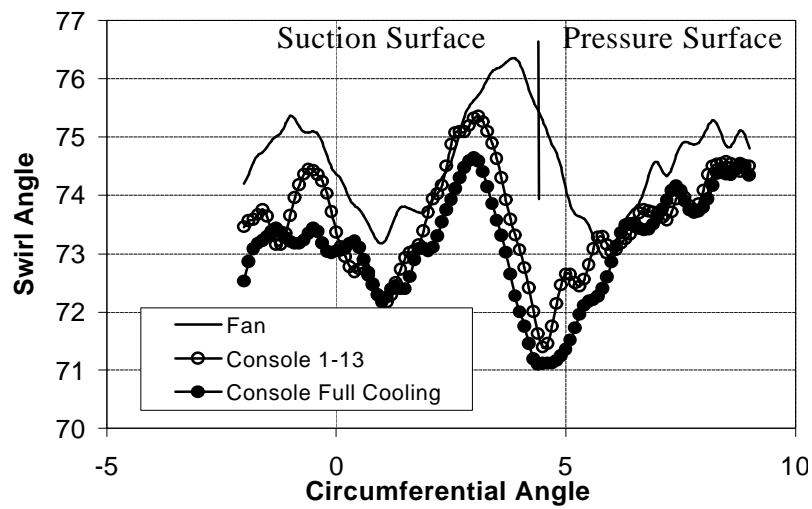




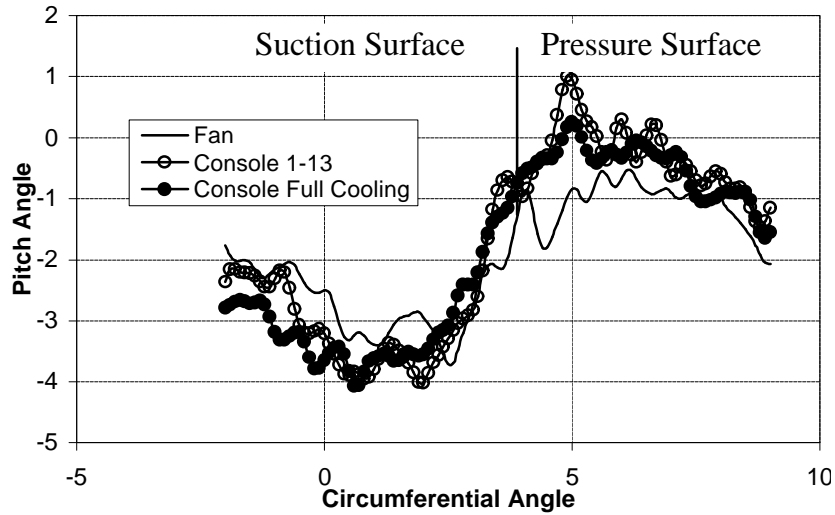
*Figure 7.10: Normalised total pressure*



*Figure 7.11: Mach number*



*Figure 7.12: Swirl angle*



**Figure 7.13: Pitch angle**

In order to investigate whether the change in wake position measured in the current work was due to the fluid mechanics of *console* film cooling or to differences in the manufacture of the NGV between the fanned and *console* NGVs that might have caused it to have a different shape, the final row of *consoles* on the suction surface was closed (*console* 1-13). The effect of this was that the wake was shifted by 0.5 degrees to the right (back towards the fanned result), indicating that there is a definite change in wake position caused by *console* film cooling flows. The differences between the *console* and fanned NGV Mach number distributions in Figure 7.11 have similar characteristics to the normalised total pressure, with a change in circumferential position of  $1.5^\circ$  and a small change in level of 0.025.

The difference in the location of the wake for the fanned and *console* NGVs indicates that there must be a difference in the amount of turning of the flow by the vane, and this is shown in the swirl angle chart in Figure 7.12. The mixed out values of swirl angle for the cooling configurations were  $74.6^\circ$  for the fanned, and  $73.1^\circ$  and  $73.6^\circ$  for the *console* NGV with and without row 14 respectively which implies that the *console* NGV did not turn the flow as much as the fanned NGV. The difference of  $0.5^\circ$  caused by adding the

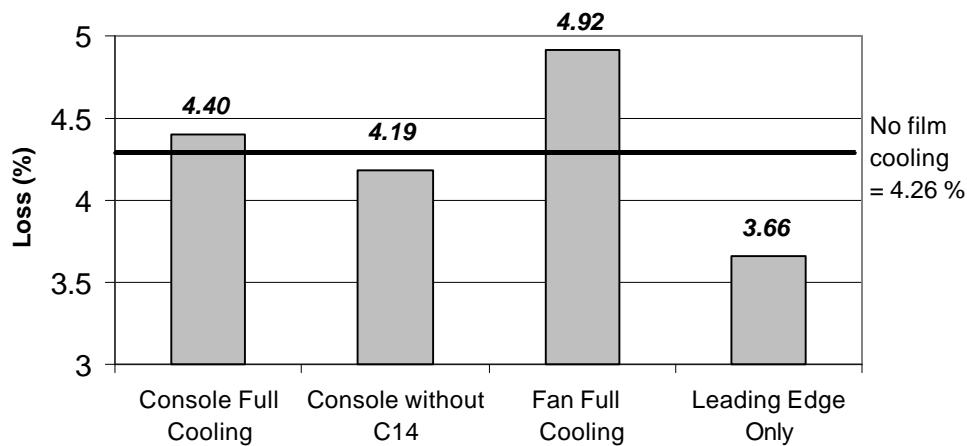
final *console* row indicates that the *console* film must have an effect on the swirl angle. In order to check that the measured changes in wake location and swirl angle were not due to differences in shape between the fanned and *console* NGVs a further experiment was conducted, with all film cooling holes covered on both NGVs by a Kapton film bonded with 3M high bond glue. The mixed out values for these solid vane experiments are given in the final two columns of Table 7.2. The swirl angle for the *console* NGV was 74.4° compared with 74.6° for the fanned NGV. This indicates that although there may be a small shape difference between the two NGVs, it can only explain differences of the order of 0.2° not the measured difference of 1.5° in swirl angle with film cooling. The conclusion must be that the fluid mechanics of *console* film cooling affects the swirl angle and the position of the wake downstream of the NGV.

	<b>Fanned</b>	<b>Console</b>	<b>Console 1-13</b>	<b>Console Solid</b>	<b>Fanned Solid</b>
Coolant pressure ratio $P_{0c}/P_m$	1.02	1.02	1.02	0	0
$P_2$ (bar)	1.12	1.10	1.10	1.14	1.17
$P_{02}$ (bar)	2.02	2.02	2.02	1.99	1.98
Swirl (°)	74.6	73.1	73.6	74.4	74.6
Mach No	0.96	0.98	0.97	0.93	0.90
$\frac{\dot{m}_c}{\dot{m}_m}$ (%)	6.0	6.1	5.9	0	0
$P_{01}$ (bar)	2.07	2.07	2.07	2.07	2.07
Efficiency	0.959	0.963	0.965	0.964	0.966
Loss	4.1%	3.7%	3.5%	3.6%	3.4%
Scaled Loss	4.9%	4.4%	4.2%	4.3%	4.1%
Normalised Loss (4.26%)	1.15	1.03	0.98	1.00	0.96

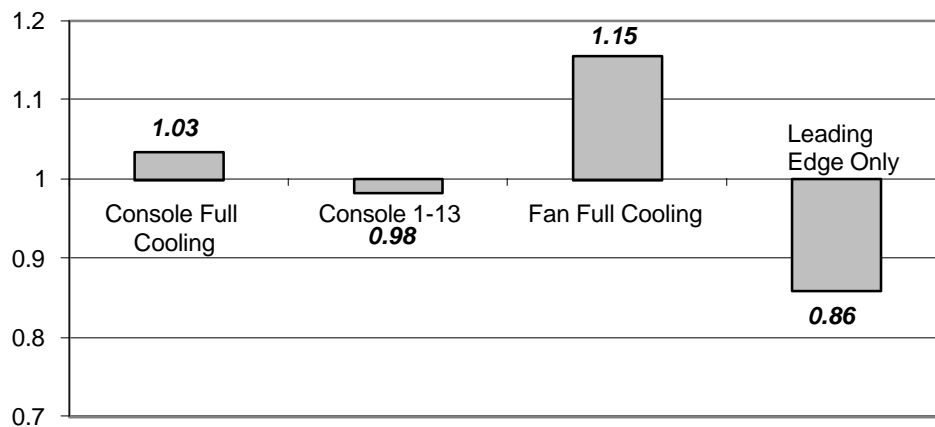
**Table 7.2: Results calculated at the mixed out plane**

Figure 7.14 shows aerodynamic loss results and Figure 7.15 shows the loss results normalised against the aerodynamic loss measured with no film cooling of 4.26% (Day et al 1999). The measured loss for the fan full cooling in the current work was 0.041, which

was slightly different to the value of 0.049 measured by Day et al and shown below. In order to compare the current results with the Day et al work, the loss values for both *console* results and the fan full cooling result were scaled by the ratio of the Day fan result to the current result. This means that the results can be compared with, for example the value for the leading edge only. This is valid, because it is the relative level of loss that is important in the present work, not the absolute values.



**Figure 7.14: Aerodynamic loss for film cooling configurations**



**Figure 7.15: Aerodynamic loss for film cooling configurations normalised against loss without film cooling (NFC)**

Figures 7.14 and 7.15 show the significant reduction in aerodynamic loss for the NGV with *console* film cooling compared with fan-shaped film cooling holes, where the additional loss due to film cooling for the *console* is only 20% of the additional loss due to film cooling for the fan-shaped holes. When the last *console* row on the suction surface

(C14) is removed, the aerodynamic loss is actually reduced compared with the level with no film cooling. The coolant films may have changed the point of transition and the state of the boundary layer over the vane.

The penalty associated with row C14 is less than the penalty associated with the equivalent fan-shaped hole row, F14, even though there is 45% more coolant ejected from row C14 (Table 6.2). This is important, because the Mach number at this row is the highest value at which film cooling is applied at  $M = 0.95$ . The loss penalty associated with film cooling is worst in high Mach number regions, so the favourable performance of the *console* in this region is particularly important.

### 7.3.5 Error and uncertainty analysis

As previously mentioned, the measurement technique, apparatus, and calibration were all identical to the methods used by Day (1997), so the uncertainty analysis for the present work is identical to the one presented by Day. There, the absolute uncertainty in measurements of efficiency was quoted as  $\pm 0.11\%$  and because the loss is simply defined as  $1 - \eta$ , the absolute error in loss is also  $\pm 0.11\%$ . Note that this is an error in percentage points of loss, not a percentage of the loss. That is, the loss with no film cooling is 4.26%  $\pm 0.11\%$ . The absolute error in the normalised loss shown in the table above is 0.025. This means that the result for the *console* rows 1-13 loss at 0.98 could be equal to one within the experimental uncertainty, but the difference between the console and fanned NGVs and the two console results is outside of the probable ranges of the error.

## 7.4 Conclusions

The aerodynamic loss due to film cooling for a *console* film cooling hole has been compared with the loss for fan-shaped holes, cylindrical holes and a slot at low speed, and

fan-shaped holes at engine representative conditions. The results have shown that the *console* demonstrates significantly reduced loss due to film cooling compared with the fan-shaped film cooling geometry. When this is considered with the data from previous chapters, it is clear that the *console* is a significant improvement on the existing geometries, because it provides a similar level of film cooling to the existing holes, but only 20% of fan-shaped hole loss at CHTT conditions and 28% of fan-shaped hole loss at low speed conditions.

## Chapter 8

### Flow Visualisation of Cooling Jets

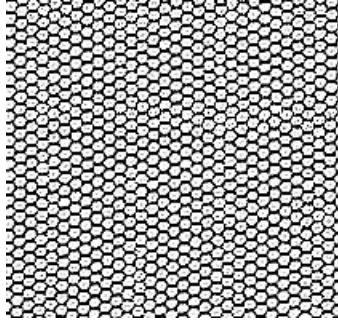
In this chapter an investigation into the performance of the *console* by measuring the temperature contours of the jet downstream of injection in the low speed wind tunnel is described. Thermochromic liquid crystals sprayed onto a nylon mesh were used to provide both flow visualisation information and contours of jet effectiveness.

Many previously identified flow features such as the kidney vortex can be seen in the data for the conventional holes. The previously mentioned explanations for the performance of the *console* are verified as it is shown that the *console* flow is indeed very similar to a slot, and that the coolant film is considerably thinner from a row of *consoles* than from fan-shaped and cylindrical holes.

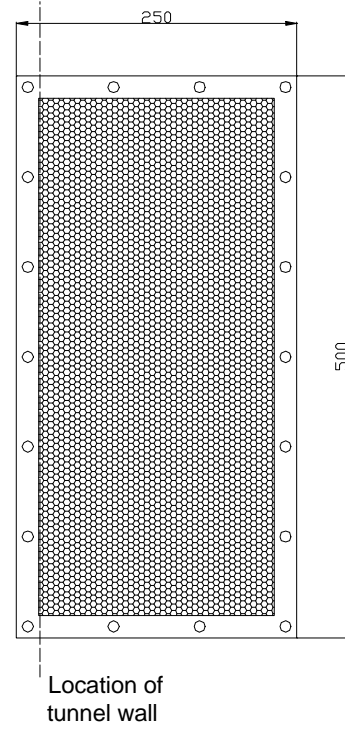
#### **8.1 Experimental apparatus**

The experiments were performed in the low speed wind tunnel described in Chapter 5, using the film cooling hole plates, coolant air heater and coolant supply described in that chapter. The flat plate heater was not used for these experiments, and the TLC layer on the flat plate was removed for the present work.

The fine nylon mesh fabric shown in Figure 8.1 was stretched onto a frame constructed from acrylic, which covered the height and half the width of the tunnel test section. The mesh was sprayed with narrow band TLC, similar to those used in the low speed



**Figure 8.1: Nylon mesh fabric (actual size)**



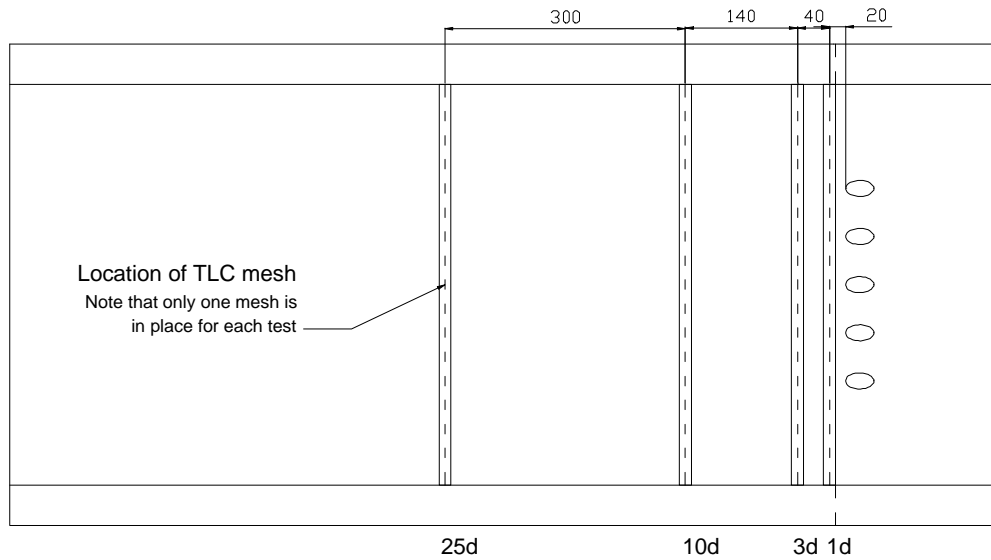
**Figure 8.2: TLC mesh**

experiments. With the entire tunnel wall upstream of the mesh painted black, it was possible to view and photograph the TLC colour play from the mesh. This mesh was similar to that used by Mee et al (1999). The TLC were calibrated using two thin wire, K Type thermocouples that were threaded into the mesh. The flat plate wall of the wind tunnel was adapted such that the mesh could be inserted at distances of 1, 3, 10 and 25 cylindrical hole diameters from the film cooling hole exit as shown in Figure 8.3.

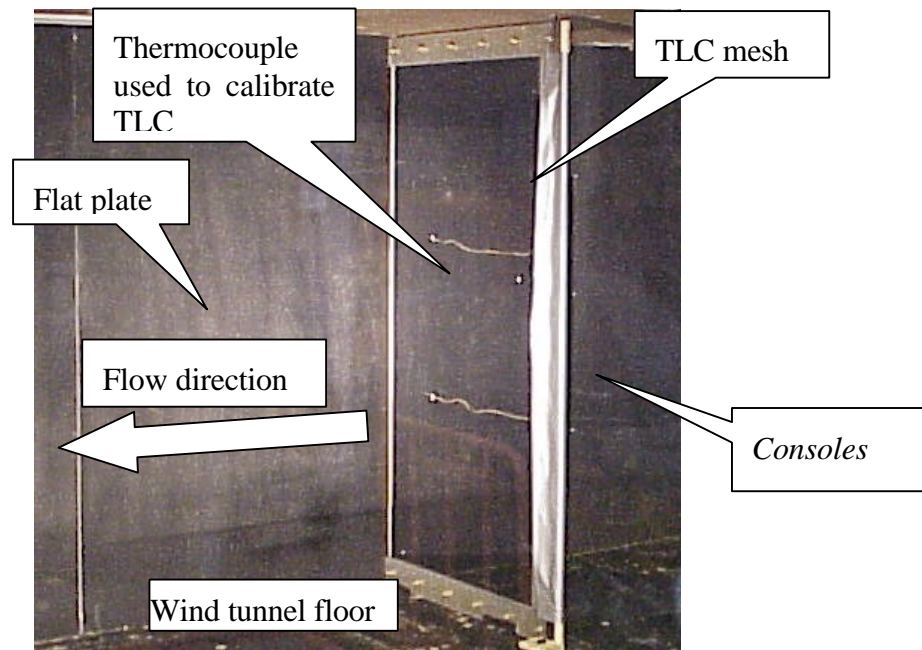
A digital camera was mounted in the wind tunnel, well downstream of the mesh, in order to record images of the crystal colour play at various coolant temperatures. A set of experiments was conducted to match the low speed experiments documented in Chapter 5, with a mainstream speed of  $26 \text{ ms}^{-1}$  (Reynolds number based on mainstream flow and cylindrical hole diameter = 36000) and ideal momentum flux ratio of 1.1. In order to test whether the *console* flow did benefit from the Coanda effect, the experiments were also conducted with a low mainstream speed of  $5 \text{ ms}^{-1}$  (Reynolds number of 6000), and without crossflow. For both these cases, the coolant driving pressure,  $P_{0c}-P_m$ , was kept



constant at the high crossflow level, resulting in an ideal momentum flux ratio of 40 for the low mainstream speed and an infinite momentum flux ratio for the case without crossflow.



**Figure 8.3: Locations of mesh in wind tunnel working section**



**Figure 8.4: Low speed wind tunnel working section with TLC mesh at 1d**

## 8.2 Analytical technique

The images of the liquid crystal colour play such as shown in Figures 8.6-8.8 were enhanced in *MATLAB* using the blue part of the RGB data, and the function *histeq*, which

equalises the colour intensity histogram for an image. The function *edge* was used to detect the regions of highest colour gradient and from this the edges of the TLC colour play could be extracted. This method was found to be the best way to extract the colour contours from the mesh, which was difficult to photograph because it was very fine.

In addition to providing information about the size and structure of the film cooling jets at constant coolant temperature, the TLC mesh technique was used to produce contours of gas effectiveness by increasing the coolant temperature and recording the TLC colour play at each steady state point. The gas effectiveness is defined similarly to the previously defined adiabatic effectiveness (Chapter 2), with the temperature at the mesh replacing the adiabatic wall temperature:

$$h_{gas} = \frac{T_{mesh} - T_r}{T_{0c} - T_{0m}} \quad (8.1)$$

The gas effectiveness contours give an indication of the shape of the jet, and the extent of mixing between the free stream and the jet at the jet edges.

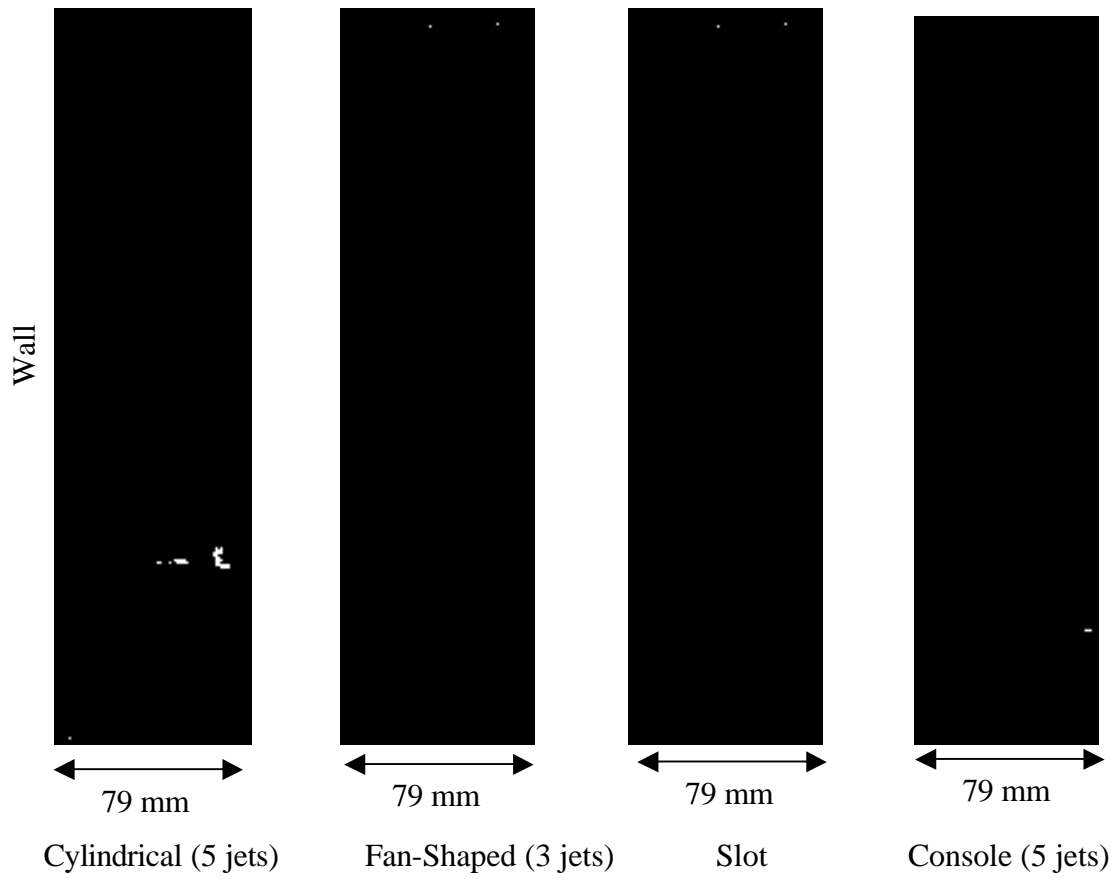
### 8.3 Experimental results

#### 8.3.1 Liquid crystal images

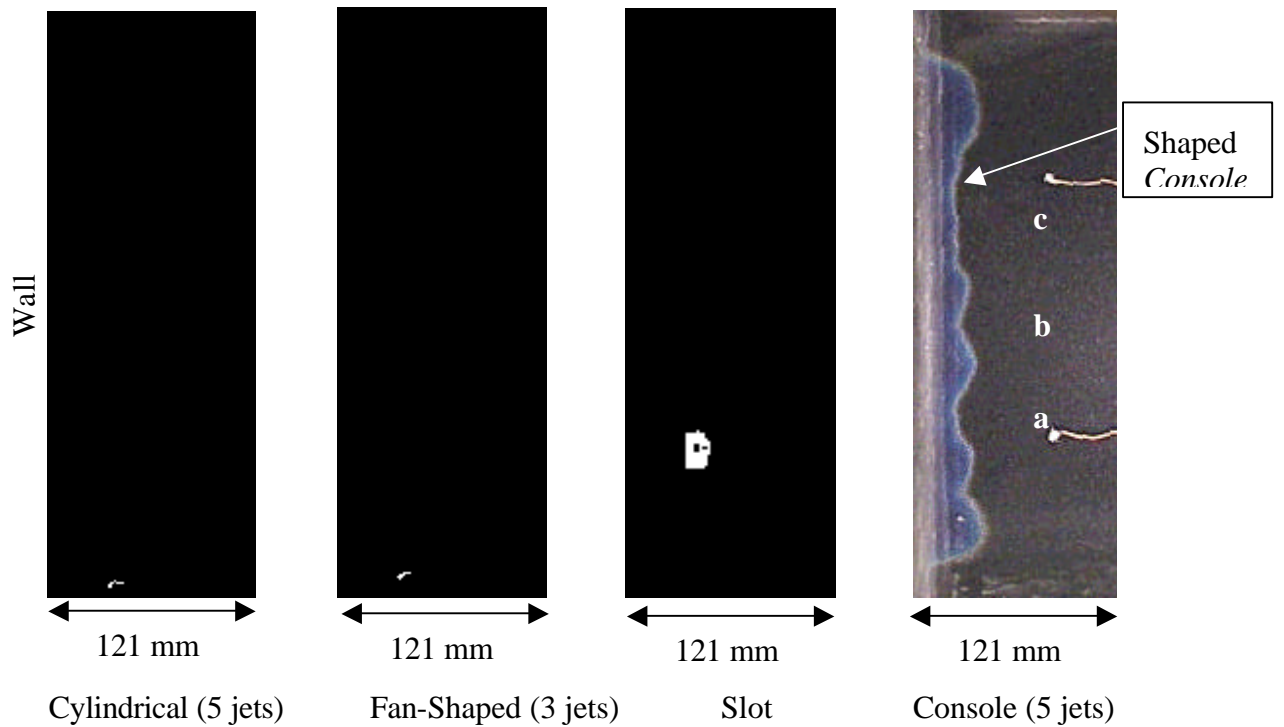
Figures 8.5 and 8.6 show the liquid crystal images at 10 *d* from injection with  $v_m = 26 \text{ ms}^{-1}$  and  $v_m = 5 \text{ ms}^{-1}$  respectively. The images shown are at the highest coolant temperature, giving a gas effectiveness of approximately 0.1. In Figure 8.5 (high  $Re_d$ , design *I*), the *console* and slot films are shown to have a similar thickness. The *console* film shows some structure, or non-uniformity compared with the slot. The fan-shaped hole film is thicker than the slot and *console* films, and the jet structure from the three fan-shaped hole jets is visible. The jets are closer to the surface downstream of the hole centre, which indicates the presence of anti-kidney vortices in the jet such as measured by Haven et al (1997) and

sketched in Figure 8.7. These vortices cause the fan-hole jets to remain close to the surface, and in conjunction with the good spreading of the jets account for the improvement of fan effectiveness over cylindrical holes. The cylindrical hole film is significantly thicker than the other films, and the jets do not meet. The jets at the edge of the row are almost lifted off the surface in this view. The centre jets show the typical cylindrical hole jet kidney vortex shape.

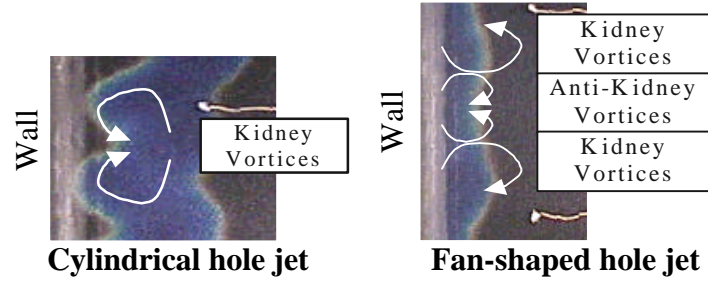
In Figure 8.6 with a much lower mainstream  $Re_d$  (6000), all of the jet features mentioned are further exaggerated. The cylindrical jets have lifted off the surface at the jet centre and the vortex structure is clear, as sketched in Figure 8.7. The fan-shaped hole structure is similarly clear. The slot flow remains very uniform, except at the edges of the slot, where wall vortices cause the jet to spread out from the surface. The *console* film shows that the two edge jets spread from the surface and the two lower jets (marked a and b) exhibit evidence of an anti-kidney vortex structure with the centre of the jet pressed towards the surface. If the vortical structure is similar to that sketched for a fan-shaped hole in Figure 8.7, it is likely that there would be an interaction between the kidney vortices at adjacent holes, because the holes are immediately adjacent, rather than a small distance apart as is the case for the fan-shaped holes. This structure is most likely the cause of the regions of higher effectiveness downstream of the intersection of two film cooling holes identified in Chapter 5. The jet marked c in the photograph is very uniform at the surface. The *console* for this jet had been shaped slightly prior to this experiment by radiusing both the inlet and outlet edges of the hole. This shows that there should be an advantage in shaping the holes, because the film becomes more similar to a slot film.



*Figure 8.5: Photographs of contours at 10 d, with  $I = 1.1$  and  $v_m = 26 \text{ ms}^{-1}$*

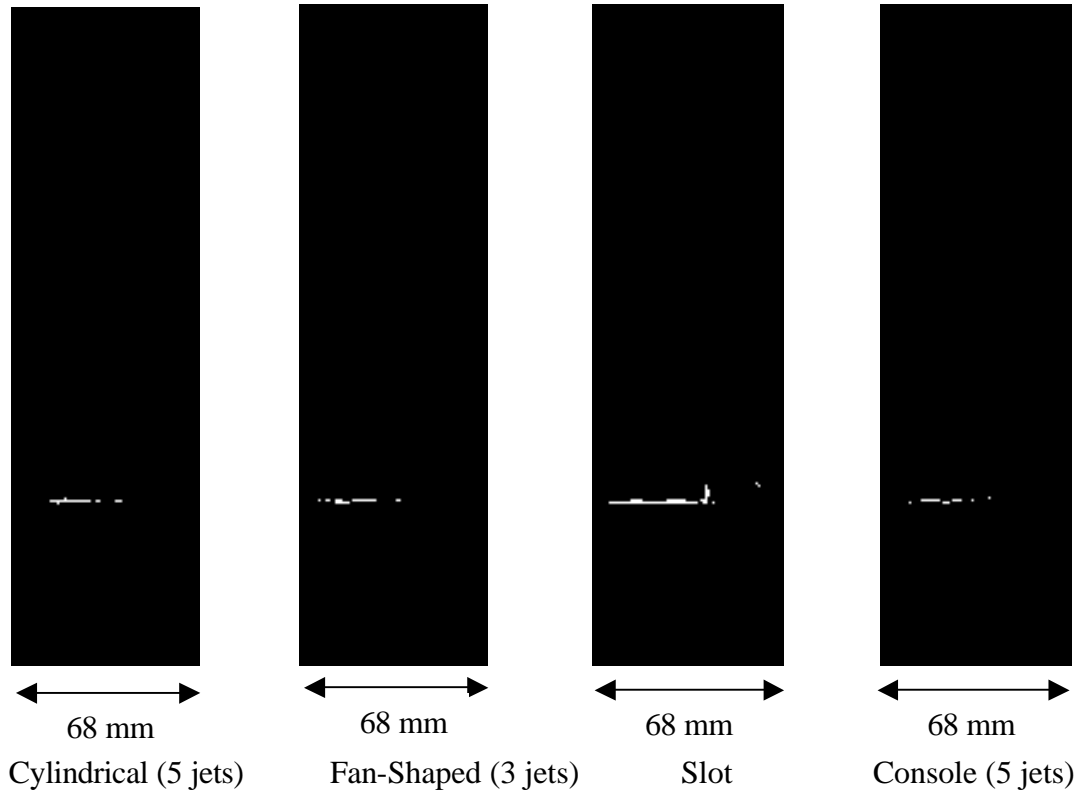


*Figure 8.6: Photographs of contours at 10 d, with  $I = 40$  and  $v_m = 5 \text{ ms}^{-1}$*



**Figure 8.7: Kidney and anti-kidney vortices in cylindrical and fan-shaped hole jets**

The images in Figure 8.8 show the jets with no crossflow. The cylindrical jets lift completely off the surface, and the fan-shaped hole film is very thick and diffused near the edges of the jet, although it does remain attached to the surface. The *console* and slot films both demonstrate the Coanda effect, because they remain attached to the surface. There is some structure in the *console* jet, and the film is completely removed from the surface for the two edge holes. At distances further downstream ( $10 d$  and  $25 d$ ) the jets were not well defined because the warm jet was mixed with the cool ambient air, and the edge contour was difficult to extract.



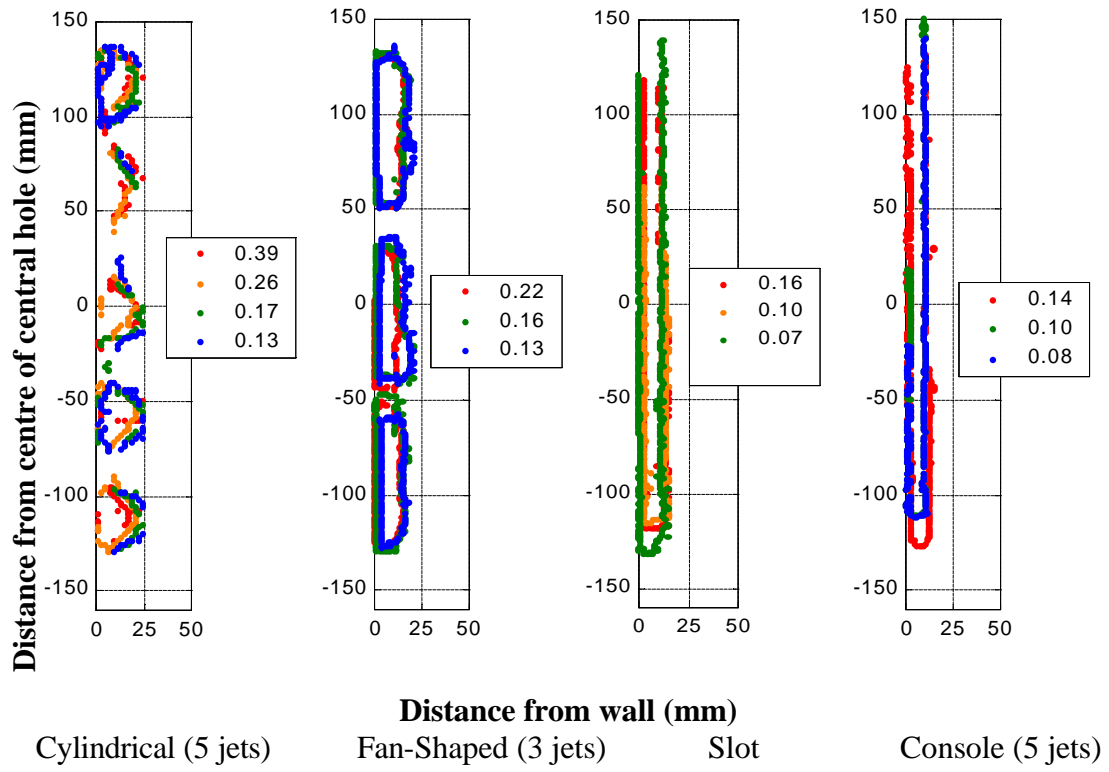
**Figure 8.8: Photographs of contours at  $3 d$ , with  $I = ¥$  and  $v_m = 0 \text{ ms}^{-1}$**

### 8.3.2 Contours of gas effectiveness

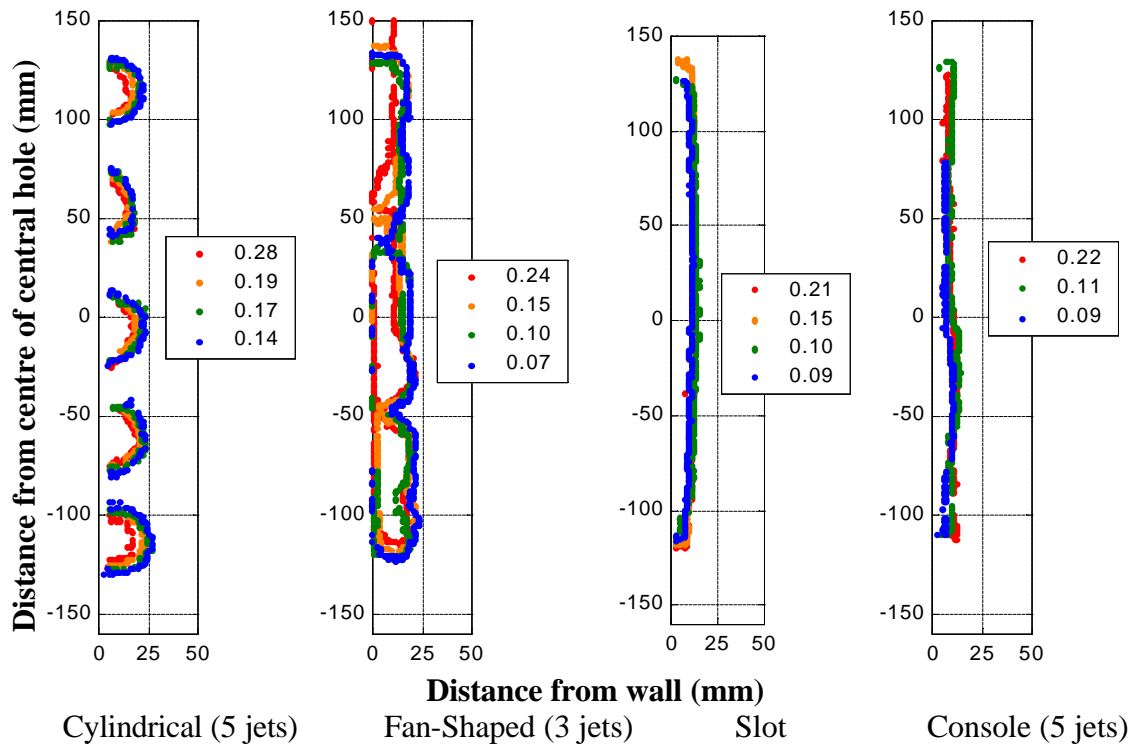
Many of the features of the jets identified in the previous section are repeated in these plots of gas effectiveness, which show the shape and location of the jets. The effectiveness decreases with increasing distance from the centre of the jets. It was found that there was a strong gradient in temperature (and hence effectiveness) at the edges of the jet, particularly with crossflow applied.

#### Contours with high crossflow and design I

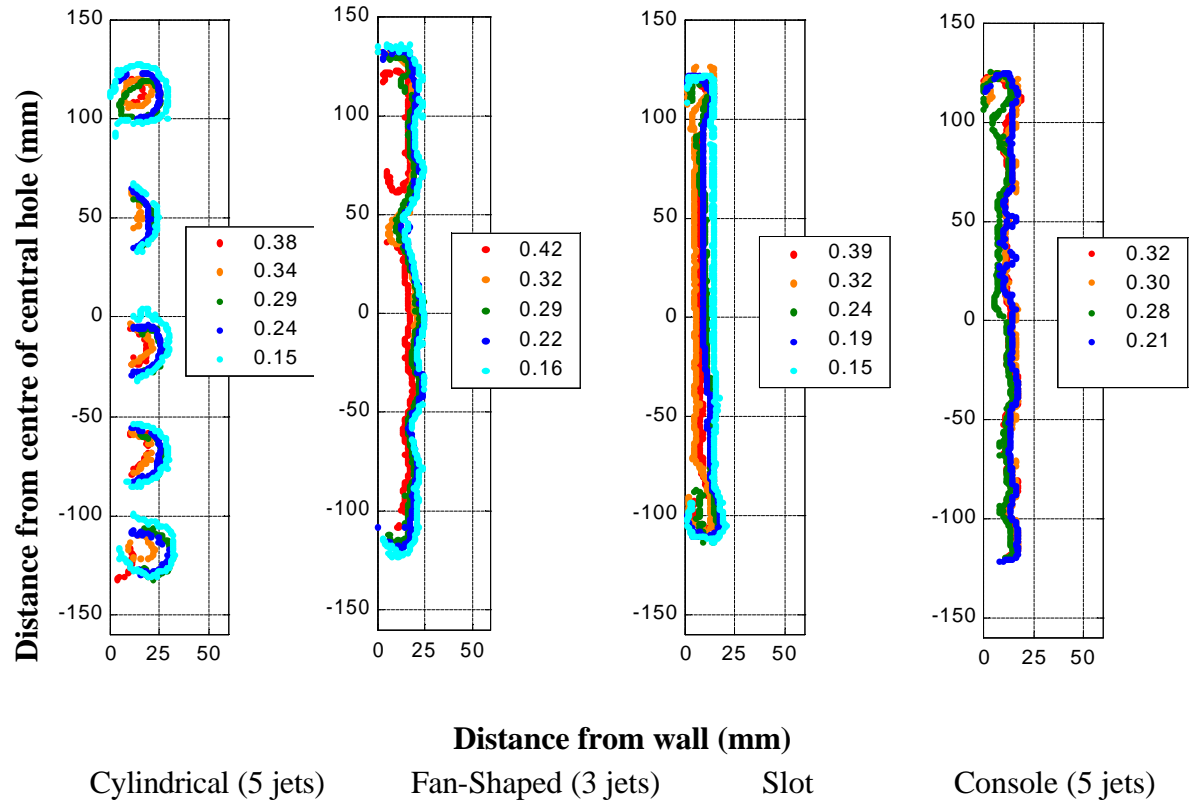
The contours in Figures 8.9-8.12 show the development of the jet flow with downstream distance from the injection location. The slot and *console* flows remain close to the surface until  $25 d$  where the jets become both more diffused near the jet boundary and the film starts to lift off the surface at the edge of the jet. This edge effect is not typical of the mid jet flow, which remains attached at all measured locations. The fan-shaped hole jets are separate close to the hole, but they spread to form a closed film from a  $3 d$  downstream. At  $25 d$  the film is completely continuous, with some small structure from the fan jet vortices as described in the previous section. The fan film is thicker than the slot and *console* films at all downstream distances. The cylindrical jets do not meet, and remain at a similar thickness until  $25 d$  where the film thickness has increased significantly and the lower three jets have joined. The two edge jets also start to lift off the surface at this location.



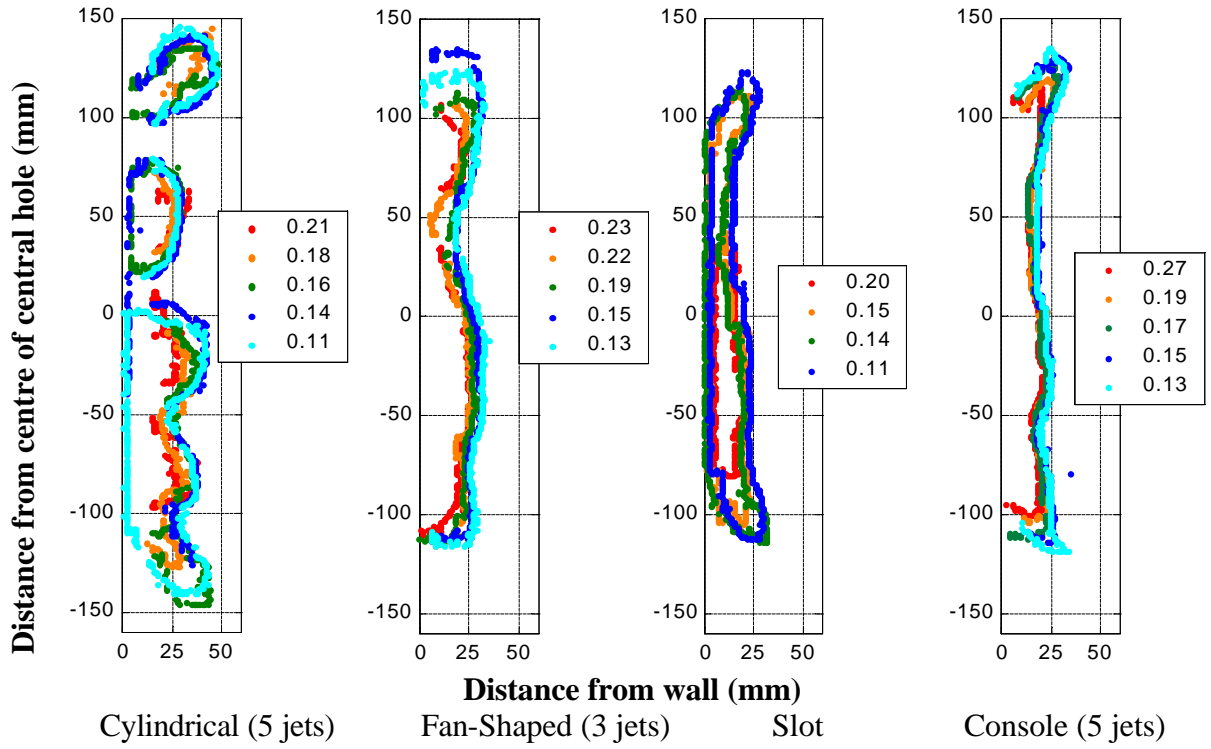
**Figure 8.9: Contours of effectiveness at 1 d,  $I=1.1$ ,  $DP_c=412$  Pa,  $v_m = 26 \text{ ms}^{-1}$**



**Figure 8.10: Contours of effectiveness at 3 d,  $I=1.1$ ,  $DP_c=412$ ,  $v_m = 26 \text{ ms}^{-1}$**



**Figure 8.11: Contours of effectiveness at 10 d,  $I=1.1$ ,  $DP_c=412$ ,  $v_m = 26 \text{ ms}^{-1}$**



**Figure 8.12: Contours of effectiveness at 25 d,  $I=1.1$ ,  $DP_c=412$ ,  $v_m = 26 \text{ ms}^{-1}$**



## Contours with no crossflow

The slot film is extremely uniform without crossflow, as might be expected, except for near the edges of the slot. Here, the coolant formed a thicker layer, although it did not lift off from the surface. For the *console* coolant film without crossflow the jets from the two outside edge holes lifted off from the surface. This was interesting because it reinforces the fact the one of the strong advantages of the *console* is the interaction of jets from adjoining holes. An individual *console* would not benefit from the Coanda effect and remain attached to the surface at very high blowing rates or without crossflow. The cylindrical jets lifted off the surface, and the spacing of the effectiveness contours shows that there was more mixing of the jet with ambient air, causing the jet boundaries to be more diffused. The fan-shaped hole film again remained attached to the surface, but in a film which was quite diffused near the edge and was spread to almost to the thickness of the cylindrical jets.

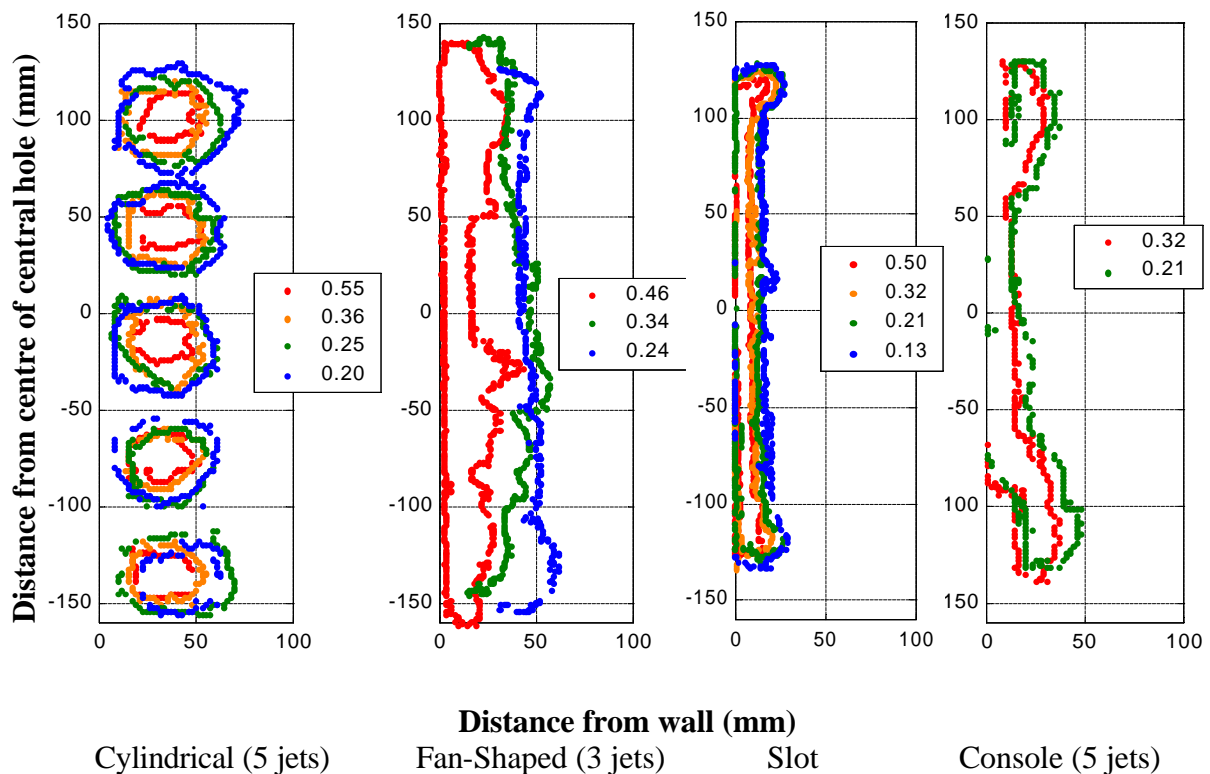
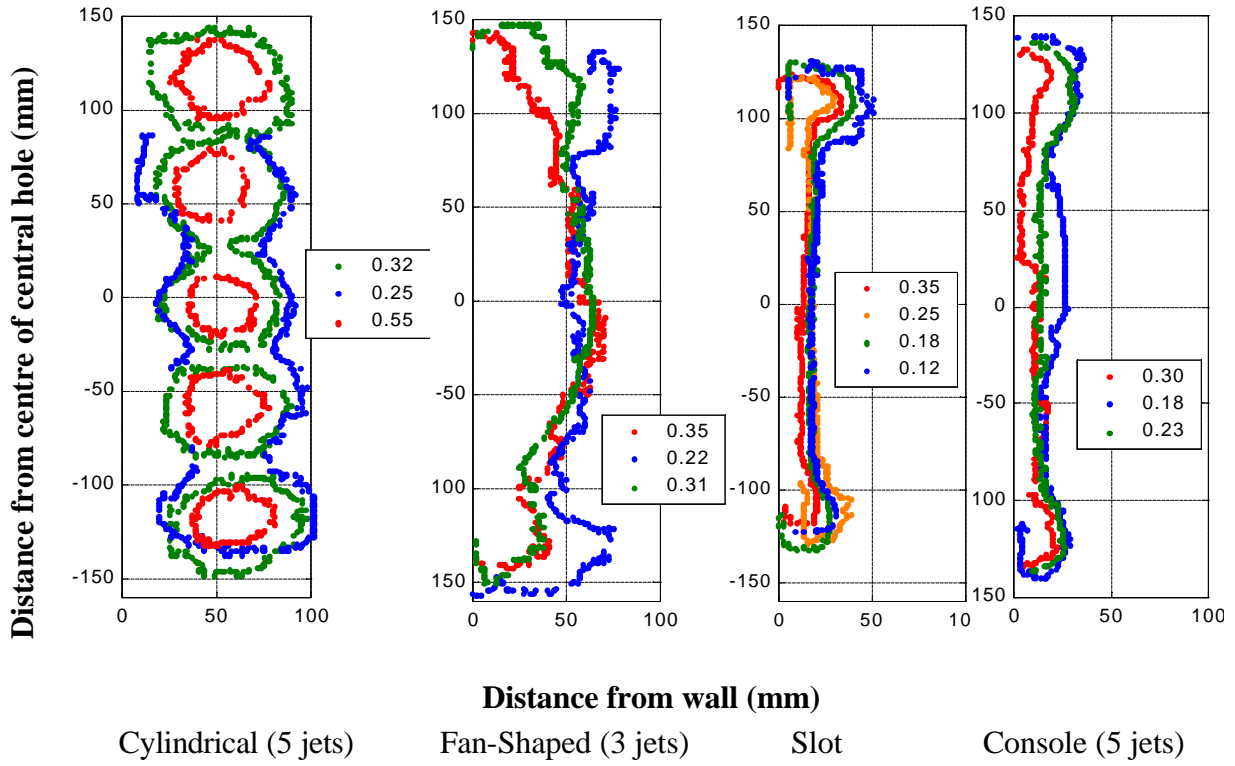
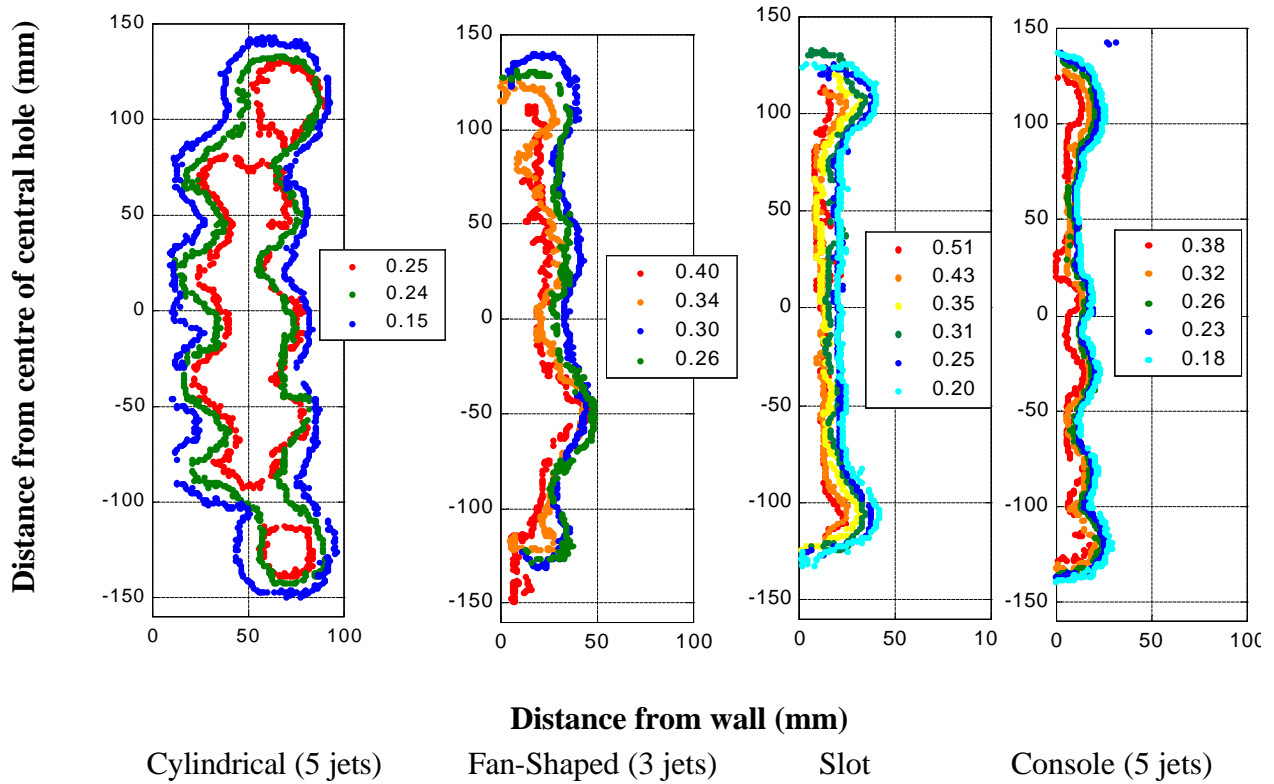


Figure 8.13: Contours of effectiveness at  $1 d$ ,  $I=\Psi$ ,  $DP_c=412$ ,  $v_m = 0 \text{ ms}^{-1}$

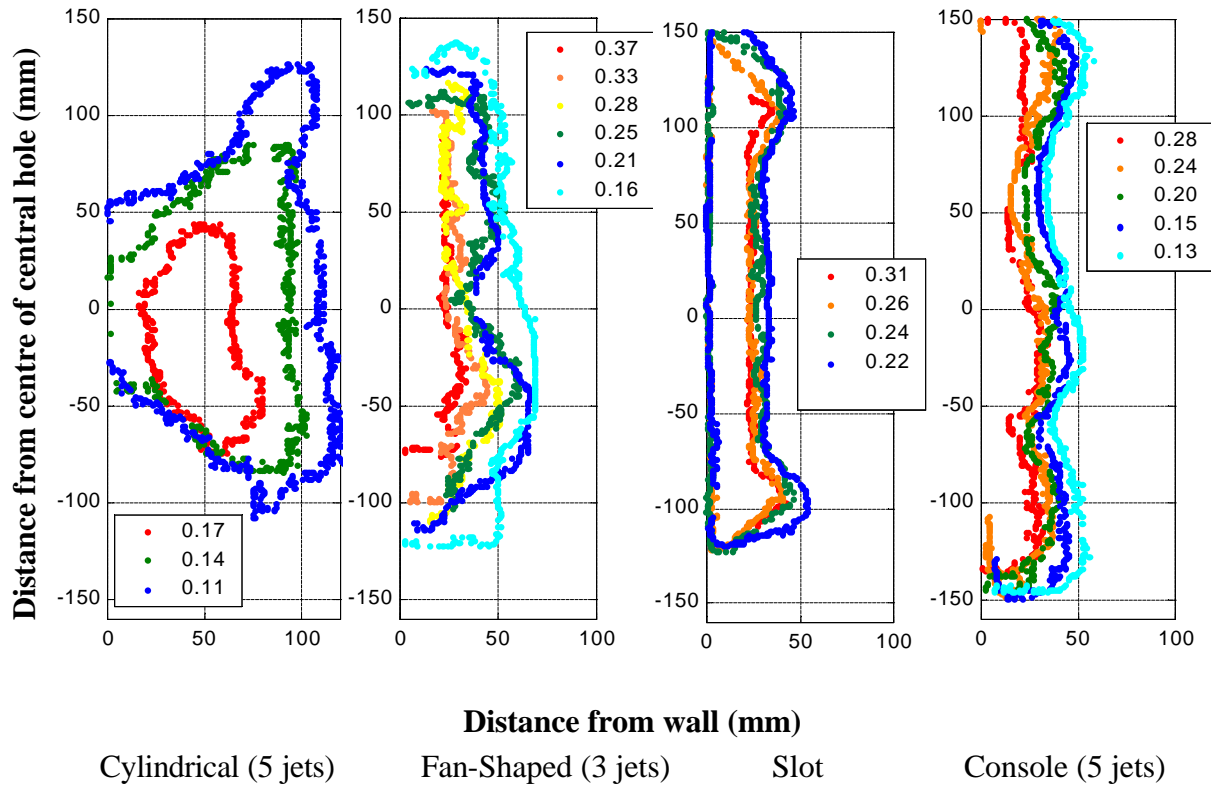


*Figure 8.14: Contours of effectiveness at 3 d,  $I=\infty$ ,  $DP_c=412$ ,  $v_m = 0 \text{ ms}^{-1}$*

**Contours with low crossflow,  $v_m = 5 \text{ ms}^{-1}$  and  $I = 40$**



*Figure 8.15: Contours of effectiveness at 10 d,  $I=40$ ,  $DP_c=412$ ,  $v_m = 5 \text{ ms}^{-1}$*



**Figure 8.16: Contours of effectiveness at  $25 d$ ,  $I=40$ ,  $DP_c=412$ ,  $v_m = 5 \text{ ms}^{-1}$**

As previously discussed, with low crossflow the jet interaction with the mainstream flow is significantly more apparent than for the high mainstream flow rate cases. The kidney and anti-kidney vortex structures for the jets is visible in Figure 8.15 at  $10 d$ , but in Figure 8.16 at  $25 d$  the jets have become rather diffused. The cylindrical jets have mixed with the mainstream to form a single mass of coolant in which patterns are not distinguishable using this technique. The slot flow remains uniform and close to the surface, and the *console* flow again exhibits some structure, but remains very close to the surface.

## 8.4 Conclusions

The purpose of the work described in this Chapter was to obtain evidence of the structure of the coolant jets issuing from the four film cooling hole shapes tested in order to better understand the heat transfer, effectiveness and loss performance described in preceding chapters. Evidence of the Coanda effect for *console* flow was found in the fact that the *console* flow remained attached to the surface even without crossflow, if there were

adjoining *consoles*. This observation confirmed the predicted performance of the *console*. The thickness of the film layer with crossflow was the same within the limitations of the measurement as the thickness of the slot film layer and significantly thinner than both the fan and cylindrical hole boundary layer thicknesses. The only difference between the *console* and the slot film profiles was that the *console* film showed some structure due to vortices formed through the hole, which was apparent at  $25\ d$  downstream for the  $I=1.1$  case, and beyond  $10\ d$  with no crossflow, and low mainstream speed. When a shaped *console* was used, the vortical structure of the jet was suppressed, and the film became more similar to a slot film, indicating that the *console* could be further improved towards slot performance by shaping the hole inlet and outlet.

## Chapter 9

### Film Cooling Performance Predictions

In this chapter, the experimental results that have been presented and discussed in previous chapters are compared with predictions using correlation and analytical prediction methods described in published literature, and Computational Fluid Dynamics (CFD). It was found that the low-speed flat-plate experimental results (Chapter 5) generally showed good agreement with a number of prediction methods. The correlation of *console* and fan-shaped hole effectiveness results were used to produce design tools for the prediction of cooling using each of these film cooling configurations. These design tools were tested by applying them to predict the results of the engine representative experiments (Chapter 6) and were found to be good models of effectiveness performance.

#### 9.1 Analytical prediction techniques

The development of analytical predictive models of heat transfer was discussed in Chapter 2. The model developed by Eckert and Drake (1972) for prediction of adiabatic effectiveness for the straight, inclined slot using a line heat source and the prediction for a discrete hole based on a point heat source will be compared with experimental data.

$$\text{For a slot: } h = \frac{1.9 Pr^{\frac{2}{3}}}{1 + 0.329(Re_s)^{-0.2} \frac{c_{pm}}{c_{pc}} \left( \frac{m_m}{m_c} \right)^{0.2} \left( \frac{r_m u_m x}{\dot{m}_c s} \right)^{0.8}} b \quad (9.1)$$

where  $Re_s = \frac{\dot{m}_c s}{m_c}$  is the slot Reynolds number,  $x$  is the distance downstream from the

slot,  $b = 1 + 1.5 \times 10^{-4} Re_s \frac{m_c}{m_m} \sin f$  and  $f$  is the injection angle.

For a discrete, cylindrical hole: 
$$\frac{q(x, y, z)}{q(x, 0, 0)} = \exp \left\{ -\frac{Pe_t}{4} \left[ \left( \frac{y}{x} \right)^2 + \left( \frac{z}{x} \right)^2 \right] \right\} \quad (9.2)$$

Where  $q = T(x, y, z) - T_r$  and  $q(x, 0, 0) = \frac{1}{2p} \left( \frac{u_\infty x}{n} \right)^{-1} \frac{u_m q}{rc_p e_M n}$

The turbulent Peclet number  $Pe_t$  is defined  $Pe_t = \frac{u_m x}{e_M}$ , and the heat flux  $q$  is defined by

$$q = rc_p \dot{m}_c A_{throat} (T_c - T_r). \quad (9.3)$$

The prediction of heat transfer coefficient is more complex than effectiveness, because  $h$  is strongly dependent on the sub boundary layer of the flow. Away from the region close to injection,  $h$  is usually found to be similar to the level without film cooling, and this assumption is often used to predict  $h$  from a distance downstream of injection. As discussed in Section 2.1, if the effectiveness is sufficiently high near the film cooling hole, the level of  $h$  is not important. Equations 9.4 and 9.5 are the analytical solutions for heat transfer from a flat plate, solved using an integral method (Kays and Crawford, 1993):

$$\text{Laminar boundary layer: } Nu_x = 0.332 Re_x^{1/2} Pr^{1/3} \quad (9.4)$$

$$\text{Turbulent boundary layer: } Nu_x = 0.0296 Re_x^{4/5} Pr^{0.4} \quad (9.5)$$

where  $x$  is the distance from the leading edge of the plate.

Simpler prediction techniques use parameters to correlate measured data, usually in terms of either the momentum flux ratio  $I$ , or the blowing ratio  $B$ . Both effectiveness and heat transfer data were correlated by Forth and Jones (1986), and Ammari et al (1990) for single and double rows of holes and single slots inclined at  $30^\circ$ .

The correlating parameter for both  $Nu$  and  $h$  for the slot, console, double rows of film cooling holes and single rows of film cooling holes with low momentum flux ratio is:

$\frac{x}{s} I^{-2/3}$ . Note that this is based on the actual momentum flux ratio of the jets.

For a single row of film cooling holes at higher blowing ratios, the aerodynamics of the jet

correlates with the velocity ratio of the jet and the correlating parameter is:  $\frac{x}{d} \left[ \frac{u_i}{u_\infty} \right]^{-4/3}$

These correlation based techniques generally produce simple expressions for  $h$  and  $h$ , but require large amounts of data to be collected at different conditions and are strongly dependent on the flow conditions covered by the experiments.

## 9.2 Comparison of low speed results with analytical predictions

The low speed experimental results are compared with the heat source prediction (Eckert and Drake, 1972) and the Forth and Jones (1985) correlation parameters are used to produce predictions that can be used as design tools.

It was found that the Eckert and Drake heat source prediction method predicted the slot and console results well as shown in Figure 9.1, except for near the end of the measurement region, where the experimental data gave a higher level of effectiveness. The prediction was generated for a slot with the same slot height and actual momentum flux ratio as the *console* and slot.

In Figure 9.2, the *console* and slot data at different  $I_{actual}$  are plotted using the Forth and Jones correlation. The data collapsed well to linear relationships for each hole for a significant portion of the curve. This correlation can be used to predict the *console* effectiveness, using a line fitted to the correlated data. The line fit produced the following expression for effectiveness:

$$h = -0.1899 \ln\left(\frac{x}{s} I_{actual}^{-\frac{2}{3}}\right) + 1.25 \quad \text{for } 30 < \frac{x}{s} I_{actual}^{-2/3} < 200 \quad (9.6)$$

This curve fit accurately predicts the experimental points in the range of interest, but far downstream from the hole reduces towards zero far more rapidly than the experimental results. This design tool will be used to predict *console* effectiveness on the NGV in the following section.

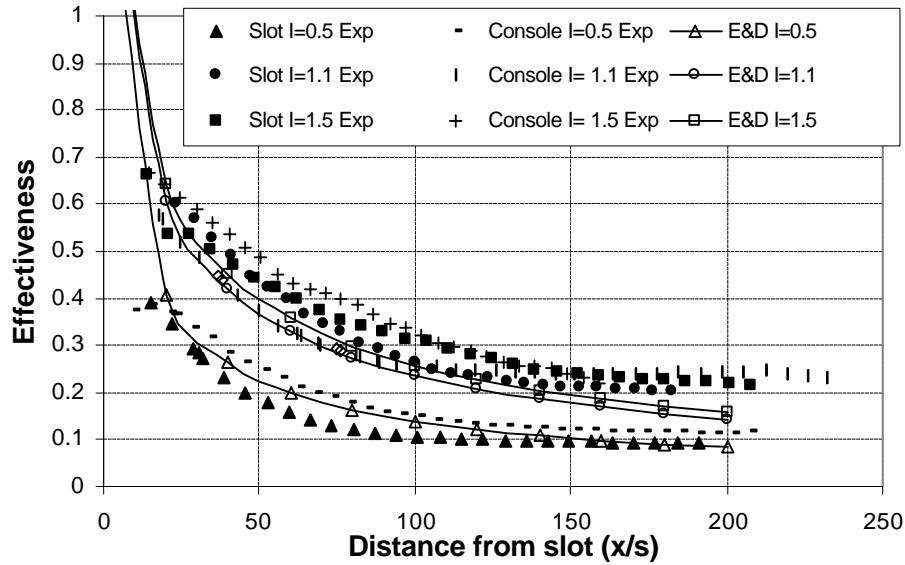
Figures 9.3 and 9.4 compare the fan and cylindrical hole effectiveness results with the Eckert and Drake discrete hole heat source prediction. The fan-shaped holes were modelled as cylindrical holes with a diameter equal to the fan inlet diameter, but using the actual blowing ratio based on the average velocity at the hole exit. The cylindrical holes in Figure 9.3 were not well predicted, but the fan-shaped hole effectiveness (Figure 9.4) was predicted to within 15% for the lowest blowing ratio. One problem with the Eckert and Drake prediction is that near the hole, and for high blowing ratios effectiveness greater than one is predicted. If the effectiveness was limited to an upper limit of one, the cylindrical effectiveness is more accurately predicted, but the fan-shaped hole prediction is worse.

In Figure 9.5, the correlation of fan-shaped hole effectiveness with the Forth and Jones parameter can be used to produce a prediction for these holes. The effectiveness can be predicted using:

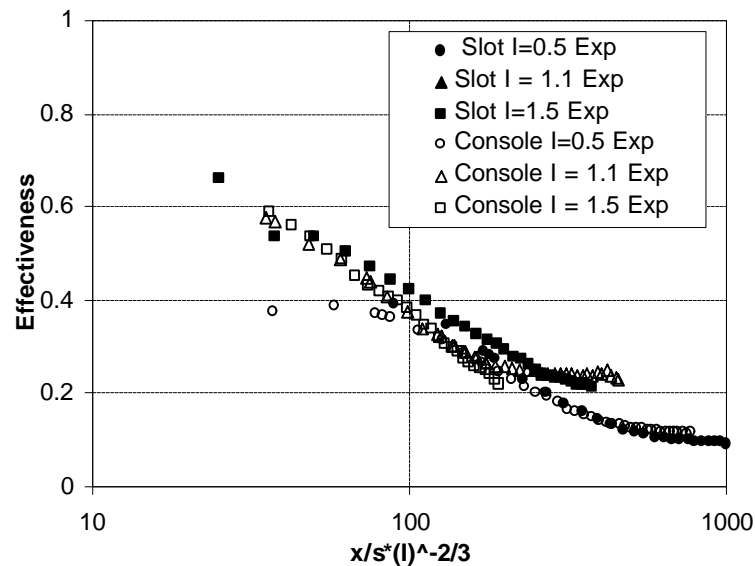
$$h = -0.1778 \ln\left(\frac{x}{d} I_{actual}^{-\frac{2}{3}}\right) + 0.90 \quad \text{for } 4 < \frac{x}{d} I_{actual}^{-2/3} < 50 \quad (9.7)$$



Similarly to the *console* prediction, this prediction is accurate within the specified range, but decreases to zero more rapidly downstream than the experimental data.



**Figure 9.1: Comparison of slot and console results (at  $I_{ideal} = 0.5, 1.1, 1.5$ ) with line heat source prediction from Eckert and Drake (1972) (E&D)**



**Figure 9.2: Comparison of slot and console experimental results using the Forth and Jones (1986) correlation**

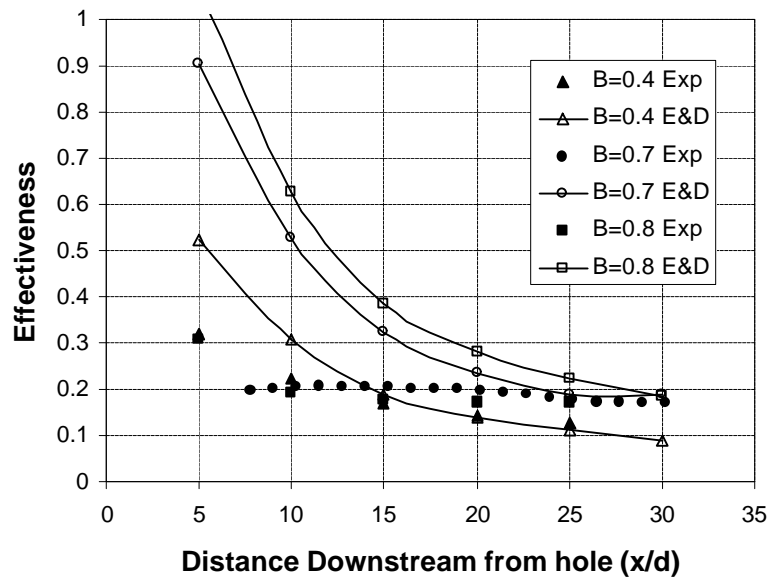


Figure 9.3: Comparison of cylindrical hole results with Eckert and Drake (1972)

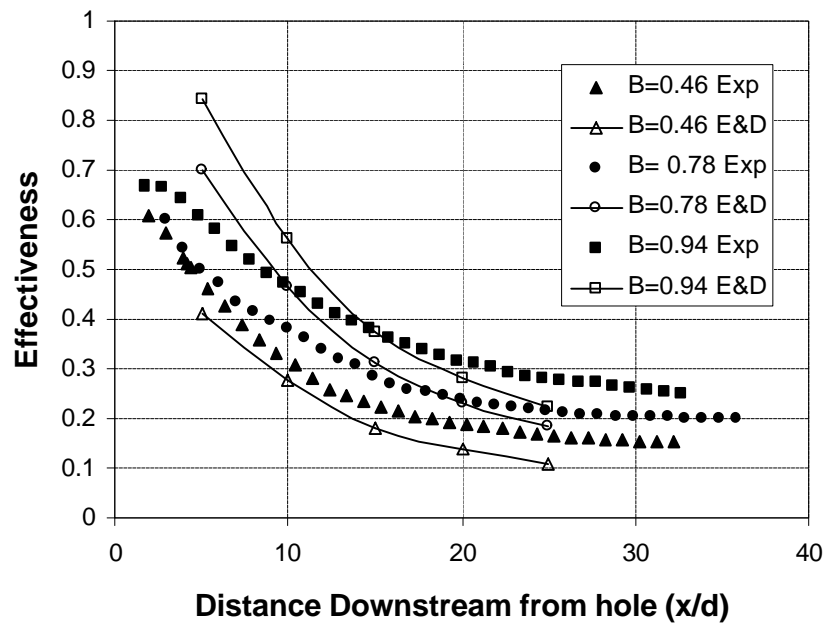
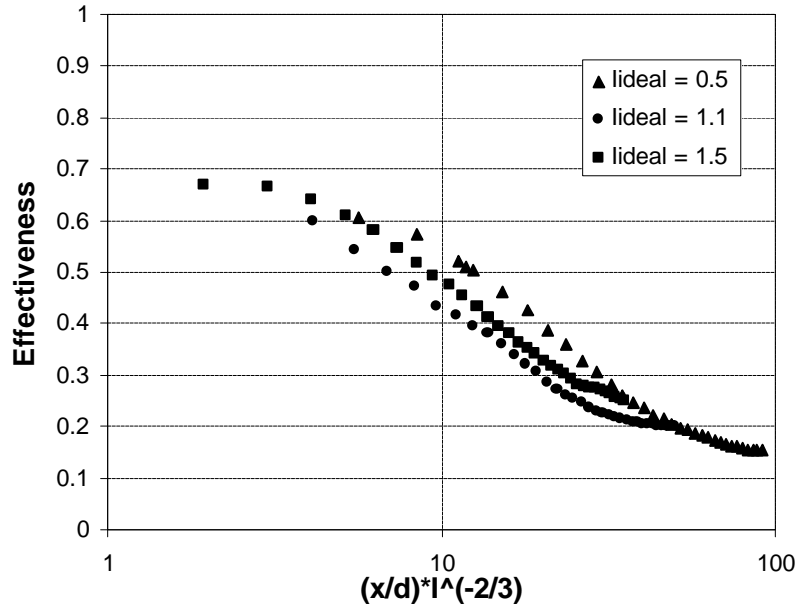


Figure 9.4: Comparison of fan-shaped hole experimental effectiveness with Eckert and Drake (1972) prediction



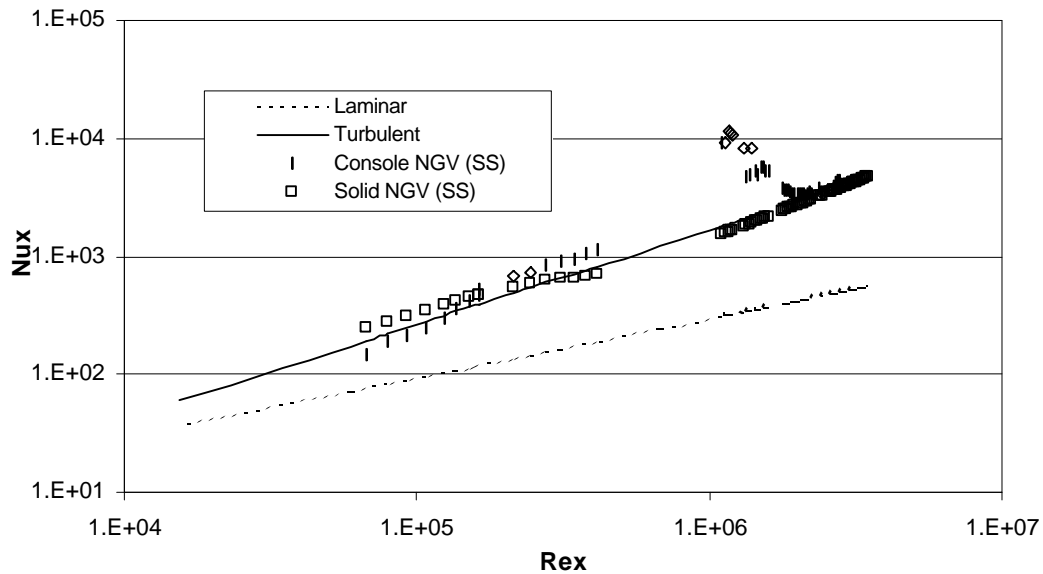
**Figure 9.5: Correlation of fan-shaped hole experimental effectiveness at varying  $I$  using Forth and Jones (1986) correlation parameter**

### 9.3 Comparison of engine representative results with predictions

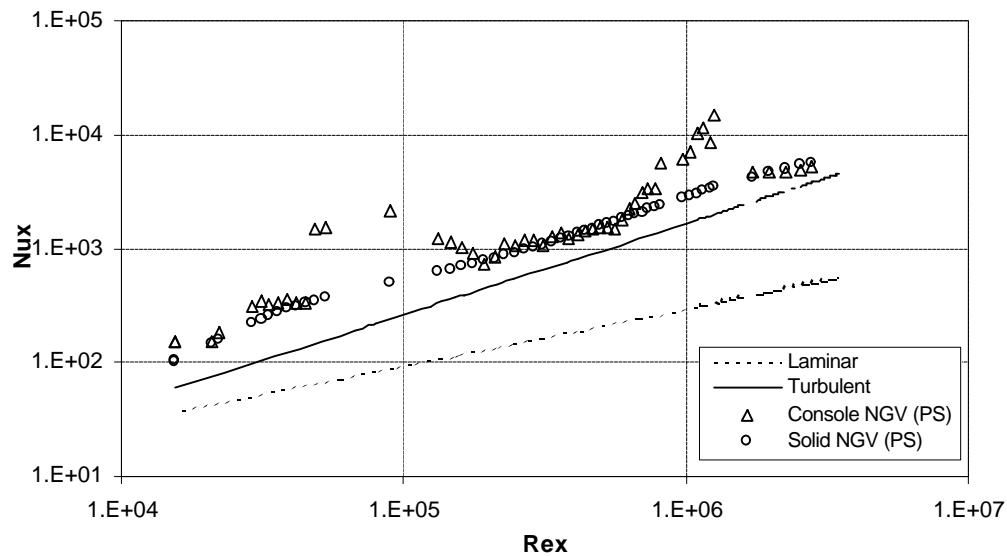
The heat transfer coefficient and adiabatic effectiveness for the NGV with film cooling measured in the CHTT can also be predicted, although the complexity of the modelling is far greater than that for the low-speed, flat-plate experiments. There exist a number of two dimensional CFD codes such as used by Lai (1999), and the system could also be modelled using a three-dimensional CFD package such as *FLUENT*.

A considerably simpler approach is applied here, by comparing the measured Nusselt number,  $Nu$  with the previously discussed analytical solutions (equations 9.4 and 9.5) for flow over a flat plate with either laminar or turbulent flow. Figures 9.6 (suction surface) and 9.7 (pressure surface) show these solutions compared with experimental data. The Reynolds number is based on the surface distance from the leading edge. The experimental data have a higher level of  $Nu$ , because of the high level of turbulence (13%)

in the CHTT, but the measured data is generally of the same order of magnitude of the analytical result, except near coolant injection locations, where  $Nu$  is enhanced.



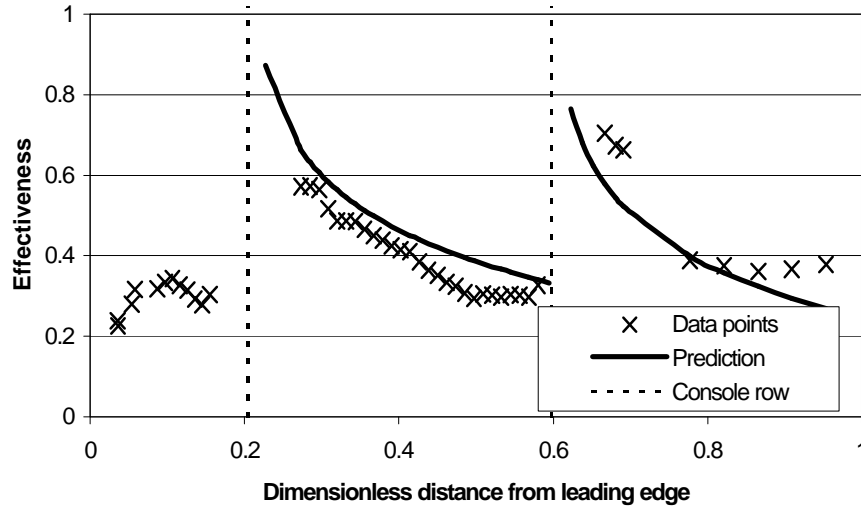
**Figure 9.6: Comparison of measured Nusselt numbers on Suction Surface for console and solid NGVs with analytical results for laminar and for turbulent flow**



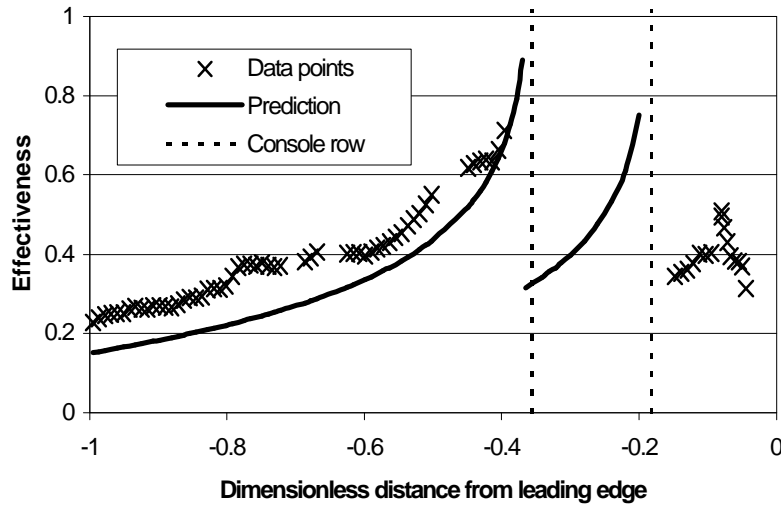
**Figure 9.7: Comparison of measured Nusselt numbers on Pressure Surface for console and solid NGVs with analytical results for laminar and for turbulent flow**

The measured effectiveness for the *console* NGV is compared with the prediction based on the Forth and Jones correlation parameter (equation 9.6) in Figures 9.8 and 9.9. The

prediction assumes that the upstream films do not contribute to the effectiveness from each *console* row. The prediction is only valid on the suction surface to the dimensionless distance  $-0.6$ , but the predicted results beyond this limit are indicated on the figure. The effectiveness is predicted to within 20% over the region in which the prediction is defined.



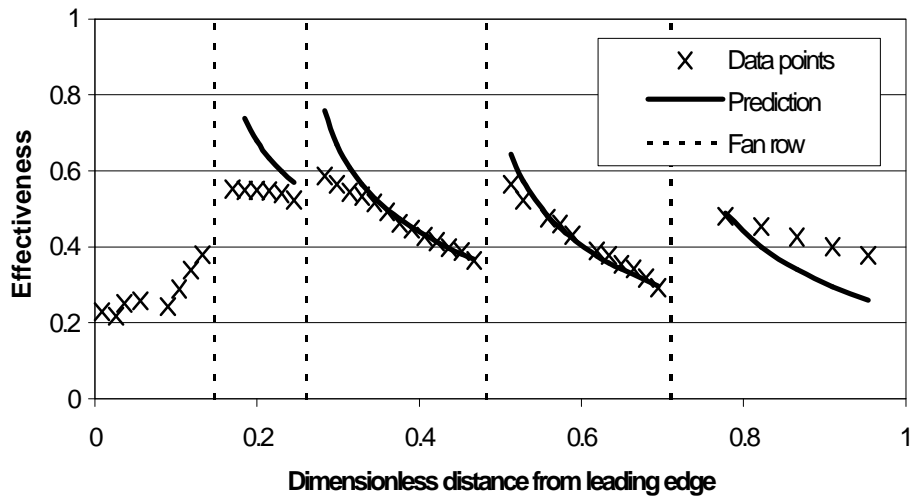
**Figure 9.8: Predicted and experimental effectiveness for console NGV pressure surface**



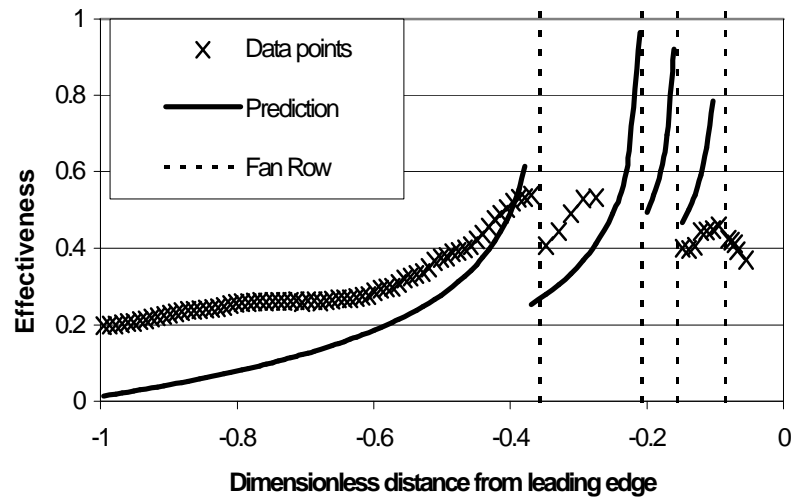
**Figure 9.9: Predicted and experimental effectiveness for console NGV suction surface**

The prediction of effectiveness (equation 9.7) for the fanned NGV is shown in Figures 9.10 and 9.11, which again shows a good agreement with the prediction, particularly on the pressure surface. The effectiveness is under predicted on the suction surface, and the error is as high as 30% at the limit of the prediction at the dimensionless distance  $-0.6$ .

Over the remainder of the surface the error is less than 20%, and less than 10% for the mid pressure surface rows.



**Figure 9.10: Predicted and experimental effectiveness for fanned NGV pressure surface**



**Figure 9.11: Predicted and experimental effectiveness for fanned NGV suction surface**

#### **9.4 Comparison of experimental results with computational model**

In the present work the CFD code, *FLUENT*, was used to predict the adiabatic effectiveness of the four hole shapes tested at low speed conditions. These results are compared with the experimental data available and, once verified, the model could be used to predict further features of the film cooling flow from each of the film cooling flows,

such as the velocity and degree of separation of the flow through the film cooling hole and the turbulence levels in the holes and at the hole exit.

The three-dimensional models of cylindrical, slot and *console* film cooling hole shapes were created in *GAMBIT*, with identical dimensions of wind tunnel working section, plenum chamber and film cooling holes as used in the low speed experiments (Chapter 5). A fan-shaped hole model was also produced, but the modelling of this hole was found to be very difficult, and instabilities recorded in experiments were also present in the CFD model, which did not converge using the same methods as for the other holes. This CFD model was not pursued in the present work. The entrance to the wind tunnel was not modelled; instead the section was modelled as a flat plate upstream of injection to the length required to produce the boundary layer thickness of one cylindrical hole diameter that was measured in the experimental apparatus. Half of the hole pitch was modelled, with planes through the hole centre and the centre of the pitch between two holes forming the vertical boundaries of the flow. These boundary planes were modelled with a symmetry boundary condition, to simulate a row of film cooling holes.

An unstructured three-dimensional grid was created throughout the volume, with reduced grid spacing in the hole, injection region and near the wall surface downstream of injection. The standard  $k$ - $\epsilon$  model provided in the software was used to model turbulence, and the near wall region was modelled using standard wall functions.

Two-dimensional models were used to predict the heat transfer coefficient at the wall with no film cooling, and for slot flow. The models had the same  $x$  and  $y$  plane dimensions as the three-dimensional grids, but had uniform 2mm grid spacing over the entire model. This grid size was the maximum size that could be used to produce an accurate result without film cooling. The adiabatic effectiveness was also predicted for the two-

dimensional slot, and this was compared with results predicted by the three-dimensional slot model.

The induced flows through the working section and plenum chamber for all models were defined by total pressure at the inlets and a lower static pressure at the mainstream flow outlet. This produced the required mainstream speed of  $26 \text{ ms}^{-1}$  and ideal momentum flux ratio of  $I = 1.1$ . The temperature, pressure and turbulence data used in the model are summarised in Table 9.1.

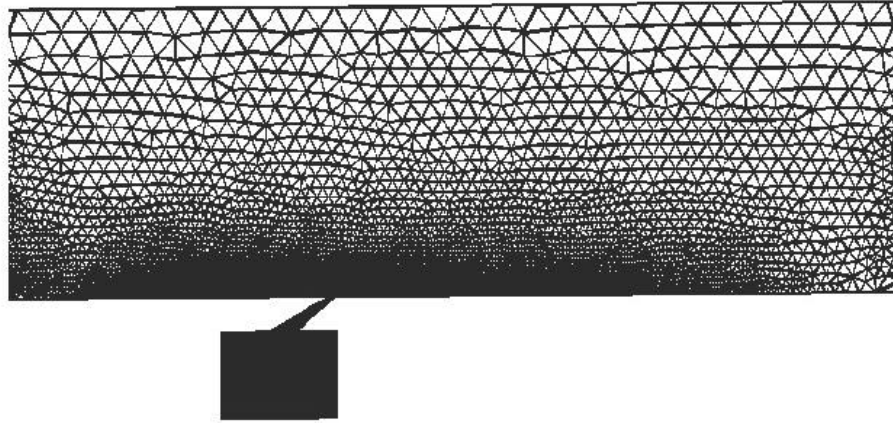
$P_{0m}$ (PaG)	0
$P_{0c}$ (PaG)	37.5
$P_m$ (PaG)	-375
Flat plate wall temperature	Measured ( $T_{aw}$ )
Heat flux from all walls	0 (adiabatic)
Turbulence intensity (%)	1 %
Turbulence length scale (m)	0.001
$T_{0c}$ (K)	313
$T_{0m}$ (K)	293

**Table 9.1: CFD model parameters**

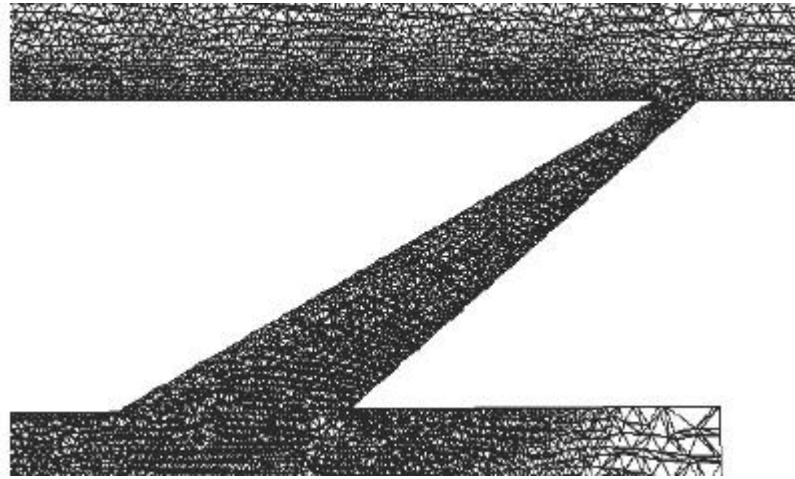
## 9.5 Results of CFD compared with measured data

It was found that the three-dimensional grid definitions shown in Figures 9.12 and 9.13 were not sufficiently fine to accurately solve the flowfield, despite the fact that there were almost  $10^6$  nodes. To increase the number of nodes to the level required, would have produced models which required significantly longer to solve. *FLUENT* uses the Reynolds analogy to calculate surface heat transfer, and it was felt that even with the increased grid points, this model was not sufficiently accurate to model the heat transfer and complicated mixing processes downstream of film cooling. Hence the CFD results included here are indicative only, but are useful for comparison of large scale features with the experimental results.





***Figure 9.12: CFD model of film cooling hole, plenum chamber and wind tunnel working section, for the console model.***



***Figure 9.13: Console grid definition through and near the hole***

The patterns of adiabatic wall temperature and effectiveness show general agreement with the measured data (Figures 9.14 – 9.16), although as shown in the plot of laterally averaged effectiveness in Figure 9.17, the level of effectiveness is under predicted by the CFD due to the modelling inaccuracy. The correction for hole discharge coefficient outlined in Chapter 5 has been applied to the results in Figure 9.17 based on the mass flow rates for the CFD models summarised in Table 9.2. Both experimental and CFD results have been corrected to the experimental cylindrical hole mass flow rate.

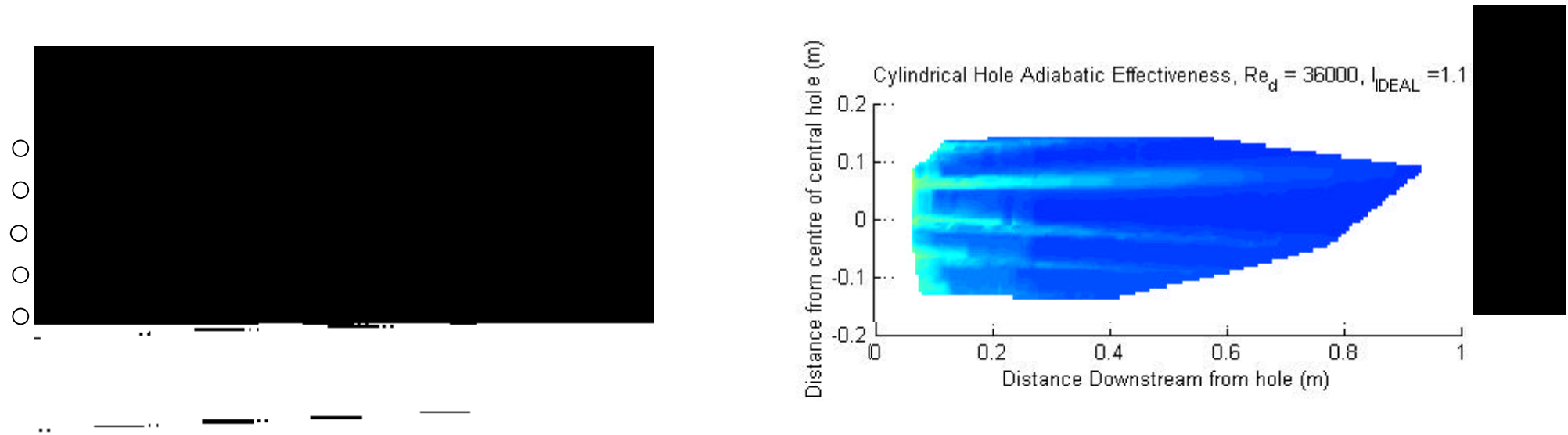


Figure 9.14: Comparison of predicted and measured surface adiabatic wall temperature for cylindrical holes,  $I_{ideal} = 1.1$ ,  $v_m = 26 \text{ ms}^{-1}$



Figure 9.15: Comparison of predicted and measured surface adiabatic wall temperature for console,  $I_{ideal} = 1.1$ ,  $v_m = 26 \text{ ms}^{-1}$

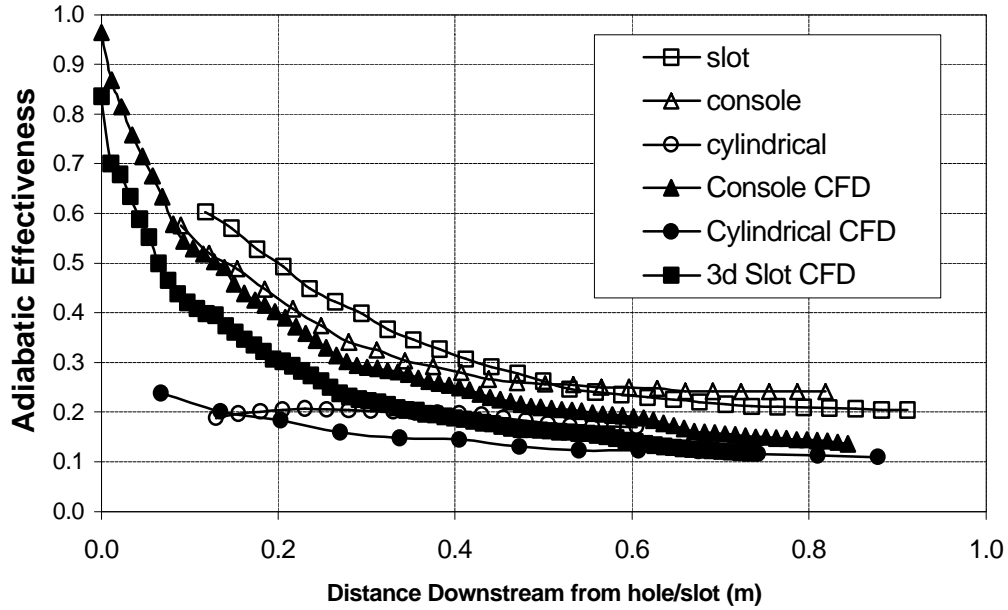


*Figure 9.16: Comparison of predicted and measured surface adiabatic wall temperature for slot,  $I_{ideal} = 1.1$ ,  $v_m = 26 \text{ ms}^{-1}$*

Hole	CFD mass flow rate (kg/s) for 5 holes	Experimental mass flow rate (kg/s) for 5 holes
Cylindrical	0.018	0.0325
Console	0.024	0.024
3-D Slot	0.028	0.022
2-D Slot	0.022	0.022

*Table 9.2: Hole mass flow rates for three dimensional CFD model and experimental results*

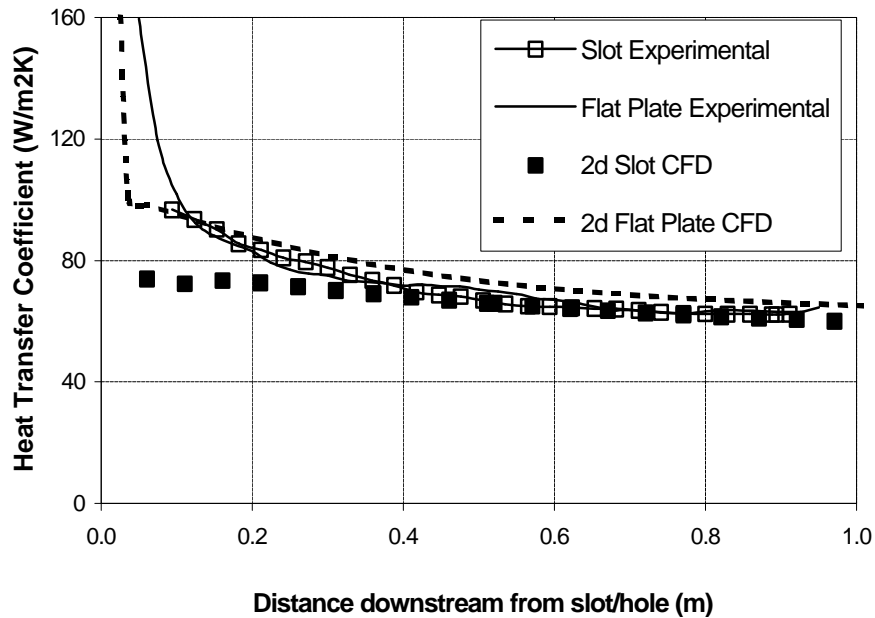
The prediction for the three-dimensional slot in Figure 9.16 shows some non-uniformity of effectiveness on the surface. This indicates that although the symmetry boundary condition was used at the edges of the slot, this did not produce the correct conditions to model an infinite slot. This may explain why the laterally averaged effectiveness was lower even than the *console* level in Figure 9.17.



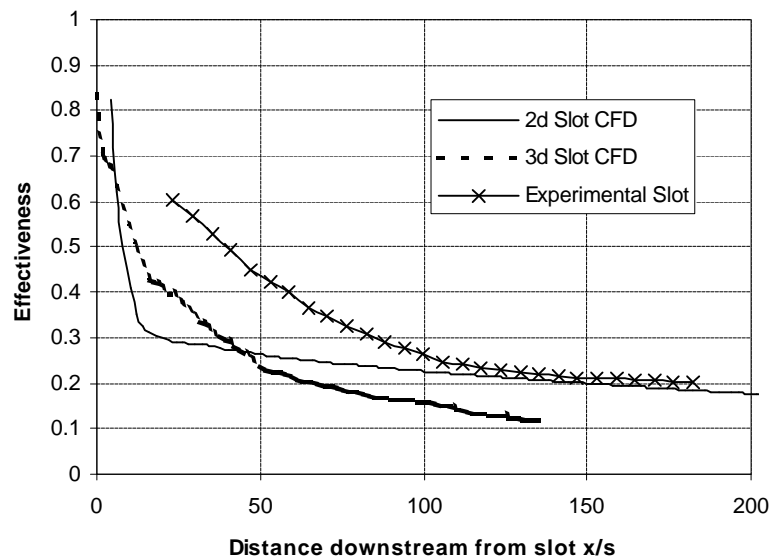
**Figure 9.17: Comparison of the console, slot and cylindrical hole laterally averaged effectiveness results at  $I_{ideal} = 1.1$  with CFD**

The results of the two-dimensional models of the system, that were used to model surface heat transfer coefficient for the flat plate with no film cooling, and slot cooling are shown in Figure 9.18. The model accurately predicted the flat plate heat transfer, but the heat transfer coefficient with slot film cooling was under predicted, particularly near the slot exit. Heat transfer prediction was not pursued in the three dimensional models because of the previously mentioned difficulty in modelling the flowfield to predict effectiveness. In Figure 9.19 the effectiveness level predicted for the two dimensional slot is compared with the predicted level for the three dimensional slot and experimental results. The two dimensional model predicts the effectiveness well from 10 slot heights downstream of the

slot, indicating that mixing near the hole is not correctly modelled, but the concentration of coolant near the wall further downstream is correct. The three-dimensional model is more similar in shape to the experimental results, with a more gradual reduction in effectiveness away from the hole, but the effectiveness level is under predicted.

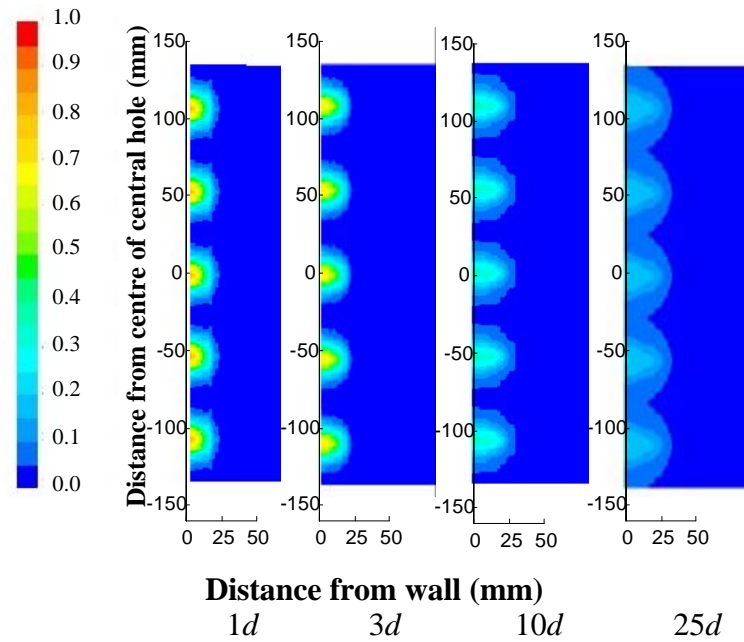


**Figure 9.18: Comparison of two-dimensional flat plate and slot heat transfer coefficient CFD results with experimental data**

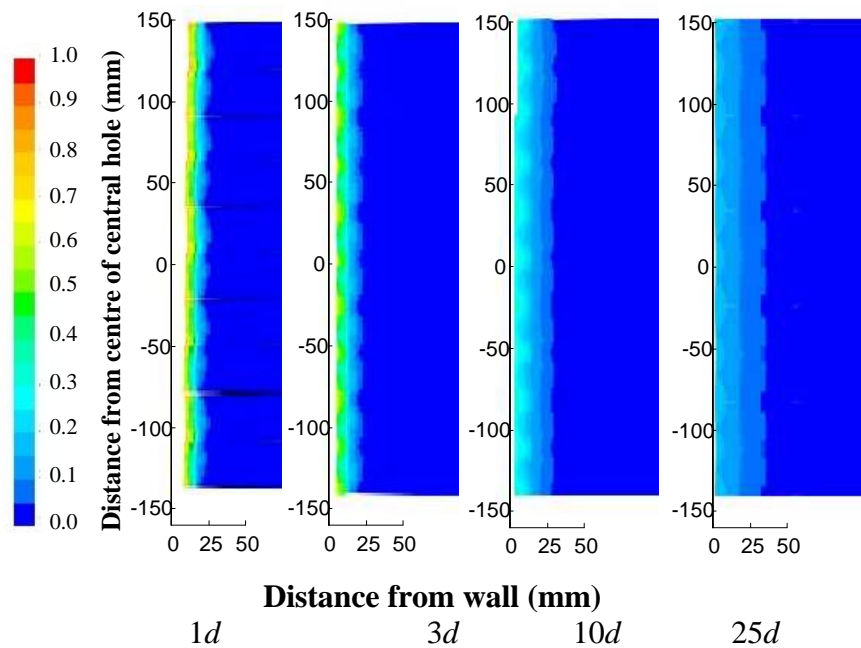


**Figure 9.19: Comparison of two-dimensional and three dimensional slot effectiveness CFD results and experimental data**

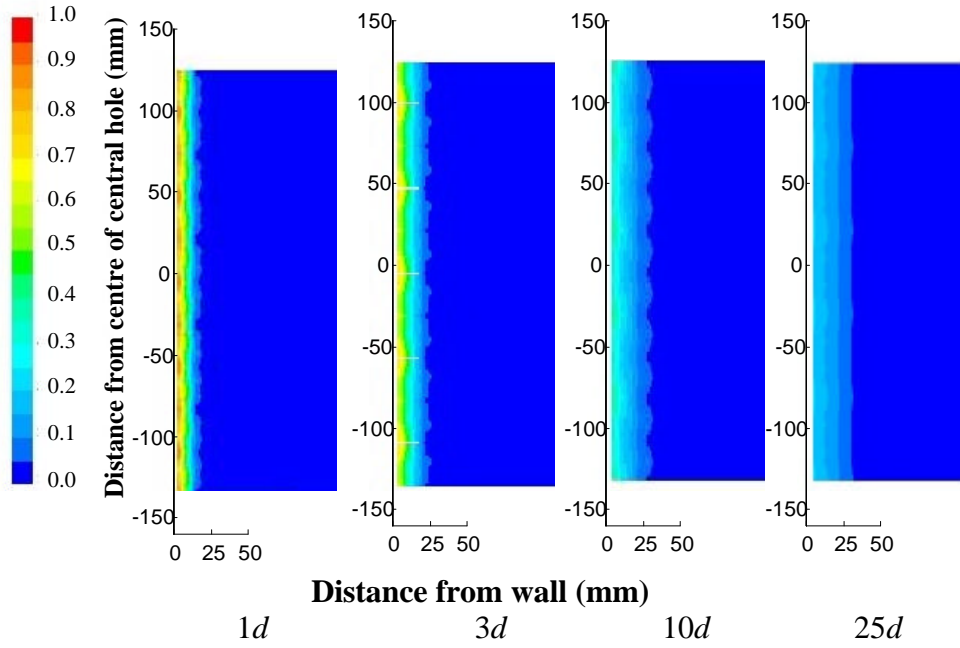
In Figures 9.20-9.22, the contours of gas effectiveness downstream from injection can be compared with the contours measured using the TLC mesh (Chapter 8). The results are representative of the experimental results for the central holes in the row. The interesting effects measured for the edge holes are not present here, because the edge holes were not modelled, and the holes shown represent an infinite row of holes.



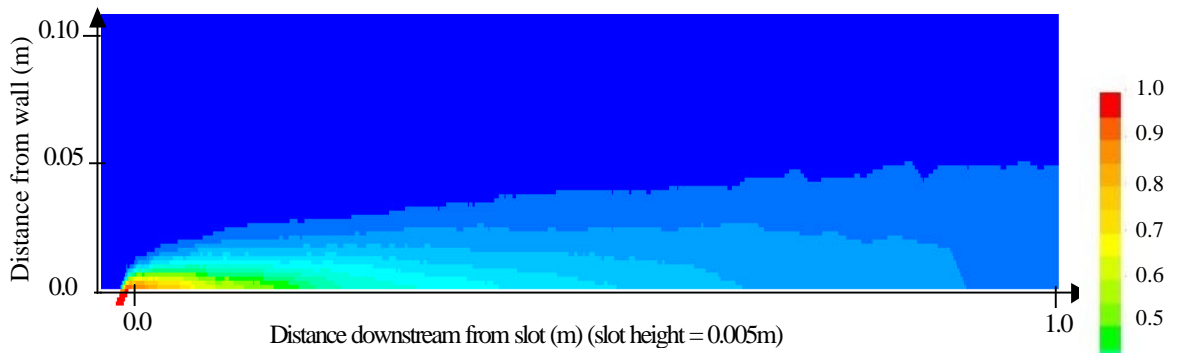
**Figure 9.20: CFD predicted contours of cylindrical hole gas effectiveness**



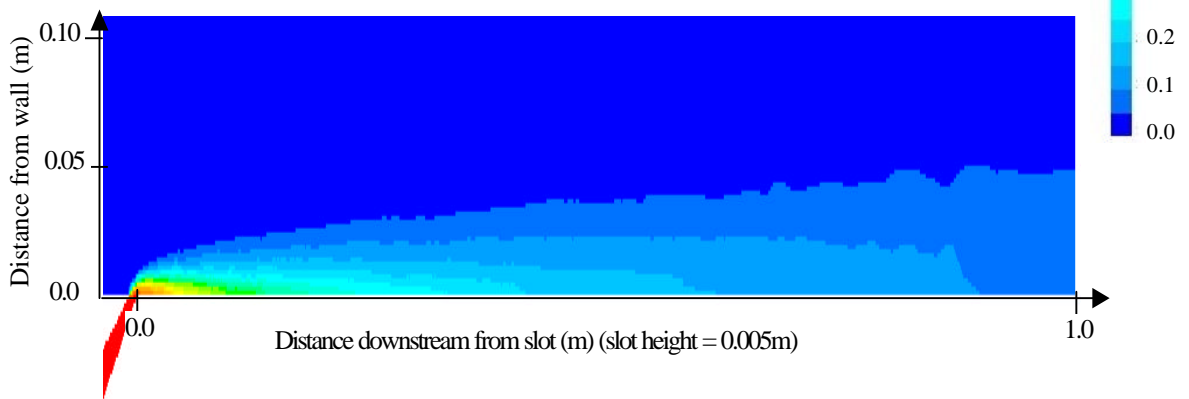
**Figure 9.21: CFD predicted contours of slot gas effectiveness**



**Figure 9.22: CFD predicted contours of console gas effectiveness**



**Figure 9.23: CFD predicted contours of gas effectiveness at edge of console**



**Figure 9.24: CFD predicted contours of gas effectiveness at centreline of console**

Figures 9.23 and 9.24 show the gas effectiveness predicted by the CFD model for the console in planes in the streamwise direction. The distribution of coolant is very similar

for both plots, at the edge of the *console* and at the *console* centreline. The only slight difference is in the mid range contours (0.3 – 0.7), which appear to extend slightly further into the flow in Figure 9.23. This may be related to the higher effectiveness measured at the wall in this region, which could be caused by the interaction of vortices downstream of the point where two *consoles* meet (i.e. downstream of the edge of a *console* in a row of *consoles* as shown in Figure 9.23).

## 9.6 Conclusions

The experimental data measured at low-speed over a flat plate have been compared with analytical and computational prediction methods, and a correlation technique has been used to produce an effectiveness prediction method for the *console* and fan-shaped hole film cooling techniques.

These correlation predictions were used to predict effectiveness at engine conditions on the *console* and fanned NGVs, and were found to be good predictions, in the defined range of the model. The heat transfer coefficient results for the *console* NGV were compared with the analytical solutions for  $h$  over a flat plate with a turbulent or laminar boundary layer. It was found that the suction surface results were close to the turbulent boundary layer prediction, and the pressure surface results were higher. The effectiveness prediction, and the similarity of the *console* heat transfer coefficient to the flat plate results and prediction, form effective design tools for the *console*.

CFD models of the low speed effectiveness experiments predicted some features of the flow for each hole shape, but it was found that the effectiveness was under predicted. A more accurate model may have been obtained if more grid points were used, particularly in the near hole region, but this was not pursued for the current work. Two-dimensional models of heat transfer without film cooling and with slot film cooling were developed.



Good agreement with experimental data was found without film cooling, but with slot cooling  $h$  was accurately predicted only some distance from the measurement location. This test highlights the difficulty in accurately modelling the complex flowfield with film cooling.

# Chapter 10

## Conclusions

### ***10.1 Summary of major themes***

The focus of this thesis was the concept, design and testing of a new film cooling hole, the Converging Slot-Hole or *console*, to meet the demand for high thermal protection systems to allow increased turbine entry temperatures and optimum reliability with a minimal reduction in aerodynamic efficiency due to film cooling. The *console* geometry, with the accelerating flow through the converging cooling hole ending in a slot exit, offers the benefits of the continuous slot, allied to low aerodynamic losses while maintaining the mechanical integrity of a row of holes. The new experimental techniques developed to measure the performance of the *console*, and the concepts explored in developing an understanding of the behaviour of the coolant from a *console* are of interest to engine designers, and to researchers in the field. This chapter summarises the work completed.

The current state of development of film cooling systems through variation of the shape and arrangement of holes was summarised in Chapter 2, and the main parameters used to quantify the thermal and aerodynamic performance of film cooling systems were defined. In view of these discussions, the concepts behind the *console* design were discussed in Chapter 3.

The requirements for similarity between the experimental and engine conditions are discussed in Chapter 4. The experiments to comparatively measure the heat transfer performance of the *console* with existing cooling configurations were presented in Chapters 5 and 6, which provided results for low-speed flat-plate and engine representative situations respectively. It was found that the thermal performance of the *console* was similar to or lower than the fan-shaped hole. Visualisation of the surface temperature using thermochromic liquid crystals, and full surface analysis of the heat transfer results showed that the *console* did provide a more uniform coolant film over the cooled surface than fan-shaped holes.

The aerodynamic performance of film cooling using rows of *consoles* was measured at the same low speed and engine representative conditions as the heat transfer performance and is documented in Chapter 7. At low speed, flat-plate conditions the loss was computed from the measured velocity traverse far downstream from the holes, by equating the measurement plane to a mixed out plane. In the engine representative annular cascade, the method proposed by Dzung (1971) was used to calculate loss from the results of a traverse using a four hole probe downstream of the NGV at midspan. In both situations, the aerodynamic loss due to film cooling for the *console* was found to be significantly less than the loss due to fan-shaped holes.

In order to more fully understand the behaviour of the film cooling flows and their interaction with the mainstream flow, a flow visualisation technique was developed and the results are presented in Chapter 8. These experiments provided evidence that the flow from a row of *consoles* does benefit from the Coanda effect.

In Chapter 9, analytical prediction models, correlations and CFD were used to model the low speed experiments. It was found that the analytical heat source prediction

models were quite capable of predicting the *console* effectiveness to a good level of accuracy, but the fan-shaped and cylindrical hole data was difficult to predict. The CFD models predicted the coolant distribution over the surface for each hole shape, but tended to under predict the film cooling effectiveness. A prediction model for effectiveness and the analytical solution for heat transfer from a flat plate were used to predict the performance of the *console* NGV and were shown to be good design tools for the *console*.

## **10.2 Assessment of aims**

The aim of this thesis was to develop a new film cooling hole geometry that provides the equivalent thermal performance to the best traditional design, using the same amount, or less coolant, with aerodynamic loss due to film cooling reduced by 40%. In order to achieve this aim, the following practical goals were met:

- To develop a ‘standard’ *console* design based on the design concept
- To measure the thermal performance of the *console* compared with standard hole shapes
- To measure the aerodynamic efficiency of the *console* compared with standard hole shapes
- To use flow visualisation and CFD to obtain some understanding of the *console* flow mechanisms
- To suggest some improvements to the basic *console* design
- To suggest design methods for the *console*

The standard *console* design was outlined in Chapter 3, with reference to the predicted performance of the hole based on the design features.

Measurement of the *console* thermal performance compared with fan-shaped and cylindrical holes and a slot at low speed flat plate conditions is described in Chapter 5. Here the *console* thermal performance was found to be lower than the fan-shaped hole, based on a combination of heat transfer coefficient and effectiveness, although the hole effectiveness was improved. In Chapter 6, the performance measurements in an annular cascade at engine representative conditions were presented. Here the *console* thermal performance was similar to the fan-shaped holes for most regions on the NGV. For both sets of measurements new experimental techniques using thermochromic liquid crystals were developed.

The measurement of aerodynamic performance at low speed, and engine representative conditions is presented in Chapter 7. The aerodynamic loss due to the *console* was found to be even lower than the required 40% reduction compared to fan-shaped holes.

A mesh covered with TLC was used to obtain flow visualisation and gas effectiveness results in across the jets, downstream from injection. The results and conclusions drawn about the size and location of the coolant from each film cooling hole shape are presented in Chapter 8. CFD models of the film cooling holes are presented in Chapter 9.

The flow visualisation provided evidence that one of the suggested improvements to the *console*, namely shaping the hole inlet and outlet, could improve the *console* performance, by causing the film to form more closely to the surface. Other improvements were outlined in Chapter 3.

From analytical predictions and a correlation technique presented in Chapter 9, a set of design tools to predict the effectiveness and heat transfer coefficient for the *console*

and for fan-shaped was developed and used to predict the performance measured on an NGV in the CHTT.

In meeting these practical goals, the overall aim of this thesis was met. The *console* that has been presented uses the same coolant mass flow and pressure requirements as currently used in the engine. Initially, the experiments showed that although the effectiveness from the *console* was high, the heat transfer coefficient was higher than that for the currently used fan-shaped holes and the thermal performance was not maintained at fan levels by the *console*. However, after applying corrections for the differences in the experiments, the engine representative experiments in the CHTT demonstrated that if the *console* is correctly designed, it should be possible to maintain the heat flux to the surface at current levels, with the same amount of coolant currently used. The significant advantage of the *console* over conventional design was shown to be in aerodynamic efficiency. The aerodynamic loss due to film cooling with the *console* is only 20% of the loss measured for cooling with fan-shaped holes over an NGV at engine representative conditions. With such an advantage in aerodynamic performance, the *console* is ideally suited to transonic regions, where traditionally designers have tried to avoid film cooling because of the high loss incurred by disturbing the flow in this region. The use of slot flows to control mainstream flow is well established in other applications, and the *console* flow could also be used to control separations. The information developed and presented in this thesis can now be used to design *console* film cooling configurations for new engine designs, and as a basis for future development of the *console*.

### 10.3 Further work

The current work has demonstrated that the *console* can provide a significant advantage in the engine, and this success opens many opportunities for further work in the optimisation of the design.

- The location and size of *console* rows on the NGV was identified in Chapter 6 as a definite area for investigation, to obtain the best thermal protection of the surface, whilst maintaining low aerodynamic loss. This could be done by producing a CFD model of the NGV, verified using the existing experimental data, and then adapting the model to find an optimum design, which could then be tested experimentally.
- The geometry of the existing *console* was chosen without any optimisation. The angle to the surface, solidity and contraction ratios of the hole could be altered to find an optimum shape of the hole. In addition to this, the flow visualisation experiments demonstrated that there could be further benefit obtained by shaping the *console* inlet and outlet. The *console* centreline could also be shaped, to make the slot exit tangential to the surface. The continuing improvement in casting technology could make these shapes possible for inclusion in the engine.
- Assumptions were made about the interaction of vortices downstream of adjacent holes, which caused an improvement in effectiveness. It would be useful to obtain additional data from flow visualisation and flow field measurements to improve the understanding of this mechanism so that it could be utilised in the optimisation of *console* performance.

The development and use of *consoles* is at an early stage and further enhancement of the concept is definitely warranted.



## Appendix A

### Impulse Response Method

In this appendix the theory behind the impulse response method used to transform the thermocouple temperature responses to heat flux is summarised and the functions used to produce the numerical models of the response of a semi infinite substrate and a double layer gauge are presented. This summary is based on Oldfield (2000).

#### ***A.1 Theory behind the impulse response method***

The impulse response method was developed from signal processing theory using filter techniques to analyse and transform a data set. The method uses deconvolution to design a filter, which can be used to transform a temperature trace  $T(t)$  to the response heat transfer rate trace  $q(t)$  or to transform  $q(t)$  to  $T(t)$ . The response generated is the same length as the data set used and is accurate up to this length.

The response of a linear time invariant (LTI) system, such as a thin film gauge, can be calculated from the impulse response  $h(t)$  of that system using the convolution integral:

$$q(t) = h(t) * T(t) = \int_{-\infty}^{\infty} h(t) T(t - \tau) d\tau \quad (\text{A.1})$$

For a set of discrete data points sampled at time intervals  $t_s$  or at sampling frequency

$$\frac{1}{t_s}, T[n] = T(nt_s) \text{ where } n = 0, 1, 2 \dots$$

When this is the case, the integral can be approximated by the discrete convolution sum:

$$q[n] = h[n] * T[n] = \sum_{k=-\infty}^{\infty} h[k]T[n-k] = \sum_{k=-\infty}^{\infty} h[n-k]T[k] \quad (\text{A.2})$$

For the present application, the region of interest is from  $n = 0 \dots N$  where  $N$  is the length of the impulse function (in this case  $T$ ). It is assumed that the impulse function  $T = 0$  for  $n < 0$ . Hence the discrete convolution sum becomes:

$$q[n] = h[n] * T[n] = \sum_{k=0}^n h[k]T[n-k] = \sum_{k=0}^n h[n-k]T[k] \quad (\text{A.3})$$

for  $k = 0, 1, 2, \dots, N-1$

If  $h[n]$  and the impulse function  $T[n]$  is known, the calculation of this convolution sum is straightforward. The *MATLAB* function `fftfilt` can be used for this calculation. In this manner, once the impulse response filter  $h[n]$  has been generated once for a particular pair of known impulse and response functions,  $q_I$  and  $T_I$  (e.g. a step change in heat flux and parabolic temperature response), the filter can be used to generate the response for different impulse data sets  $T[n]$ .

The unknown impulse response function  $h[n]$  is defined by the expression:

$$q_I[n] = h[n] * T_I[n] \quad (\text{A.4})$$

where the functions  $q_I$  and  $T_I$  are known. Applying a z-transform to this expression, the convolution is transformed to a multiplication:

$$Q_I(z) = H(z)T_I(z) \quad \text{or} \quad H(z) = \frac{Q_I(z)}{T_I(z)} \quad (\text{A.5})$$

Convoluting the impulse response with an impulse function will, by definition, simply reproduce the impulse response, so that

$$H(z) = H(z)\Delta(z) = \frac{Q_I(z)}{T_I(z)}\Delta(z) \quad (\text{A.6})$$

where  $\Delta(z)$  is the  $z$ -transform of  $d[n]$ .

Thus the required impulse response can be obtained by digitally filtering the impulse function  $d[n] = [1, 0, 0, \dots]$  by the IIR filter whose coefficients are given by  $\frac{Q_1(z)}{T_1(z)}$ .

The *MATLAB* command used to generate this impulse response is:

$$h = \text{filter}(q_1, T_1, \text{impulse})$$

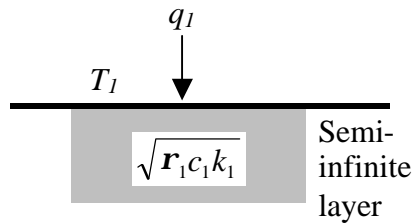
The impulse response  $h[n]$  can be generated once for a particular system and substrate properties based on an assumed theoretical  $q_1$  and  $T_1$  and then used to generate the heat transfer rate for measured  $T$  using the *MATLAB* command:

$$q = \text{fftfilt}(h, T)$$

from the *MATLAB Signal Processing Toolbox*.

The function `filter` used in the design process will not work if the first term of  $q_1[n]$  is zero. In that case, the  $q_1[n]$  sequence is moved one place to the left and a flag `shift` is set to the shift necessary to correct the output when using the filters.

## A.2 Semi infinite surface



**Figure A.1: Semi-infinite substrate, heat transfer rate  $q_1$ , surface temperature  $T_1$**

For a semi infinite surface, with some method of surface temperature measurement, the impulse response filter  $h[n]$  can be generated based on the theoretical response of the wall temperature to a particular heat flux situation, or from a known heat flux

resulting from a temperature change situation. Both the  $q$  to  $T$  and the  $T$  to  $q$  transformations can be generated using the relationships for a step change in  $q$ . The solutions of the semi infinite heat transfer equations can be written in Laplace transform form (from Schultz and Jones, 1973):

$$\bar{T}_1(s) = \frac{1}{\sqrt{r_1 c_1 k_1}} \frac{1}{\sqrt{s}} \bar{q}_1(s) \quad (\text{A.7})$$

For a step in  $q_1(t) = u(t)$ ,  $\bar{q}_1(s) = \frac{1}{s}$ , which gives

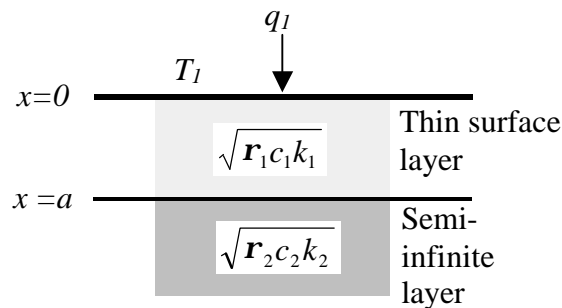
$$\bar{T}_1(s) = \frac{1}{\sqrt{r_1 c_1 k_1}} s^{-\frac{3}{2}} \quad (\text{A.8})$$

Taking the inverse Laplace transform:

$$T_1(t) = \frac{2}{\sqrt{r_1 c_1 k_1}} \sqrt{\frac{t}{p}} \quad (\text{A.9})$$

Sampling  $q_1(t)$  and  $T_1(t)$  and applying the impulse response theory above (A.6) gives the required impulse functions.

### A.3 Two layer substrate



**Figure A.2: Two layer substrate with surface layer 1 thickness  $a$ , semi-infinite layer 2, heat transfer rate  $q_1$ , and surface temperature  $T_1$**

The functions used to produce the impulse response filter for the two layer substrate are based on a step in  $q_1(t)$ , similarly to the response for a semi-infinite substrate. The

solution of the heat conduction equations for a two layer substrate can be written in Laplace transform form (Doorly and Oldfield, 1987):

$$\bar{T}_1(s) = \frac{1}{\sqrt{\mathbf{r}_1 c_1 k_1}} \frac{1}{\sqrt{s}} \bar{q}_1(s) \left[ \frac{1 + A \exp\left(-2a\sqrt{\frac{s}{\mathbf{a}_1}}\right)}{1 - A \exp\left(-2a\sqrt{\frac{s}{\mathbf{a}_1}}\right)} \right] \quad (\text{A.10})$$

where  $A = \frac{\sqrt{\mathbf{r}_1 c_1 k_1} - \sqrt{\mathbf{r}_2 c_2 k_2}}{\sqrt{\mathbf{r}_1 c_1 k_1} + \sqrt{\mathbf{r}_2 c_2 k_2}}$  and the thermal diffusivity  $\mathbf{a}_1 = \frac{k_1}{c_1}$ .

For a step in  $q_1(t) = u(t)$ ,  $\bar{q}_1(s) = \frac{1}{s}$ , which gives:

$$\bar{T}_1(s) = \frac{1}{\sqrt{\mathbf{r}_1 c_1 k_1}} s^{-\frac{3}{2}} \bar{q}_1(s) \left[ \frac{1 + A \exp\left(-2a\sqrt{\frac{s}{\mathbf{a}_1}}\right)}{1 - A \exp\left(-2a\sqrt{\frac{s}{\mathbf{a}_1}}\right)} \right] \quad (\text{A.11})$$

Expanding the denominator as a power series, and taking inverse Laplace transform

$$T_1(t) = \frac{2}{\sqrt{\mathbf{r}_1 c_1 k_1}} \left[ \sqrt{\frac{t}{\mathbf{p}}} + \sum_{n=1}^{\infty} 2A^n \left\{ \sqrt{\frac{t}{\mathbf{p}}} \exp\left(-\frac{k_s^2}{4t}\right) - \frac{k_s}{2} \operatorname{erfc}\left(\frac{k_s}{2\sqrt{t}}\right) \right\} \right] \quad (\text{A.12})$$

where  $k_s = \frac{2an}{\sqrt{\mathbf{a}_1}}$ .

Sampling  $q_1(t)$  and  $T_1(t)$  and applying the impulse response theory above gives the required impulse functions.

## Appendix B

### Analysis of Transient Heat Transfer Results

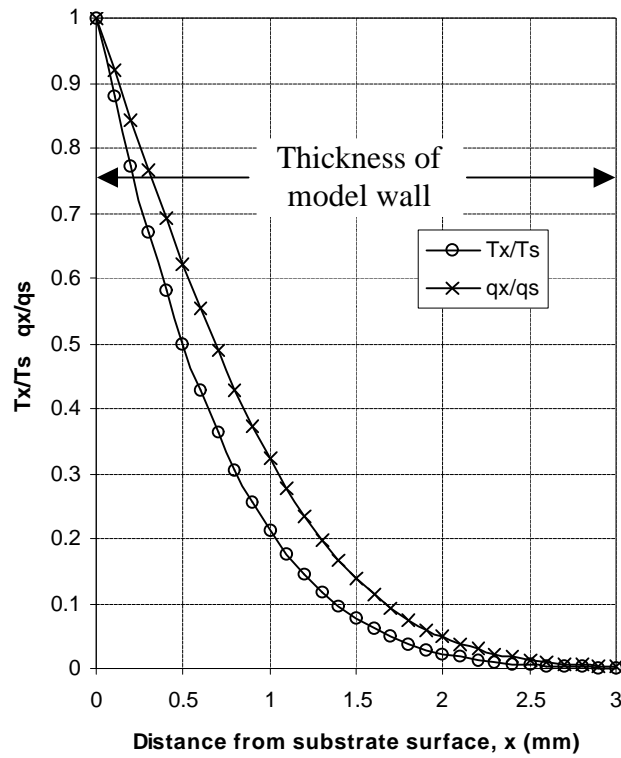
The development of the ramp method of analysing the transient heat transfer data measured in the CHTT was outlined in Chapter 6. The validity of the ramp change curve fitting technique depends on a number of conditions, some of which were mentioned in the discussion in Chapter 6, and others which are identified in this appendix. The purpose of this appendix is to provide the data used to verify the method, and test the accuracy and stability of the analysis.

#### ***B.1 Semi infinite substrate calculation***

The first assumption made in the development of either the step change or ramp change transient analysis technique was that the model substrate was semi infinite. This means that the thermal pulse generated by a temperature change at the surface of the substrate does not penetrate completely through the substrate. Both the step and ramp change solutions to the transient heat transfer depend on the substrate being semi infinite.

Schultz and Jones (1973) present an analysis that can be used to check that the model used does effectively provide a semi infinite substrate for the maximum experimental run time of 5 seconds. From Schultz and Jones, the temperature  $T_x$  and the heat flux  $q_x$

at a depth  $x$  from the surface of the substrate can be written (based on a step change solution):



**Figure B.1: Penetration of 5 second thermal pulse into stereolithography substrate at distance  $x$  (mm) due to a step function in heat flux ( $q_s$ ) at the surface ( $x = 0$ ) (after Schultz and Jones 1973)**

$$T_x = \frac{q_s}{\sqrt{rck}} \left[ \frac{2\sqrt{t}}{\sqrt{p}} e^{-\frac{x^2}{4at}} - \frac{x}{\sqrt{a}} \operatorname{erfc} \sqrt{\frac{x^2}{4at}} \right] \quad (\text{B.1})$$

$$q_x = -k \frac{\partial T}{\partial x} = q_s \operatorname{erfc} \sqrt{\frac{x^2}{4at}} \quad (\text{B.2})$$

Introducing a dimensionless depth  $x^* = \frac{x}{\sqrt{4at}}$ , and setting  $x=0$  to obtain surface

values, these equations can be rewritten:

$$\frac{T_x}{T_s} = e^{-x^{*2}} - \sqrt{p} x^* \operatorname{erfc} x^* \quad (\text{B.3})$$

$$\frac{q_x}{q_s} = \operatorname{erfc} x^* \quad (\text{B.4})$$

For the stereolithography resin substrate, which has the properties  $\sqrt{rck} = 720 \text{ Js}^{-0.5} \text{ m}^{-2}$  and  $k = 0.23 \text{ Wm}^{-1} \text{ K}^{-1}$ , the variation of  $\frac{T_x}{T_s}$  and  $\frac{q_x}{q_s}$  with the distance from the surface  $x$  (in mm) for  $t = 5 \text{ s}$  is shown in Figure B.1. The depth of substrate required for 1% of the surface temperature or heat flux is 2.3 mm for temperature and 2.6 mm for heat flux. The wall thickness over the majority of the NGV model is 3 mm, so the semi infinite assumption is valid. The only region where the wall thickness is less than this value is at the trailing edge, where the effective wall thickness reduces to 1.5 mm for the final 20 mm of the surface. In this region,  $\frac{q_x}{q_s}$  is 14% and  $\frac{T_x}{T_s}$  is 7%. Typically the run time of the experimental was only 3 seconds, which would further reduce this error.

## **B.2 Thermocouple time response**

The method used to generate the ramp change curve fit to the wall temperature trace depended on the use of the thermocouple signal as an accurate measurement of the thermal response of the surface. The thermocouple measurement of the wall temperature was used to show that the ramp change was a more accurate representation of the system than a step change, and to find the time parameters of the system for each test. The thermal product and thickness of the liquid crystal layer were sufficient that the layer could be considered to be the same material as the substrate, but the thermocouple material was significantly different to the epoxy substrate, creating a different temperature response at the outer surface of the thermocouple to the wall temperature response in the same location without the presence of the thermocouple. The significance of these factors meant that a number of points needed to be checked. Firstly, it needed to be shown that the ramp response was due to the thermal process occurring over the entire surface, not just a delay in the thermal response of the thermocouple. If this was established, then the time parameters of the ramp

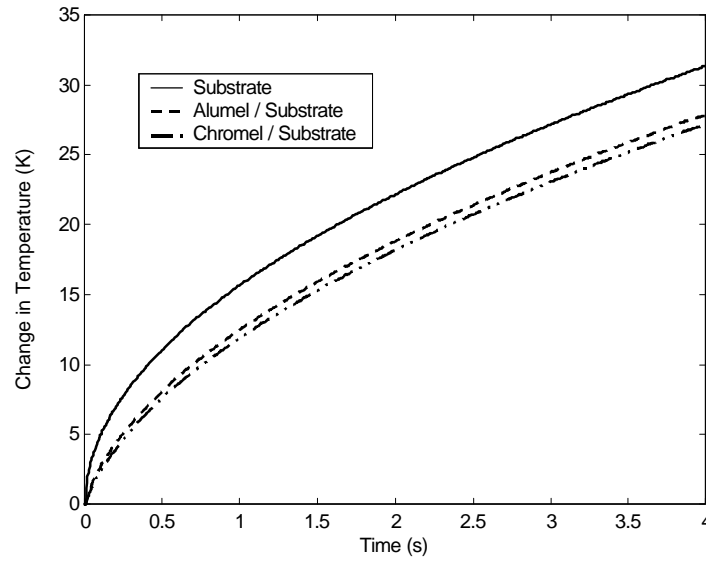


process measured at the thermocouple must be the same as the time parameters of the response of the surface. It was not obligatory to measure accurately the level of overshoot,  $I$ , because this was determined by the curve fitting routine for each individual point on the surface.

In order to check that the assumption that the difference between the thermocouple and the surface temperature responses was negligible, the double layer gauge analysis (Doorly and Oldfield, 1987) was used to model the response of the thin thermocouple layer to an applied heat flux. The impulse response method was used to generate the temperature response for substrate alone, and the temperature response at the surface of the thermocouple modelled as a layer on the surface of the substrate. The thermocouple was a 0.002 inch thick K type foil thermocouple, with thermal product and conductivity of the components (Nickel Chromium and Nickel Aluminium) as summarised in Table B.1. The two thermocouple materials were each treated separately as a layer on the substrate surface for the analysis.

	Nickel Chromium	Nickel Aluminium
Thermal product: $\sqrt{rck}$ ( $\text{Js}^{-0.5}\text{m}^{-2}$ )	7227	11728
Molecular thermal diffusivity, $a = \frac{k}{\rho c}$ ( $\text{m}^2\text{s}^{-1}$ )	$3.5 \times 10^{-6}$	$6.3 \times 10^{-6}$
$a/k$ ( $\text{m}(\text{Wm}^{-1}\text{K}^{-1})^{-1}$ )	$3.76 \times 10^{-6}$	$1.73 \times 10^{-6}$

***Table B.1 Thermal properties of thermocouple foil***

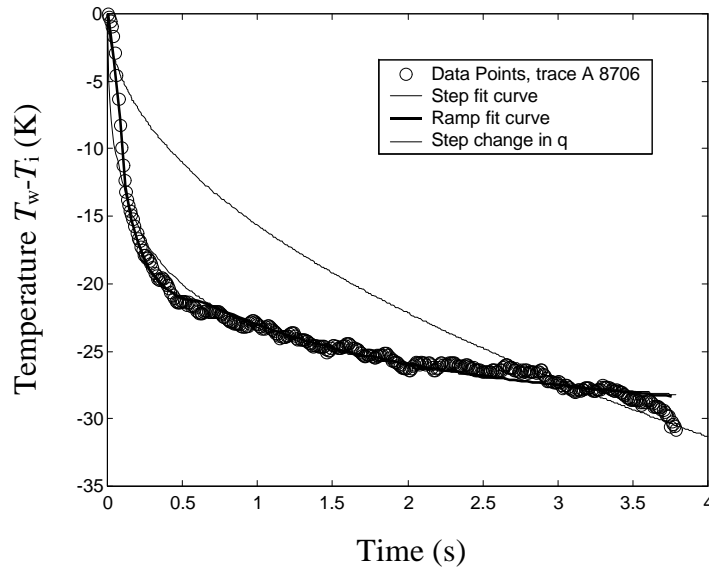


**Figure B.2: Temperature response to a step change in heat flux of  $10^4 \text{ Wm}^{-2}$**

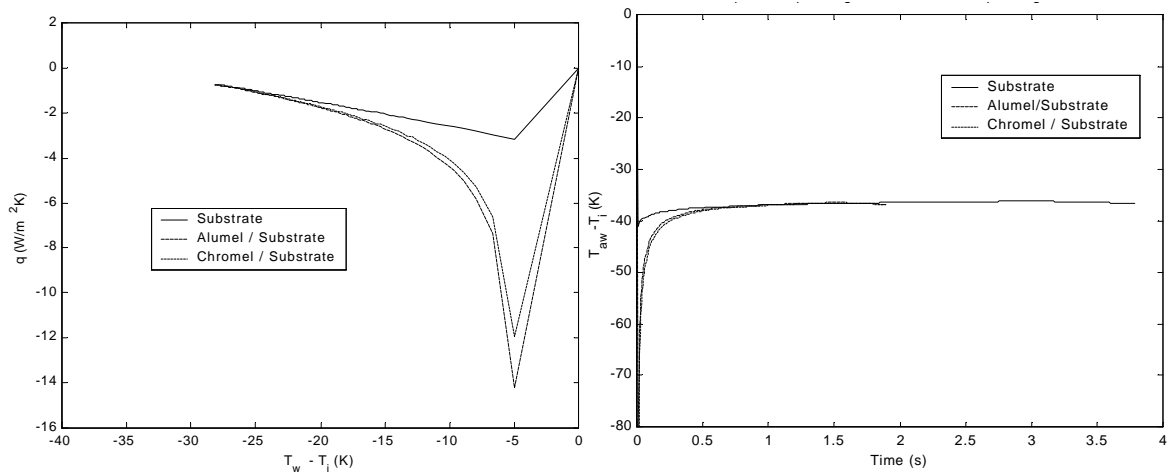
The temperature response to a step change in heat flux from 0 to  $10^4 \text{ Wm}^{-2}$  at time 0 is shown in Figure B.2. The response at each thermocouple material is similar, indicating that the measured temperature would be near the average of these. There is a significant difference between the temperature of the surface and the temperature of the thermocouple, although the shape of the curves is similar. This chart demonstrates why the thermocouples cannot be used to measure the surface temperature directly, because the temperature response is not fast enough. However, although the gradient of the response in the first 0.5 seconds is less than the gradient of the substrate response, the initial delay visible in the experimental temperature traces (e.g. Figure B.3) is not present.

Having identified that the temperature response at the thermocouple layer lags the response of the uncovered substrate layer, the following tests were devised to ensure that the method used was valid. An ‘ideal’ temperature response was assumed. This was analysed using the techniques for a semi infinite substrate and a double layer gauge described above to produce a heat flux distribution. From this an adiabatic wall temperature distribution was produced using the relationship:  $T_{aw} = T_w - \frac{q}{h}$

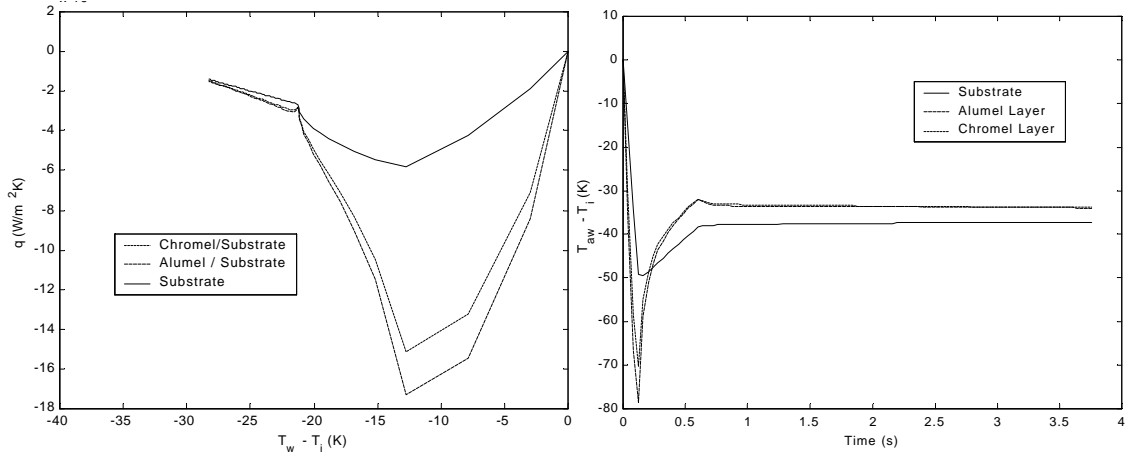
The three temperature profiles used are shown in Figure B.3. The heat flux and adiabatic wall temperature distributions generated for each of these curves are shown in Figures B.4 – B.6.



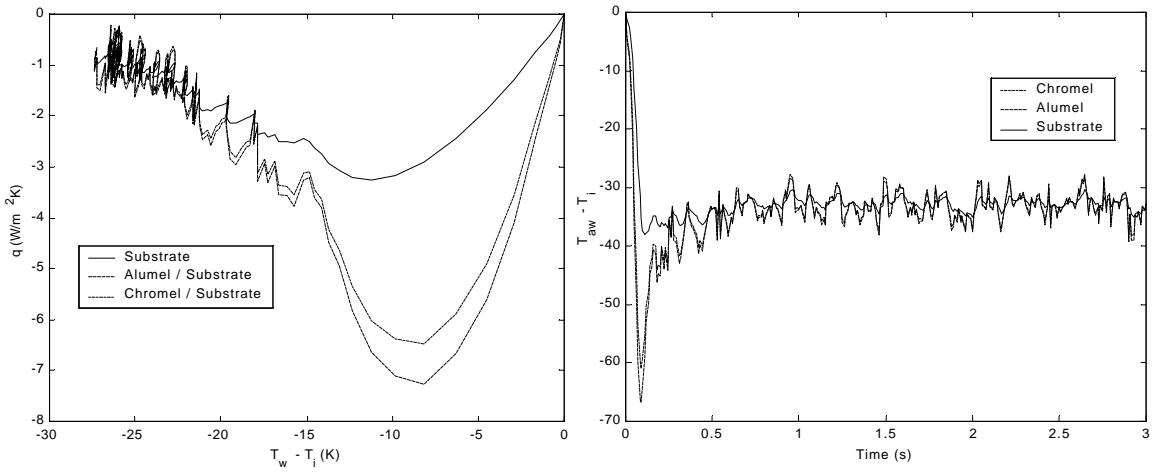
**Figure B.3: Temperature response used for the analysis**



**Figure B.4: Heat Flux and Adiabatic wall temperature distributions generated from the temperature response to a step change in  $T_{aw}$**



**Figure B.5: Heat Flux and Adiabatic wall temperature distributions generated from the temperature response to a ramp change in  $T_{aw}$**

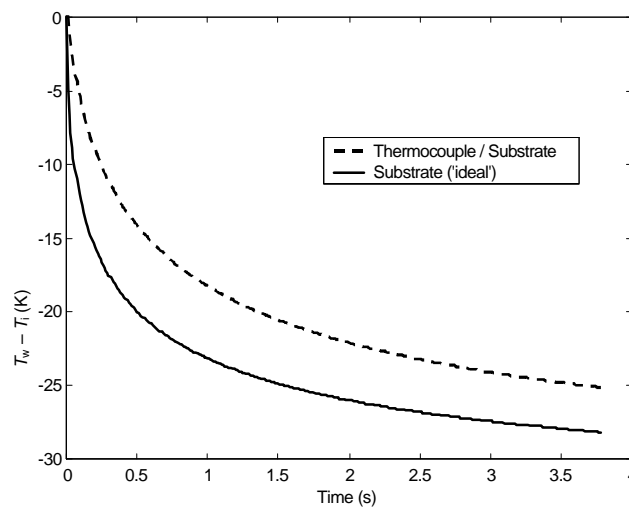


**Figure B.6: Heat Flux and Adiabatic wall temperature distributions generated from the measured temperature response from test 8706 (Pressure Surface)**

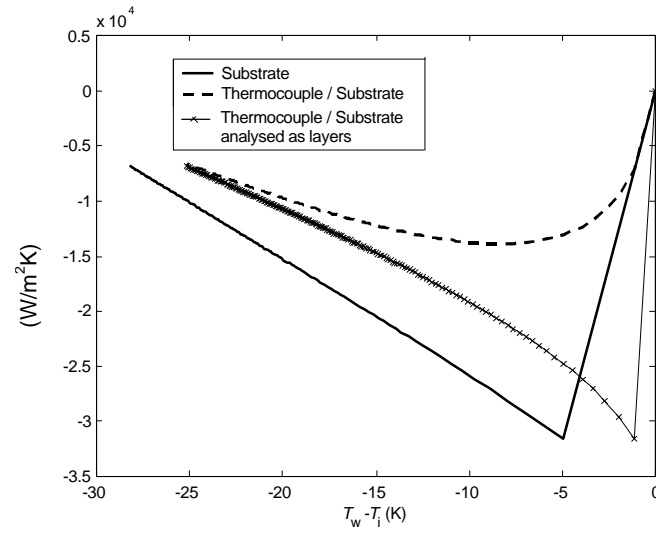
This analysis has assumed that the temperature measurement obtained from the thermocouple is the ideal temperature response from either a step or a ramp change in  $T_{aw}$  and generated from it variations in heat flux and adiabatic wall temperature. The step change temperature response produces an adiabatic wall temperature distribution from the thermocouple that is not a true step. The variation is an initial step and asymptotic response, not a two time parameter step change. The analysis of the ramp temperature response gives a ramp in  $T_{aw}$ , and although there is some curvature of the second ramp, the time parameters that would be measured from this response are equal to the actual time

parameters of the system. The heat flux distribution and adiabatic wall temperature for the ramp are similar in shape to those from the experimental data points.

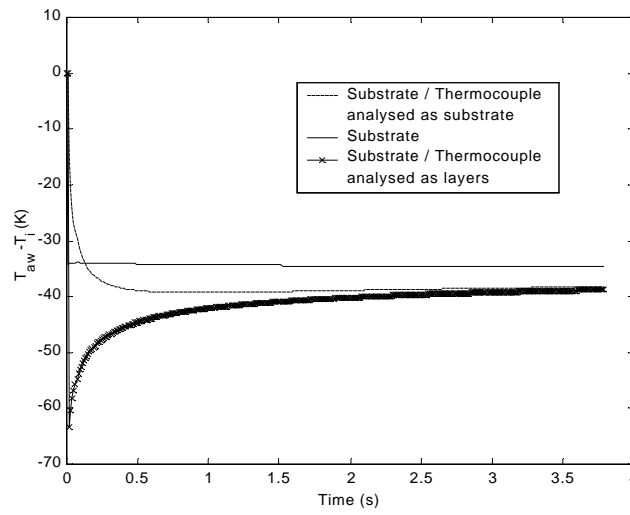
If the ideal temperature response of the surface is a step change, then the ideal heat flux from the surface that produces the temperature change can be obtained using impulse response method for the substrate material. This is shown in Figure B.4 above, for the substrate. If it is then assumed that the heat flux from the surface is uniform in the region near the thermocouple (i.e. equal to that level just calculated from a step change response), the temperature response at the thermocouple can be generated using the layer gauge method, from the substrate heat flux (Figure B.7a). If the analysis that assumes that the material is substrate is applied to this temperature response (Figure B.7a) to obtain the heat flux and adiabatic wall temperature distribution shown in Figure B.7b, then the situation that was assumed in these experiments has been modelled. That is, if there was an ideal step response, then the equivalent response with the thermocouple delay has been obtained, and analysed using the method that was used in the analysis of the results, neglecting the fact that the thermocouple had some delay. This procedure was repeated for a ramp change temperature response curve (Figures B.8a-c).



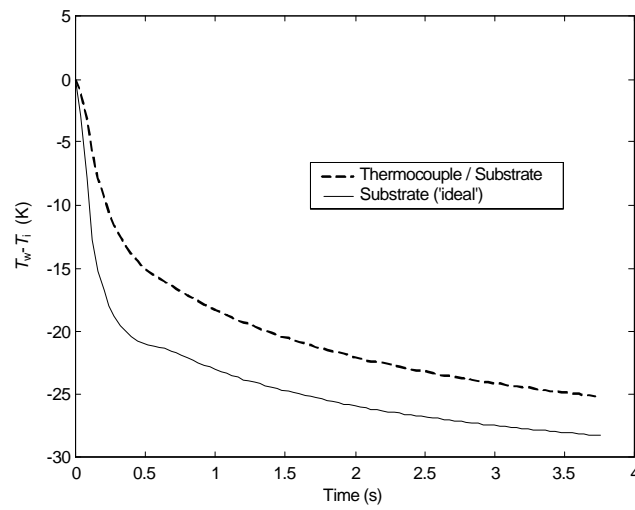
**Figure B.7a: Measured and ideal temperature responses to step change in  $T_{aw}$**



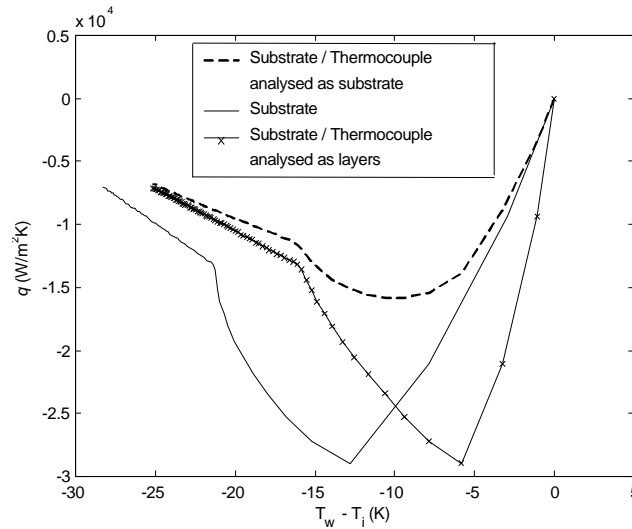
**Figure B.7b: Heat flux variation from measured temperature response to step change**



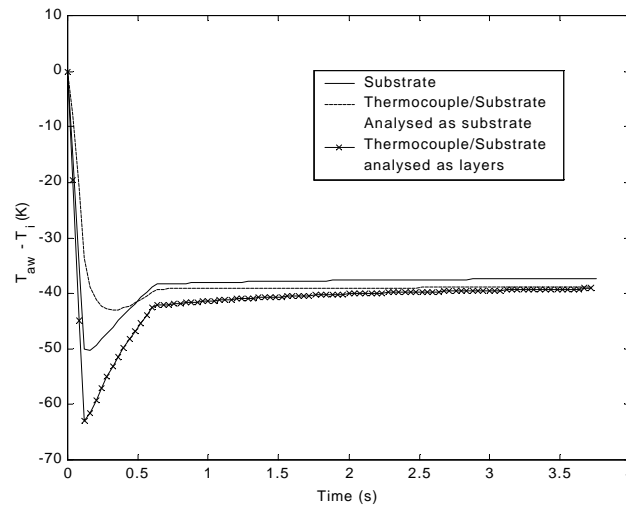
**Figure B.7c: Adiabatic wall temperature distribution obtained from analysis for step change in  $T_{aw}$**



**Figure B.8a: Measured and ideal temperature response to ramp change in  $T_{aw}$**



**Figure B.8b: Heat flux variation from measured temperature response to ramp change**



**Figure B.8c: Adiabatic wall temperature distribution obtained from analysis for ramp change in  $T_{aw}$**

The variable that was matched in these comparisons was the heat flux pulse that was input to the model, from which a ‘measured’ temperature response was obtained. In Figures B.7a and B.8a the actual temperature response at the surface is shown as a solid line and the temperature response that would be measured by the thermocouple is a dashed line. Here the error in the thermocouple measurement is again apparent.

In Figures B.7b and B.8b, the heat flux has been calculated by applying the impulse response method to the temperature traces. The solid line is the ideal heat flux, which was

used to generate the temperature curve for the thermocouple. The dashed line is the heat flux trace for the thermocouple temperature response, analysed using only the simple substrate model. The difference between this curve and the former demonstrates the amount of data that is lost in the thermocouple delay. The third curve shows the thermocouple temperature trace analysed using the thermocouple model.

The significant part of this analysis is shown in Figures B.7c, which was based on a step change temperature response and B.8c based on the ramp change response. Analysing the thermocouple temperature response from a step change results in a slight delay at the beginning of the experiment and the adiabatic wall temperature is not an ideal step change, but the variation is asymptotic to the final  $T_{aw}$ . There is no evidence of a two time parameter ramp change in this response. In contrast, the thermocouple temperature response to a ramp change in  $T_{aw}$  in Figure B.8c clearly shows that there is a two time parameter ramp change in  $T_{aw}$  remaining after the signal has been processed. The other important conclusion from this chart is that the time parameters of the system are identical, and correct, whether the thermocouple system is modelled neglecting the time delay between ideal and measured temperature responses or whether the double gauge analysis is used. This important conclusion validates the fact that the ramp change response found by analysis of the thermocouple signal is a real feature of the system being modelled, and that the time parameters measured from the thermocouple signal are the correct time parameters of the system.

### ***B.3 Ramp change curve fit***

#### **The effect of changing the variables**

The temperature profile generated by the ramp change curve fitting routine is dependent on five variables, namely the heat transfer coefficient,  $h$ , adiabatic effectiveness,  $\mathbf{h}$ , the

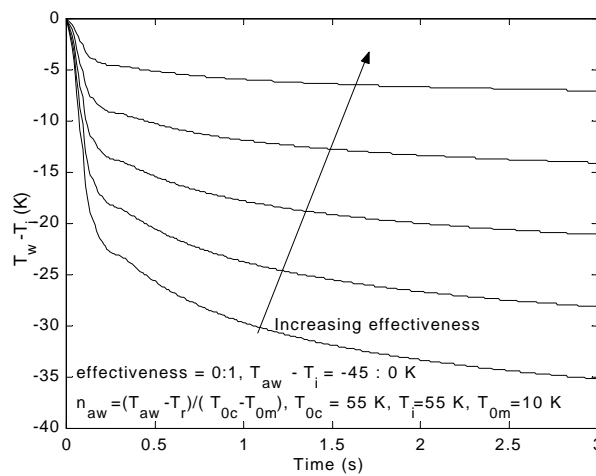


ramp overshoot factor,  $I$ , and the two ramp time parameters,  $t_1$  and  $t_2$ . The latter three parameters are generated by the assumed ramp variation in adiabatic wall temperature, whilst  $h$  and  $\mathbf{h}$  are functions of the transient heat transfer, and are found through the curve fitting process. The following figures summarise the effects of changing each of the variables whilst the others are held at a nominal value.

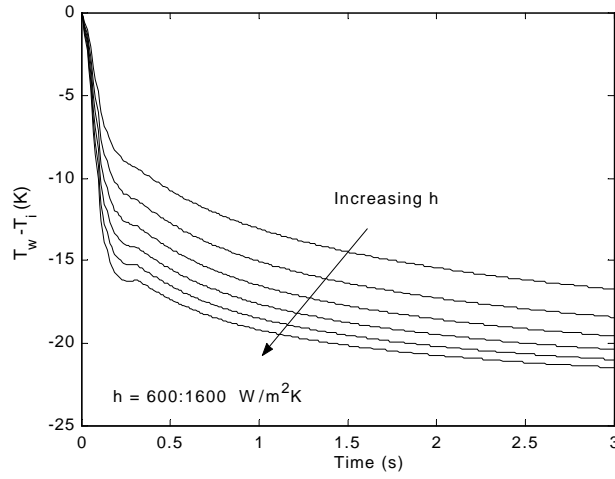
The variation of effectiveness, or adiabatic wall temperature in Figure B.9, demonstrates that the shape of the curve remains similar, but the final temperature that the wall approaches increases with increasing adiabatic wall temperature corresponding to increasing effectiveness. There is also an increase in the slope of the curve in the steady state region at lower effectiveness levels.

Figure B.10 shows that for increasing  $h$ , the initial drop in temperature at the beginning of the experiment is increased, but otherwise the curves are similar in shape.

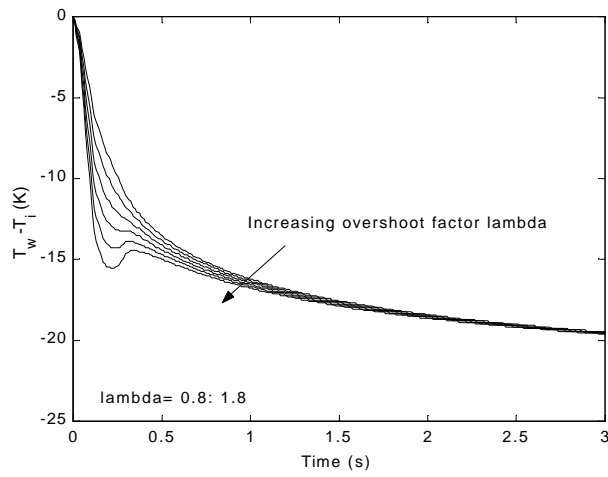
In Figures B.11- B.13, the changes in overshoot factor and time parameters only affect the first 1.5 seconds of the wall temperature variation. These affects are only important for the initial unsteady heat transfer, and should only alter the early part of the curve fit.



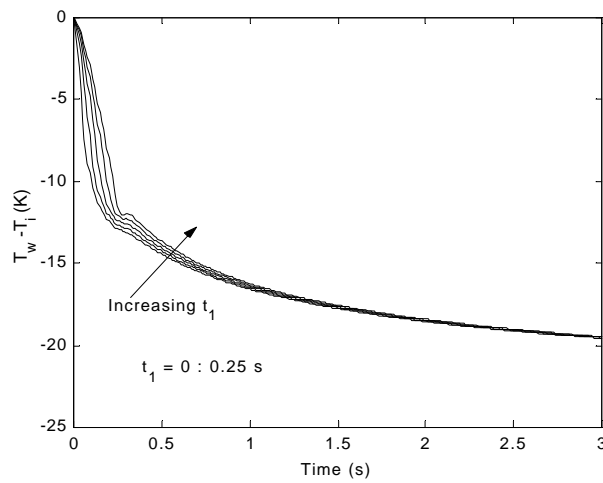
**Figure B.9: Variation in adiabatic effectiveness,  $h$ , by variation in adiabatic wall temperature,  $T_{aw}$**



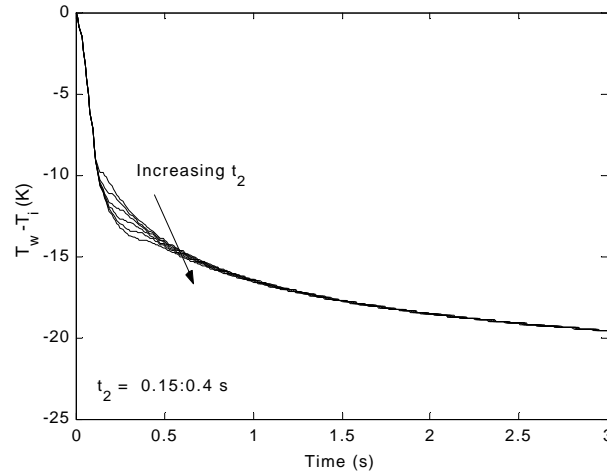
**Figure B.10: Variation in heat transfer coefficient,  $h$**



**Figure B.11: Variation in overshoot factor,  $\lambda$**



**Figure B.12: Variation in first time parameter,  $t_1$**



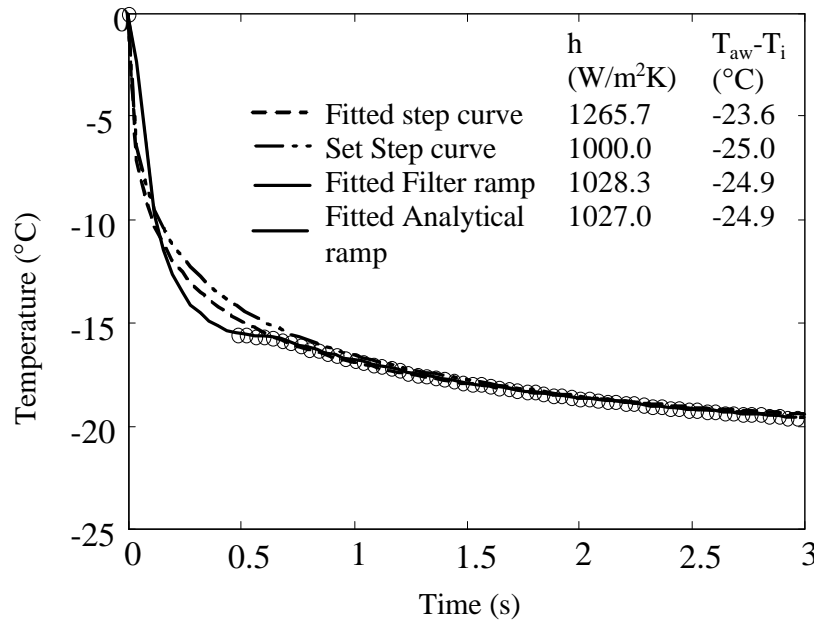
**Figure B.13: Variation in second time parameter,  $t_2$**

### **The effect of adding random noise**

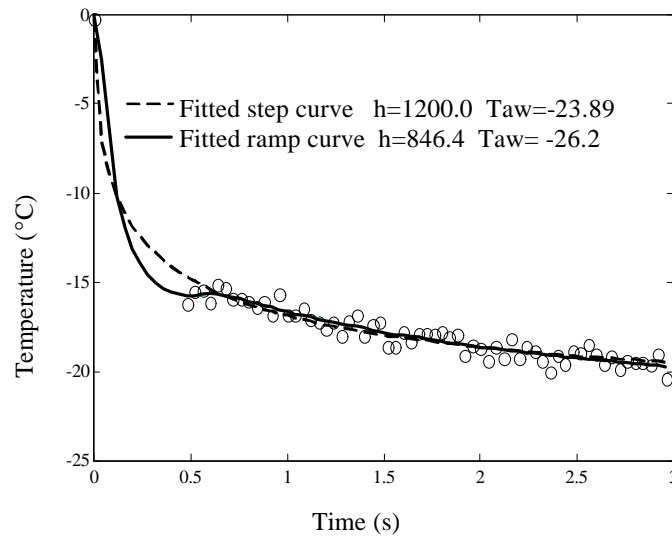
The sensitivity of the method to the levels of random noise that could be expected in the experimental results was tested for the analytical and filter ramp change techniques and these results were compared with a step change curve fit. A set of hypothetical data points was generated from the analytical ramp solution with parameters  $h=1000 \text{ W/m}^2\text{K}$ ,  $T_{\text{aw}}=-25^\circ\text{C}$ ,  $I=1.3$ ,  $t_1=0.1$  and  $t_2=0.6$ .

Figure B.14 shows the hypothetical data points (o) and the curve fits that might have been used to calculate  $h$  and  $T_{\text{aw}}$  from them. The fitted step curve is an attempt to model fit a step curve to the data points using least squares regression, and the set step curve is the step curve which corresponds to the same  $h$  and  $T_{\text{aw}}$  as the data points. The fitted step curve clearly over predicts both  $h$  and  $T_{\text{aw}}$ . The analytical ramp function is the method outlined in Section 6.3, which fits an analytical solution to the data points using least squares regression, and the filter ramp method is the method described in Section 6.4.6, using an impulse response filter to generate the fitted curve for a two layer substrate (although in this instance it uses the same material for both layers). Both of the ramp methods give results very similar to the ideal values of  $h$  and  $T_{\text{aw}}$  for the data.

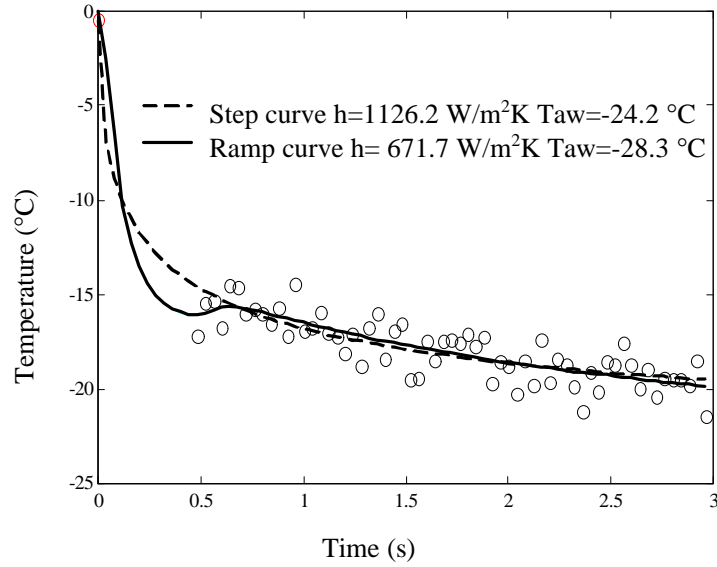
Figures B.15 and B.16 show the hypothetical data with random noise added to the temperature values. The noise introduces some error, but it should be noted that as shown in the typical set of experimental data with noise in Figure B.17, the noise measured in the experiments was typically fairly low, so Figure B.15 is an overestimate of the level of noise and hence error that can be expected.



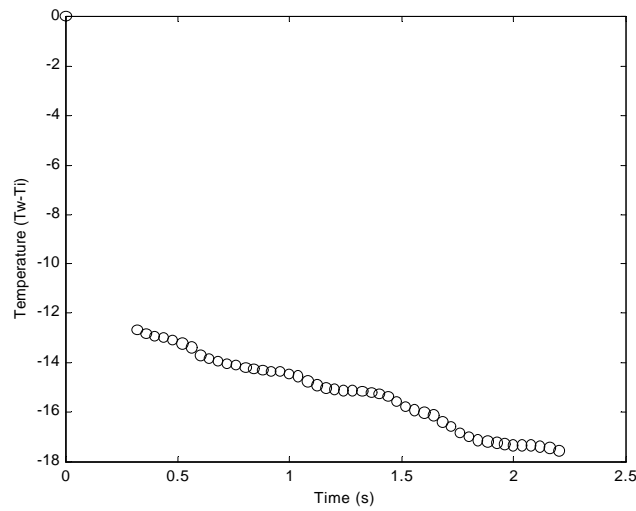
**Figure B.14: Generated data points with analytical and filter ramp and step change curve fits and step change curve with correct  $h$  and  $T_{aw}$**



**Figure B.15: Generated data points with random noise, step and ramp change curve fits (noise mean = 0, limits =  $\pm 1$ )**



**Figure B.16:** *Generated data points with random noise, step and ramp change curve fits (noise mean = 0, std dev = 1)*



**Figure B.17:** *Typical data set with experimental noise*

## Error Analysis

In Section 6.5, a summary of the analysis of the sources of error in the measurement and calculation of heat transfer coefficient,  $h$ , and adiabatic wall temperature,  $T_{aw}$ , were discussed. The hypothetical data set used for the noise calculations in the previous section. The contribution of each source of error was estimated by making an adjustment to the

relevant data input to the curve fitting routine, to set it to be at the outside error estimate. The error in  $h$  and  $T_{aw}$  was then obtained by comparing the values obtained from the curve fitting routine with the adjusted data, with the ideal values of  $h$  and  $T_{aw}$  used to generate the initial data set. The sensitivity of  $h$  and  $T_{aw}$  to the changes in parameters was calculated using the following definition of sensitivity:

$$\text{Sensitivity} = \frac{\% \text{ Change in output}}{\% \text{ Change in input}} \quad (B.5)$$

<b>Change applied to data fed to curve fit</b>	<b><math>h</math> (<math>\text{Wm}^{-2}\text{K}^{-1}</math>) (ideal value 1000)</b>	<b><math>T_{aw} - T_i</math> (K) (ideal value -25)</b>	<b>Sensitivity in <math>h</math> (%)</b>	<b>Sensitivity in <math>T_{aw} - T_i</math> (%)</b>
$t_2 = 0.65$ s	1030.6	-24.9	37	5
$t_2 = 0.55$ s	1012.4	-24.9	15	5
$t_1 = 0.05$ s	998.2	-25.0	0	0
$t_1 = 0.15$ s	1058.4	-24.7	12	2
$\sqrt{rck} = 730 \text{ Wm}^{-2}\text{K}^{-1}\text{s}^{0.5}$	1041	-24.8	295	58
$\sqrt{rck} = 710 \text{ Wm}^{-2}\text{K}^{-1}\text{s}^{0.5}$	1012.7	-24.9	91	29
Add 0.2 K to all surface temperatures	1012.4	-24.7	186	180
Subtract 0.2 K from all surface temperatures	1041.5	-25.0	623	0
Initial Temperature +1 K	1099.7	-25.7	499	140
Initial Temperature -1 K	954.2	-24.0	229	200
Add 0.04 s to all data points	971.9	-25.2	105	30
Subtract 0.04 s from all data points	1027.0	-24.9	101	15

**Table B.2: Data perturbation used to estimate the effects of error sources on the calculation of  $h$  and  $T_{aw}$**

## Chapter 11 Bibliography

- Ainsworth, R.W., Allen, J.L., Davies, M.R.D., Doorly, J.E., Forth, C.J.P., Hilditch, M.A., Oldfield, M.L.G. and Sheard, A.G., 1989, "Developments in Instrumentation and Processing for Transient Heat Transfer Measurements in a Full Stage Model Turbine", *ASME Journal of Turbomachinery*, **111**: 20-27
- Ammari, H.D., Hay, N. and Lampard, D., 1990, "The Effect of Density Ratio on the Heat Transfer Coefficient from a Film-Cooled Flat Plate", *ASME Journal of Turbomachinery*, **112**: 444 – 450
- Andreopoulos, J., Rodi, W., 1984, "Experimental Investigation of Jets in a Crossflow", *Journal of Fluid Mechanics*, **138**: 93-127
- Arts, T., and Bourguignon, A.E., 1990, "Behaviour of a Coolant Film with Two Rows of Holes Along the Pressure Side of a High-Pressure Nozzle Guide Vane", *ASME Journal of Turbomachinery*, **112**: 512-521
- Baier, R.D., Koschel, W., Broichhausen, K.D. and Fritsch, G., 1997, "Systematic Study on the Fluid Dynamical Behaviour of Streamwise and Laterally Inclined Jets in Crossflow", ASME Paper 97-GT-98
- Ballal, D.R. and Lefebvre, A.H., 1973, "Film-Cooling Effectiveness in the Near-Slot Region", *ASME Journal of Heat Transfer*, May 1973, pp 265-266
- Berhe, M.K. and Patankar, S.V., 1998a, "Curvature Effects on Discrete-Hole Film Cooling", ASME Paper 98-GT-373
- Berhe, M.K. and Patankar, S.V., 1998b, "Investigation of Discrete-Hole Film Cooling Parameters using Curved Plate Models", ASME Paper 98-GT-374
- Boyle, R.J., Spuckler, C.M., Lucci, B.L., and Camperchioli, W.P., 2000, "Infrared Low Temperature Turbine Vane Rough Surface Heat Transfer Measurements", ASME Paper 2000-GT-0216
- Burd, S.W., Oke, R.A. and Simon, T.W., 1998, "Measurements of Aerodynamic Penalties Associated with Film Cooling", HTD-Vol. 361-3/PID-Vol.3, *Proceedings of the ASME Heat Transfer Division - Volume 3*
- Burns, W.K. and Stollery, J.L., 1969, "The influence of Foreign Gas Injection and Slot Geometry on Film Cooling Effectiveness" *International Journal of Heat and Mass Transfer*, **12**: 935-951
- Burggraf, F., Chin, J.H. and Hayes, L.E., 1961, "Film Cooling with Multiple Slots and Louvers", *ASME Journal of Heat Transfer*, **83**: 281-292

- Casciaro, C., Treiber, M., Sell, M., Saxer, A.P., Gyarmathy, G., 1998**, “A Comparison of Experimental with Computational Results in an Annular Turbine Cascade with Emphasis on Losses”, ASME Paper 98-GT-146
- Chen, P.H., Ai, D. and Lee, S.H., 1998**, “Effects of Compound Angle Injection on Flat-Plate Film Cooling Through a Row of Conical Holes”, ASME Paper 98-GT-459
- Chen, P.H., Hung, M.S. and Ding, P.P., 2000**, “Film Cooling Performance on Curved Walls with Compound Angle Hole Configuration”, *Proceedings of Turbine-2000, International Symposium on Heat Transfer in Gas Turbine Systems*, Turkey
- Chernobrovkin, A. and Lakshminarayana, B., 1998**, “Numerical Simulation and Aerothermal Physics of Leading Edge Film Cooling”, ASME Paper 98-GT-504
- Cohen, H., Rogers, G.F.C. and Saravanamuttoo, H.I.H., 1996**, “Gas Turbine Theory”, 4th edition, Longman Group Ltd, England
- Davies, M.R.D and O'Donnell, F.K., 1999**, “Local Measurements of Loss using Heated Thin Film Sensors”, *ASME Journal of Turbomachinery*, **121**: 814-818 also ASME Paper 98-GT-380
- Day, C.R.B., 1997**, “Aerodynamics of an Annular Film-Cooled Turbine Cascade”, DPhil Thesis, University of Oxford
- Day, C.R.B., Oldfield, M.L.G., Lock, G.D. and Dancer, S.N., 1998**, “Efficiency Measurements of an Annular Nozzle Guide Vane Cascade with Different Film Cooling Geometries”, ASME Paper 98-GT-538
- Day, C.R.B., Oldfield, M.L.G. and Lock, G.D., 1999**, “The Influence of Film Cooling on the Efficiency of an Annular Nozzle Guide Vane Cascade”, *ASME Journal of Turbomachinery*, **121**: 145-151, also ASME Paper 97-GT-521
- Day, C.R.B., Oldfield, M.L.G. and Lock, G.D., 2000**, “Aerodynamic performance of an annular cascade of film cooling nozzle guide vanes under engine representative conditions”, *Experiments in Fluids*, **29**: 117-129
- Denton, J.D., 1993**, “Loss Mechanisms in Turbomachines”, *ASME Journal of Turbomachinery*, **115**: 621-650
- Dominy R.G. and Hodson, H.P. 1992**, “An Investigation of Factors Influencing the Calibration of 5-Hole Probes for 3D Flow Measurements”, ASME Paper 92-GT-216
- Doorly, J.E. and Oldfield, M.L.G., 1987**, “The Theory of Advanced Multi-layer Thin Film Heat Transfer Gauges”, *International Journal of Heat and Mass Transfer*, **30**: 1159-1168
- Dzung, L.S., 1971**, “Konsistente Mittelwerte in der Theorie der Turbomaschinen fur Kompressible Medien”, *BBC-Mitt*, **58**: 485-492
- Eckert, E.R.G. and Drake, R.M., 1972**, “Analysis of Heat and Mass Transfer”, *McGraw Hill* pp. 453-466
- Ekkad, S.V., Zapata, D. and Han, J.C., 1997a** “Heat Transfer Coefficient over a Flat Surface with Air and CO<sub>2</sub> Injection Through Compound Angle Holes Using a Transient Liquid Crystal Image Method” *ASME Journal of Turbomachinery*, **119**: 580-586 also ASME Paper 95-GT-10
- Ekkad, S.V., Zapata, D. and Han, J.C., 1997b**, “Film Effectiveness over a Flat Surface with Air and CO<sub>2</sub> Injection Through Compound Angle Holes Using a Transient Liquid



Crystal Image Method”, *ASME Journal of Turbomachinery*, **119**: 587-592 also ASME Paper 95-GT-11

**Farmer, J.P., Seager, D.J., and Liburdy, J.A. 1997** “The Effect of Shaping Inclined Slots on Film Cooling Effectiveness and Heat Transfer Coefficient” ASME Paper 97-GT-399

**Forth, C.J.P. and Jones, T.V., 1986**, “Scaling Parameters in Film-Cooling” *Proceedings of the 8<sup>th</sup> International Heat Transfer Symposium*, San Francisco, 1986

**Garg, V.K. and Gaugler, R.E., 1997**, “Effect of Velocity and Temperature Distribution at the Hole Exit on Film Cooling of Turbine Blades”, *ASME Journal of Turbomachinery*, **119**: 343-351

**Giebert, D., Gritsch, M., Schulz, A. and Wittig, S., 1997**, “Film-Cooling from Holes with Expanded Exits: A Comparison of Computational Results with Experiments”, ASME Paper 97-GT-163

**Gehrer, A., Woisetschlaeger, J. and Jericha, H., 1997**, “Blade Film Cooling by Underexpanded Transonic Jet Layers”, ASME Paper 97-GT-246

**Goldstein, R.J., Shavit, G. and Chen, T.S., 1965**, “Film-Cooling Effectiveness with Injection through a Porous Section”, *ASME Journal of Heat Transfer*, **87**: 353-360.

**Goldstein, R.J., Eckert, E.R.G., and Ramsey, J.W., 1968**, “Film Cooling with Injection Through Holes: Adiabatic Wall Temperatures Downstream of a Circular Hole”, *ASME Journal of Engineering for Power* **90**: 384-395

**Goldstein, R.J., Eckert, E.R.G., Eriksen, V.L. and Ramsey, J.W., 1970**, “Film Cooling Following Injection through Inclined Circular Tubes”, *Israel Journal of Technology*, **8**: 145-154 (summarised in Goldstein et al 1971)

**Goldstein, R.J., 1971** “Film Cooling”, *Advances in Heat Transfer*, Academic Press, **7**: 321-379

**Goldstein, R.J., Eckert, E.R.G. and Burggraf, F. 1974**, “Effects of Hole Geometry and Density on Three-Dimensional Film Cooling”, *International Journal of Heat and Mass Transfer*, **17**: 595-607

**Goldstein, R.J., Jin, P. and Olson, R.L., 1998**, “Film Cooling Effectiveness and Mass / Heat Transfer Coefficient Downstream of One Row of Discrete Holes”, ASME Paper 98-GT-174

**Gonzalez, R.C. and Woods, R.E., 1993**, “Digital Image Processing”, *Addison-Wesley*

**Gritsch, M., Schulz, A., and Wittig, S. 1997**, “Discharge Coefficient Measurements of Film Cooling Holes with Expanded Exits”, ASME Paper 97-GT-165

**Gritsch, M., Schulz, A., and Wittig, S., 1998a**, “Heat Transfer Coefficient Measurements of Film Cooling Holes with Expanded Exits”, ASME Paper 98-GT-28

**Gritsch, M., Schulz, A., and Wittig, S. 1998b**, “Adiabatic Wall Effectiveness Measurements of Film Cooling Holes with Expanded Exits”, *ASME Journal of Turbomachinery*, **120**: 549-556 also ASME Paper 97-GT-164

**Guo, S.M., 1997**, “Heat Transfer and Aerodynamic Studies of a Nozzle Guide Vane and the Development of New Heat Transfer Gauges”, DPhil Thesis, University of Oxford

- Guo, S.M., Lai, C.C., Jones, T.V., Oldfield, M.L.G., Lock, G.D. and Rawlinson, A.J., 1998** “The Application of Thin-Film Technology to Measure Turbine-Vane Heat Transfer and Effectiveness in a Film-Cooled, Engine-Simulated Environment”, *International Journal of Heat and Fluid Flow*, **19**: 594-600
- Hartnett, J.P., Birkebak, R.C., and Eckert, E.R.G., 1961**, “Velocity distributions, Temperature Distributions, Effectiveness and Heat Transfer for Air Injected Through a Tangential Slot into a Turbulent Boundary Layer”, *ASME Journal of Heat Transfer* **83**, No.3: 293-306
- Hartsel, J.E., 1972**, “Prediction of Effects of Mass-Transfer Cooling on the Blade-Row Efficiency of Turbine Airfoils”, AIAA Paper No. 72-11, AIAA 10<sup>th</sup> Aerospace Sciences Meeting
- Harvey, N.W., 1991**, “Heat Transfer on Nozzle Guide Vane End Walls”, DPhil Thesis, University of Oxford
- Haslinger, W. and Hennecke, D.K., 1996**, “The Ammonia and Diazo Technique with CO<sub>2</sub>- Calibration for Highly Resolving and Accurate Measurement of Adiabatic Film Cooling Effectiveness with Application to a Row of Holes”, ASME Paper 96-GT-438
- Haven, B.A. and Kurosaka, M., 1996**, “Improved Jet Coverage through Vortex Cancellation”, *AIAA Journal* **34** No. 11: 2443-2444
- Haven, B.A. and Kurosaka, M., 1997**, “Kidney and Anti-Kidney Vortices in Crossflow Jets”, *ASME Journal of Fluid Mechanics* **352**: 27-64
- Haven, B.A., Yamagata, D.K., Kurosaka, M., Yamawaki, S., Maya, T., 1997**, “Anti-kidney Pair of Vortices in Shaped Holes and their Influence on Film Cooling Effectiveness” ASME Paper 97-GT-45
- Hoffs, A., Drost, U. and Bolcs, A., 1996**, “Heat Transfer Measurements on a Turbine Airfoil at Various Reynolds Numbers and Turbulence Intensities Including Effects of Surface Roughness”, ASME Paper 96-GT-169
- Hyams, D.G., McGovern, K.T., Leylek, J.H., 1996**, “Effects of Geometry on Slot-Jet Film Cooling Performance”, ASME Paper 96-GT-187
- Ireland, P.T. and Jones, T.V., 1987**, “The Response Time of a Surface Thermometer Employing Encapsulated Thermochromic Liquid Crystals”, *Journal of Physics E*, **20**: 1195-1199
- Ireland, P.T., Wang, Z.W. and Jones T.V., 1993**, “Liquid Crystal Heat Transfer Measurements”, von Karman Institute for Fluid Dynamics 1992-1993 Lecture Series
- Ireland, P.T. and Jones, T.V., 2000**, “Liquid Crystal Measurement of Heat Transfer and Shear Stress”, *Measurement Science Technology*, **11**: 969–986
- Ito, S., Goldstein, R.J. and Eckert, E.R.G., 1978**, “Film Cooling of a Gas Turbine Blade”, *ASME Journal of Engineering for Power*, **100**: 476-481
- Jabbari, M.Y. and Goldstein, R.J., 1978**, “Adiabatic Wall Temperature and Heat Transfer Downstream of Injection Through Two Rows of Holes”, *ASME Journal of Engineering for Power*, **100**: 303-307
- Jones, T.V., 1978**, “A Cold Heat Transfer Tunnel” OUEL Internal Report No. 1274/78

- Jones, T.V., 1991**, “Definition of Heat Transfer Coefficient in the Turbine Situation”, IMechE 1991-3, C423/046, *Turbomachinery: Latest Developments in a Changing Scene*, pp. 201-206
- Jones, T.V., Oldfield, M.L.G., Ainsworth, R.W. and Arts, T., 1993**, “Transient Cascade Testing”, *Advanced Methods for Cascade Testing, Chapter 5, AGARD AG-328*
- Jones, T.V., 1999**, “Theory for the use of Foreign Gas in Simulating Film Cooling”, *International Journal of Heat and Fluid Flow* **20**: 349-354
- Kays, W.M. and Crawford M.E., 1993**, “Convective Heat and Mass Transfer”, 3<sup>rd</sup> Edition, *McGraw-Hill Inc*
- Ko, S.Y., Yao, Y.Q., Xia, B. and Tsou, F.K., 1986**, “Discrete Hole Film Cooling Characteristics over Concave and Convex Surfaces”, *Proceedings of the 8<sup>th</sup> International Heat Transfer Conference*, Hemisphere Publishing Corp, New York, **3**: 1297-1301
- Lai, C.C., 1999**, “Fully Film Cooled Nozzle Guide Vane Heat Transfer Measurement and Prediction”, DPhil Thesis, University of Oxford
- Lakshminarayana, B., 1996**, “Fluid Dynamics and Heat Transfer of Turbomachinery”, *Wiley and Sons Inc*
- Langston, L.S., 2000**, “Secondary flows in Axial Turbines - A Review”, *Proceedings of Turbine-2000, International Symposium on Heat Transfer in Gas Turbine Systems*, Turkey
- Leboeuf, F. and Sgarzi, O., 2000**, “The Detailed Structure and Behaviour of Discrete Cooling Jets in a Turbine”, *Proceedings of Turbine-2000, International Symposium on Heat Transfer in Gas Turbine Systems*, Turkey
- Leylek, J.H. and Zerkle, R.D., 1994**, “Discrete-Jet Film Cooling: A Comparison of Computational Results with Experiments”, *ASME Journal of Turbomachinery*, **116**: 358-368
- Ligrani, P.M., Ortiz, A., Joseph, S.L. and Evans, D.L., 1989**, “Effects of Embedded Vortices on Film-Cooled Turbulent Boundary Layers”, *ASME Journal of Turbomachinery*, **111**: 71-77
- Ligrani, P.M., Ciriello, S. and Bishop, D.T., 1992**, “Heat Transfer, Adiabatic Effectiveness, and Injectant Distributions Downstream of a Single Row and Two Staggered Rows of Compound Angle Film-Cooling Holes”, *ASME Journal of Turbomachinery*, **114**: 687-700.
- Ligrani, P.M., Wigle, Ciriello, S., and Jackson, 1994**, “Film-Cooling from Holes with Compound Angle Orientations: Part 1 - Results Downstream of Two Staggered Rows of Holes with 3d Spanwise Spacing”, *ASME Journal of Heat Transfer*, **116**: 341-352
- Lin, Y.L., Shih, T.I.P., 1998**, “Computations of Discrete-Hole Film Cooling over Flat and Convex Surfaces”, *ASME Paper 98-GT-436*
- Lopez Penz, F. and Arts, T., “ On the Development of a Film Cooling Layer”, AGARD-CP-527**
- Main, A. J., 1994**, “Annular Cascade Aerodynamics”, DPhil thesis, University of Oxford.
- Main, A.J., Day, C.R.B., Lock G.D. and Oldfield, M.L.G., 1996**, “Calibration of a four-hole pyramid probe and area traverse measurements in a short-duration transonic turbine cascade tunnel”, *Experiments in Fluids*, **21**: 302-311

- Main, A.J., Oldfield, M.L.G., Lock, G.D. and Jones, T.V., 1997**, “Free Vortex Theory for Efficiency Calculations from Annular Cascade Data”, *ASME Journal of Turbomachinery*, **119**: 247-255 also ASME Paper 95-GT-186
- Mathelin, L., Bataille, F., Lallemand, A., 2000**, “Comparison between two models of cooling surfaces using blowing”, *Proceedings of Turbine-2000, International Symposium on Heat Transfer in Gas Turbine Systems*, Turkey
- Martinez-Botas, R.F., Main, A.J., Lock, G.D., and Oldfield, M.L.G., 1993**, “A Cold Heat Transfer Tunnel for Gas Turbine Research on an Annular Cascade”, ASME Paper 93-GT-248
- Martinez-Botas, R.F., Lock, G.D., and Jones, T.V., 1994**, “Heat Transfer Measurements in an Annular Cascade of Transonic Gas Turbine Blades using the Transient Liquid Crystal Technique”, *ASME Journal of Turbomachinery*, **117**: 425-431
- Martinez-Botas, R.F., Yuen, C.H.N., 2000**, “Measurement of Local Heat Transfer Coefficient and Film Cooling Effectiveness through Discrete Holes”, ASME Paper 2000-GT-243
- Mee, D.J., Ireland, P.T. and Bather, S., 1999**, “Measurement of the temperature field downstream of simulated leading-edge film-cooling holes”, *Experiments in Fluids*, **27**: 273-283
- Metzger, D.E., Carper, H.J. and Swank, L.R., 1968**, “Heat Transfer With Film Cooling near Nontangential Injection Slots”, *ASME Journal of Engineering for Power*, April 1968: 157-163
- Moon, H.K. and Jaiswal, 2000**, “Cooling Effectiveness Measurements with Thermal Radiometry in a Turbine Cascade”, ASME Paper 2000-GT-0207
- Moser, S., Ivanisin, M., Woisetschlager, J., and Jericha, H., 2000**, “Novel Blade Cooling Engineering Solution”, ASME Paper 2000-GT-242
- Moskowitz, S.L. and Lombardo, S., 1971**, “2750 Deg F Engine Test of a Transpiration Air-Cooled Turbine”, *Journal of Engineering for Power*, **93**: 238-248
- Moss, R.W. and Oldfield, M.L.G., 1991**, “Measurements of Hot Combustor Turbulence Spectra”, ASME Paper 91-GT-351
- Muldoon, F. and Acharya, S., 1999**, “Dynamics of Large-Scale Structures for Jets in a Crossflow”, *ASME Journal of Turbomachinery*, **121**: 577-587, also ASME Paper 98-GT-19
- Munson, B.R., Young, D.F. and Okiishi, T.H., 1994**, “Fundamentals of Fluid Mechanics”, Second edition, *John Wiley and Sons Inc*
- Oates, G.C. (Editor), 1985**, “Aerothermodynamics of Aircraft Engine Components”, *American Institute of Aeronautics and Astronautics Inc*
- Oldfield, M.L.G., Jones, T.V. and Schultz, D.L., 1978**, “Online Computer for Transient Turbine Cascade Instrumentation”, *IEEE Transactions on Aerospace and Electronic Systems*, AES-14, 5
- Oldfield, M.L.G. and Guo, S.M., 1997**, “Aero-thermal Properties of Foreign Gas (SF<sub>6</sub>/Ar) and Air: Recommended Formulae from 160-100 K”, OUEL Report 2141/97
- Oldfield, M.L.G. and Lock, G.D., 1998**, “Coolant Passages for Gas Turbine Components”, Patent Application No 9821639.3

- Oldfield, M.L.G., 2000**, “Guide to Impulse Response Heat Transfer Signal Processing: Version 2”, OUEL Report 2233/2000
- Osnaghi, C., Perdichizzi, A., Savini, M., Harasgama, P. and Lutum, E., 1997**, “The Influence of Film Cooling on the Aerodynamic Performance of a Turbine Nozzle Guide Vane”, ASME Paper 97-GT-522
- Pietrzyk, J.R., Bogard, D.G. and Crawford, M.E., 1989**, “Hydrodynamic Measurements of Jets in Crossflow for Gas Turbine Film Cooling Applications”, *ASME Journal of Turbomachinery*, **111**: 139-145
- Rogers, G.F.C. and Mayhew, Y.R., 1957**, “Engineering Thermodynamics Work and Heat Transfer”, *Longman*, London and New York
- Rolls-Royce Publications, 1986**, “The Jet Engine”, Fourth Edition, ISBN 0 902121235
- Rowbury, D.A., Oldfield, M.L.G., and Lock, G.D., 1997**, “Engine-Representative Discharge Coefficients Measured in an Annular Nozzle Guide Vane Cascade”, ASME Paper No. 97-GT-99
- Rowbury, D.A., 1998**, “Discharge Coefficients of Nozzle Guide Vane Film Cooling Holes”, DPhil Thesis, University of Oxford
- Rowbury, D.A., Oldfield, M.L.G. and Lock, G.D., 2000**, “A Method for Correlating the Influence of External Crossflow on the Discharge Coefficients of Film Cooling Holes”, ASME Paper 2000-GT-0294
- Sargison, J.E., Guo, S.M., Oldfield, M.L.G., Lock G.D. and Rawlinson, A.J., 2000a**, “Use of Liquid Crystal Techniques for Gas Turbine Film Cooling Study in a Transonic Tunnel”, Paper 409, *Proceedings of the 9<sup>th</sup> International Symposium on Flow Visualisation*, Edinburgh
- Sargison, J.E., Guo, S.M., Oldfield, M.L.G., and Rawlinson, A.J., 2000b**, “The Variation of Heat Transfer Coefficient, Adiabatic Effectiveness and Aerodynamic Loss with Film Cooling Hole Shape”, *Proceedings of the Turbine-2000, International Symposium on Heat Transfer in Gas Turbine Systems*, Turkey
- Sargison, J.E., Guo, S.M., Oldfield, M.L.G., Lock G.D. and Rawlinson, A.J., 2001a**, “A Converging Slot-Hole Film-Cooling Geometry. Part 1: Low Speed Flat-Plate Heat Transfer and Loss”, ASME Paper 2001-GT-0126 to be published
- Sargison, J.E., Guo, S.M., Oldfield, M.L.G., Lock, G.D., and Rawlinson, A.J., 2001b**, “A Converging Slot-Hole Film-Cooling Geometry. Part 2: Transonic Guide Vane Heat Transfer and Loss”, ASME Paper 2001-GT-0127 to be published
- Sargison, J.E., Guo, S.M., Oldfield, M.L.G., Jones, T.V., and Rawlinson, A.J., 2001c**, “A Heat Transfer Study of a Film Cooled Nozzle Guide Vane”, Paper submitted to the Applied Vehicle Technology Panel (AVT) Symposium on “Advanced Flow Management”, Loen, Norway
- Schlichting, H., 1979**, “Boundary-Layer Theory”, Seventh Edition, *McGraw-Hill Book Company*, New York.
- Schultz, D.L. and Jones, T.V., 1973**, “Heat Transfer Measurements in Short-Duration Hypersonic Facilities”, AGARD AG-165
- Schwarz, S.G., and Goldstein, R.J., 1989**, “The Two-Dimensional Behaviour of Film Cooling Jets on Concave Surfaces”, *ASME Journal of Turbomachinery* **111**: 124-130

- Seban, R.A., 1960**, “Heat Transfer and Effectiveness for a Turbulent Boundary Layer with Tangential Fluid Injection”, *ASME Journal of Heat Transfer* **82**: 303-312
- Sen, B., Schmidt, D.L. and Bogard D.G., 1996** “Film Cooling with Compound Angle Holes: Heat Transfer” *ASME Journal of Turbomachinery*, **118**: 800-806
- Sinha, A.K., Bogard, D.G. and Crawford, M.E., 1991**, “Film-Cooling Effectiveness Downstream of a Single Row of Holes with Variable Density Ratio”, *ASME Journal of Turbomachinery*, **113**: 442-449
- Spencer, M.C., Jones, T.V. and Lock, G.D., 1996**, “Endwall Heat Transfer Measurements in an Annular Cascade of Nozzle Guide Vanes at Engine Representative Reynolds and Mach Numbers”, *International Journal of Heat and Fluid Flow*, **17**: 139-147
- Springer, A., 1998**, “Evaluating Aerodynamic Characteristics of Wind-Tunnel Models Produced by Rapid Prototyping Methods”, *Journal of Spacecraft and Rockets*, **35**, No.6: 755-759
- Takahashi, H., Nuntadusit, C., Kimoto, H., Ishida, H., Ukai, T. and Takeishi, K., 2000**, “Characteristics of Various Film Cooling Jets Injected in a Conduit”, *Proceedings of the Turbine-2000, International Symposium on Heat Transfer in Gas Turbine Systems*, Turkey
- Teekaram, A.J.H., Forth, C.J.P., and Jones, T.V., 1989**, “The Use of Foreign Gas to Simulate the Effects of Density Ratios in Film Cooling”, *ASME Journal of Turbomachinery*, **111**: 57-62
- Thole, K.A., Gritsch, M., Schulz, A. and Wittig, S., 1998** “Flowfield Measurements for Film-Cooling Holes with Expanded Exits”, *ASME Journal of Turbomachinery* **120**: 327-336 also ASME Paper 96-GT-174
- Urban, M.F., Hermeler, J., Hosenfeld, H.G., 1998**, “Experimental and Numerical Investigations of Film-Cooling Effects on the Aerodynamic Performance of Transonic Turbine Blades”, ASME Paper 98-GT-546
- Vogel, D., 1998**, “Numerical Investigation of the Influence of Specific Vortex Generation on the Mixing Process of Film Cooling Jets”, ASME Paper 98-GT-210
- Wieghardt, K., 1943**, “Hot Air Discharge for De-Icing”, ATI 24536, original in Deutsche Luftfahrtforschung, Forschungsbericht